Many-electron effects in transition metal and rare earth compounds : Electronic structure, magnetic properties and point defects from first principles

Pascal Delange

NNT : 2017SACLX040

THESE DE DOCTORAT
DE
L'UNIVERSITE PARIS-SACLAY
PREPAREE A
L'ÉCOLE POLYTECHNIQUE

ECOLE DOCTORALE N° 564
Physique en Ile-de-France

Spécialité de doctorat : Physique de la matière condensée

Par

Mr Pascal Delange

Many-electron effects in transition metal and rare earth compounds: Electronic structure, magnetic properties and point defects from first principles

Soutenance de thèse à l'Ecole Polytechnique, Palaiseau, le 29 septembre 2017 :

Composition du Jury :

Mme Odile Stéphan	Professeur, Université Paris-Sud	Présidente
Mr Olle Eriksson	Professeur, Uppsala University	Rapporteur
Mr Frank Lechermann	Professeur, Universität Hamburg	Rapporteur
Mr Dipankar Das Sarma	Professeur, Indian Institute of Science	Examinateur
Mr Igor Abrikosov	Professeur, Linköping University	Examinateur
Mme Silke Biermann	Professeur associée, École Polytechnique	Directrice de thèse
Mr Leonid Pourovskii	Ingénieur de recherche, École Polytechnique	Co-Directeur de thèse

Abstract for the general public

The structural, spectral, magnetic, and many other properties of materials are mostly determined by the behavior of the electrons that glue the atoms together.

Some of the most important technological advances of the 20^{th} century were made in the field of semi-conductors, where electrons behave like a dilute gas of weakly interacting particles. In contrast, many of the most promising materials for technological applications today are oxides. In transition metal or rare earth oxides, but also in some pure metals or alloys, the Coulomb repulsion between the electrons can give rise to exotic properties and phase transitions.

In this thesis, we developed and applied first-principles (i.e. based on fundamental laws of physics) methods to evaluate the behavior of electrons interacting with each other and the physical properties stemming from it. We use these tools to study several materials of fundamental and technological interest, in particular iron, vanadium dioxide and hard magnets.

Résumé "grand public"

Les propriétés structurelles, magnétiques et de conduction des matériaux sont déterminées par le comportement des électrons qui lient leurs atomes.

Parmi les plus importantes avancées technologiques du 20^{e} siècle ont eu lieu dans le domaine des semi-conducteurs, dans lesquels les électrons se comportent comme un gaz peu dense interagissant faiblement. En revanche, les oxydes sont des matériaux prometteurs pour les applications technologiques à venir. Dans les oxydes de métaux de transition ou de terres rares, ainsi que dans certains métaux purs et alliages, la répulsion entre électrons peut donner lieu à des propriétés exotiques et à des transitions de phase.

Dans cette thèse, nous avons développé et utilisé des méthodes partant des "premiers principes" de la physique pour évaluer le comportement d'électrons en interaction et les propriétés physiques qui en découlent. Nous avons appliqué ces outils à plusieurs matériaux, en particulier le fer, le dioxyde de vanadium et les aimants permanents.

Abstract

The topic of this thesis is the first-principles theory of the electronic structure of materials with strong electronic correlations. Tremendous progress has been made in this field thanks to modern implementations of Density Functional Theory (DFT). However, the DFT framework has some limits. First, it is designed to predict ground state but not excited state properties of materials, even though the latter may be just as important for many applications. Second, the approximate functionals used in actual calculations have more limited validity than conceptually exact DFT: in particular, they are not able to describe those materials where many-electron effects are most important.

Since the 1990's, different many-body theories have been used to improve or complement DFT calculations of materials. One of the most significant non-perturbative methods is Dynamical Mean-Field Theory (DMFT), where a lattice model is self-consistently mapped onto an impurity model, producing good results if correlations are mostly local. We briefly review these methods in the first part of this thesis. Recent developments on DMFT and its extensions were aimed at better describing non-local effects, understanding out-of-equilibrium properties or describing real materials rather than model systems, among others. Here, we focus on the latter aspect.

In order to describe real materials with DMFT, one typically needs to start with an electronic structure calculation that treats all the electrons of the system on the same footing, and apply a many-body correction on a well-chosen subspace of orbitals near the Fermi level. Defining such a low-energy subspace consistently requires to integrate out the motion of the electrons outside this subspace. Taking this into account correctly is crucial: it is, for instance, the screening by electrons outside the subspace strongly reduces the Coulomb interaction between electrons within the subspace. Yet it is a complex task, not least because DFT and DMFT are working on different observables. In the second part of this thesis, we discuss low-energy models in the context of the recently proposed Screened Exchange + DMFT scheme. In particular, we study the importance of non-local exchange and dynamically-screened Coulomb interactions. We illustrate this by discussing semi-core states in the d^{10} metals Zn and Cd.

In the third and last part, we use the methods described above to study the electronic structure of three fundamentally and technologically important correlated materials. First, we discuss the physics of point defects in the paramagnetic phase of bcc Fe, more precisely the simplest of them: the monovacancy. Surprisingly for such a simple point defect, its formation energy had not yet been reported consistently from calculations and experiments. We show that this is due to subtle but nevertheless important correlation effects around the vacancy in the high-temperature paramagnetic phase, which is significantly more strongly correlated than the ferromagnetic phase where DFT calculations had been done.

Second, we study the metal-insulator phase transition in the metastable VO_2 B phase. We show that this transition is similar to that between the conventional rutile and M_2 VO_2 phases, involving both bonding physics in the dimer and an atom-selective Mott transition on the remaining V atoms. Motivated by recent calculations on $SrVO_3$, we study the possible effect of oxygen vacancies on the electronic structure of VO_2.

Finally, we propose a scheme beyond DFT for calculating the crystal field splittings in rare earth intermetallics or oxides. While the magnitude of this splitting for the localized $4f$ shell of lanthanides does not typically exceed a few hundred Kelvin, it is crucial for their hard-magnetic properties. Using a modified Hubbard I approximation as DMFT solver, we avoid a nominally small but important self-interaction error, stressing again the importance of carefully tailored low-energy models.

Résumé

Le sujet de cette thèse est la théorie à partir des premiers principes de la structure électronique de matériaux présentant de fortes corrélations électroniques. D'importants progrès ont été faits dans ce domaine grâce aux implémentations modernes de Théorie de la Fonctionelle de Densité (DFT). Néanmoins, la méthode DFT a certaines limitations. D'une part, elle est faite pour décrire les propriétés de l'état fondamental mais pas des états excités des matériaux, bien que ces derniers soient également importants. D'autre part, les approximations de la fonctionnelle employées en pratique réduisent la validité de la DFT, conceptuellement exacte : en particulier, elles décrivent mal les matériaux aux effets de corrélations les plus importants.

Depuis les années 1990, différentes théoriques quantiques à N corps ont été utilisées pour améliorer ou compléter les simulations à base de DFT. Une des plus importantes est la Théorie du Champ Moyen Dynamique (DMFT), dans laquelle un modèle sur réseau est relié de manière auto-cohérente à un modèle plus simple d'impureté, ce qui donne de bons résultats à condition que les corrélations soient principalement locales. Nous présentons brièvement ces théories dans la première partie de cette thèse. Les progrès récents de la DMFT visent, entre autres, à mieux décrire les effets non-locaux, à comprendre les propriétés hors équilibre et à décrire de "vrais" matériaux plutôt que des modèles.

Afin d'utiliser la DMFT pour décrire de vrais matériaux, il faut partir d'un calcul de structure électronique traitant tous les électrons au même niveau, puis appliquer une correction traitant les effets à N corps sur un sous-espace de basse énergie d'orbitales autour niveau de Fermi. La définition cohérente d'un tel sous-espace nécessite de tenir compte de la dynamique des électrons en-dehors de cet espace. Ces derniers, par exemple, réduisent la répulsion de Coulomb entre électrons dans le sous-espace. Néanmoins, combiner la DFT et la DMFT n'est pas aisé car les deux n'agissent pas sur la même observable. Dans la deuxième partie de cette thèse, nous étudions les modèles de basses énergies, comme la technique "échange écranté + DMFT" récemment proposée. Nous analysons l'importance de l'échange non-local et des interactions de Coulomb retardées, et illustrons cette théorie en l'appliquant aux états semi-cœur dans les métaux d^{10} Zn et Cd.

Dans la dernière partie, nous utilisons ces méthodes pour étudier trois matériaux corrélés importants d'un point de vue technologique. Dans un premier temps, nous nous intéressons à la physique des monolacunes dans la phase paramagnétique du fer. De façon surprenante pour un défaut aussi simple, son énergie de formation n'a toujours pas été obtenue de manière cohérente par la théorie et l'expérience. Nous démontrons que cela est dû à de subtils effets de corrélations autour de la lacune dans la phase paramagnétique à haute température : cette phase est plus fortement corrélée que la phase ferromagnétique, où des calculs de DFT ont été faits.

Dans un deuxième temps, nous étudions la transition métal-isolant dans la phase métastable VO_2 B. Nous montrons que cette transition ressemble à celle entre la phase conventionnelle rutile et la phase M_2 de VO_2, mettant en jeu à la fois des liaisons covalentes dans les dimères et une transition de Mott sur les atomes V restants. Nous étudions également l'effet de lacunes d'oxygène sur la structure électronique de VO_2.

Enfin, nous proposons une technique au-delà de la DFT pour calculer le champ cristallin dans les oxydes et alliages de terres rares. Bien que l'amplitude de ce champ soit faible pour les orbitales localisées $4f$ des lanthanides, il est crucial pour leur caractère d'aimant permanent. En modifiant l'approximation Hubbard I pour résoudre les équations de DMFT, nous évitons une erreur d'auto-interaction faible en valeur absolue mais physiquement importante, démontrant à nouveau l'importance de modèles de basse énergie correctement définis.

Acknowledgements

While I had to write the present manuscript by myself, everything else during this thesis certainly was a collective journey. I obtained the results presented in the thesis, and indeed learned most of what I needed to get so far, with the support of all of you that taught me, advised me, stimulated me, since graduating from my engineering studies and even before that.

The most important "thanks" goes, of course, to my two advisors, Silke and Leonid. You helped me make these three years successful by guiding me, counseling me, sharing your ideas and your network and, most importantly, by giving me the freedom to explore the physical problems I was most interested in. Having two advisors with sometimes different but always complementary opinions was really helpful.

I thank my referees, Olle Eriksson and Frank Lechermann, for taking time during their summer holidays to read and review the present manuscript, and of course all of my commitee - including Odile Stéphan, DD Sarma and Igor Abrikosov - for coming to Paris for my defense. I really appreciated your comments that helped me improve the manuscript, as well as your challenging but always insightful questions.

I have met and worked with many amazing people during my three years in this laboratory. I am really grateful to all of you for helping me out to learn the tools of the trade when I first arrived, collaborating with me on papers, proofreading my thesis, allowing me to give oral presentations of my work, making the computer systems work with almost 100% uptime, taking care of the administrative burdens, teaching with me and, last but not least, for all these moments spent together in the coffee room of CPHT and Collège de France, at Magnan, or sometimes in a bar in Paris. I would like to thank all of you (roughly in order of appearance, though that is highly degenerate): Ambroise van Roekeghem, Thomas Ayral, Priyanka Seth, Sophie Chauvin, Feng Wu, Philipp Hansmann Benjamin Madon, Loic Herviou, Antoine Doche, Michel Ferrero, Antoine Georges, Alaska Subedi, Jan Tomczak, Olivier Parcollet, Florence Auger, Malika Lang, Fadila Debbou, Danh Pham Kim, Jean-Luc Bellon, Hong Jiang, Akiyuki Tokuno, Jernej Mravlje, Arnd Specka, Mathias Kobylko, Sébastien Corde, Daniel Suchet, Yiteng Dang, Oleg Peil, Wenya Rowe, Sergei Simak, Yusuke Nomura, Swarup Panda, Giacomo Mazza, Minjae Kim, Wei Wu, Kalobaran Maiti, Takashi Miyake, José Moran, Jakob Steinbauer, Alice Moutenet, Oscar Akerlund, DD Sarma, Steffen Backes, Benjamin Lenz, Marcello Turtulici, Michael Pasek, Laurent Sanchez-Palencia, Julien Despres, Yao Hepeng, Sumanta Bhandary, Anna Galler, Thomas Schäfer... and all the others I may have forgotten in this list. It is your presence that made CPHT one of the best labs to do a PhD!

I am grateful to the Fondation de l'X that sponsored my PhD through the Monge scholarship programme. I was very happy to be part of ERC project CORRELMAT 617196 and DFG-ANR project RE-MAP.

I am, of course, extremely grateful to my whole family for always supporting me in my endeavor and pushing me to enjoy and make the best out of this thesis. None of this would have been possible without you.

And my last words go to you, Sisi, who shared my life since our days as young "polytechniciens", in Palaiseau, Cambridge, Paris and Montrouge. Who knows where the next stop is? It will certainly be a happy one, as long as we are together! Your support has always pushed me to give my best, so let's keep it up!

List of publications

1. *Large effects of subtle electronic correlations on the energetics of vacancies in α-Fe*
   P. Delange, T. Ayral, S.I. Simak, M. Ferrero, O. Parcollet, S. Biermann, L.V. Pourovskii
   Physical Review B 94, 100102(R) (2016)

2. *Novel approaches to spectral properties of correlated electron materials: from generalized Kohn-Sham theory to Screened-Exchange Dynamical Mean Field Theory*
   P. Delange, S. Backes, A. van Roekeghem, L.V. Pourovskii, H. Jiang, S. Biermann,
   Journal of the Physical Society of Japan (accepted, to be published)

3. *Crystal field splittings in rare earth-based hard magnets: an ab initio approach*
   P. Delange, T. Miyake, S. Biermann, L.V. Pourovskii
   Physical Review B 96, 155132 (2017)

4. *Phase transition in the epitaxially stabilized VO_2 (B) phase (working title)*
   P. Delange, B. Pal, L.V. Pourovskii, S. Biermann, D.D. Sarma, *et al.*
   In preparation

Contents

Part I

Introduction

Chapter 1

Correlated materials

1.1 Context

A remarkable early success of quantum mechanics was the determination of the electronic structure and the resulting optical spectrum of the hydrogen atom H. Even at present, this problem is famous for being one of the few fully analytically solvable textbook problems in quantum mechanics. The next step was of course to study the electronic structure of systems with a larger number of particles, in particular with more electrons. These systems may be, for example, molecules and crystals. In this manuscript we will focus on the ideal crystal. In particular we will not discuss the electronic structure of amorphous materials, quasicrystals, or finite size effects in crystals. While these are all important subjects of research, the electronic structure of the perfect crystal is the starting point in the electronic structure calculation of materials. Understanding this important model system is the first step that allows for an understanding of many physical properties of real materials.

The equations that describe a crystal are in fact surprisingly well known. The hamiltonian of a set of N_n nuclei with masses $(M_i)_{i\leq N_n}$ and atomic numbers $(Z_i)_{i\leq N_n}$, and N_e electrons with mass m_0 and charge $-e$ can be written as follows:

$$\begin{aligned} H = &-\sum_{i=1}^{N_n}\frac{\hbar^2}{2M_i}\nabla^2_{\mathbf{r}_i} + \sum_{\substack{i,j=j\\ i<j}}^{N_n}\frac{Z_iZ_je^2}{4\pi\varepsilon_0|\mathbf{r}_i-\mathbf{r}_j|} \\ &-\sum_{i=1}^{N_e}\frac{\hbar^2}{2m_0}\nabla^2_{\mathbf{r}_i} + \sum_{\substack{i,j=j\\ i<j}}^{N_n}\frac{e^2}{4\pi\varepsilon_0|\mathbf{r}_i-\mathbf{r}_j|} - \sum_{i=1}^{N_e}\sum_{j=1}^{N_n}\frac{Z_je^2}{4\pi\varepsilon_0|\mathbf{r}_i-\mathbf{r}_j|} \end{aligned} \tag{1.1}$$

The two first terms represent the kinetic energy and Coulomb repulsion between nuclei, the third and fourth the same quantities for the electrons, and the last term the Coulomb attraction between nuclei and electrons. All the parameters of this Hamiltonian are known with great precision. To this we should add relativistic corrections, the largest one being the spin-orbit coupling between the electron's spin and orbital. Once this is established, though, we still know essentially nothing about the physics of electrons in a crystal. Indeed, a macroscopic quantity of matter (say, a few grams of essentially any solid) contains a number of atoms within a few orders of magnitude of Avogadro's number $\mathcal{N}_A = 6.022\times10^{23}$. Schrödinger's equation for Hamiltonian H, however, can hardly be solved even approximately when the number of particles exceeds 10. Indeed, its full solution is of the form

$$\Psi(\mathbf{r}_1,\mathbf{r}_2...\mathbf{r}_{N_e}) \tag{1.2}$$

The memory necessary to store this many-body wave function increases exponentially with the number of particles: if n_b bytes of memory are needed to store the wave function of one particle, then $n_b^{N_e}$ bytes are needed for the full many-body wave function of N_e particles.

A common approximation to equation 1.1 is the so-called Born-Oppenheimer approximation, that consists in neglecting the degrees of freedom of the nuclei. The justification for this approximation lies in the large difference between the electron mass m_0 and the nucleus mass M_j. Because $M_j > 10^4 \times m_0$ for most atoms, the timescales for electron dynamics and nuclei dynamics are very different, so that it makes sense to study the electronic structure for some instantaneous set of positions of the nuclei.

This leads to the simpler equation

$$H = \sum_{i=1}^{N_e} \left(-\frac{\hbar^2}{2m_0} \nabla^2_{\mathbf{r}_i} + V(\mathbf{r}_i) \right) + \sum_{\substack{i,j=j \\ i<j}}^{N_n} \frac{e^2}{4\pi\varepsilon_0 |\mathbf{r}_i - \mathbf{r}_j|} \tag{1.3}$$

Here, $V(\mathbf{r})$ is a periodic potential with the periodicity of the crystal, created by the nuclei and acting on the electrons. By writing this, we removed an additional term that depends only on the nuclei's relative positions, and becomes constant if only the electronic degrees of freedom are considered.

This approximation does not mean, however, that the lattice dynamics is to be neglected. Phonons (elementary lattice excitations) are at play in many physical phenomena, ranging from indirect gap excitations in semiconductors to the "glue" that binds electron pairs in the Bardeen-Schrieffer-Cooper picture of superconductivity[1], or to the stabilizing mechanism behind the high-temperature body-centered phase of iron, δ-Fe[2]. By writing equation 1.3, all we imply is that it often makes sense to talk about the equilibrium distribution and excitations of electrons in a crystal for a given set of atomic positions, valid at a given time for a duration far longer than that of electron dynamics. The above remark on the impossibility to numerically solve equation 1.1 remains true for equation 1.3. Indeed, we still have to find a many-body wave function with a macroscopic number of particles, which is numerically impossible. The Born-Oppenheimer approximation is no more than a convenient way to separate the dynamics of two many-body problems with different time scales.

Indeed, the term in equation 1.3 that makes the problem so difficult is the right-hand term, that is to say the electron-electron Coulomb repulsion. This term means it is impossible to discuss the wave function $\psi(\mathbf{r}_i)$ of a single electron in the system. Crucially, it is not even possible to discuss the wave function of a single electron *knowing the wave functions of all other electrons*. The only exact description of the system is the many-body wave function $\Psi(\mathbf{r}_1, \mathbf{r}_2 ..., \mathbf{r}_{N_e})$, describing N_e electrons in interaction in a potential created by the nuclei. *Correlations* is the general name we give to the notion that electrons exist as a many-body wave function, or more precisely a wave function beyond a Slater determinant of one-body wave functions

$$\Psi(\mathbf{r}_1, \mathbf{r}_2 ..., \mathbf{r}_{N_e}) = \det\left(\psi_1(\mathbf{r}_1), \psi_2(\mathbf{r}_2), ..., \psi_{N_e}(\mathbf{r}_{N_e})\right) \tag{1.4}$$

so that acting on one electron of a system is impossible without affecting all the others. Correlations may be strong, weak or almost inexistent. This classification obviously depends on the material considered, but also, more subtly, on the probe that is used to study the material of interest. We discuss weakly and strongly correlated materials in section 1.3.

1.2 Electronic band theory: the Bloch theorem and the independent electron picture

Let us suppose for a while that the electron-electron interaction term can be simplified as an effective periodic potential acting on a given electron.

$$H = \sum_{i=1}^{N_e} -\frac{\hbar^2}{2m_0} \nabla^2_{\mathbf{r}_i} + V_{\text{eff}}(\mathbf{r}_i) \tag{1.5}$$

where $V_{\text{eff}}(\mathbf{r})$ is an effective periodic potential created by the nuclei and the mean field of surrounding electrons. While this is a drastic approximation compared to Eq. 1.3, it can still be a reasonable description for some materials. More importantly, this effective periodic potential hypothesis is at work in the

most widely used *ab initio* calculation techniques, that are in turn often used as a starting point for more accurate models describing correlated electrons. In this – much simpler – case, what can we say about the solutions of Schrödinger's equation?

It turns out that the spatial periodicity of the potential simplifies the problem tremendously, and leads to the famous band picture of electrons in a solid. Below, we introduce the Bloch's theorem that, based on the sole assumption of translational invariance, justifies the picture of electronic "bands" forming in a reciprocal space of crystal momentum, and is thus a fundamental theorem of solid state physics.

Bloch's theorem:

If the Hamiltonian H is periodic in space, that is to say H commutes with the translation operator T: $[H, T] = 0$, where T is the translation in space along the Bravais lattice vector $\mathbf{R}$, then the eigenfunctions of H can be written as:

$$H\psi_{n\mathbf{k}}(\mathbf{r}) = \varepsilon_{n\mathbf{k}}\psi_{n\mathbf{k}}(\mathbf{r}) \tag{1.6}$$

with

$$\psi_{n\mathbf{k}}(\mathbf{r}) = e^{i\mathbf{k}.\mathbf{r}}u_{n\mathbf{k}}(\mathbf{r}) \tag{1.7}$$

where $\mathbf{k}$ is a reciprocal space vector within the first *Brillouin zone* (BZ), n is a band index and the function u has the periodicity of the lattice: $u(\mathbf{r} + \mathbf{R}) = u(\mathbf{r})$. All quantities that depend on $\mathbf{k}$ are invariant by translation of any reciprocal lattice vector $\mathbf{k}$, so that we may restrict ourselves to reciprocal vectors $\mathbf{k}$ in the first BZ. For a 1D chain of atoms with spacing a, this amounts to $-\frac{\pi}{a} \leq k \leq \frac{\pi}{a}$. The values that k can take are quantified (by $\frac{\pi}{L}$, with L the crystal size) in a finite crystal, calculated with periodic boundary conditions, but become continuous in a perfect, infinite crystal.

Equation 1.6 means that wave functions in the periodic potential still essentially look like plane waves, or more precisely that they combine a short-range varying eigenfunction multiplied by a longer-range modulating plane wave. This is what is called a Bloch wave. The quantum number defining the plane wave part is its crystal momentum $\mathbf{k}$, similar to a wave vector but periodic in the reciprocal space. However, because the eigenfunctions and eigenvalues are invariant by translation of $\mathbf{k}$ by a reciprocal lattice vector, there is an infinity of acceptable wave vectors likes this. Hence $\mathbf{k}$ is not associated to a momentum through $\boldsymbol{p} = \hbar\mathbf{k}$, but rather to a *pseudomomentum*.

Eigenvalues $\varepsilon_{n\mathbf{k}}$ of the Hamiltonian are indexed by $\mathbf{k}$, the plane wave's wave vector, and n, the band index. These eigenvalues form energy bands of possible energies, with *band gaps* or regions in energy without any admissible wave function in between. The formation of bands can be seen in the *tight-binding model* as a generalization of molecular bonding for a large (infinite) number of atoms, or in the *nearly free electron picture* as a degeneracy lifting opening the parabola of free electrons. Either way, the result is that the electronic structure of materials in the independent electron picture or band picture is formed of energy bands, filled with electrons in increasing energy order, with up to two electrons per state due to the Pauli principle.

This gives two possibilities for a material, depending on its number of electrons and possible overlap of bands.

1. Either the last filled band is completely filled, and it takes finite energy (the band gap E_g) to promote an electron to a higher-lying state. In this case, the material is insulating. The last filled band is then called the *valence band*, the first empty band is called the *conduction band* (because promoting electrons to this band allows electric conduction), and the material is a *band insulator*. In insulators, E_g, and more generally the dispersion relation of the excited states, are quantities of the utmost interest. Other types of insulators, where a localization of electrons due to interactions rather than the filling of a band forbids conductivity, are discussed in chapter 3.

2. Or the last filled band is not completely filled. In this case, the marginal energy cost to go from the ground state to an excited state is 0, and the material is conducting or *metallic*. The density of states at the Fermi level, that is to say the differential number of available states around the

last occupied state, is an important physical quantity, and is one good indicator of the strength of correlations. Indeed, a high density of states at the Fermi level indicates weakly dispersive (hence localized) bands and can cause for instance a Stoner magnetic instability[3] where the electrons rearrange to reduce the Coulomb interaction.

1.3 Beyond band theory: correlations

In reality, as we discussed above, this description is too simplistic. Correlations can appear in different forms, that we briefly discuss qualitatively below, and more in detail in the following chapters. For a general discussion of correlations in a solid, we refer the reader to one of the many textbooks on solid-state physics and many-body physics[4–7].

- One of the most basic and most important ways in which electrons in a solid react to the presence of any given electron on a given site is *screening*. In vacuum, the Coulomb potential between two point charges is
$$V(\mathbf{r}_1 - \mathbf{r}_2) = \frac{q_1 q_2}{4\pi\varepsilon_0 |\mathbf{r}_1 - \mathbf{r}_2|}$$
In presence of a charge density, the potential is screened by a non-trivial dielectric function $\varepsilon(\omega, \mathbf{r}_1 - \mathbf{r}_2)$:
$$V(\mathbf{r}_1 - \mathbf{r}_2) = \frac{q_1 q_2}{4\pi\varepsilon_0 \varepsilon |\mathbf{r}_1 - \mathbf{r}_2|}$$
ε may take different shapes: in metals a simple approximation for screening is Thomas-Fermi screening, which postulates exponential decay of V as a function of distance. In insulators, screening is less efficient and a simple approximation is to take a constant $\varepsilon > 1$.

- Static screening is, in fact, effectively present in the effective potential of equation 1.5, and is compatible with the band picture. Frequency dependent screening $\varepsilon(\omega)$, however, leads to satellite peaks in the emission and absorption spectrum, and accordingly to reduced spectral weight at the Fermi level.

- Landau's Fermi Liquid theory[6, 8] postulates that, when electron-electron interactions are adiabatically turned on in a normal metal, the band picture does not break down completely. More precisely, there exists a one-to-one correspondence between the one-electron excitations of the non-interacting system and the quasi-particles of the interacting system, close to the Fermi level. The quasi-particles are characterized by a lifetime that becomes arbitrarily long close enough to the Fermi level and at zero temperature, and by a renormalized mass (the quasi-particles are heavier than free electrons), synonymous of a spectral weight transfer.

- In more extreme cases, the repulsion between electrons may be so strong that they effectively become localized on a given site. In this case, a material that ought to be metallic according to band theory and electron counting becomes a so-called *Mott insulator*[9]. Mott physics arises when the (screened) Coulomb energy becomes important with respect to the kinetic energy. This is for example the case in many transition metal oxides, including the famous high-T_c superconducting cuprates, as well as in rare-earth based materials. Mott insulators are a typical example (but not the only one) of what we call strongly correlated materials.

Above are but a few examples of how electronic correlations qualitatively modify the effective equations describing electrons in solids, as well as the corresponding physically measurable effects. This list is not a comprehensive one (such a list would be much longer) and, more importantly, these aspects of correlations are not mutually exclusive. Often, a material shows different signs of correlations when probed at different energy levels, and can go from weakly to strongly correlated when a parameter is tuned, for example by electronic doping or by applying pressure.

In the following, for simplicity, we use a unit system where $\hbar = m_e = e^2 = 4\pi\varepsilon_0 = 1$.

Chapter 2

Ab initio electronic structure calculations: from Hartree to the GW approximation

Despite the complexity of studying the electronic structure of materials with a macroscopic number of electrons, enormous progress has been made since the early days of quantum mechanics. Materials have been approached from two somewhat different perspectives. Model-based calculations have been widely used to describe, at least qualitatively, complex physical phenomena occurring in materials. The main goal is to keep only the most relevant physical degrees of freedom in a model as simple as possible. The downside is that such models often have to focus on a certain energy window (for example, physics close to the Fermi level), with phenomena occurring outside this window (for example screening) described by ad hoc parameters. Examples of such models include the Anderson impurity model and the Hubbard model used for strongly correlated materials, or model Hamiltonian techniques used for studying topological insulators.

In contrast, *ab initio* calculations try to take as few parameters as possible, at best none at all, and to make general predictions about a material. Furthermore, there is usually a stronger emphasis on making quantitative, not only qualitative, predictions. Because this requires to take into account a much larger number of electrons and orbitals, *ab initio* approaches usually require some tricks to make computations tractable. As we will see below, a famous and useful approach is to forget about wave functions, and study the electronic density instead.

In the present chapter, we introduce some of the modern techniques used for *ab initio* electronic structure calculations. Models for strongly correlated materials, in particular the Hubbard model, will be discussed in chapter 3. An important subject of modern research, and the subject of the present manuscript, is to interface *ab initio* techniques with more accurate many-body techniques in order to make quantitative predictions for strongly correlated real materials. We will introduce these methods in chapter 4.

2.1 Early approaches: Hartree-Fock theory

The Hartree and Hartree-Fock (HF) theories are two conceptually simple theories, relatively straightforward from the physical point of view (though not necessarily so numerically). As such, they count among the first methods introduced in the 20's to study the electronic structure of materials[10–13]. Both are based on strong approximations, so that purely Hartree or HF calculations for real materials give results that are far from reliable. However, both – in particular HF – remain an important building block in

modern *ab initio* techniques such as hybrid functionals in density functional theory, or a simple reference system in GW theory, which we discuss in section 2.3. For this reason, we believe it is best to introduce the Hartree and HF approximations before moving to more modern techniques.

2.1.1 The Hartree approximation

The Hartree approximation[10, 11] is what we obtain if we consider a variational principle where the wave function of the full Hamiltonian 1.3 is searched for in the form of the most simple many-body wave function there is: a product of one-particle wave functions. In other words, $\Psi(\mathbf{r}_1, \mathbf{r}_2 ... \mathbf{r}_{N_e}) = \psi_1(\mathbf{r}_1) \times \psi_2(\mathbf{r}_2) \times ... \times \psi_{N_e}(\mathbf{r}_{N_e})$. The variational principle then leads to independent one-electron equations:

$$h_i^{\text{Hartree}} \psi_i = \varepsilon_i \psi_i \tag{2.1}$$

$$h_i^{\text{Hartree}} = -\nabla^2_{\mathbf{r}_i} + v^{\text{Hartree}}(\mathbf{r}) \tag{2.2}$$

$$v^{\text{Hartree}}(\mathbf{r}) = \int d\boldsymbol{r'} \frac{\rho(\boldsymbol{r'})}{|\mathbf{r} - \boldsymbol{r'}|} + v_{\text{nuclei}}(\mathbf{r}) \tag{2.3}$$

The Hartree potential contains the potential felt by one electron from the ions and the static, mean-field electron density. The Hartree equations can then be solved self-consistently, by using in the Hartree potential the density $\rho = \sum_{\text{occ}} |\psi_i|^2$. This is reasonably easy to do numerically because the potential in the Hartree Hamiltonian 2.2 is local, i.e. involves a term $v(\mathbf{r})\psi(\mathbf{r})$.

The weakest point of the Hartree method is that the trial wave functions are not antisymmetric with respect to particle permutation, and hence do not respect the Pauli exclusion principle. This causes excessive overlap of the electrons.

2.1.2 The Hartree-Fock method

Hartree-Fock theory, in turn, builds on Hartree theory while forcing wave functions the respect the Pauli principle, i.e. by taking Slater determinants of one-particle wave functions as trial wave functions[12, 13]. By performing again the variational principle over this new set of wave functions we obtain similar equations, with an additional "exchange" or Fock term:

$$h_{i\sigma}^{\text{HF}} \psi_{i\sigma} = \varepsilon_{i\sigma} \psi_{i\sigma} \tag{2.4}$$

$$h_{i\sigma}^{\text{HF}} = -\nabla^2_{\mathbf{r}_i} + v^{\text{Hartree}}(\mathbf{r}) + v_{i\sigma}^{ex}(\mathbf{r}) \tag{2.5}$$

$$v_{i\sigma}^{ex}(\mathbf{r})\psi_{i\sigma}(\mathbf{r}) = -\sum_{j=1}^{N_e} \int d\boldsymbol{r'} \psi_{i\sigma}(\boldsymbol{r'}) \psi_{j\sigma}(\boldsymbol{r'})^* \frac{1}{|\mathbf{r} - \boldsymbol{r'}|} \psi_{j\sigma}(\mathbf{r}) \tag{2.6}$$

Note the sum over j, so that the term $j = i$ removes the interaction of a given electron with itself. Unlike the Hartree term, $\psi_{i\sigma}(\mathbf{r})$ appears in an integral in the HF exchange term, so that Schrödinger's equation involves a term of the form $\int dr' v(\mathbf{r} - \boldsymbol{r'}) \psi(\boldsymbol{r'})$.

The Hartree-Fock method breaks down when screening is important, as it only contains unscreened Coulomb potentials. This is why it performs badly in solids, particularly metals, but somewhat better in molecules. Missing screening means that Hartree-Fock calculations tend to excessively delocalize electrons (contrarily to Hartree), that is to say, to produce excessively dispersive band structures. This shortcoming is however not a critical one. Indeed, we know exactly what physical phenomena are described or not by the Hartree-Fock equations, which makes them a useful tool in hybrid functionals, or a starting point which we may generalize to *screened exchange* (see chapter 6) or GW calculations (see section 2.3).

2.2 Modern approaches: Density Functional Theory, the Kohn-Sham scheme and the GW equations

2.2.1 Density Functional Theory

The huge conceptual and computational difficulty of many-body quantum physics resides in the nature of the question: diagonalizing the Hamiltonian for many-body wave functions that are difficult to imagine – beyond some basic qualitative properties – and perhaps impossible to solve numerically. Indeed, if even drastically simplified theories like HF theory are numerically challenging, is there any reason to believe that we could store in a computer, let alone study the properties of, a wave function that depends on a macroscopic number of variables?

"*If you don't like the answer, change the question*" is the approach followed by Pierre Hohenberg and Walter Kohn in 1964[14], when they introduced *Density Functional Theory* (DFT). As its name indicates, the idea behind DFT is to study not the complicated many-variable wave function $\Psi(\mathbf{r}_1, \mathbf{r}_2 ..., \mathbf{r}_{N_e})$ of the electrons in the solid, but rather the infinitely more simple electronic density $\rho(\mathbf{r})$. The achievement of Hohenberg and Kohn was to show that such a simple approach allows to determine all ground state properties of the system (at least in principle). What has over the years made DFT one of the most popular methods in condensed matter physics, however, is that, perhaps surprisingly, it delivered much more than just that. In particular, as we discuss below, DFT is a useful and lightweight tool to obtain an approximation to excited state properties of materials, even though it is not formally designed for this.

For a general review of DFT, see Ref [15, 16]. For a more historical and retrospective point of view, as well as some remarks on the future of DFT, see the recent review by Jones [17]. Below, we first introduce the Hohenberg-Kohn theorems, and then briefly discuss the Kohn-Sham Ansatz and how practical DFT calculations are performed.

The Hohenberg-Kohn theorems

1. *For a system of interacting electrons described by a Hamiltonian of the shape 1.3, the external potential* $v_{\text{ext}}(\mathbf{r})$ *is uniquely defined (up to an additive constant) by the ground state density* $\rho_0(\mathbf{r})$. *In other words, two different potentials* $v_{\text{ext}}(\mathbf{r})$ *cannot have the same ground state density.*
   Since the external potential in turn fully determines the Hamiltonian, and knowledge of the Hamiltonian defines the expectation value of all observables in the ground state $\langle \hat{\mathcal{A}} \rangle_{GS}$, it follows that all these ground state expectation values can be expressed as a functional of the ground state density $\rho_0(\mathbf{r})$: $\langle \hat{\mathcal{A}} \rangle_{GS} = F_{\mathcal{A}}[\rho_0]$

2. *The ground state energy is given by a Rayleigh-Ritz variational principle over all possible densities,*

$$\forall \rho, E_0 \leq E_{\text{HK}}[\rho] \tag{2.7}$$

   with equality only when $\rho = \rho_0$. $E_{\text{HK}}[\rho]$ *is a functional of the density only, parameterized by the external potential.* E_{HK} *can be written*

$$E_{\text{HK}}[\rho] = F[\rho] + \int v_{\text{ext}}(\mathbf{r})\rho(\mathbf{r})d^3\mathbf{r} \tag{2.8}$$

   where F *is a* universal *functional of the density, and does not depend on the system. Formally,* F *gives the sum of kinetic and Coulomb repulsion energy for a given density* ρ.

The incredible simplification in the Hohenberg-Kohn theorems is the fact that, contrary to intuition, knowledge of the many-body ground state wave function is not required to determine ground state properties: the ground state density is sufficient. As usual, there is no free lunch: the two Hohenberg-Kohn theorems are respectively unicity and existence theorems, but are not constructive: we don't know the formula that gives $F[\rho]$. There is no reason to believe, in fact, that such a "formula" exists in closed analytic form.

At first sight, the practical way to use Hohenberg-Kohn DFT appears to consist, in taking an approximation of $F[\rho]$ and using the variational principle. Much of the success of DFT is due to fact that there exists a better, algorithmic way to find the ground state density. We present this method in the following section.

2.2.2 Kohn-Sham equations and approximate functionals

Very often in condensed matter theory, a practical way to solve a complicated problem with correlations present is to make use of a simpler reference system with similar properties. This approach is used, as we have seen, in HF theory; another typical example is the mean-field treatment of a spin in an Ising model or, as we will see in chapter 3, an impurity model in Dynamical Mean Field Theory. Often, the best reference model is a simple one. However, not all reference models are good, and finding the one that is useful in practice is usually difficult. The second important step that made the success of DFT was the introduction of such a reference system, to be used in an algorithm that solves (at least approximately) the original problem. Kohn and Sham proposed in 1965[18] to use a reference system of non-interacting electrons to solve the Hohenberg-Kohn variational principle.

The ground state energy functional of equation 2.8 can as well be written

$$E_{\mathrm{HK}}[\rho] = T_s[\rho] + \int v_{\mathrm{ext}}(\mathbf{r})\rho(\mathbf{r})d^3\mathbf{r} + \int v_{\mathrm{Hartree}}(\mathbf{r})\rho(\mathbf{r})d^3\mathbf{r} + E_{xc}[\rho] \tag{2.9}$$

where $T_s[\rho]$ is the ground-state kinetic energy of a set of non-interacting electrons with density ρ. We call the new functional $E_{xc}[\rho]$ the *exchange-correlation* functional. We did not introduce any new information, because $E_{xc}[\rho]$ is formally unknown, just as is $F[\rho]$. In practice, however, removing all the terms that are known from the functional, in particular large ones like the Hartree energy and the kinetic energy, should make it easier to find approximations to the exact functional.

In Kohn-Sham (KS) DFT, we study a system of non-interacting electrons in an external potential v_{KS}, defined such that the ground state density ρ_{KS} of this effective system is identical to the ground state density ρ_0 of the initial system. This is useful only if we can deduce the ground state electronic density and total energy of the interacting system, from the same quantities calculated in the effective non-interacting system. We will now see how this can be done in practice.

By applying the variational principle 2.7 to equation 2.9, we obtain

$$\frac{\partial E[\rho, V_{\mathrm{ext}}]}{\partial\rho(\mathbf{r})} = \frac{\partial T_s}{\partial\rho(\mathbf{r})} + v_{\mathrm{ext}}(\mathbf{r}) + v_{\mathrm{Hartree}}(\mathbf{r}) + \frac{\partial E_{xc}[\rho]}{\partial\rho(\mathbf{r})} + \mu \tag{2.10}$$

where μ is the Lagrange multiplier associated with the constraint of conserved particle number, $\int\rho(\mathbf{r})d\mathbf{r} = N_e$. On the other hand, applying the same variational principle to the corresponding equation for a system of non-interacting particles in some external potential v_{KS}, we obtain

$$\frac{\partial E[n]}{\partial\rho(\mathbf{r})} = \frac{\partial T_s}{\partial\rho(\mathbf{r})} + v_{\mathrm{KS}}(\mathbf{r}) + \mu \tag{2.11}$$

Equations 2.10 and 2.11 give the same stationarity condition if the Kohn-Sham potential v_{KS} is such that

$$v_{\mathrm{KS}}(\mathbf{r}) = v_{\mathrm{ext}}(\mathbf{r}) + v_{\mathrm{Hartree}}(\mathbf{r}) + v_{xc}(\mathbf{r}) \tag{2.12}$$

$$v_{xc}(\mathbf{r}) = \frac{\partial E_{xc}[\rho]}{\partial\rho(\mathbf{r})} \tag{2.13}$$

The calculation scheme consists in solving the Schrödinger equation for the effective set of non-interacting electrons with potential v_{KS}, where this very potential depends on the density of the system as per equation 2.12 and has to be obtained self-consistently. This procedure is in principle exact, as long as stationarity of the self-consistency equation 2.12 is reached.

In practice, approximations have to be made, since we still do not know the exchange-correlation functional $E_{xc}[\rho]$, nor the corresponding potential v_{xc}.

2.2.3 Exchange-correlation potentials in practice

While the true exchange-correlation functional is not known exactly, the original publication by Kohn and Sham[18] introduced an approximate functional that allowed computationally inexpensive calculations to be done with high precision. Their *Local Density Approximation* (LDA) treats the Kohn-Sham potential as a local potential. Its value is equal, at each point in space $\mathbf{r}$, to the exchange-correlation potential of a homogenous electron gas with density equal to the density $\rho(\mathbf{r})$.

$$E_{xc}^{\mathrm{LDA}}\left[\rho(\mathbf{r})\right] = \int d^3\mathbf{r}\rho(\mathbf{r})\varepsilon_{xc}\left[\rho(\mathbf{r})\right] \tag{2.14}$$

For a homogenous electron gas, the exchange energy density is known analytically as $\varepsilon_x\left[\rho\right] = -\frac{3}{4}\left[\frac{3}{\pi}\rho\right]^{\frac{1}{3}}$. The correlation part, on the other hand, has been computed numerically using a quantum Monte-Carlo method[19]. As its name indicates, the LDA exchange-correlation potential is local: this was implied in equation 2.12, but is not necessary. It is, in fact, a rather drastic approximation, indeed one that was corrected in more recent approximate potentials. DFT with LDA exchange-correlation potential tends to excessively delocalize electrons (in other words, to overestimate bonding). It also suffers from self-interaction, known as the erroneous interaction of a given electron with itself through the exchange-correlation potential, or missing correction of the self-interaction term in the Hartree term by the exchange-correlation potential. Self-interaction is particularly problematic on atoms with localized orbitals, where correlations are usually the strongest. Conceptually, it is most easily seen in the H atom, where DFT LDA predicts wrong ionization energies even though the system has only one electron and should therefore not have exchange nor correlations.

Still, the locality of the LDA exchange-correlation potential means that converging DFT calculations using the KS ansatz and the LDA potential is about as fast as Hartree calculations, and orders of magnitude faster than HF calculations or derivatives thereof, that were largely used before DFT. Partly non-local exchange-correlation functionals with the same computational advantage have been introduced[20–23], commonly known as *generalized gradient approximation* (GGA), where the same form of equation 2.14 is kept but $\varepsilon_{xc}^{\mathrm{GGA}}$ also depends on the local gradient of ρ, and not only the value of ρ itself. Other extensions of DFT, usually called hybrid functionals[24], use a fraction of exact Fock exchange. They further improve on the non-local exchange and improve many structural properties. However, hybrid functionals are (like HF exchange) defined in terms of orbitals and not just density, hence carry the full computation cost of nonlocal HF calculations.

2.2.4 Obtaining spectra from density functional theory

DFT at first suffered significant criticism on two fronts: first on the lack of control of the approximations that are made on the exchange-correlation potential, second by prominent condensed matter theorists because of the lack of physical insight in the results, since DFT can feel like a "black box". However, since it was realized in the early 1990's in the chemistry community that DFT gave better predictions of most structural and physical parameters of a whole range of molecules than HF-based methods, DFT and its derivatives have become one of the most ubiquitous methods in both applied and theoretical chemistry and condensed matter physics.

In principle, DFT is only a ground state theory, and can only be used to predict quantities such as crystal structures, lattice parameters, bond lengths, ionization energies, as well as the energetic response to all kinds of structural changes. Yet, part of the success of DFT is that, in many cases, DFT can be used to predict spectra (photoemission, optics) with remarkably little error, or at least with somewhat systematic, hence predictable errors.

The Kohn-Sham reference system of non-interacting electrons in a self-consistent potential is only designed so that after convergence, the electronic density is equal to the ground state density of the real system. In the KS scheme, one computes the eigenvalues of the KS Hamiltonian, which gives a set of Bloch eigenfuctions and energy eigenvalues, so that one may associate a band structure to the interacting

system. There is no a priori reason to expect this band structure to describe the interacting system correctly, except for one energy value: the energy of the highest lying occupied state should be equal to the first ionization energy, due to the identification of Lagrange parameter μ as the chemical potential in equation 2.10. In practice, it turns out that Kohn-Sham DFT band structures are very often at least qualitatively close to measured quasi-particle excitation energies, with systematic and well known errors on some parameters, such as band gaps in insulators and band widths. It is very common to simply talk of "the DFT band structure" instead of "the band structure of the KS Hamiltonian calculated for the DFT density": we will do the same in this thesis.

To conclude, let us note that we have not mentioned here one of the most critical aspects of the development of DFT techniques. There has been a huge effort since the early days of DFT to develop software that solves the KS equations in an efficient, precise and reproducible way. This required, above all, considerable effort on the optimization of basis sets that are used: plane-waves, augmented plane-waves (APW)[25], linearized muffin-tin orbitals (LMTO)[26], full-potential linearized augmented plane-waves (FLAPW)[27]... as well as pseudo-potentials[25] for a simplified treatment of core electrons in some codes. There are tens of available codes, optimized for different types of systems. For our DFT calculations, we used the Wien2k software[27], an all electron, FLAPW implementation of DFT. The aim of the present thesis is not to compare technical aspects of DFT, but rather to look at methods beyond DFT for real material electronic structure calculations, hence we will not dwell further on this subject.

2.3 Many-body theory: Hedin's equations and perturbation theory

2.3.1 Hedin's equations

Often, computing wave-functions of a complicated Hamiltonian is not the best approach. In DFT, this idea leads to the use of the electronic density as the main variable, but calculating quasi-particle excitations beyond the band picture is then difficult. To compute these, precisely, the Green's function formalism can be useful. We remind some definitions for Green's functions in Appendix B.

In 1965, Lars Hedin[28] introduced a closed set of coupled integral equations, using the full many-body Hamiltonian and the equations of motion, now known as Hedin's equations. They can be expressed as follows, where a variable i represents space and time dependence (r_i, t_i), and i^+ always comes before i in time-ordered Green's functions:

$$G(1,2) = G_0(1,2) + \int d(34) G_0(1,3)\Sigma(3,4)G(4,2) \tag{2.15}$$

$$\Gamma(1,2,3) = \delta(1,2)\delta(1,3) + \int d(4567) \frac{\partial \Sigma(1,2)}{\partial G(4,5)} G(4,6)G(7,5)\Gamma(6,7,3) \tag{2.16}$$

$$P(1,2) = -i \int d(34) G(1,3)\Gamma(3,4,2)G(4,1^+) \tag{2.17}$$

$$W(1,2) = v(1,2) + \int d(3,4) v(1,3)P(3,4)W(4,2) \tag{2.18}$$

$$\Sigma(1,2) = i \int d(3,4) G(1,3^+)W(1,4)\Gamma(3,2,4) \tag{2.19}$$

They involve the one-body Green's function G, the screened Coulomb interaction W, the polarization P, the self-energy Σ and the vertex function Γ.

The screened Coulomb interaction W describes how two charges, present in the solid, interact: the usual Coulomb repulsion, that decays as $1/r$ in the vacuum, decays much faster due to the screening from all the other charges present in the solid. The polarization P is precisely what determines how these other charges react: in fact, Eq. 2.18 is the equivalent of the Dyson equation 2.19 (see also Eq. B.8

and B.9 in the Appendix) for the Coulomb interaction, where the polarization takes the place of a self-energy. Finally, the vertex Γ is a diagrammatic object containing the "bare" vertex $\Gamma = 1$ and the vertex corrections corresponding to higher-order electron-electron and electron-boson couplings. Γ is expected to be small in weakly interacting systems.

Hedin's equation are formally exact, but solving them in practice is quite intractable. A self-consistent scheme could in principle be used, but computing the integrals is a formidable computational task, and even then the procedure can easily become divergent. This should not come as a surprise: since the original problem is computationally intrinsically complex, an exact method can hardly be expected to solve it in a simple way. In practice, approximations are required to use Hedin's equations for model systems, let alone real materials.

2.3.2 The GW equations

One such approximation, commonly used, is the so-called GW approximation[28]. For a review on the GW method, see for instance [29, 30], or [31] for a more recent point of view. It does not take its name from the person who first derived it, but from the formula used for the self-energy: $\Sigma = iGW$. More specifically, the GW approximation is obtained by neglecting the integral term, that is to say the most difficult to calculate, in the vertex Γ in equation 2.16. This leads to a simplified set of equations

$$G(1,2) = G_0(1,2) \tag{2.20}$$
$$\Gamma(1,2,3) = \delta(1,2)\delta(1,3) \tag{2.21}$$
$$P(1,2) = -iG(1,2)G(2,1^+) \tag{2.22}$$
$$W(1,2) = v(1,2) + \int d(3,4)v(1,3)P(3,4)W(4,2) \tag{2.23}$$
$$\Sigma(1,2) = iG(1,2)W(2,1^+) \tag{2.24}$$

with equation 2.24 giving its name to the method. We now have a simpler set of equations, that can be used for real systems (though they are still much more computationally challenging to solve than the DFT equations). They are typically used in a *one-shot* scheme, rather than self-consistently like Hedin's equations, so that we sometimes call this method "G_0W_0". One starts from a non-interacting Green's function G_0, obtains a polarization P, the corresponding dynamical screened exchange W, and finally a self-energy Σ. One can then obtain a k and ω-resolved spectrum by constructing the interacting Green's function G from Dyson's equation 2.15.

This supposes that we know a reasonable non-interacting initial Green's function G_0. In practice, a converged DFT spectrum is often a convenient starting point, for which the GW self-energy correction to the spectrum significantly improves agreement with measured spectra for many materials, metals or semi-conductor, at least when correlations are not too strong. This is one of the reasons why actual implementations of GW were done much later than implementations of DFT: working DFT codes were needed to apply the equations that were derived in the same year as the KS equations. Even now, GW calculations are not routinely done for metallic systems. In Fig. 2.1, we give an example of how a one-shot GW calculation improves the band structure and in particular the band gap of semiconducting Si.

Self-consistency in the GW approximation

On the other hand, for all its successes, this procedure is not intellectually very satisfying, and it would be desirable to obtain results that are independent from the starting point. In principle, an intuitive form of self-consistency can be introduced by updating G using Dyson's equation, computing new P, W, Σ, until convergence is reached. This of course increases the computational cost very significantly, but is still possible. A limited version of self-consistency, the GW_0 approximation, consists in keeping $W = W_0$, and only converging with respect to G. In both cases, the surprising result is that self-consistency seems to make agreement with measured band structures worse[32, 33], as the bands become wider, while the

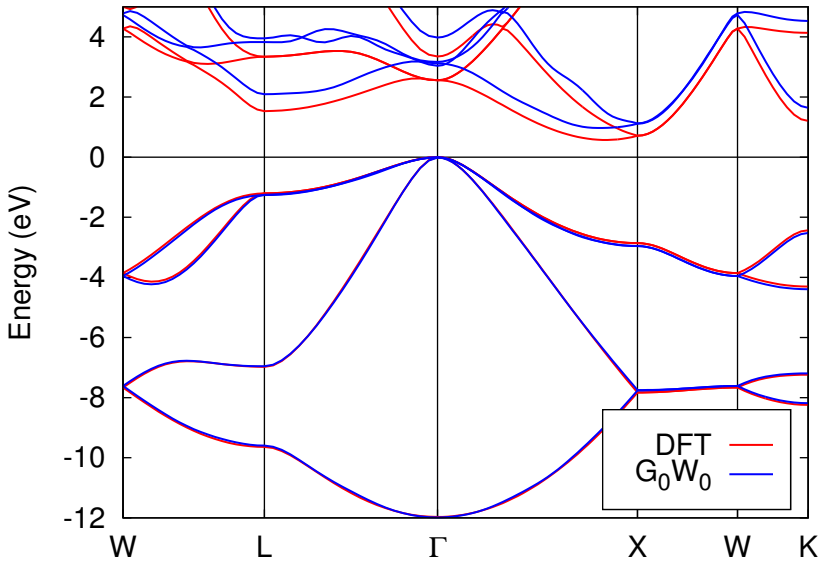

Figure 2.1 – DFT LDA and GW (G_0W_0) band structure of Si. The band gap E_g is severely underestimated in DFT (0.52 eV) compared to the experimental band gap (1.17 eV). The GW calculation (0.96 eV) partly corrects this, without significantly changing the overall shape of the occupied or excited part of the spectrum. The GW calculation is performed on a 10x10x10 Brillouin zone mesh.

satellites are broadened and lose spectral weight. Surprisingly, full self-consistency seems to be worse than the partial variant, as the screened interaction W suffers from the previous effects. The generally held opinion is that G_0W_0 improves on the non-interacting quasi-particles energies but does not give correct quasi-particle weights, and self-consistency only enhances this error. Local vertex-corrections in Eq. 2.24 (to restore Eq. 2.19) have been studied[34]. A similar idea is also behind the GW+EDMFT method, that we discuss in the following chapter (4.4).

On the other hand, self-consistency in GW may be useful to determine total energies, as such a scheme would satisfy conservation equations[35]. Calculations on the electron gas[36] seem to support this view.

An alternative way to treat self-consistency is quasi-particle self-consistent GW, as proposed by van Schilfgaarde *et al.*[37]. The physical intuition behind quasi-particle self-consistent GW was already present in the review by Aryasetiawan[29]. Instead of using the GW equations 2.20 to 2.24 in a loop, a non-interacting Hamiltonian H^0 is constructed (self-consistently) such that the time-dependence of this non-interacting system is as close as possible to that of the interacting system, computed within GW. This procedure was shown to improve band gaps in a wide range of semi-conductors, compared to simple one-shot GW calculations.

GW in practice

A last weak point of the GW method comes from the technical challenge in actually implementing it. It is twofold. First, the full GW polarization, self-energy and Green's function with $\mathbf{k}$ and ω dependence are computationally heavy objects. In systems with many particles, manipulating them is complicated, the scaling both of computation time and memory usage with the particle number and the Brillouin zone discretization is not favorable (at best $O(N^3)$ in the number of atoms and $O(N_k)$ in the Brillouin zone discretization).

Second, the output of a GW calculation, and in particular the calculation of the screened interaction

W, is strongly sensitive to the choice of basis functions and **k**-mesh[38–40]. Therefore, band structures calculated within the GW approximation tend to vary a lot between different codes (at least for metals). Even for a given code, convergence of the basis set may be excessively slow. This is to be compared with usual implementations of DFT that are much less sensitive to such issues.

Simplified forms of GW

An interesting feature of GW theory is that, in its diagrammatic form, it appears as a very natural improvement on HF theory. Indeed, HF is obtained as a (very) simplified GW theory if we set $P = 0$, hence $W = v$. The HF self-energy can then simply be expressed as $\Sigma_{\text{HF}} = iGv$. As mentioned in section 2.1, one important shortcoming of HF theory is the fact that it ignores the screening of Coulomb interactions by the charges present in the solid. It is then natural (though this is not a formal proof of the method) to replace the bare Coulomb interaction v by the fully screened, dynamic interaction $W(\mathbf{k}, \omega)$.

As full-fledged GW calculations are still heavy, further approximations may be introduced. One such approximation, introduced by Hedin in 1965 in his seminal paper, is the Coulomb Hole - Screened Exchange (CoHSEx) approximation, that separates the poles due to the Green's function G and poles due to the screened interaction W in the integral expression of the self-energy. The real part of the self-energy is then given by the sum of

$$\text{Re}\Sigma_{\text{SEx}}(\mathbf{r}, \mathbf{r}', \omega) = -\sum_{i}^{\text{occ}} \psi_i(\mathbf{r})\psi_i^*(\mathbf{r}')\text{Re}W(\mathbf{r}, \mathbf{r}', \omega - \varepsilon_i) \tag{2.25}$$

$$\text{Re}\Sigma_{\text{CoH}}(\mathbf{r}, \mathbf{r}', \omega) = \sum_{i} \psi_i(\mathbf{r})\psi_i^*(\mathbf{r}') \int_0^\infty d\omega' \frac{D(\mathbf{r}, \mathbf{r}', \omega')}{\omega - \varepsilon_i - \omega'} \tag{2.26}$$

where $D(\mathbf{r}, \mathbf{r}', \omega') = -\frac{1}{\pi}\text{Im}W^c(\mathbf{r}, \mathbf{r}', \omega')$ and $W^c = W^c - v_{\text{bare}}$ is the frequency-dependent part of W.

Such a decomposition can always be made, but it becomes more simple in the static approximation where the Coulomb hole term becomes local:

$$\Sigma_{\text{SEx}}(\mathbf{r}, \mathbf{r}') = -\sum_{i}^{\text{occ}} \psi_i(\mathbf{r})\psi_i^*(\mathbf{r}')W(\mathbf{r}, \mathbf{r}', \omega = 0) \tag{2.27}$$

$$\Sigma_{\text{CoH}}(\mathbf{r}, \mathbf{r}) = \frac{1}{2}\delta(\mathbf{r} - \mathbf{r}')\left[W(\mathbf{r}, \mathbf{r}', \omega = 0) - v(\mathbf{r} - \mathbf{r}')\right] \tag{2.28}$$

The GW self-energy is then separated into two terms, one of which is purely local:

$$\Sigma_{GW} \approx \Sigma_{\text{SEx}}(\mathbf{k}) + \Sigma_{\text{CoH}} \tag{2.29}$$

$\Sigma_{\text{SEx}}(\mathbf{k})$ can be seen as the HF exchange self-energy with static screening, and Σ_{CoH} corresponds to the interaction energy between a quasi-particle and the exchange hole created around itself due to screening. CoHSEx calculations are not as accurate as GW calculations, but being static they do not suffer the same issues as GW as far as self-consistency is concerned. Moreover, CoHSEx represents a good starting point to understand more complicated methods based on the GW approximation, so we will come back to this concept when we discuss the validity of DFT+DMFT in chapter 4 and chapter 6.

Chapter 3

When correlations are too strong: the Hubbard model and Dynamical Mean Field Theory

The DFT and GW methods both describe the physics of *correlated* electrons, in the sense that both take into account electron-electron interactions beyond Hartree and Fock exchange. In particular, both methods contain the notion of electronic screening – explicitly for GW, self-consistently in the one-particle Kohn-Sham potential for DFT. Both methods, however, break down when calculating the properties of *strongly correlated* systems, where the notion of *strong correlations* depends on a criterion to be defined below.

In the case of GW, this breakdown happens because of the neglected vertex when going from Hedin's equations to the GW equations. DFT is in principle expected to give exact results for ground state properties of such systems, but:

1. Approximate exchange-correlation functionals, in particular simple ones like the LDA functional, work better for systems with delocalized electrons

2. One-particle spectra obtained from KS DFT (which, as we mentioned, have no *a priori* reasons to coincide with measured spectra) tend to be qualitatively worse for such systems

While comparison with experiments is an obvious way to determine whether or not a material behaves as predicted in GW or DFT, hence if it should be considered *strongly correlated* or not, it is a longstanding goal of electronic structure theory to determine this *a priori*, and of course to determine the physics of strongly correlated materials.

When studying such systems, it is often convenient to study low energy models with a reduced number of degrees of freedom, typically involving only electrons around the Fermi level. In this section, we discuss low energy models often used to study strongly correlated systems, and some techniques to solve them. We further discuss how such models can be defined and parameterized in chapter 4.

3.1 The Hubbard model and the Mott transition: from band theory to local physics

In 1963[41], John Hubbard defined an improved tight-binding model including electron-electron interactions, the eponymous Hubbard model, also derived by Kanamori and Gutzwiller in the same year[42, 43].

Many variations exist, but the simplest form of Hubbard's model describes one band, nearest-neighbor hopping and on-site interactions only. It can be written in second quantization as

$$H = (\epsilon_0 - \mu) \sum_{i,\sigma} n_{i\sigma} - \sum_{\langle i,j \rangle,\sigma} t_{ij} \left(c^\dagger_{i\sigma} c_{j\sigma} + c^\dagger_{j\sigma} c_{i\sigma} \right) + U \sum_i n_{i\uparrow} n_{i\downarrow} \tag{3.1}$$

where the sum $\langle i, j \rangle$ runs over all pairs of nearest neighbor sites of the lattice, ϵ_0 is the reference energy level of the band, μ the chemical potential, t_{ij} the hopping amplitude between sites i and j, and U the on-site Coulomb interaction strength. This Hamiltonian is fairly simple, but it is not analytically solvable (except in one dimension) because of the $U n_{i\uparrow} n_{i\downarrow}$ interaction term. In fact, Hamiltonian 3.1 is widely considered to contain most of the physics of a wide range of strongly correlated materials, not least the high-temperature superconductors of the cuprates family[44, 45]. It has a complex phase diagram in terms of the lattice shape (square, triangular, Bethe...), t, U, μ (or electron count), temperature T, and dimension[46, 47]. In the limit of $t/U \to 0$, the electrons are completely localized while in the opposite limit of $t/U \to \infty$, the band picture of non-interacting particles is recovered.

If such a model is to describe a real material, even qualitatively, then physically relevant values for the parameters, in particular t and U, must be chosen. These values depend on the full electronic structure, while the Hubbard model only describes the physics of a band around the Fermi level. Moreover, in most real systems a multi-orbital model is required. We come back to the derivation of such a lattice model from the full many-body problem in chapter 4. Here, we first discuss methods that can be used to study the Hubbard model.

3.2 How to solve the Hubbard model: Dynamical Mean-Field Theory

3.2.1 The Curie-Weiss mean-field

The concept of a *mean field* is an important one in physics, first introduced in the context of phase transitions by Curie and Weiss in the early 20$^{\text{th}}$ century[48, 49]. The most simple example of mean-field theory is given in the case of the Ising model[50]. This Ising model describes a set of spins $\{s_i\}$ on a lattice, coupled to one-another by an exchange interaction J between nearest neighbors $\langle i, j \rangle$ and in an external uniform magnetic field h_{ext}.

$$H = -J \sum_{\langle i,j \rangle} s_i s_j - h_{\text{ext}} \sum_i s_i \tag{3.2}$$

where s_i can take the values ± 1. In practice, s_i represents the z component S^z_i of a full spin operator $\vec{S}_i$, and J stems from the exchange interaction of electrons rather than direct spin-spin coupling. If $J < 0$, two neighboring spins lower the energy level by pointing in opposite directions, and the ground state of this Ising model is fully antiferromagnetically ordered (in the absence of frustration in the lattice, for example on a 2D square lattice). If $J > 0$, on the other hand, the ground state is ferromagnetically ordered.

While determining the ground state of the ferromagnetic Ising model is fairly simple, things become more complicated at non-zero temperature. The Ising Hamiltonian is in essence a many-body Hamiltonian, so that direct calculation of the partition function is not possible. Thus, computing the magnetization is not trivial. At high temperature, entropy is dominating and the Ising model paramagnetic, with a symmetry breaking to the ferromagnetic phase as the temperature is lowered.

Let us isolate a given spin s_0. The Hamiltonian acting on this spin is

$$H_0 = \left(-J \sum_{\langle 0,j \rangle} s_j - h_{\text{ext}} \right) s_0$$

$$H_0 = - \left(Jzm + J \sum_{\langle 0,j \rangle} (s_j - m) + h_{\text{ext}} \right) s_0 \tag{3.3}$$

where z is the number of nearest neighbors of a given spin (or connectivity of the lattice) and $m = \langle s_i \rangle$.

The Curie-Weiss mean-field approximation consists in neglecting the second term in the brackets, containing the fluctuations around the average of the neighboring spins, in second order in the fluctuations (the first order term is zero by construction). This becomes justified in the infinite dimension limit, where the central limit theorem ensures that the sum over all neighboring sites of this fluctuation stays smaller than the first term, Jzm, by a factor of the order of $\sqrt{z}$. Our spin s_0 is then only feeling an effective field depending on the average magnetization m

$$h_{\text{eff}} = Jzm + h_{\text{ext}} \tag{3.4}$$

The partition function of Hamiltonian H_0 is readily obtained as

$$Z_0 = 2 \cosh \left(\frac{h_{\text{ext}} + zJm}{k_B T} \right) \tag{3.5}$$

where k_B is the Boltzmann constant and $\beta = \frac{1}{k_B T}$. From this one can self-consistently compute the average magnetization

$$m = \tanh \left(\beta (h_{\text{ext}} + zJm) \right) \tag{3.6}$$

predicting a paramagnetic to ferromagnetic transition below $T_c = \dfrac{zJ}{k_B}$. The mean-field description is of course a strong approximation: it assumes that fluctuations around the mean value are negligible.

Still, even in finite dimensions, a mean field theory can give a good picture of the physical behavior. A classical result of statistical field theory is that for continuous order parameters (which is not the case of the Ising model) and in dimensions $d \geq 4$, the critical exponents computed with mean-field theories are exact. In dimension $2 \leq d < 4$, fluctuations modify the critical exponents but the phase transitions stay. Only when $d < 2$, the Mermin-Wagner theorem states that long-range fluctuation destroy long-range order.

3.2.2 From Ising to Hubbard: a mean-field description of the electrons

Since the Hubbard model is defined on a lattice, like the Ising model, it is rather natural to consider a mean-field approximation. However, the physics of the Hubbard model is much more complex than the one of the Ising model. Indeed, in the simplest limiting case, the half-filled Hubbard Hamiltonian can be shown to simplify to the antiferromagnetic Heisenberg model in the limit of infinite U[51]. It follows that we cannot expect a simple scalar mean-field to describe the system well, like in the case of the Ising model: the mean-field parameter has to be something more complex than a scalar.

A first important step towards solving the Hubbard model was made by Metzner and Vollhardt, who showed in 1989[52] that a limit of infinitely large lattice coordination z can be defined for the Hubbard model if the hopping parameter is adequately renormalized by $\sqrt{2z}$. Furthermore, it was shown in the same year that the self-energy becomes local in this limit[53].

The second step came in 1992, when Georges and Kotliar[54] showed that the lattice Hubbard model can be self-consistently mapped onto a local impurity problem of an atom with local Coulomb interactions, exchanging electrons with a bath. Similarly to the mean-field treatment of the Ising model, this implies

to make an approximation, namely to consider a purely local self-energy. As previously mentionned, this approximation becomes exact in the limit of infinite coordination, as well as in the limit of vanishing hopping. The equivalent in DMFT of an isolated spin in an self-consistent magnetic field in the Ising model, is then an isolated atom, exchanging electrons with a self-consistent bath.

For a general review on DMFT, we refer the reader to the review paper by Georges *et al.* [55], or [47] for a more qualitative description.

3.2.3 The Anderson impurity model

The Anderson impurity model (AIM) was first introduced in 1961 by Anderson[56] to describe magnetic impurities in a metal, to treat Kondo-like problems. The AIM Hamiltonian can be written as follows:

$$\begin{aligned} H_{\text{AIM}} &= H_{\text{atom}} + H_{\text{bath}} + H_{\text{coupling}} \\ H_{\text{atom}} &= U n_\uparrow n_\downarrow + (\varepsilon_0 - \mu)(n_\uparrow + n_\downarrow) \\ H_{\text{bath}} &= \sum_{l\sigma} \varepsilon_{l\sigma} a^\dagger_{l\sigma} a_{l\sigma} \\ H_{\text{coupling}} &= \sum_{l\sigma} V_l (c^\dagger_\sigma a_{l\sigma} + a^\dagger_{l\sigma} c_\sigma) \end{aligned} \tag{3.7}$$

where $c^\dagger_\sigma$ creates an electron with spin σ on the atom and $a^\dagger_{l\sigma}$ creates an electron with spin σ and energy $\varepsilon_{l\sigma}$ in the bath (that is to say, e.g. a conduction electron). The coupling term is exchanging electrons between the atom and the bath. The bath electrons are considered to be non-interacting, but the electrons on the local atom carry the full local Coulomb interaction term $U n_\uparrow n_\downarrow$.

The critical point is that, while directly solving the full Hubbard model is rather untractable, efficient and numerically exact methods exist for solving such impurity models. One method that was widely used throughout this thesis is continuous time quantum Monte-Carlo (CTQMC). For a review of CTQMC techniques, we refer the reader to Ref. [57].

3.3 The Dynamical Mean-Field Theory equations

In this part, we derive the DMFT equations using the cavity method, following the review paper by Georges *et al.* [55]. We already employed this same cavity method above on the Ising model (without citing its name); it turns out that a similar method can be used to derive a solution for the Hubbard model in infinite dimensions.

The Hubbard model, written in Hamiltonian form in Eq. 3.1, can equivalently be expressed using a path integral formalism[58]. The Hubbard action is given by

$$S_{\text{Hubbard}} = \int_0^\beta d\tau \left[-\sum_{ij\sigma} c^\dagger_{i\sigma}(\tau) \left((\partial_\tau - \mu)\, \delta_{ij} + t_{ij} \right) c_{j\sigma}(\tau) + U \sum_i n_{i\uparrow}(\tau) n_{j\downarrow}(\tau) \right] \tag{3.8}$$

From this action, the partition function is calculated as an integral over all Grassmann variables $c_{i\sigma}, c^\dagger_{i\sigma}$:

$$Z = \int \prod_{i,\sigma} \mathcal{D}\left[c^\dagger_{i\sigma} c_{i\sigma} \right] e^{-S_{\text{Hubbard}}} \tag{3.9}$$

Similarly to the above treatment of the Ising model, one may choose a given site (say, site 0) of the lattice, and split the full action into three terms: a local action on site 0 (S_0), an action containing the terms coupling site 0 to the others (ΔS), and the rest, $S^{(0)}$, describing the lattice with site 0 removed.

$$S_{\text{Hubbard}} = S_0 + \Delta S + S^{(0)} \tag{3.10}$$

This allows us to define an effective action on site 0 by integrating out all the other degrees of freedom:

$$\frac{1}{Z_{\text{imp}}} e^{-S_{\text{imp}}(c^\dagger_{0\sigma}, c_{0\sigma})} = \frac{1}{Z} \int \prod_{i\neq 0,\sigma} \mathcal{D}\left[c^\dagger_{i\sigma} c_{i\sigma}\right] e^{-S_{\text{Hubbard}}} = \frac{e^{-S_0}}{Z} \int \prod_{i\neq 0,\sigma} \mathcal{D}\left[c^\dagger_{i\sigma} c_{i\sigma}\right] e^{-(S^{(0)}+\Delta S)} \tag{3.11}$$

At this point, we have not introduced any approximations. This effective (or impurity) action S_{imp} can be used to compute all the local correlators, in particular the local or impurity Green's function:

$$G_{\text{loc}}(\tau - \tau') = G_{\text{imp}}(\tau - \tau') = - < Tc(\tau)c^\dagger(\tau') >_{S_{\text{imp}}} \tag{3.12}$$

The expression giving S_{imp} is a rather complicated infinite sum, but with some bookkeeping one can show that, in the limit of infinite dimensions and rescaling the hopping parameters appropriately, the expression simplifies to

$$S_{\text{imp}} = -\int_0^\beta d\tau \int_0^\beta d\tau' \sum_\sigma c^\dagger_\sigma(\tau)\mathcal{G}_0^{-1}(\tau - \tau')c_\sigma(\tau') + U\int_0^\beta n_\uparrow(\tau)n_\downarrow(\tau) \tag{3.13}$$

where $\mathcal{G}_0$ is given by

$$\mathcal{G}_0^{-1}(i\omega_n) = i\omega_n + \mu - \varepsilon_0 - \sum_{ij\neq 0} t_{0i}t_{0j}G^{(0)}_{ij}(i\omega_n) \tag{3.14}$$

$G^{(0)}_{ij}(i\omega_n)$ is the Green's function of the Hubbard model without site 0. One can show (see [55]), using again the infinite dimension limit, that this is equivalent to

$$\mathcal{G}_0^{-1} = G_{\text{loc}}^{-1} + \Sigma_{\text{imp}} \tag{3.15}$$

where the self-energy Σ becomes local[53], hence equal to the "impurity" self-energy Σ_{imp} on site 0 computed from the impurity action S_{imp}. The local Green's function G_{loc} is calculated as follows

$$G_{\text{loc}}(i\omega_n) = \sum_{\mathbf{k}} \frac{1}{i\omega_n + \mu - \varepsilon_0 - \varepsilon_{\mathbf{k}} - \Sigma_{\text{imp}}(i\omega_n)} = \sum_{\mathbf{k}} G(i\omega_n, \mathbf{k}) \tag{3.16}$$

where $\varepsilon_{\mathbf{k}}$ are the non-interacting band energies (or Fourier transform of the hopping), or equivalently, using the non-interacting density of states $D(\omega)$ from the dispersion relation $\varepsilon_{\mathbf{k}}$:

$$G_{\text{loc}}(i\omega_n) = \int_{-\infty}^{+\infty} \frac{D(\varepsilon)d\varepsilon}{i\omega_n + \mu - \varepsilon_0 - \varepsilon - \Sigma_{\text{imp}}(i\omega_n)} \tag{3.17}$$

We thus have all the DMFT self-consistency equations. In practice, the DMFT self-consistency loop is the following:

1. Start from an initial approximation for the self-energy, and compute the local Green's function from Eq. 3.16.
2. Use the self-consistency equation to obtain the Weiss dynamical mean-field $\mathcal{G}_0$ by Eq. 3.15.
3. Compute the impurity Green's function from the impurity action 3.12 and update the self-energy by re-applying Eq. 3.15.
4. Go back to the first step with the new self-energy, until self-consistency is reached.

This procedure is exact in infinite dimensions. In the general case, an approximation is made by assuming that G_{loc} can be expressed using a local self-energy.

The present equations are written in the case of a one-band Hubbard model. The generalization to a multi-band model is straightforward, the quantities involved ($\varepsilon_{\mathbf{k}}$, ε_0, G, $\mathcal{G}_0$ and Σ) being matrices rather than scalars. The local Green's function should in this case be calculated from Eq. 3.16.

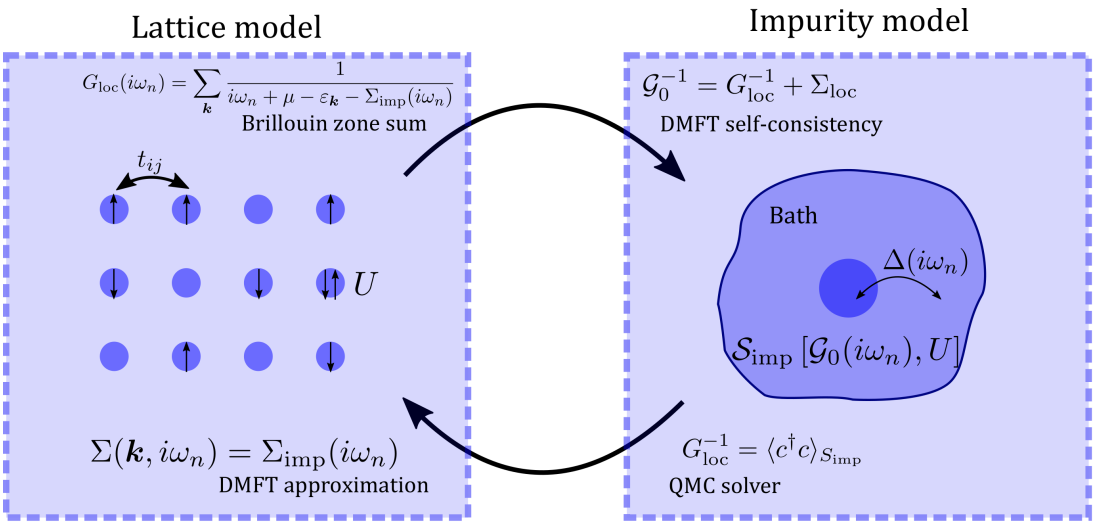

Figure 3.1 – DMFT self-consistency cycle, illustrating Eq. 3.12 to 3.15.

3.4 The Anderson impurity model in Dynamical Mean-Field Theory

The effective action S_{imp} and the dynamical mean-field $\mathcal{G}_0$ in its formula (3.13) can be conveniently parameterized as the action of a self-consistent (Anderson) impurity model, described by Eq. 3.7. Indeed, we can rewrite Eq. 3.14 by introducing a hybridization function

$$\mathcal{G}_0^{-1}(i\omega_n) = i\omega_n + \mu - \varepsilon_0 - \Delta(i\omega_n) \tag{3.18}$$

In practice, this hybridization function is computed as

$$\Delta(i\omega_n) = i\omega_n + \mu - \varepsilon_0 - \mathcal{G}_0^{-1}(i\omega_n) \tag{3.19}$$

from the self-consistent dynamical mean-field $\mathcal{G}_0$. In the AIM of Eq. 3.7, the action takes the same form as 3.13 with $\mathcal{G}_0^{-1}(i\omega_n)$ given by Eq. 3.18 above, and the hybridization is given by

$$\Delta(i\omega_n) = \sum_l \frac{|V_l|^2}{i\omega_n - \varepsilon_{l\sigma}} \tag{3.20}$$

If we were to choose actual parameters for V_l and $\varepsilon_{l\sigma}$, they should be chosen self-consistently so that the impurity Green's function of the AIM coincides with the local Green's function of the initial Hubbard model. In practice, only the full function $\Delta(i\omega_n)$ is useful, so there is no need to explicitly define the AIM by its parameters. Still, this analogy gives a better physical understanding of the DMFT equations: they describe a lattice where local correlations are those of an impurity exchanging electrons with a *non-interacting* bath, itself self-consistently parameterized by the *interacting* local Green's function (as seen in Eq. 3.14.) This technique of using an auxiliary system is reminiscent of the Kohn-Sham system of non-interacting electrons used self-consistently in DFT, while the cavity construction is similar to the the Curie-Weiss mean-field approximation in the Ising model.

This DMFT self-consistency loop is illustrated in Fig. 3.1. In table 3.1, we summarize the analogy between the classical Ising Weiss mean-field and DMFT.

	Ising mean-field	DMFT
Hamiltonian	$H = -\sum_{ij} J_{ij} s_i s_j - h \sum_i s_i$	$H = (\epsilon_0 - \mu) \sum_{i,\sigma} n_{i\sigma}$ $- \sum_{\langle i,j \rangle,\sigma} t_{ij} \left(c^\dagger_{i\sigma} c_{j\sigma} + c^\dagger_{j\sigma} c_{i\sigma} \right) + U \sum_i n_{i\uparrow} n_{i\downarrow}$
Local Observable	$m_i = < s_i >$	$G_{\text{loc}}(\tau - \tau') = - < T c^\dagger_i(\tau) c_i(\tau') >$
Effective local model	$H_{\text{eff}} = -h_{\text{eff}} s_i$	$U n_\uparrow n_\downarrow + (\varepsilon_0 - \mu) n + \sum_{l\sigma} \varepsilon_{l\sigma} a^\dagger_{l\sigma} a_{l\sigma}$ $- \sum_{l\sigma} V_l (c^\dagger_\sigma a_{l\sigma} + a^\dagger_{l\sigma} c_\sigma)$
Weiss field	h_{eff}	$\mathcal{G}_0^{-1}(i\omega_n) = i\omega_n + \mu - \Delta(i\omega_n)$ $\Delta_\sigma(i\omega_n) = \sum_l \frac{\lvert V_l \rvert^2}{i\omega_n - \varepsilon_{l\sigma}}$
Self-consistency relation	$h_{\text{eff}} = \sum_j J_{ij} m_j + h$	$G(i\omega_n) = \sum_{\mathbf{k}} \left[i\omega_n + \mu - \varepsilon_0 - \varepsilon_{\mathbf{k}} + G^{-1}(i\omega_n) - \mathcal{G}_0^{-1}(i\omega_n) \right]^{-1}$ $\mathcal{G}_0^{-1} = G^{-1}_{\text{imp}} + \Sigma_{\text{imp}} = G^{-1}_{\text{loc}} + \Sigma_{\text{imp}}$

Table 3.1 – Analogy between the classical Ising mean-field and dynamical mean-field theory applied to the Hubbard model. Adapted from Ref. [59].

3.5 Strengths and limitations of Dynamical Mean-Field Theory

DMFT has several strong points. First, contrary to other methods like the GW method, it is not a perturbative method. This allows us to treat systems with arbitrarily strong correlations. Furthermore, DMFT becomes exact in a number of limiting cases:

- Infinite dimensions (or infinite lattice coordination)
- The non-interacting limit, $U = 0$.
- The atomic limit, $t = 0$.

Being exact in these opposite limiting cases opens the possibility for reasonable results in the intermediate regime, where kinetic energy or hopping t is of similar magnitude as Coulomb interaction U. Indeed, as we discuss below, DMFT provides a good description of the one-band Hubbard model's Mott insulating transition, when the ratio U/t is varied.

More generally, DMFT is expected to work well as long as local quantum fluctuations are more important than non-local fluctuations. In particular, phenomena like charge or spin-density waves are not captured in single-site DMFT. Several extensions of DMFT have been proposed in order to treat long-range correlations, long-range interactions and the coupling of electrons to boson modes (plasmons, spin-waves, etc) in a similar framework. Regarding long-range interactions, prominent examples are extended DMFT and its combination with GW theory (see section 4.4), or the dual boson approach[60]. Extensions of DMFT that include non-local correlation effects (i.e. non-local self-energies) include cluster extensions (cluster DMFT or dynamical cluster approximation, see section 4.4), diagrammatic extensions like the dynamical vertex approximation (or DΓA)[61], the TRILEX[62] and QUADRILEX[63] methods, and the dual fermion method[64]. For a recent and extensive discussion of non-local extensions of DMFT, we refer the reader to the review paper by Rohringer et al[65].

Most of these methods are still computationally heavy, so that first principles calculations of real systems with multiple orbitals are, if not impossible, not yet routinely done (though an *ab initio* DΓA scheme has recently been tested on the benchmark strongly correlated material, $SrVO_3$[66]). In a recent review, Lechermann *et al.*[67] suggested there are two main routes worth pursuing in the field of strongly correlated electronic structure calculations: one aims at better describing material-specific electronic

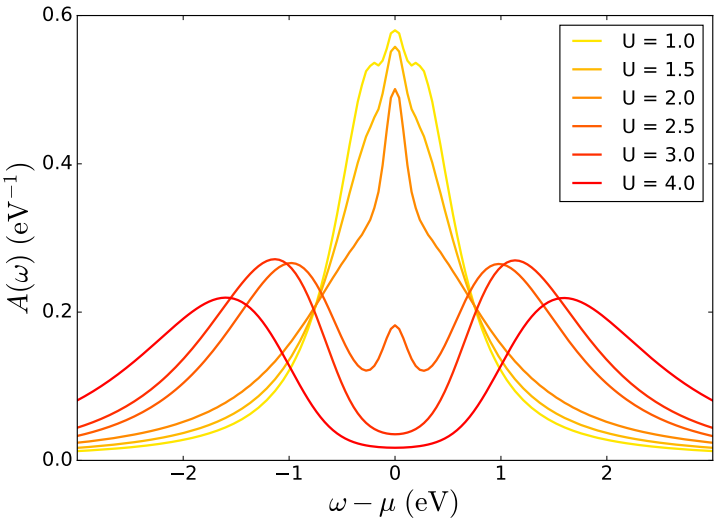

Figure 3.2 – Spectral function of the single orbital Hubbard model on Bethe lattice, at $\beta = 100$ eV^{-1}. The half-bandwidth is $t = 1$ eV. A continuous time quantum Monte-Carlo (CTQMC) hybridization expansion algorithm is used in the DMFT cycle, and the real frequency spectral function is obtained by a maximum entropy (Bryan) algorithm [69].

structures, the other aims at going beyond local mean-field theory. In this thesis, we choose to discuss the former aspect.

3.6 Dynamical Mean-Field Theory treatment of the single-orbital Hubbard model on Bethe lattice

As an illustration, we show below how DMFT captures the metal-insulator transition in the one-orbital Hubbard model on the infinite-connectivity Bethe lattice.

The Bethe lattice (or Cayley tree) is an infinite cycle-free graph where each node has the same number of neighbors z[68]. It does not appear at first sight a reasonable description of a lattice made of atoms and carrying electrons. Nevertheless, the Bethe lattice has been a popular tool in the context of DMFT. Indeed, as mentioned earlier, in the limit of large connectivity z, DMFT becomes exact[52]. Furthermore, and only in the case of the Bethe lattice, the density of states becomes semi-circular (or semi-elliptic with more that one band) and the self-consistency equation becomes much simpler in this limit, allowing for simpler equations. Last but not least, in many cases the physics of correlated electrons does not depend too much on the geometry of the lattice.

In Fig. 3.2, we show the spectral function calculated with DMFT for the one-orbital, Bethe lattice Hubbard model at half-filling. The temperature is $\beta = 80$ eV^{-1}, for different ratios of U/t. At $U/t = 0$, we recover the semi-circular density of states of the non-interacting Bethe lattice. For large values of U/t, the density of states is separated into two so-called *Hubbard bands*, separated by the energy U. Note that these bands are qualitatively different from non-interacting bands: each Hubbard band can only contain one electron, instead of two (taking into account spin-degeneracy) for a non-interacting band. This means that at half-filling and large U/t, the system becomes insulating, whereas non-interacting bands are necessarily metallic with an odd electron number. If the limiting case $U/t = 0$ describes completely delocalized (dispersive) electrons on a lattice, where all of the energy is kinetic energy, the large U limit is the opposite: it consists in perfectly localized electrons on the atom sites, stuck in place because the cost of double occupancy is too high to hop (even briefly) to a neighboring site.

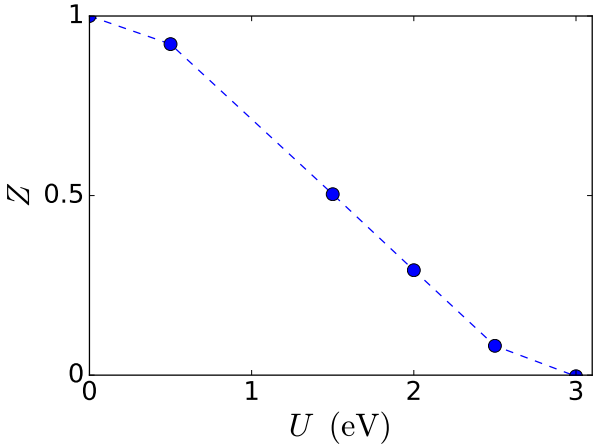

Figure 3.3 – quasi-particle weight Z as a function of Hubbard U, in the same model as in Fig. 3.2.

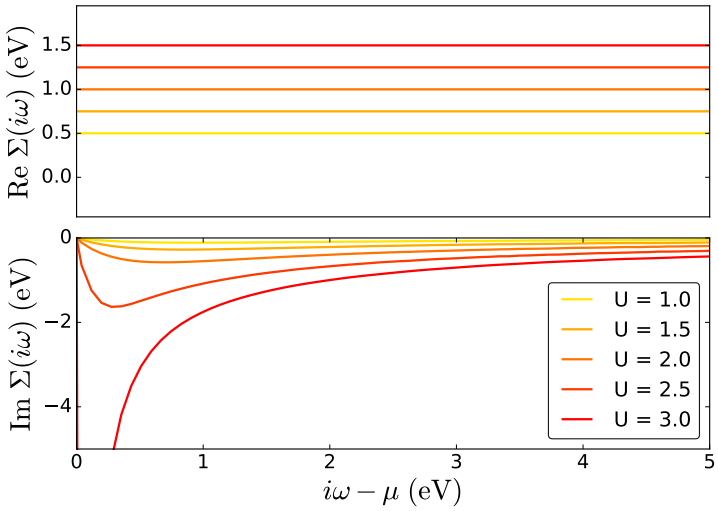

Figure 3.4 – Real (upper panel) and imaginary (lower panel) part of the self-energy on the Matsubara axis for the single orbital Hubbard model on Bethe lattice, at $\beta = 80$ eV^{-1} at different values of U. At half-filling, the real part of Σ is equal to $U/2$, the Hartree-Fock self-energy, and the imaginary part goes to zero at high frequencies. Below the Mott transition, which happens between $U = 2.5$ eV and $U = 3.0$ eV, the self-energy is that of a Fermi liquid, as can be seen in the imaginary part, that goes linearly to zero. Above the Mott transition, in the particle-hole symmetric case, Σ has a divergence around $i\omega = 0$.

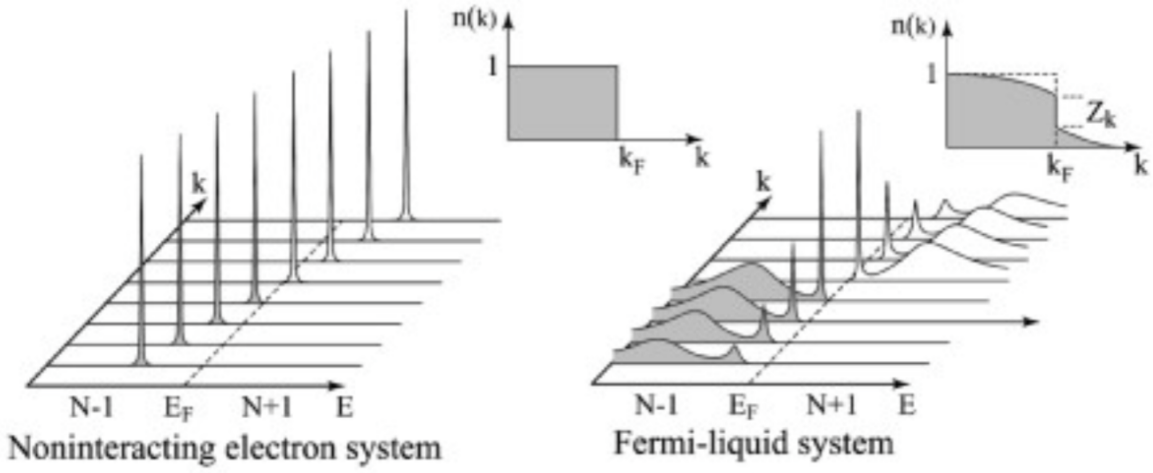

Figure 3.5 – Illustration of non-interacting bands (left-hand side) and correlated-quasi-particles with Hubbard bands (right-hand side). Reproduced from Ref. [70]

In the intermediate regime, partially formed Hubbard bands and a quasi-particle peak at the Fermi level, narrowing as U/t is increased, until it vanishes.

The quasi-particle weight Z can be defined as

$$\begin{aligned} Z &= (1 - \partial_\omega \mathrm{Re}\Sigma(\omega)|_{\omega=0})^{-1} \\ &= (1 - \partial_{i\omega} \mathrm{Im}\Sigma(i\omega_n)|_{i\omega=0})^{-1} \end{aligned} \tag{3.21}$$

depending on whether we are working with real or imaginary frequency Green's functions (see Appendix B). It is shown in Fig. 3.3 in the case of the one-band Hubbard model.

If we look at a $\mathbf{k}$- and ω-resolved Green's function, on a lattice where $\mathbf{k}$ is properly defined, and compute the spectral function $A(\mathbf{k}, \omega)$, the signification of the quasi-particle weight Z becomes more apparent. A non-interacting system of electrons in a periodic lattice has perfectly defined electronic bands, so that $A(\mathbf{k}, \omega)$ is a sum of Dirac peaks (one per band) when $\mathbf{k}$ or ω are varied. This is illustrated in the left panel of Fig. 3.5. At zero temperature, the distribution function is given by a step function, with a step of height one as one goes through the Fermi level.

This picture of non-interacting bands changes in the presence of correlations, where the system has a non-trivial self-energy. The Dirac peaks that form the bands are gradually widened as the imaginary part of the self-energy increases, and the integral of the peak becomes less than unity. The new weight of this quasi-particle peak is precisely given by Z, as defined in Eq. (3.21). Since there is conservation of the particle numbers, this implies a spectral weight transfer to higher and / or lower energies, for example in the form of Hubbard bands or plasmon satellites. In addition, a reduced step of height Z appears in the zero-temperature distribution function, as a consequence of correlations. This case is illustrated in the right-hand panel of Fig. 3.5.

What is implied by the above discussion and Fig. 3.5 is that, in presence of correlations, the band picture becomes invalid but does not break down altogether. This situation is described by Landau's Fermi liquid (FL) theory[8]. If correlations are not excessively strong, the Dirac peak of non-interacting bands can be adiabatically traced back to the widened main peak in the interacting spectral function. One-particle excitations corresponding to thus derived photoemission peaks cannot really be called "particles", as they do not correspond to the removal of an electron with well-defined energy and momentum. This means that a Fermi liquid is characterized by quasi-particles with a finite lifetime. More precisely, quasi-

particles in Fermi liquid theory have a lifetime $\tau_{\mathbf{k}}$ such that

$$\frac{1}{\tau_{\mathbf{k}}} \propto (\varepsilon_{\mathbf{k}} - \varepsilon_F)^2 + (\pi k_B T)^2 \tag{3.22}$$

where ε_F is the Fermi energy and $\varepsilon_{\mathbf{k}}$ the eigenenergy of a quasi-particle. In other words, at low temperatures, quasi-particles close enough to the Fermi level can be long-lived. However, their lifetime decreases as one moves away from the Fermi level, as illustrated in the right-hand panel of Fig. 3.5.

All of the properties of the quasi-particles are encoded in the self-energy $\Sigma(\omega)$ of the system. In particular, quasi-particles in a Fermi liquid:

1. have a finite lifetime away from the Fermi level, encoded by the low-energy dynamical behavior of the imaginary part of $\Sigma(\omega)$.
2. have a renormalized mass (usually heavier than non-interacting electrons) proportional to $1/Z_{\mathbf{k}}$, encoded by the low-energy dynamical behavior of the real part of $\Sigma(\omega)$.
3. have a renormalized dispersion relation near the Fermi level, also encoded by the real part of the self-energy.

Let us go back to the one-band Hubbard model previously discussed to see what happens during the metal-insulator transition. In Fig. 3.2, the decrease of the bandwidth as U is switched on is visible, synonymous of heavier quasi-particles and transfer of spectral weight to satellites. The renormalization factor Z decreases until it reaches 0 between $U = 2.5$ and 3 eV, which marks the transition to the insulating phase (Fig. 3.3). The reduced quasi-particle lifetime is not so easily visible here, and would appear more clearly in a $\mathbf{k}$-resolved spectral function on a "real" (not Bethe) lattice.

The corresponding self-energies $\Sigma(\omega)$ also show this transition. In Fig. 3.6, we display the analytical continuation of the Matsubara frequency self-energies calculated in Fig. 3.4. For small values of U and at zero temperature, the imaginary part of $\Sigma(\omega)$ is going to 0 quadratically as $-\Gamma\omega^2$ at $\omega = \mu$, where Γ is the electron-electron scattering rate, equal to the inverse quasi-particle lifetime. At finite temperature T,

$$\mathrm{Im}\Sigma(\omega) = -(\Gamma\omega^2 + \pi^2(k_{\mathrm{B}}T)^2) \tag{3.23}$$

When U is greater than a critical value (here, slightly below 3 eV), $\mathrm{Im}\Sigma(\omega)$ does not go to zero at the Fermi level anymore (even at $T = 0$), so that no quasi-particles with arbitrarily long lifetime can be defined: the Fermi liquid picture breaks down. The real part of Σ is quasi-linear at $\omega = \mu$, and its slope gives the quasi-particle weight as in Eq. 3.21.

In the one-band model, a metal-insulator transition has to be caused by a vanishing quasi-particle peak, as Brinkman and Rice showed in 1970[71]. This seems in fact quite straightforward: correlations increase the effective mass of quasi-particles, until the mass diverges and electrons become localized. This is not sufficient to describe all correlation-driven metal-insulator transitions: in a multi-orbital system, the effect of the self-energy can be to shift one band with respect to the others, and thus open a band gap[9].

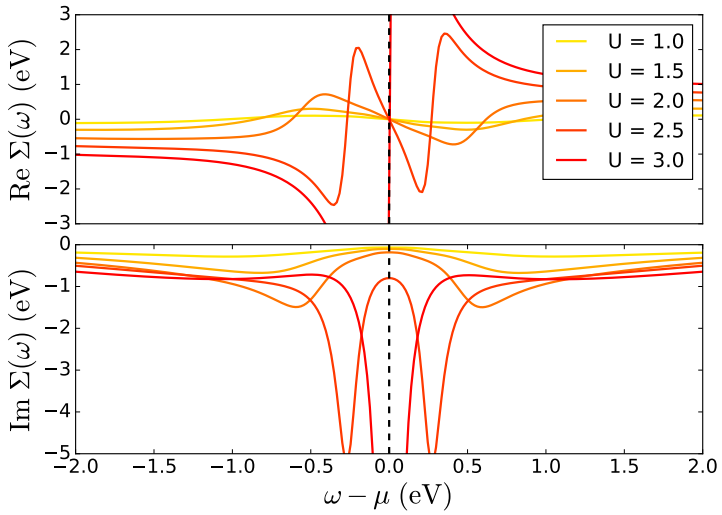

Figure 3.6 – Real (upper panel) and imaginary (lower panel) part of the self-energy on the real axis for the single orbital Hubbard model on Bethe lattice, at $\beta = 100$ eV^{-1} at different values of U. The real axis functions are obtained by analytical continuation of the Matsubara self-energies of Fig. 3.4. We removed the static real contribution corresponding to the chemical potential, $\mu = U/2$, in order to compare the different self-energies more easily. In the Fermi liquid regime, the real part of $\Sigma(\omega)$ is linear around $\omega = 0$, with the slope giving the mass renormalization factor Z, and the imaginary part vanishes at $\omega = 0$. Near and above the Mott transition, the imaginary part of the self-energy does not go to zero at the Fermi level, but becomes a Dirac peak in the limit of large U.

Chapter 4

Bridging the gap to realistic material calculations: combined Density Functional Theory and Dynamical Mean-Field Theory

DMFT and its extensions have demonstrated their value for solving Hubbard-like problems in a large variety of configurations: two-dimensional or three-dimensional lattices of square, triangular, honeycomb or Bethe type, with local Coulomb interaction U only or with additional nearest-neighbor Coulomb interaction V, with one or several orbitals... Such models can, to some extent, be made material specific.

A first approach is to measure the parameters. This is not trivial, but can be done, for example in photoemission experiments. In a single-orbital system, the distance between two Hubbard bands, U, is obtained by comparing the position of the lower Hubbard band in direct photoemission and of the upper Hubbard band in inverse photoemission (this is the more difficult part). A more general theory for measuring U from spectroscopy experiments, including for multi-orbital systems, was proposed by Sawatzky *et al.* [72]. The hopping parameter t can in principle be obtained by angle resolved photoemission spectroscopy by measuring the bandwidth[70], but in practice (and in materials where DMFT would be useful) this only gives an effective t_{eff}, renormalized by correlations.

The second approach, more often followed, consists in exploring phase diagrams by varying one or several parameters. This gives information on a whole family of materials, and a specific material can be understood by comparing calculated observables and measured ones, and placing the material on the phase diagram. The "true" parameters of the system are then considered to be those that best fit the experiments.

Either way, model-based DMFT calculations are more often used to qualitatively understand materials than to make predictions. The need for input parameters is, in fact, a consequence of the fact that DMFT and similar methods can only be used to solve low-energy models with few bands, and do not provide a general description of the electronic structure of materials. An ideal theory would:

- Reasonably describe bands far away from the Fermi level (core states and excited states), both in terms of the energetic position and of the charge density of occupied bands
- Use some form of many-body technique to treat the low-energy degrees of freedom, where correlations are typically most present and upon which many important physical properties (conductivity, magnetism...) depend
- Have a consistent link between both parts of the energy spectrum: this is probably the most difficult

requirement.

The need for such a theory became evident as soon as DMFT demonstrated its efficiency for treating low-energy models in the mid-90's. A first approach was proposed in 1997 by Anisimov *et al.*[73] and in 1998 by Lichtenstein *et al.*[74]. Their "DFT+DMFT" formalism has had great success to quantitatively describe very diverse strongly correlated metals and oxides in the last twenty years (see section 4.2 for examples). In the present chapter, we briefly review the philosophy behind DFT+DMFT, present a few achievements of this method, and finally discuss some of its extensions.

4.1 The combined Density Functional Theory + Dynamical Mean-Field Theory method

Extensions of DFT (in practice, LDA or GGA) such as the DFT+U method have been developed for systems with partly filled d or f orbitals before DFT+DMFT[75–77]. DFT+U considers a Hamiltonian

$$H^{\mathrm{DFT+U}} = H^{\mathrm{DFT}} + H^{\mathrm{U}} - H^{\mathrm{dc}} \tag{4.1}$$

where H^{DFT} is the usual DFT Hamiltonian, H^{U} is a Coulomb term screened by itinerant states and acting on a d or f shell, and H^{dc} is a double-counting term that corrects for local Coulomb interactions already present in H^{DFT}. The local Coulomb interaction of H^{U} is treated in a Hartree-Fock approximation, giving a static and real local self-energy. This can be sufficient to, for instance, open a gap in the fully ordered phases of antiferromagnetic Mott insulators. DFT+DMFT can be understood as a natural improvement on DFT+U, because it starts from the same Hamiltonian 4.1. It opens, however, the possibility for a fully dynamical self-energy and all that it implies: quasi-particle lifetimes, bandwidth renormalization...

As in DFT+U, in DFT+DMFT a subset of localized states around the Fermi level for which KS DFT does not work well is designated as "correlated" and treated within DMFT, while the other orbitals are simply treated at the KS DFT level. By using (for example) projectors, a projected Hamiltonian $H^{\mathrm{proj}}_{\mathbf{k}}$ is defined, and, after removing a double-counting term, used as a non-interacting Hamiltonian in DMFT. The density matrix of the correlated shell, obtained from the converged DMFT calculation, can be fed back into the DFT loop, updating the charge density around the correlated atom.

DFT+DMFT can be used in two similar but different ways:

- A first way to use the DFT+DMFT method, introduced in 1997 and 1998[73, 74], is to use the DFT density and KS wave functions to parameterize a material-specific Hubbard model, to be solved in DMFT. A number of properties, for example spectral functions, magnetizations or quasi-particle effective masses, can then be obtained by embedding the impurity self-energy obtained by DMFT into the DFT KS Hamiltonian. This approach is often called "one-shot" DFT+DMFT.

- A slightly more recent and more sophisticated method is to see the DFT+DMFT equations as deriving from a more general energy functional. This paves the way for fully charge self-consistent DFT+DMFT calculations and allows to compute total energies in a similar fashion to DFT, but with local correlations taken into account more accurately.

In this manuscript, we follow the framework for DFT+DMFT using Wannier functions described in Lechermann *et al.* in Ref. [78], and its implementation in FLAPW DFT by Amadon *et al.* and Aichhorn *et al.*[79, 80]. A general review of DFT+DMFT can be found in [81]. [59, 82] provide a more qualitative and pedagogical introduction.

In the following sections, we discuss the basic ideas behind both approaches.

4.1.1 One-shot Density Functional Theory + Dynamical Mean-Field Theory equations

One typically starts from a converged KS DFT calculation. This means that for each **k**-point in the Brillouin zone mesh, we have a set of Bloch waves $\psi^{\sigma}_{\mathbf{k}\nu}$ with eigenenergies $\varepsilon^{\sigma}_{\mathbf{k}\nu}$. The Bloch waves are by essence delocalized and not of pure atomic and orbital character, though some may be predominantly formed by a given orbital. In a window around the Fermi level (since DMFT is typically useful to study low-energy degrees of freedom around the Fermi level, in partly filled d or f shells), Bloch waves with different atomic and orbital characters may be present. In the simplest case, the only bands crossing the Fermi level belong to a subset of orbitals considered as correlated. This can, for example, be the t_{2g} states of a transition metal in an oxide. The situation is more complicated when other bands are also present, for example dispersive states of predominant s character in metalic Fe.

Either way, the challenge is to define a mapping to go from the Bloch space to a correlated space with less orbitals, and inversely. One way of doing so, that was extensively applied in the present thesis, is described below. An initial set of atomic-like orbitals $|\chi^{\alpha\sigma}_{m}\rangle$ is created from atomic-like functions in the KS DFT basis set. This is very natural in implementations of DFT that work with localized functions, as is the case in the FLAPW DFT code Wien2k. At each **k**-point, these atomic-like orbitals are then expanded in the Bloch functions:

$$|\chi^{\alpha\sigma}_{\mathbf{k}m}\rangle = \sum_{\nu} \langle \psi^{\sigma}_{\mathbf{k}\nu} | \chi^{\alpha\sigma}_{\mathbf{k}m} \rangle | \psi^{\sigma}_{\mathbf{k}\nu} \rangle \tag{4.2}$$

Subsequently, this expansion is truncated in an energy window $\mathcal{W}$ around the Fermi level

$$|\tilde{\chi}^{\alpha\sigma}_{\mathbf{k}m}\rangle = \sum_{\nu \in \mathcal{W}} \langle \psi^{\sigma}_{\mathbf{k}\nu} | \chi^{\alpha\sigma}_{\mathbf{k}m} \rangle | \psi^{\sigma}_{\mathbf{k}\nu} \rangle \tag{4.3}$$

This defines a set of projectors

$$\tilde{P}^{\alpha\sigma}_{m\nu}(\mathbf{k}) = \langle \psi^{\sigma}_{\mathbf{k}\nu} | \tilde{\chi}^{\alpha\sigma}_{\mathbf{k}m} \rangle \tag{4.4}$$

for m in the subspace of correlated orbitals and $\nu \in \mathcal{W}$. The atomic-like orbitals $|\tilde{\chi}^{\alpha\sigma}_{\mathbf{k}m}\rangle$ thus obtained are not orthonormal, but can be made so by computing the overlap elements

$$O^{\alpha\alpha'}_{mm'}(\mathbf{k},\sigma) = \langle \tilde{\chi}^{\alpha\sigma}_{\mathbf{k}m} | \tilde{\chi}^{\alpha'\sigma}_{\mathbf{k}m'} \rangle \tag{4.5}$$

and transforming the functions to

$$|w^{\alpha\sigma}_{\mathbf{k}m}\rangle = \sum_{\alpha' m'} S^{\alpha\alpha'}_{mm'} |\tilde{\chi}^{\alpha'\sigma}_{\mathbf{k}m'}\rangle \tag{4.6}$$

where

$$S^{\alpha\alpha'}_{mm'} = \{O(\mathbf{k},\sigma)^{-1/2}\}^{\alpha\alpha'}_{mm'} \tag{4.7}$$

is the inverse square root of the (hermitian, definite positive) matrix O, and $|w^{\alpha\sigma}_{\mathbf{k}m}\rangle$ defines a set of orthonormal Wannier-like orbitals. A final set of projectors $P^{\alpha\sigma}_{m\nu}(\mathbf{k})$ is defined in the same way by

$$P^{\alpha\sigma}_{m\nu}(\mathbf{k}) = \sum_{\alpha' m'} S^{\alpha\alpha'}_{mm'} \tilde{P}^{\alpha'\sigma}_{m'\nu}(\mathbf{k}) \tag{4.8}$$

so that the Wannier-like functions $w^{\alpha\sigma}_{\mathbf{k}m}$ can be expanded in the Bloch basis as

$$|w^{\alpha\sigma}_{\mathbf{k}m}\rangle = \sum_{\nu} P^{\alpha\sigma}_{m\nu}(\mathbf{k}) |\psi^{\sigma}_{\mathbf{k}\nu}\rangle \tag{4.9}$$

At each **k**-point, $P^{\alpha\sigma}(\mathbf{k})$ is a matrix whose dimensions are given by the number of Bloch bands N_ν in the energy window $\mathcal{W}$ on one hand, and the size L of the correlated subspace on the other hand (for example, $L = 5$ for a d shell, 7 for an f shell or 3 for a t_{2g} shell, times the number of independent correlated atoms). The rows of the matrix $P^{\alpha\sigma}(\mathbf{k})$ contain the decomposition of Wannier functions $|w^{\alpha\sigma}_{\mathbf{k}m}\rangle$ over the Bloch waves $|\psi^{\sigma}_{\mathbf{k}\nu}\rangle$.

If the correlated bands are perfectly separated from the other ones (say, t_{2g} states in a transition metal oxide), the matrix $P_{\mathbf{k}}^{\sigma}$ is unitary, and the transformation from the Bloch space to the space of correlated orbitals is quite simple. If the bands are entangled (which is typically the case in pure metals), $P_{\mathbf{k}}^{\sigma}$ is only semi-unitary: $P_{\mathbf{k}}^{\sigma} P_{\mathbf{k}}^{\sigma\dagger} = \mathrm{Id}_L$ but $P_{\mathbf{k}}^{\sigma\dagger} P_{\mathbf{k}}^{\sigma} \neq \mathrm{Id}_{N_\nu}$, where Id_n is the identity matrix of size n and $A^\dagger$ is the transposed conjugate of matrix A.

We can then define the notion of up- and down-folding of a matrix. Projecting a (matrix) quantity defined in the Bloch space to the space of correlated orbitals is called *down-folding*, and corresponds to the operation $A \rightarrow P_{\mathbf{k}}^{\sigma} A P_{\mathbf{k}}^{\sigma\dagger}$. The inverse operation of bringing a quantity defined in the space of correlated orbitals (say, the DMFT self-energy) back into the Bloch space is called *up-folding*, and corresponds to the operation $B \rightarrow P_{\mathbf{k}}^{\sigma\dagger} B P_{\mathbf{k}}^{\sigma}$.

The DFT+DMFT self-consistency loop is then obtained by going back and forth from the Bloch space to the correlated subspace. The lattice Green's function of the solid in the Bloch space is given by

$$G^{\sigma,\mathrm{latt}}(\mathbf{k}, i\omega_n)^{-1}_{\nu\nu'} = (i\omega_n + \mu - \varepsilon^{\sigma}_{\mathbf{k}\nu})\delta_{\nu\nu'} + \Sigma^{\sigma}_{\nu\nu'}(\mathbf{k}, i\omega_n) \tag{4.10}$$

and obtained by up-folding the DMFT impurity self-energy in subsequent iterations:

$$\Sigma^{\sigma}_{\nu\nu'}(\mathbf{k}, i\omega_n) = \sum_{\alpha m m'} P^{\alpha\sigma\dagger}_{m\nu}(\mathbf{k}) \Sigma^{\sigma,\mathrm{imp}}_{mm'}(i\omega_n) P^{\alpha\sigma}_{m'\nu'}(\mathbf{k}) \tag{4.11}$$

with $\Sigma^{\sigma,\mathrm{imp}}_{mm'}$ is the impurity self-energy. In practice, an additional double-counting term must be subtracted from the self-energy, as discussed in section 4.1.2. The local Green's function G^{loc} is in turn obtained from the Green's function of the solid by down-folding it and summing over the Brillouin zone:

$$G^{\sigma,\mathrm{loc}}_{\alpha m}(i\omega_n) = \sum_{\mathbf{k}\nu\nu'} P^{\alpha\sigma}_{m'\nu'}(\mathbf{k}) G^{\sigma,\mathrm{latt}}_{\nu\nu'}(\mathbf{k}, i\omega_n) P^{\alpha\sigma\dagger}_{m\nu}(\mathbf{k}) \tag{4.12}$$

Finally, the DMFT self-consistency condition giving the dynamical Weiss field $\mathcal{G}_0$ is, as in regular DMFT:

$$\mathcal{G}_0^{-1} = \Sigma_{\mathrm{imp}} + G^{-1}_{\mathrm{loc}} \tag{4.13}$$

The one-shot DFT+DMFT self-consistency cycle is the following:

1. Compute an initial local Green's function in the correlated space by down-folding the lattice Green's function.
2. Solve the local impurity model to obtain the impurity self-energy.
3. Up-fold the impurity self-energy to insert it in the lattice Green's function, and update the chemical potential μ
4. Compute the new local Green's function, iterate until convergence

The need to repeatedly switch between two spaces can seem surprising, but is crucial to obtain physical results in the case where additional, non-correlated bands cross the Fermi level. Indeed, applying the self-consistency condition directly on the level of the correlated subspace would be wrong, and in particular would not conserve the electron number. Again, in the case of well separated bands, the equations simplify and it is possible to work directly in the correlated subspace: in this case, the DFT+DMFT method is equivalent to parameterizing the non-interacting part of a Hubbard-like model with parameters obtained from the projected DFT Hamiltonian.

4.1.2 The double-counting term

In Eq. 4.11, we introduced a double counting correction $\Sigma^{\sigma,\mathrm{dc}}_{mm'}$ to the impurity self-energy. Indeed, local Coulomb interactions are taken into account explicitly at the DMFT level, but are at least partly

present in the DFT exchange-correlation and Hartree potentials, hence in the DFT Hamiltonian used to construct the Green's function in Eq. 4.10. This problem has been recognized early on in the context of DFT+U[75, 83], and different approaches have been proposed to correct for double-counting. However, finding an exact correction is impossible, because DFT and DMFT are by construction two methods based on different observables: the key quantity in DFT is the electronic density, upon which the KS exchange-correlation potential acts. In contrast, DMFT works with Green's functions, orbital-resolved by construction. The interface between DFT and DMFT (typically a projection scheme as described above) does not allow for an explicit formula for Σ^{dc}.

Nevertheless, various schemes exist and are ubiquitous in DFT+U and DFT+DMFT calculations. Among the most used are:

- The *fully localized limit* (FLL) approximation[83], whereby

$$\Sigma^{\sigma,\mathrm{dc}}_{mm'} = \left[U(N_c - \frac{1}{2}) - J(N_c^\sigma - \frac{1}{2})\right]\delta_{mm'} \tag{4.14}$$

  where N_c is the total number of particles in the correlated subspace, U the Coulomb interaction parameter, and J the Hund's coupling. The assumption behind the FLL approximation is that total energies are determined well in DFT when orbital shells are either empty or completely filled.

- The *around mean-field* (AMF) approximation[75], whereby

$$\Sigma^{\sigma,\mathrm{dc}}_{mm'} = \left[U(N_c - n^\sigma) - J(N_c^\sigma - n^\sigma)\right]\delta_{mm'} \tag{4.15}$$

  where n is the average occupancy per orbital, and n^σ the average occupancy per orbital with spin σ. The assumption behind the AMF approximation is that exchange and correlation effects are partly included in DFT, but only in an orbitally averaged way. For a half-filled band, the FLL and AMF expressions coincide.

- The *Lichtenstein's correction* for metallic systems[84], based on the idea that static correlation effects are described reasonably well in DFT for such systems:

$$\Sigma^{\sigma,\mathrm{dc}}_{mm'} = \frac{1}{2}\mathrm{Tr}[\Sigma(\omega = 0)] \tag{4.16}$$

Depending on what kind of properties (and what material) one wants to describe, the double-counting correction may or may not be important. The crucial idea is that a correct double-counting correction is needed to correctly describe the energetic position of the subset of correlated orbitals with respect to other orbitals present in the system. These "other" orbitals can be either states not considered as correlated within DMFT *or* another inequivalent shell, also treated as correlated.

As a consequence, the double-counting correction becomes less relevant, for example, in the context of studying a Mott metal-insulator transition in a system with well separated bands at the Fermi level, or quantities like the quasi-particle lifetime in such a system. Indeed, in this configuration, the double-counting correction amounts to a trivial shift of the chemical potential.

It is, however, critical when other bands cross the Fermi level, or to compute excitations of the system corresponding to transitions to excited states implying other orbitals, or describing a charge-transfer metal-insulator transition.

We also note that orbital-dependent double-counting schemes have been tested [85], motivated by the fact that different orbitals of a given shell on an atom are not equally occupied in a solid. Finally, charge self-consistency in DFT+DMFT has been shown to somewhat decrease the dependence of results on the choice of double-counting correction[86].

Overall, it is not an overstatement to say that double-counting corrections are important more often than not, so that efforts to design double-counting free *ab initio* electronic structure methods remain crucial.

4.1.3 Charge self-consistency and total energies in Density Functional Theory + Dynamical Mean-Field Theory

One-shot DFT+DMFT calculations are very useful to compute spectral properties of real materials, providing a welcome extension of DMFT model calculations. However, they are not sufficient to achieve what DFT was initially designed for: total energy and electronic density distribution calculations, the spectral properties of the KS auxiliary system coming as a "bonus". Kotliar and Savrasov derived in the early 2000's a functional formulation of DFT+DMFT[81, 87, 88], introducing a free energy functional Γ of four variables: the total charge density ρ, the local Green's function of the correlated subspace G_{loc}, an effective interaction potential $v^{\text{int}} = v^{xc} - v^{\text{ext}}$ conjugate to the charge density, and a local self-energy Σ_{loc} conjugate to G_{loc}. This functional is derived in the more general framework of spectral density functional theory, and its approximate expression in DFT+DMFT is given by

$$\begin{aligned}\Gamma\left[\rho, G_{\text{loc}}, v^{\text{int}}, \Sigma_{\text{loc}}\right] = &- \text{Tr}[\ln G_{\text{latt}}] - \int d\mathbf{r} v^{\text{int}}(\mathbf{r})\rho(\mathbf{r}) - \text{Tr}\left[G_{\text{loc}}(\Sigma_{\text{loc}} - \Sigma_{\text{DC}})\right] \\ &+ E^{\text{H}}[\rho] + E^{xc}[\rho] + \Phi_{\text{LW}}^{\text{DMFT}}[G_{\text{loc}}] - \Phi^{\text{DC}}[G_{\text{loc}}]\end{aligned} \tag{4.17}$$

where G_{latt} is obtained from the up-folding procedure of Eq. 4.10, and E^{H} and E^{xc} are respectively the Hartree and DFT exchange-correlation functionals. The two last terms are respectively the DMFT approximation to the Luttinger-Ward functional[89] and the double-counting correction to it. The Luttinger-Ward functional is a diagrammatic object whose value does not carry direct physical meaning, but is useful in DMFT because its functional derivative with respect to the local Green's function is equal to the self-energy:

$$\frac{\partial \Phi_{\text{LW}}^{\text{DMFT}}[G_{\text{loc}}]}{\partial G_{\text{loc}}(i\omega_n)} = \frac{1}{\beta}\Sigma_{\text{loc}}(i\omega_n) \tag{4.18}$$

The stationarity of the Γ functional with respect to v^{int} gives the charge self-consistency relation:

$$\rho(\mathbf{r}) = \text{Tr}\langle \mathbf{r}|G_{\text{latt}}|\mathbf{r}\rangle \tag{4.19}$$

where the trace is over all Matsubara frequencies and Bloch orbitals: $\text{Tr} = \frac{1}{\beta}\sum_{i\omega_n,\nu\nu'}$. In practical implementations of charge self-consistent DFT+DMFT, one first determines a $\mathbf{k}$-dependent density matrix from the interacting lattice Green's function (a generally non-diagonal matrix, contrary to the DFT density matrix)

$$N^{\mathbf{k}} = \frac{1}{\beta}\sum_{i\omega_n} G_{\text{latt}}(\mathbf{k}, i\omega_n) \tag{4.20}$$

and the updated real space density obtained, as described in Ref. [78], by

$$\rho(\mathbf{r}) = \sum_{\mathbf{k}}\sum_{\nu\nu'} \psi_{\mathbf{k}\nu}(\mathbf{r}) N^{\mathbf{k}}_{\nu\nu'} \psi_{\mathbf{k}\nu'}(\mathbf{r}) \tag{4.21}$$

in the step of the DFT code that calculates the occupation of the orbitals. Thereafter, one may calculate a new KS potential, new eigenvalues and projectors, and perform a new DMFT cycle, until convergence is reached. The resulting DFT+DMFT self-consistency cycle is illustrated in Fig. 4.1

The stationarity of Γ with respect to Σ_{loc}, on the other hand, recovers the relation between the lattice Green's function and the correlated subspace's local Green's function, as described in Eq. 4.10. Finally, the stationarity conditions of Γ with respect to ρ and G_{loc} amount respectively to Eq. 2.12 defining the KS potential in DFT, and to Eq. 4.18 giving the self-energy from the Luttinger-Ward functional.

Given the stationarity conditions, it follows that the total energy of the system can be written as a functional of only two variables: the charge density ρ and the local Green's function in the correlated subspace G_{loc}. Introducing G^0_{loc}, the local Green's function without the self-energy, the total energy functional reads[81, 90, 91]

$$E^{\text{DFT+DMFT}} = E^{\text{DFT}} + \sum_{\mathbf{k},\nu}\left[\varepsilon^{\text{KS}}_{\mathbf{k}\nu}(N^{\mathbf{k}}_{\nu\nu} - f(\varepsilon_{\mathbf{k},\nu} - \mu))\right] + \langle H_U\rangle - E_{\text{DC}} \tag{4.22}$$

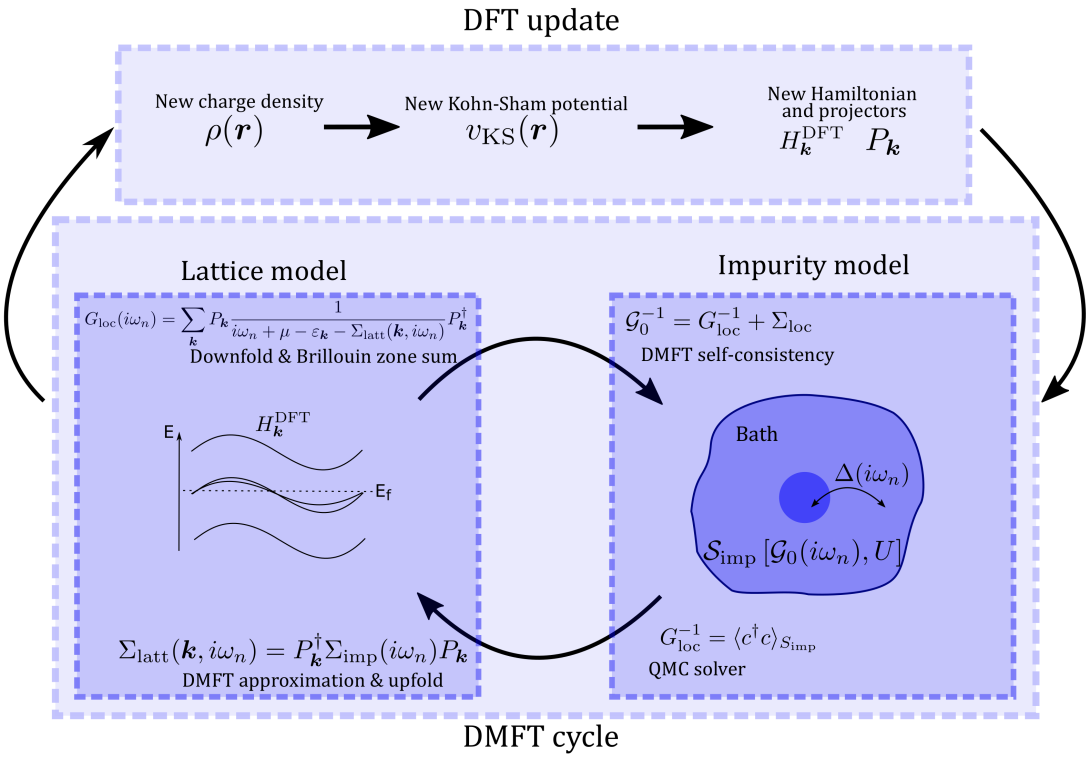

Figure 4.1 – Full DFT+DMFT self-consistency cycle.

where $\varepsilon_{\mathbf{k},\nu}$ denotes the KS eigenvalues and f is the Fermi-Dirac distribution. The first term is none other than the KS DFT total energy of Eq. 2.9,

$$E_{\mathrm{HK}}\left[\rho\right] = T_s\left[\rho\right] + \int v_{\mathrm{ext}}(\mathbf{r})\rho(\mathbf{r})d^3\mathbf{r} + \int v_{\mathrm{Hartree}}(\mathbf{r})\rho(\mathbf{r})d^3\mathbf{r} + E_{xc}\left[\rho\right]$$

where in the present notations,

$$T_s\left[\rho\right] = \sum_{\mathbf{k}} \mathrm{Tr}\left[H_{\mathbf{k}}^{\mathrm{KS}} G_{\mathrm{latt}}^{0}\right] = \sum_{\mathbf{k},\mathrm{occ}} \varepsilon_{\mathbf{k}}^{n}$$

is the sum of occupied Kohn-Sham eigenenergies. The second term of Eq. 4.22 is the DMFT correction to the occupation of the KS eigenstates, and can also be seen as the DMFT correction the the electronic kinetic energy. Finally, the last terms $\langle H_U \rangle - E_{\mathrm{DC}}$ contain the effect of the double-counting correction on the total energy. The double-counting term E_{DC} is computed from the double-counting energy formula[75, 83] from the DFT occupancies of orbitals. The local Coulomb energy $\langle H_U \rangle$ can be computed conveniently in DMFT from the Migdal formula

$$\langle H_U \rangle = \frac{1}{2} \mathrm{Tr}\left[\Sigma G_{\mathrm{imp}}\right] \tag{4.23}$$

Alternatively, for a density-density Hamiltonian and if the solver used in DMFT allows to directly measure the correlator $\langle n_m n_{m'} \rangle$, $\langle H_U \rangle$ can be calculated directly as

$$\langle H_U \rangle = \frac{1}{2} \sum_{mm'} H_{mm'}^{U} \langle n_m n_{m'} \rangle_{\mathrm{imp}} \,. \tag{4.24}$$

In applications using numerical quantum Monte-Carlo methods, the latter may have less noise or statistical error than Migdal's formula.

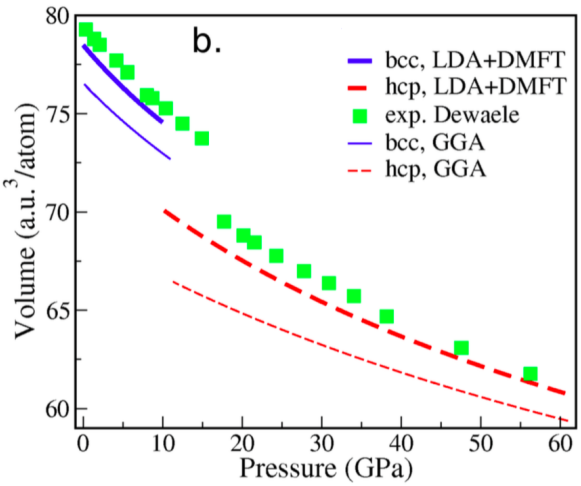

Figure 4.2 – Volume vs pressure dependence in low-temperature ferromagnetic body-centered-cubic (bcc) and paramagnetic hexagonal compact (hcp) Fe. GGA DFT significantly underestimates the lattice constants the the slope or bulk modulus. DFT LDA+DMFT values are much closer to experimental values. Reproduced from Ref. [105]

4.2 Overview of achievements

In the last two decades, DFT+DMFT has been used extensively to study from first principles a wide variety of transition metal oxides [74, 92–101], pure transition metals [84, 102–106], lanthanides [107, 108] and actinides [109–111].

The first implementations, without full charge self-consistency, were used to describe the spectral and conduction properties of materials, for instance transition metal oxides at or near a phase transition. The method has been particularly useful to understand the physics of materials with intermediate correlation strength, presenting interaction-driven metal-insulator transitions and other exotic properties.

More recently, as fully charge self-consistent implementations of DFT+DMFT have become more widespread and QMC solvers more powerful, this technique has been applied to describe the structural properties (crystal structures, lattice constants, bulk moduli...) of pure transition metals, lanthanides and actinides in their more strongly correlated phases. In these, DFT+DMFT total energies significantly improve on results obtained within DFT with "standard" approximate exchange-correlation functionals like LDA or GGA[103, 105], as illustrated in Fig. 4.2. The phonon spectrum is also improved[104].

4.3 Determining H_U: the constrained random phase approximation

The DFT+DMFT method, as described above, is a material-specific alternative to model-based DMFT. It provides an *ab initio* way of deriving the equivalent of the hopping parameter t and the local level positions (in the multi-orbital case) of the Hubbard model (Eq. 3.1), allows to treat systems with many bands of different natures crossing the Fermi level, and to compute total energies (hence structural properties) of strongly correlated materials.

Nevertheless, an important parameter of the calculations has yet to be determined: the Coulomb interaction parameter U (or, more generally, the interaction Hamiltonian H_U). Indeed, the DFT+DMFT method is frequently criticized for not being truly *ab initio* because of this parameterization.

It should of course be possible to determine H_U from first principles in the context of a complete,

self-contained electronic structure theory. But what exactly is H_U? Here, it is useful to remember how DFT+DMFT was derived: a low-energy model containing only a subset of states around the Fermi level is defined by down-folding a Hamiltonian (or Green's function) describing all the orbital degrees of freedom of a system. It is reasonable that this same idea of down-folding should also be present in the definition of H_U. Let us first state what H_U is *not*:

- H_U is *not* the local interaction Hamiltonian obtained by taking the matrix elements of the bare Coulomb interaction,

$$V^{\text{bare}}_{m_1m_2m_3m_4} = \int d\mathbf{r}d\mathbf{r}'\phi_{m_1}(\mathbf{r})\phi^*_{m_3}(\mathbf{r})v^{\text{bare}}(\mathbf{r},\mathbf{r}')\phi_{m_2}(\mathbf{r}')\phi^*_{m_4}(\mathbf{r}') \tag{4.25}$$

  Indeed, this expression does not take into account screening. It would lead to values of U so large (typically of the order of 10 to 30 eV for transition metals or rare-earths), that virtually every metal should become a Mott insulator.

- In Eq. 2.22 and 2.23, we introduced a way to compute the screened Coulomb interaction W. Yet, H_U is also *not* the local interaction Hamiltonian obtained by taking the matrix elements of the fully screened Coulomb interaction W. The reason for this is slightly more subtle, but not surprising: W is also screened (indeed, most stronly screened) by transitions within the very subspace whose low-energy degrees of freedom we want to describe in DMFT, so that W is significantly over-screened.

- Screening is involved, and we know from GW theory that screening is a dynamical effect. Therefore, it seems reasonable that H_U is not a static quantity but should have some frequency-dependence like $W(\omega)$, and simplify to the expression of Eq. 4.25 above in the limit of infinite frequency $\omega \to +\infty$.

In other words, to determine H_U consistently from first principles, a down-folding procedure should be used, like in DFT+DMFT. Only screening channels outside the correlated subspace should be allowed to screen the bare Coulomb interaction.

A popular method in the 90's, applied for DFT+U calculations, is constrained LDA (cLDA)[112, 113]. By constraining the occupation of the d or f shell on a given atom in a supercell, and computing the second derivative of the total energy with respect to the d or f occupation, a value can be deduced for U^{cLDA} and J^{cLDA}. DFT implementations with local basis functions like LMTO are best suited for such calculations. However, cLDA has a tendency to overestimate U because the screening channels are not described correctly[114]. For a long time, this was not considered to be an important problem, since somewhat inflated values of U were required in DFT+DMFT to reproduce experimental results. More recently, it was understood that this is due to the neglect of effects like dynamical screening[115].

To improve on these deficiencies, building on the ideas of GW theory, Aryasetiawan *et al.* introduced the idea of the constrained Random Phase Approximation (cRPA)[114, 116]. In cRPA, the polarization function is computed in the random phase approximation, separating transitions within the correlated subspace and the others:

$$P = P^{d-d} + P^{\text{rest}} \tag{4.26}$$

considering for instance a correlated d shell. The correlated subspace can conveniently be defined with the same projectors as the one used in DFT+DMFT, so that the determination and usage of U and J are consistent. The partially screened interaction W^{rest}, of which U and J are respectively direct and Fock-like matrix elements, can then be calculated as

$$W^{\text{rest}} = \frac{V_{\text{bare}}}{1 - P^{\text{rest}}V_{\text{bare}}} \tag{4.27}$$

This equation is similar to Eq. 2.23, with a partial screening. Incidentally, since the polarization computed in RPA is frequency-dependent, so is $W^{\text{rest}}(\omega)$ and its matrix elements. Fig. 4.3 illustrates equations 4.26 and 4.27 with diagrams.

cRPA has been used extensively with DFT+DMFT, to make the calculations *ab initio*[80, 118] and analyze which screening channels are important (see, for instance, [119, 120]). Nevertheless, cRPA is not

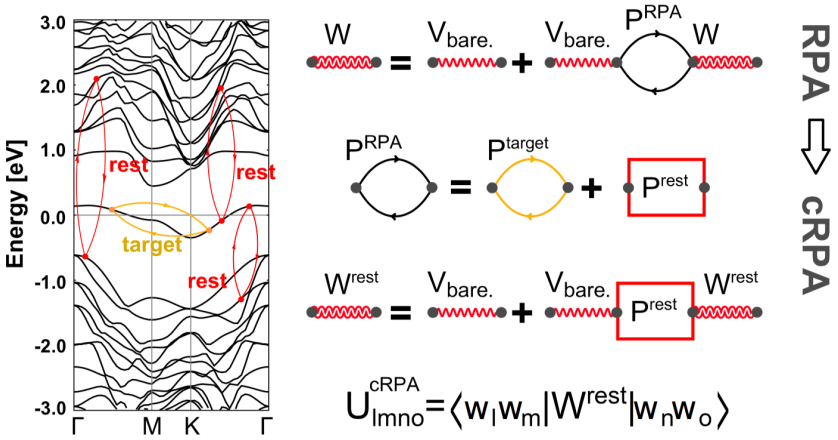

Figure 4.3 – Summary of the cRPA procedure, applied to a system with a single correlated band at the Fermi level. Reproduced from Ref. [117]. P_{target} denotes the polarization from transitions within the low-energy subspace, while P_{rest} denotes the polarization due to all transitions between bands outside the low-energy subspace *or* between a band within, and a band outside of it.

equally powerful for all systems. It produces reasonably good results when the bands corresponding to the correlated subspace are well separated from the others (so that the projectors are unitary), but less so when other (dispersive) bands cross the Fermi level. In this case, residual metallic character after the projection often leads to overscreening or requires additional approximations. A disentanglement procedure has been proposed[121] and successfully applied to consistently compute H_U even in such cases. Indeed, it is not trivial to cut out transitions within the correlated subspace when other bands with mixed orbital character co-exist in the energy window. However, the issues above are not strictly a a defect of cRPA method: rather, they emphasize the fact that defining a good low-energy model, starting from an all-electron electronic structure calculation, is difficult.

Moreover, for states hybridizing strongly with bands from different atoms (for example, e_g states in transition metal oxides hybridizing with oxygen $2p$ states), some ambiguity exists on how to best construct the projectors. In oxides with partially filled e_g states, a common procedure is to exclude transitions within the d orbital subspace but construct Wannier functions with a window containing transition metal d and ligand $2p$ states. Such a model is called a "$d - dp$" model[119]. Several "$A - B$" models like this have been used in the context of cRPA calculations, where the notation "$A - B$" indicates that Wannier functions are constructed and orthonormalized in a space A (which may for instance include only d orbitals, or d and p orbitals) and transitions within the space B, included in A, are removed when calculating the partially screened Coulomb interaction. Finally, the output of cRPA depends somewhat on the input DFT calculation. Ideally, it should be performed self-consistently with the DFT+DMFT cycle, where the positions and occupation of bands can be reshuffled.

In conclusion, cRPA is a powerful tool that gives both qualitative and quantitative indications on the values of the local interaction Hamiltonian H_U used in DMFT or DFT+DMFT, and is defined in a framework compatible by construction with DFT+DMFT calculations. It also provides the full frequency-dependence of H_U, as well as its non-local components if supercells are used. Still, DFT+cRPA+DMFT (as we may call such a scheme) feels like an awkward way of combining building bricks that are not exactly compatible, and does not define a full electronic structure theory.

4.4 Methods beyond Density Functional Theory + Dynamical Mean-Field Theory

DMFT, and likewise its combination with DFT, rely on a set of approximations that are often, but not always justified. The most obvious approximation is of course the locality of the self-energy $\Sigma(\omega)$, which is exact only in infinite dimensions. This was shown to be insufficient in, among others, the high critical temperature superconducting cuprates (a family of materials that happen to be quasi two-dimensional)[70].

Other approximations include the supposed locality of effective Coulomb interactions in the Hubbard model, or the lack of self-consistence with respect to the screening and dependence on an approximate double-counting correction in DFT+DMFT.

Extending DMFT and DFT+DMFT to improve on these issues has been a longstanding field of research, and several solutions have indeed been applied. In this section, I briefly present the main ideas behind some of them.

4.4.1 Cellular Dynamical Mean-Field Theory

A first way to partially restore the non-locality of the self-energy is to define a cluster of impurities, coupled to a common bath with non-local hybridization[122, 123]. In this real-space picture, called cellular DMFT (or CDMFT), the DMFT hybridization Δ, dynamical Weiss field $\mathcal{G}_0$, Green's function G_{loc} and self-energy Σ all take the matrix form

$$G = \begin{pmatrix} (G_{1-1}) & (G_{1-2}) \\ (G_{2-1}) & (G_{2-2}) \end{pmatrix}$$

where (G_{i-j}) represents the (matrix) quantity between atoms i and j in the cell, instead of the block-diagonal form in single-site DMFT:

$$G = \begin{pmatrix} (G_{1-1}) & (0) \\ (0) & (G_{2-2}) \end{pmatrix}$$

The problem is then treated in a way similar to DMFT, with $\mathbf{k}$-independent self-energy

$$[\Sigma(i\omega_n, \mathbf{k})]_{mm'} = \left[\Sigma^{\text{cell}}(i\omega_n)\right]_{mm'} \tag{4.28}$$

This may be misleading: while the self-energy appears local in the $\mathbf{k}$-space, it is a matrix and the non-locality is partially restored by non-local off-diagonal elements, that link different sites (indexed by a and b above) in real space.

CDMFT was instrumental for understanding the metal-insulator transition in oxides such as VO_2[96] (more on this in chapter 8) or the d-wave superconductivity of cuprates[122].

4.4.2 Dynamical cluster approximation

The counterpart to CDMFT in the reciprocal space is the Dynamical Cluster Approximation (DCA)[124, 125]. In DCA, rather than using a constant self-energy in the $\mathbf{k}$-space, a coarse graining of the Brillouin zone in a finite number N_c of patches is introduced. DCA has been used on the single band Hubbard model to explain the $\mathbf{k}$-dependence of the quasi-particle lifetime in cuprates.

However, the QMC fermionic sign problem (see chapter 5) increases exponentially with the number of atoms in the cluster N_c, so that exploring long-range correlations, low-temperatures and multi-orbital systems is difficult, if not impossible.

4.4.3 Extended Dynamical Mean-Field Theory

It is well known that, while the bare Coulomb interaction is long-ranged (it decreases as $1/r$), the screened one is much shorter-ranged. However, considering it to be purely local, as in the Hubbard model, is a somewhat rough approximation that deserves to be discussed. Arguably, a better model is the extended Hubbard model, which can be written in the single band case as follows:

$$H = (\epsilon_0 - \mu)\sum_{i,\sigma} n_{i\sigma} - t\sum_{\langle i,j\rangle,\sigma}\left(c^\dagger_{i\sigma}c_{j\sigma} + c^\dagger_{j\sigma}c_{i\sigma}\right) + U\sum_i n_{i\uparrow}n_{i\downarrow} + \sum_{i\neq j} V_{ij}n_i n_j \tag{4.29}$$

where V_{ij} describes non-local Coulomb interactions: they can act on nearest neighbors, second-nearest neighbors, or even be more long-ranged. Such non-local interactions are usually smaller than the local sort, but are physically important in some cases. In surface systems, for instance, reduced screening means the Coulomb interaction decays more slowly than in the bulk, so that non-local interactions can make the difference between metallic or insulating behavior[126]. In the square lattice Hubbard model, non-local interactions can give rise to a charge-ordering[127]. Finally, on a triangular lattice, non-local interactions can cause frustration and bring forth exotic charge-ordered metallic phases[128].

Extended DMFT (EDMFT)[129–131] is (at its name indicates) an extension of DMFT, used to describe this extended Hubbard model. The bottom line is that, as in DMFT, the extended Hubbard model can be treated by mapping the lattice problem onto an single-site impurity model, at the cost of introducing a retarded Coulomb interaction.

Thanks to a Hubbard-Stratonovich transformation of the non-local part of the action

$$e^{\int_0^\beta d\tau \sum_{ij}\frac{1}{2}V_{ij}n_i(\tau)n_j(\tau)} = \int \mathcal{D}[\phi] e^{-\int_0^\beta d\tau \frac{1}{2}\sum_{ij}\phi_i(\tau)[-V^{-1}_{ij}]\phi_j(\tau) \pm \int_0^\beta \sum_i \phi_i(\tau)n_i(\tau)} \tag{4.30}$$

we integrate out the bosonic degrees of freedom, which allows to define an impurity action similarly to single-site DMFT:

$$S_{imp} = -\int_0^\beta d\tau \int_0^\beta d\tau' \sum_\sigma c^\dagger_\sigma(\tau)\mathcal{G}_0^{-1}(\tau-\tau')c_\sigma(\tau') + \frac{1}{2}\int_0^\beta d\tau \int_0^\beta d\tau' \mathcal{U}(\tau-\tau')n_\uparrow(\tau)n_\downarrow(\tau') \tag{4.31}$$

where a bosonic dynicamical interaction $\mathcal{U}(\tau-\tau')$ (or equivalently, $\mathcal{U}(\omega)$) has been introduced. $\mathcal{U}$ is an additional bosonic mean-field, similar to the fermionic dynamical mean-field $\mathcal{G}_0$. Thus the problem with static, non-local interactions is reduced to a problem with local, dynamical interactions.

A local screened interaction $W_{\text{loc}}(i\Omega_n)$ (bosonic equivalent of the local Green's function $G_{\text{loc}}(i\omega_n)$) and a polarization $P_{\text{imp}}(i\Omega_n)$ (bosonic equivalent of the self-energy $\Sigma_{\text{imp}}(i\omega_n)$) are introduced, and computed self-consistently in the EDMFT loop. Here, $i\Omega_n$ represents a bosonic Matsubara frequency, $i\Omega_n = \frac{2n\pi}{\beta}$, whereas $i\omega_n = \frac{(2n+1)\pi}{\beta}$. The self-consistency equations in EDMFT read

$$\begin{aligned}\mathcal{G}_0^{-1}(i\omega_n) &= G^{-1}(i\omega_n) + \Sigma_{\text{imp}}(i\omega_n)\\ \mathcal{U}^{-1}(i\Omega_n) &= W^{-1}(i\Omega_n) + P_{\text{imp}}(i\Omega_n)\end{aligned} \tag{4.32}$$

Both self-consistency loops are performed at the same time and are not linked, except inside the impurity solver that gives $\Sigma_{\text{imp}}(i\omega_n)$ and $P_{\text{imp}}(i\Omega_n)$ as an output. Note that the polarization P and self-energy Σ are *local*, even though the problem has non-local interaction.

We refer the reader to Ref. [132] for a more technical description of EDMFT. We discuss the physical implications of a dynamical interaction in section 6.

4.4.4 GW + Extended Dynamical Mean-Field Theory

More generally, among the requirements for an "ideal" ab initio electronic structure theory, the following points stand out:

1. Have a $\mathbf{k}$-dependent self-energy, $\Sigma(\omega, \mathbf{k})$.
2. Treat correlations in a non-perturbative way as DMFT does, *at least* in the subspace of correlated bands around the Fermi level.
3. Contain the full, non-local screened Coulomb interaction.
4. Be double-counting free.
5. Be as parameter-free as possible. (At least in principle. In reality, having some parameters in the implementation, for example the basis set for the GW calculation, may be unavoidable)

   To this we may add a last point, but this may be wishful thinking:

6. Be computationally tractable with today's algorithms and hardware.

The GW+EDMFT method[132–134] is an attempt at providing such a theory, mostly fulfilling the requirements above (except for point 6., one may argue). In GW+EDMFT, as its name suggests, a non-local and non-perturbative self-energy and polarization by adding the (local, non-perturbative) values and the non-local part of the GW values:

$$\begin{aligned} \Sigma^{\mathrm{GW+DMFT}}(i\omega_n, \mathbf{k}) &= \Sigma_{\mathrm{imp}}(i\omega_n) + \Sigma^{\mathrm{GW}}_{\mathrm{nloc}}(i\omega_n, \mathbf{k}) \\ P^{\mathrm{GW+DMFT}}(i\Omega_n, \mathbf{k}) &= P_{\mathrm{imp}}(i\Omega_n) + P^{\mathrm{GW}}_{\mathrm{nloc}}(i\Omega_n, \mathbf{k}) \end{aligned} \tag{4.33}$$

where the non-local part of the self-energy and polarization are computed as

$$\begin{aligned} \Sigma^{\mathrm{GW}}_{\mathrm{nloc}}(i\omega_n, \mathbf{k}) &= \Sigma^{\mathrm{GW}}(i\omega_n, \mathbf{k}) - \sum_{\mathbf{k}} \Sigma^{\mathrm{GW}}(i\omega_n, \mathbf{k}) \\ P^{\mathrm{GW}}_{\mathrm{nloc}}(i\Omega_n, \mathbf{k}) &= P^{\mathrm{GW}}(i\Omega_n, \mathbf{k}) - \sum_{\mathbf{k}} P^{\mathrm{GW}}(i\Omega_n, \mathbf{k}) \end{aligned} \tag{4.34}$$

The GW contributions to Σ and P are calculated according to the GW equations 2.22 and 2.24. The (dynamical) screening $\mathcal{U}(i\Omega_n)$ is treated in the same fashion as in EDMFT, except it is not obtained from a set of parameters V_{ij} but from the Eq. 2.23 applied on the bare Coulomb interaction v with a constrained polarization, obtained as a by-product in Eq. 2.22.

GW and EDMFT are both based on Green's functions, and thus interface well. Indeed, the GW+EDMFT equations can be derived from a functional $\Gamma[G, W]$. It follows that no double-counting correction is needed, as the diagrams entering Γ from the local DMFT part and the non-local GW part can be clearly separated.

GW+EDMFT calculations can, at least in principle, be performed self-consistently. Indeed, while self-consistent GW are known to deteriorate the results of one-shot GW due to neglect of the vertex, the approximation in GW+EDMFT is less drastic. In practice, full self-consistent GW+EDMFT calculations have been implemented only for one-band systems[126, 127, 132, 135]. In multi-band systems, the computational cost is so formidable that approximations must be made. GW+DMFT calculations have for instance been performed on a classical benchmark system of ab initio many-body methods, $SrVO_3$, an perovskite oxide with partly filled t_{2g} bands[136, 137]. Therein, the full self-consistency in GW and EDMFT was dropped, so that a self-consistent EDMFT calculation was made on top of a one-shot GW calculation, taking the GW polarization $P^{\mathrm{GW}}(i\Omega_n, \mathbf{k})$ as an input.

Let us note that, for all of its conceptual strengths, GW+EDMFT does not capture all physical effects that can be observed in materials. In particular, long-range collective modes are better described by methods that impose lesser approximations on the full many-body vertex, like the recently proposed TRILEX approximation[138].

Finally, computing the full dynamical GW self-energy can be challenging for large realistic systems. One advantage of GW+EDMFT is that we understand rather clearly what physical phenomena are described by it. This means further approximations can be made to keep the computation charge reasonable (which is often needed) while keeping track of the physical aspects that are described. This aspect is further discussed in the next chapter, Chap. 6.

Chapter 5

Technical aspects

As we have seen in section 3.2, DMFT allows to map a lattice problem onto a self-consistently determined impurity model describing a lattice site exchanging particles with a non-interacting bath, the solution of which provides an approximation to the self-energy (or indeed the exact one in the limit of infinite dimensions). We have not yet, however, discussed how this very impurity model is solved. Moreover, though we discussed how the interaction Hamiltonian H_U can be determined from first principles, for instance using the cRPA method, we have not yet discussed the forms of H_U used in practice.

We do not plan here to give a full discussion of either aspect: we refer the reader to [57] for a review on modern quantum Monte-Carlo impurity solvers, and to [139] for a discussion of local interaction Hamiltonians. Rather, for the sake of completeness, we discuss a few aspects impurity solvers and interaction Hamiltonians that were applied in this thesis.

5.1 Local interaction Hamiltonians

5.1.1 The Slater Hamiltonian

In single band models, H_U is a simple scalar U. Many-band cases are more complicated. The most general local interaction Hamiltonian is a four-dimensional matrix $U_{m_1m_2m_3m_4}$, where $(m_i)_{1<i\leq 4}$ refer to orbital indices in the correlated subspace. The corresponding Slater Hamiltonian is

$$H = \frac{1}{2} \sum_{m_1m_2m_3m_4,\sigma\sigma'} U_{m_1m_2m_3m_4} c^\dagger_{m_1\sigma} c^\dagger_{m_2\sigma'} c_{m_3\sigma'} c_{m_4\sigma} \tag{5.1}$$

This Hamiltonian is rotationally invariant.

$U_{m_1m_2m_3m_4}$ is generally parameterized from a set of Slater integrals:

$$U_{m_1m_2m_3m_4} = \sum_{k=0}^{2l} \alpha_k(m_1m_2m_3m_4) F^k \tag{5.2}$$

where $\alpha_k(m_1m_2m_3m_4)$ are the Racah-Wigner parameters (see [139, 140]) and F^k are material-dependent Slater integrals that describe the monopole (F^0) or higher-order moments (the others) part of the Coulomb interaction. In practice, only F^0, F^2, F^4 are required for d orbitals, or F^0, F^2, F^4, F^6 for f orbitals. F^0 is most affected by screening and varies most for different materials. The higher-order integrals vary somewhat with materials, but their ratios not so much:

$$F^4/F^2 \approx 0.625 \text{ (in } 3d \text{ shells)} \tag{5.3}$$

$$F^4/F^2 \approx 0.67 \text{ and } F^6/F^2 \approx 0.49 \text{ (in } 4f \text{ shells)} \tag{5.4}$$

This property allows to define the Hamiltonian with only two parameters: the Hubabrd U and Hund's exchange J_H, with

$$U = F^0 \tag{5.5}$$

$$J_H = \frac{F^2 + F^4}{14} \text{ (in } d \text{ shells)} \tag{5.6}$$

$$J_H = \frac{286F^2 + 195F^4 + 250F^6}{6435} \text{ (in } f \text{ shells)} \tag{5.7}$$

5.1.2 The density-density interaction Hamiltonian

A simpler type of interaction Hamiltonian is the density-density Hamiltonian

$$H = \frac{1}{2} \sum_{(m\sigma)\neq(m'\sigma')} U^{\sigma\sigma'}_{mm'} n_{m\sigma} n_{m'\sigma'} \tag{5.8}$$

where

$$U^{\sigma\bar{\sigma}}_{mm'} = U^{\text{Slater}}_{mm'mm'} \tag{5.9}$$

$$J_{mm'} = U^{\text{Slater}}_{mm'm'm} \tag{5.10}$$

$$U^{\sigma\sigma}_{mm'} = U^{\text{Slater}}_{mm'mm'} - J_{mm'} \tag{5.11}$$

The density-density Hamiltonian is not rotationally invariant, and does not contain all interaction terms. For instance, it does not have the spin-flip terms $J_{mm'} c^\dagger_{m\uparrow} c_{m\downarrow} c^\dagger_{m'\uparrow} c_{m'\downarrow}$. However, it allows much faster calculations in some cases (see section 5.2.2), which makes it useful in calculations with many orbitals.

5.1.3 The Hubbard-Kanamori Hamiltonian for t_{2g} systems

When working in a cubic basis, in particular for t_{2g} orbitals, it is necessary to employ the same basis in Eq. 5.2. One can show (see [139]) that the density-density part of the Hamiltonian can in that case be parameterized from the Slater integrals as

$$U^{\sigma\bar{\sigma}}_{mm} = \mathcal{U} \tag{5.12}$$

$$U^{\sigma\sigma}_{m\neq m'} = \mathcal{U} - 3\mathcal{J} \tag{5.13}$$

$$U^{\sigma\bar{\sigma}}_{m\neq m'} = \mathcal{U} - 2\mathcal{J} \tag{5.14}$$

$$\tag{5.15}$$

with

$$\mathcal{U} = F^0 + \frac{4}{49}F^2 + \frac{4}{49}F^4 \tag{5.16}$$

$$\mathcal{J} = \frac{3}{49}F^2 + \frac{20}{441}F^4 \tag{5.17}$$

giving the Hubbard-Kanamori Hamiltonian

$$H = \sum_m \mathcal{U} n_{m\uparrow} n_{m\downarrow} + \sum_{\sigma, m>m'} (\mathcal{U} - 2\mathcal{J})\, n_{m\bar{\sigma}} n_{m'\sigma} + (\mathcal{U} - 3\mathcal{J})\, n_{m\sigma} n_{m'\sigma} \tag{5.18}$$

In the context of cRPA (see section 4.3), however, $\mathcal{U}$ and $\mathcal{J}$ are often computed by averaging the

matrix elements of $U_{m_1m_2m_3m_4}$ directly in the cubic basis:

$$\mathcal{U} = \frac{1}{N}\sum_{m=1}^{N=3} U_{mmmm} \tag{5.19}$$

$$\mathcal{J} = \frac{1}{N(N-1)}\sum_{m\neq m'}^{N=3} U_{mm'm'm} \tag{5.20}$$

because this makes it easier to remove the screening channels within the t_{2g} sub-space.

5.2 Impurity solvers

5.2.1 The Hubbard I approximation

In the Hubbard I or atomic approximation[41, 74], the impurity problem is solved by neglecting the dynamical hybridization with the bath. Only its static part, or in other words the effective atomic levels $H_{1\text{el}}$ of the impurity given by

$$\hat{H}_{1\text{el}} = -\mu + \langle H^c \rangle - \Sigma_{\text{DC}} \tag{5.21}$$

is used to obtain the self-energy, where $\langle H^c \rangle$ is the projected Kohn-Sham Hamiltonian on the correlated d or f orbitals of the atom, summed over the Brillouin zone. Note that $H_{1\text{el}}$ is a matrix and may contain off-diagonal elements: this is not an issue.

The full impurity Hamiltonian is $H_{\text{imp}} = H_{1\text{el}} + H_U$, where H_U is the Slater Hamiltonian 5.1. For a single atom that does not exchange particles with a bath, it can be solved analytically.

The first step consists in diagonalizing H_{imp} for N, $N-1$ and $N+1$ electrons, where the ground state has N electrons. The interacting Green's function is then obtained from the Lehmann representation formula

$$G_{ij}(i\omega_n) = \frac{1}{Z}\sum_{nn'} \frac{\langle n|c_i|n'\rangle\langle n'|c_j^\dagger|n\rangle}{i\omega_n + E_n - E_{n'}}(e^{-\beta E_n} + e^{-\beta E_{n'}}) \tag{5.22}$$

where the sum is formally over all atomic states n, n' with all possible electron numbers, though in practice the Boltzmann factors $e^{-\beta E_n} + e^{-\beta E_{n'}}$ usually mean that the contribution of states with $N-2$ electrons or less, and $N+2$ electrons or more, is negligible. The self-energy is then readily obtained from the Dyson equation:

$$\Sigma(i\omega_n) = G_0^{-1}(i\omega_n) - G^{-1}(i\omega_n) \tag{5.23}$$

Conveniently, the real-frequency Green's function (and, correspondingly, the self-energy) can be obtained in the same way

$$G_{ij}(\omega) = \frac{1}{Z}\sum_{nn'} \frac{\langle n|c_i|n'\rangle\langle n'|c_j^\dagger|n\rangle}{\omega + E_n - E_{n'} + i\eta}(e^{-\beta E_n} + e^{-\beta E_{n'}}) \tag{5.24}$$

with η an infinitesimal small real number.

The Hubbard I approximation makes for very quick calculation: in the worst case, corresponding to a half-filled f shell, the longest part of the calculation is the diagonalization of H_{imp} with a Hilbert space of dimension $\binom{14}{7} = 3432$, which takes of the order of 10 minutes. In more favorable cases, the diagonalization is almost immediate.

In practice, the Hubbard I approximation gives good results (and is mostly used) to describe the physics of partly filled $4f$ shells[108, 141, 142] where the hybridization with the other orbitals is small. It fails to describe some properties of the nominally d^1 and d^{13} lanthanides Ce and Yb, in particular in the parameter regimes or phases where Kondo physics is at play[142, 143] and the $4f$ electrons become delocalized. Extensions of the Hubbard I approximation can also be used to study some well-chose properties of transition metal oxides[144].

5.2.2 Continuous-time quantum Monte-Carlo and the hybridization expansion

Continuous-time Quantum Monte-Carlo (CTQMC) solvers[57, 145] allow to obtain numerically exact (assuming ergodicity and sufficient sampling) interacting Green's functions of impurity models. In particular, contrary to the Hirsch-Fye quantum Monte-Carlo algorithm[146], CTQMC solvers do not have an imaginary time discretization bias.

We recall the expression of the impurity DMFT action in a multiorbital case

$$S_{\text{imp}} = -\sum_{mm'} \int_0^\beta d\tau \int_0^\beta d\tau' \sum_\sigma c^\dagger_{m\sigma}(\tau) \left[(\partial_\tau + H^{\text{1el}}_{mm'})\delta(\tau-\tau') + \Delta_{mm'}(\tau-\tau') \right] c_{m'\sigma}(\tau') + \int_0^\beta d\tau H_U(\tau) \tag{5.25}$$

where E_{ab} is a matrix containing level positions (the static part of the hybridization), and $H_U(\tau)$ is the interaction part of the action. In a single-band case and for a density-density interaction Hamiltonian,

$$H_U(\tau) = \sum_{mm'\sigma\sigma'} U^{\sigma\sigma'}_{mm'} n_{m\sigma}(\tau) n_{m'\sigma'}(\tau) \tag{5.26}$$

The partition function is given by

$$Z = \int \mathcal{D}[c^\dagger c] e^{-S_{\text{imp}}} \tag{5.27}$$

Different types of CTQMC algorithms[145, 147, 148] are obtained by choosing a part of the action to expand Eq. 5.27 as an infinite series. In this thesis, we used the hybridization expansion CTQMC algorithm[145], obtained as follows. One separates the action 5.25 into a hybridization term and a local term

$$S_{\text{imp}} = S_{\text{loc}} + \sum_\sigma S^\sigma_{\text{hyb}} \tag{5.28}$$

which allows to compute the partition function as

$$Z = Z_{\text{loc}} \left\langle \prod_\sigma S^\sigma_{\text{hyb}} \right\rangle_{\text{loc}} \tag{5.29}$$

After replacing the hybridization term by its expression and some algebra (see Ref. [57, 145] for the details) one obtains the diagrammatic expansion

$$Z = Z_{\text{loc}} \sum_{k_\sigma=0}^{\infty} \int d\tau_1 ... d\tau_{k_\sigma} \int d\tau'_1 ... d\tau'_{k_\sigma} \sum_{j_1 ... j_{k_\sigma}} \sum_{j'_1 ... j'_{k_\sigma}}$$
$$\text{Tr}_d \left[T_\tau e^{-\beta H_{\text{loc}}} d_{j_{k_\sigma}}(\tau_{k_\sigma}) d_{j_{k_\sigma}}(\tau_{k_\sigma}) d^\dagger_{j'_{k_\sigma}}(\tau'_{k_\sigma}) ... d_{j_1}(\tau_1) d^\dagger_{j'_1}(\tau'_1) \right] \det \mathbf{\Delta}^\sigma \tag{5.30}$$
$$= \sum_c \det \mathbf{\Delta}^\sigma(c) w_{\text{loc}}(c) \tag{5.31}$$

where we introduced a sum over all diagrammatic configurations c (a set of creation and annihilation operators $(c_i, c_i^\dagger)$ at times τ_i), a trace over the local Hamiltonian $w_{\text{loc}}(c)$ and a hybridization determinant $\det \mathbf{\Delta}_\sigma$ where $\mathbf{\Delta}^\sigma$ is a matrix whose coefficients are given by $\mathbf{\Delta}^\sigma_{lm} = \Delta_{j_l j_m}(\tau_l - \tau_m)$, the letter j designating an orbital index.

One can then use a Metropolis-Hastings[149, 150] (Monte-Carlo) algorithm, adding and removing creation and annihilation operators at random times τ_i and using the configuration weight

$$w_c = \det \mathbf{\Delta}^\sigma(c) w_{\text{loc}}(c) \tag{5.32}$$

Crucially, this allows to sample not only the partition function but also different types of correlators, notably the local Green's function. Both the calculation (or update) of $\det \mathbf{\Delta}^\sigma(c)$ and $w_{\text{loc}}(c)$ in a Monte-Carlo move are fairly costly in terms of computational time. In particular, the hybridization expansion

CTQMC solver becomes slow at very high and low temperatures, for systems with many orbitals, and when the hybridization function takes large values.

Another practical issue is that w_c as defined above is not necessarily a good Monte-Carlo weight. When the hybridization $\Delta_{ij}(\tau)$ has off-diagonal elements (which is usually the case in multi-orbital systems, unless they are zero by symmetry), w_c can take negative values due to the fermion sign problem[57]. In this case its absolute value $|w_c|$ should be used as Monte-Carlo weight in the Metropolis algorithm, but all measured observables must then be rescaled by $\langle \text{sign} \rangle_{\text{MC}}$, the average sign of w_c over the Monte-Carlo steps, dramatically reducing the accuracy when the average sign is close to 0. Empirically, the sign problems is under control at high temperatures but grows exponentially worse at low temperatures. It has also been demonstrated that the fermionic sign problem is "NP hard", meaning there is no polynomial solution to it[151].

5.2.3 Density-density interactions and the segment picture

We conclude this chapter by pointing out a convenient property of density-density interaction Hamiltonians. For such a local interaction Hamiltonian like that of Eq. 5.8, one may use the so-called "segment picture" in the CTQMC algorithm[57], where the calculation of $w_{\text{loc}}(c)$ in the Monte-Carlo weight 5.32 becomes almost immediate. The only remaining bottleneck is then the time spent calculating the determinant $\det \mathbf{\Delta}^{\sigma}(c)$.

For multi-orbitals systems, the difference can be quite dramatic. For instance, in the DMFT calculations discussed in Chapter 7, involving the full $3d$ shell of metallic Fe (7 electrons), using the density-density Hamiltonian and segment picture in CTQMC makes for calculations about ten times faster than using the full Slater Hamiltonian and standard hybridization expansion solver.

Part II

Methods: construction of low-energy models

Chapter 6

Screened exchange and bosonic renormalizations: novel approaches to simple metals

In section 4.4, we introduced the GW+EDMFT method. This approximation is superior to the more simple DFT+DMFT method in terms of accurately predicting the electronic structure of weakly to strongly correlated electron materials. We do not repeat here all of its advantages over DFT+DMFT, but let us simply recall two points we wish to discuss in the present chapter:

- GW+EDMFT has non-local exchange, given by a dynamically screened HF self-energy from GW theory[152]

- It also incorporates the band renormalization effects coming from the dynamically screened Coulomb interaction in the correlated subspace, as described in EDMFT

The main drawback of GW+EDMFT – but an important one – is its computational cost, which is much higher compared to DFT+DMFT.

Here, we discuss a simplification to GW+EDMFT that brings the computational cost back to a more reasonable level. This scheme uses a screened exchange band structure and a renormalization of the bandwidth due to dynamical screening effects[120, 153–155]. In the following, we will refer to this scheme as SEx+Z_B, where SEx is short for "screened exchange" and Z_B is the typical name given to the bosonic renormalization factor that arises from the self-energy when dynamical Coulomb interactions are considered.

Note that in this chapter, we are interested in the methodological aspect of constructing consistent low-energy models for many-body calculations rather than in the details of how to solve them. For all the merits of the DFT+DMFT method, it contains approximations beyond the locality of the self-energy, inherent in the construction of the low-energy correlated subspace. For a more in-depth discussion of the conceptual difficulty of constructing consistent models without double-counting of interactions and without over-simplifying high-energy degrees of freedom, as well as a proposed "multi-scale *ab initio* model for correlated electrons", we refer the reader to a recent publication by Hirayama *et al.*[156].

6.1 From GW + Dynamical Mean-Field Theory to Screened Exchange + renormalization Z_B

6.1.1 Separation of the GW self-energy

The GW self-energy, computed via Eq. 2.21 to 2.24, is at the same time non-local and dynamical:

$$\Sigma_{GW} = \Sigma_{GW}(\mathbf{k}, \omega)$$

In this aspect, it is qualitatively different from the HF self-energy (which is non-local but static) or the DMFT self-energy (dynamical but local). Interestingly, however, the two aspects can to some extent be decoupled. Though this is an empirical observation rather than a mathematically provable statement, Tomczak *et al.*[137, 157] have shown that in the context of pnictides, chalocogenides and $SrVO_3$, and van Roekeghem *et al.*[120] in the context of the cobalt pnictide $BaCo_2As_2$, the GW self-energy can be split into a local dynamical part $\Sigma_{\text{loc}}(\omega)$ and a static non-local part $\Sigma_{\text{nloc}}(\mathbf{k})$.

This separation cannot be universally valid. Indeed, by construction the static part of Σ_{GW} is given by the unscreened non-local Fock potential v_F. However, in practical calculations one observes that the effects of Σ_{GW} arising from non-local components can be well approximated by a statically screened Fock potential.

Therefore, it is often found that, within a low-energy subspace, a decomposition as

$$\Sigma_{GW} = [GW(\omega = 0)]_{\text{nloc}} + [GW]_{\text{loc}} \tag{6.1}$$

is a good approximation. Here $GW(\omega = 0)$ is the GW self-energy computed with a static screening, and its non-local part $[GW(\omega = 0)]_{\text{nloc}}$ is computed in the same way as in Eq. 4.34. $[GW]_{\text{loc}}$ is the local (or $\mathbf{k}$-summed) part of the full GW self-energy. When dealing with strongly correlated materials, the next natural step is to replace this local part by the non-perturbative, fully dynamical DMFT self-energy. Another way to think about this is to start from the CoHSEx approximation of Eq. 2.29, and replace the local Coulomb hole term by the DMFT self-energy, which should better account for strong local correlations.

A further approximation[120] that greatly decreases the computational cost is to replace the statically screened, non-local GW self energy $[GW(\omega = 0)]_{\text{nloc}}$ by a simpler Fock term with a Yukawa potential as implemented in Wien2k[27]

$$V_{\text{SEx}} = -\sum_{\text{occ bands i}} \psi_i(r)\psi_i(r')^* W(r, r', 0) \tag{6.2}$$

with

$$W(r, r', \omega = 0) = e^{-k_{\text{TF}}.|r-r'|}\frac{1}{|r - r'|} \tag{6.3}$$

k_{TF} is a Thomas-Fermi wave-vector encoding how quickly the Coulomb interaction decays due to screening. In metals, k_{TF} can be related to the density of states at the Fermi level, and therefore can then be obtained self-consistently. In semi-conductors or Mott insulators, this scheme is less appropriate, as dielectric screening should allow more long-range exchange than in metals[158].

6.1.2 Screened Exchange + Dynamical Mean-Field Theory with dynamical U

A scheme combining SEx with DMFT has been tested on iron pnictides coumpounds and discussed in Ref. [120]. The authors compared angle-resolved photoemission spectroscopy (ARPES) experiments to the momentum-resolved spectral functions calculated within different schemes: DFT (LDA), DFT+DMFT, SEx+DMFT, and SEx+DMFT with dynamical $U(\omega)$. They found that the $3d$ bands calculated within

LDA are too wide, an issue that is partially corrected by the DMFT self-energy. However, DFT+DMFT does not correctly reproduce the experimental Fermi surface.

A SEx+DMFT calculation reproduces the bandwidths and Fermi surface better than DFT+DMFT, but *only* when dynamical screening effects ($U(\omega)$ in the impurity action, similarly to the EDMFT action 4.31) are taken into account. Indeed, the non-local exchange from SEx leads to a significant widening of the LDA bands, and even more compared to the measured bandwidths from ARPES. An additional renormalization of the bands, arising from the frequency-dependence of the local Coulomb interaction, is required to get correct bandwidths. At first sight, this looks similar to the error cancellation effect in the LDA exchange-correlation potential, where the underestimation in the correlation effects effectively cancels the overestimation in the exchange contribution to yield a bandwidth that is not too far off from experiment. in SEx+DMFT with dynamical U, the effects of correlations and exchange also cancel each other to some degree, but they are calculated more accurately, and eventually lead to a bandwidth closer to the correct one than LDA or DFT+DMFT.

This should not come as a surprise: if we consider that GW+EDMFT contains all the important physical effects (non-local self-energy, dynamical screening...) then it is reasonable that, even as we make the approximation of replacing the non-local self-energy by its static part (thus making bands wider) we should keep the counter-acting dynamical screening present in EDMFT.

6.1.3 Band renormalization with dynamical U

The effect of dynamical (or retarded) Coulomb interactions, a by-product of the downfolding to a low-energy subspace, on the bandwidth, is discussed in a publication by Casula *et al.*[115]. The authors consider a Hubbard-Holstein Hamiltonian[159–161]:

$$\begin{aligned} H = &- \sum_{ij\sigma} t_{ij} d^\dagger_{i\sigma} d_{j\sigma} + v \sum_i n_{i\uparrow} n_{i\downarrow} + \lambda \sum_{i\sigma} n_{i\sigma}(b_i + b_i^\dagger) \\ &+ \omega_0 \sum_i b_i^\dagger b_i + \mu \sum_{i\sigma} n_{i\sigma} \end{aligned} \tag{6.4}$$

where $d^\dagger$ and d represent fermionic creation and annihilation operators, n the corresponding density ($n = d^\dagger d$), v is the bare on-site Coulomb interaction, $b^\dagger$ and b are bosonic creation and annihilation operators, ω_0 the corresponding plasmon frequency, and λ a coupling term between electrons and bosons. The bosons in this model are coupling to the charge density, so we can interpret them as plasmon modes. A Lang-Firsov transformation of this Hamiltonian (see [162]) replaces H by $e^S H e^{-S}$, where

$$S = \frac{\lambda}{\omega_0} \sum_{i\sigma} n_{i\sigma}(b_i^\dagger - b_i)$$

so that the electron operators are replaced by polaron operators

$$c^\dagger_{i\sigma} = \exp\left(\frac{\lambda}{\omega_0}(b_i^\dagger - b_i)\right) d^\dagger_{i\sigma}$$

$$c_{i\sigma} = \exp\left(\frac{\lambda}{\omega_0}(b_i - b_i^\dagger)\right) d_{i\sigma}$$

The transformed Hamiltonian can be written as

$$H_{\mathrm{LF}} = - \sum_{ij\sigma} t_{ij} c^\dagger_{i\sigma} c_{j\sigma} + U_0 \sum_i c^\dagger_{i\uparrow} c_{i\uparrow} c^\dagger_{i\downarrow} c_{i\downarrow} + \omega_0 \sum_i b_i^\dagger b_i + \mu \sum_{i\sigma} n_{i\sigma} \tag{6.5}$$

where $U_0 = v - \frac{2\lambda^2}{\omega_0}$ is the local effective Coulomb interaction, screened by the plasmon mode. To build a low-energy model (supposing the plasmon frequency is large enough), one may project the Hamiltonian

onto the subspace with zero bosons, $H_{\text{eff}} = \langle 0|H_{\text{LF}}|0\rangle$. Then, H_{eff} is given by

$$H_{\text{eff}} = -\sum_{ij\sigma} Z_B t_{ij} d^\dagger_{i\sigma} d_{j\sigma} + U_0 \sum_i d^\dagger_{i\uparrow} d_{i\uparrow} d^\dagger_{i\downarrow} d_{i\downarrow} + \mu \sum_{i\sigma} n_{i\sigma} \tag{6.6}$$

by introducing a bosonic renormalization factor

$$Z_B = \exp\left(-\lambda^2/\omega_0\right) \tag{6.7}$$

that renormalizes the hopping t_{ij}. More precisely, in a general model including itinerant p states as well as more localized d states, it is shown that each d operator is renormalized by $\sqrt{Z_B}$, so that the hopping term of the Hamiltonian becomes

$$(p^\dagger d^\dagger) \begin{pmatrix} t_{pp} & \sqrt{Z_B} t_{pd} \\ \sqrt{Z_B} t^\dagger_{pd} & Z_B t_{dd} \end{pmatrix} \begin{pmatrix} p \\ d \end{pmatrix} \tag{6.8}$$

Finally, Casula *et al.*[115] generalize expression 6.7 to a general screened $U(\omega)$ by considering a continuum of boson modes:

$$Z_B = \exp\left(\frac{1}{\pi} \int_0^\infty \text{Im}U(\omega)/\omega^2 d\omega\right) \tag{6.9}$$

where U is expressed in real frequencies.

In section 4.3, we discussed cRPA as a tool to obtain partially screened values of the Coulomb parameters (U and J_H) for usage in DFT+U or DFT+DMFT calculations from first principles. However, it turns out that using the static screened U given by cRPA in such calculations tends to systematically underestimate the strength of correlations in materials (see Table III of Ref. [115] and references therein), so that artificially larger values must be used to reproduce experimental findings. Casula, Werner *et al.*[115, 161] explain this by the neglect of band-renormalization due to coupling to plasmons, which is contained effectively in the DFT exchange-correlation potential – but only to some degree.

Recently, using dynamical Coulomb interactions in DMFT (or similar) calculations has become more common, and several QMC solvers have been implemented with this in mind[62, 163, 164].

6.2 Screened Exchange as a generalized Kohn-Sham scheme

6.2.1 Generalized Kohn-Sham

The SEx+DMFT method described above can also be seen as a specific approximation to a spectral density functional theory based on the Generalized Kohn-Sham (GKS) scheme of Seidl *et al.*[165]. This view was recently put forward in Ref. [166]. In GKS theory, alternative choices for the reference system that are different than the familiar Kohn-Sham system of DFT are explored. Following similar theorems as one of the Hohenberg-Kohn theorems, GKS theory allows (in principle) to find the exact ground state energy and electronic density, just like DFT.

Rather than the non-interacting Kohn-Sham system, a different auxiliary reference system is used in order to obtain eigenvalues of the reference system, that is to say a band structure, closer to the real, fully interacting spectrum. In particular, a generalized Kohn-Sham scheme where the reference system is a screened exchange Hamiltonian can be constructed. The main motivation for the inclusion of screened exchange in the literature has been to improve upon the band gap problem in semiconductors. Indeed, it can be shown that the screened exchange contribution, which corresponds to a non-local potential, effectively reintroduces to some degree the derivative discontinuity that is missing in the pure DFT description based on local exchange-correlation potentials[167]. Since the derivative discontinuity corresponds to the discrepancy between the true gap and the Kohn-Sham gap in exact DFT, a substantial improvement of the theoretical estimate for band gaps can be expected on physical grounds and has indeed been found.

Here, our goal is somewhat different: motivated by the analysis of the role of screened exchange in GW+DMFT described above, we would like to connect the screened Exchange DMFT scheme introduced above to generalized KS schemes making direct use of the non-local screened exchange potential. With this goal in mind, we briefly review the generalized Kohn-Sham construction in the case of an effective Kohn-Sham system including screened exchange. Hereby, we follow closely Seidl *et al.*[165], both in notation and presentation.

6.2.2 The generalized Kohn-Sham equations

First, one defines a functional $S[\Phi]$, where Φ are Slater determinants of single-particle states $\{\phi_i\}$. Several possibilities exist for $S[\Phi]$: three examples are

$$S[\Phi] = \left\langle \Phi \left| \hat{T} \right| \Phi \right\rangle \tag{6.10}$$

$$S[\Phi] = \left\langle \Phi \left| \hat{T} \right| \Phi \right\rangle + v_H[\{\phi_i\}] + E_x[\{\phi_i\}] \tag{6.11}$$

or

$$S[\Phi] = \left\langle \Phi \left| \hat{T} \right| \Phi \right\rangle + v_H[\{\phi_i\}] + E_x^{sx}[\{\phi_i\}] \tag{6.12}$$

where $\hat{T}$ is the kinetic energy operator, v_H the Hartree potential and E_x (respectively E_x^{sx}) the exact exchange (respectively, screened exchange) functional. Eq. 6.10 will lead to the standard KS DFT equations with a reference system of non-interacting particles, Eq. 6.11 describes a reference system of interacting particles with an exchange energy given by exact HF exchange, and Eq. 6.12 describes a reference system of interacting particles where the exchange energy is given by a Thomas-Fermi screened Fock term

$$E_x^{sx}[\{\phi_i\}] = -\sum_{i<j}^{N} \int d\boldsymbol{r} d\boldsymbol{r'} \times \frac{\phi_i^*(\boldsymbol{r})\phi_j^*(\boldsymbol{r'})e^{-k_{\mathrm{TF}}|\boldsymbol{r}-\boldsymbol{r'}|}\phi_j(\boldsymbol{r})\phi_i(\boldsymbol{r'})}{|\boldsymbol{r}-\boldsymbol{r'}|} \tag{6.13}$$

where the indices i, j range over all Bloch eigenfunctions. The other terms are the familiar kinetic energy term $\langle\Phi|\hat{T}|\Phi\rangle$ and the Hartree energy $U_H[\{\phi_i\}]$. In the following, for simplicity, we consider the case of a screened exchange reference system deriving from Eq. 6.12. The more general equations are given in [165].

In order to derive a functional of the density Seidl *et al.* define a functional F^s via the minimization

$$F^S[\rho] = \min_{\Phi\to\rho(\boldsymbol{r})} S[\Phi] = \min_{\{\phi_i\}\to\rho(\boldsymbol{r})} S[\{\phi_i\}] \tag{6.14}$$

that is to be used in a similar way to the non-interacting kinetic energy of the reference Kohn-Sham system in KS DFT. Next, we define the energy functional

$$E^S[\{\phi_i\}; v_{\mathrm{eff}}] = S[\{\phi_i\}] + \int d\boldsymbol{r} v_{\mathrm{eff}}(\boldsymbol{r})\rho(\boldsymbol{r}) \tag{6.15}$$

where now the potential v_{eff} does not only include the external potential v_{ext} as in usual KS DFT, but also a contribution by the exchange-correlation part

$$v_{\mathrm{eff}} = v_{\mathrm{ext}} + v_{xc}^{sx}[\rho] \tag{6.16}$$

The additional contribution, the generalized (local) exchange-correlation potential

$$v_{xc}^{sx} = \frac{\partial E_{xc}^{sx}[\rho]}{\partial \rho} \tag{6.17}$$

is the functional derivative of the generalized (local) exchange-correlation functional

$$E_{xc}^{sx}[\rho] = E_{xc}[\rho] - E_x^{sx}[\rho] + T[\rho] - T^{sx}[\rho] \tag{6.18}$$

which comprises the difference between the exchange-correlation potential of standard Kohn-Sham DFT and the non-local exchange energy defined above, as well as the difference between the kinetic energies of the standard and generalized Kohn-Sham systems. The functional derivative will eventually have to be evaluated self-consistently at the converged density.

The generalized KS equations that define the eigenvalues of the auxiliary reference system (and, in turn, the electronic density) are then given by

$$-\nabla^2\phi_i(\boldsymbol{r}) + v_{\text{ext}}(\boldsymbol{r})\phi_i(\boldsymbol{r}) + u([\rho];\boldsymbol{r})\,\phi_i(\boldsymbol{r}) - \int d\boldsymbol{r'} v_x^{sx,\text{NL}}(\boldsymbol{r},\boldsymbol{r'})\phi_i(\boldsymbol{r'}) + v_{xc}^{sx}([\rho];\boldsymbol{r})\,\phi_i(\boldsymbol{r}) = \varepsilon_i\phi_i \tag{6.19}$$

with the Hartree potential u for density ρ, the non-local screened Fock potential

$$v_x^{sx,\text{NL}}(\boldsymbol{r},\boldsymbol{r'}) = -\sum_{j=1}^{N} \frac{\phi_i(\boldsymbol{r})e^{-k_{\text{TF}}|\boldsymbol{r}-\boldsymbol{r'}|}\phi_j^*(\boldsymbol{r'})}{|\boldsymbol{r}-\boldsymbol{r'}|} \tag{6.20}$$

and the effective (local) generalized Kohn Sham potential v_{xc}^{sx} defined by Eq. 6.17. The generalized Kohn-Sham equations take the form

$$\hat{\mathcal{O}}[\{\phi_i\}]\,\phi_j + \hat{v}_{\text{eff}}\phi_j = \varepsilon_j\phi_j \tag{6.21}$$

where $\hat{\mathcal{O}}$ is a non-local operator, generalizing the standard Kohn-Sham operator consisting solely of the kinetic energy and Hartree potential.

The ground state energy for a system with the external potential v_{ext} is then given by the expression

$$E_{\text{SEx}-\text{DFT}}[v] = F^S\left[\rho_0^S[v_{\text{eff}}]\right] + E_{xc}^{sx}\left[\rho_0^S[v_{\text{eff}}]\right] + \int dr v_{\text{ext}}(r)\rho_0^S[v_{\text{eff}}] \tag{6.22}$$

where the self-consistently determined density $\rho_0^S([v_{\text{eff}}],\mathbf{r})$ is obtained by minimizing

$$E_0^S[v_{\text{eff}}] = \min_{\rho(\mathbf{r})\to N}\left\{F^S[\rho] + \int v_{\text{eff}}(\mathbf{r})\rho(\mathbf{r})d\mathbf{r}\right\} \tag{6.23}$$

and v_{eff} is determined therein by Eq. 6.16. To actually perform calculations with such a GKS scheme, approximations must be made on the screened exchange-correlation functional E_{xc}^{sx} or on the corresponding potential v_{xc}^{sx}. The relevant approximations, similar to the LDA expressions, are proposed in [165].

Let us insist one more time on the nature of the approximation that is made: a SEx GKS scheme is in no way equivalent to solving self-consistently the HF equations with a screened Fock term. The latter is known to be physically wrong, while the former is conceptually exact if the exact exchange-correlation potential was known. The goal is not to improve on the total energy or electronic density given by KS DFT, but rather to ensure that the band structure derived from the auxiliary reference system be closer to the "exact" one.

6.2.3 A word on the choice of parameters: k_{TF}

Since the beginning, we have introduced the Thomas-Fermi screening vector k_{TF} without specifying its value. Surprisingly, in the GKS scheme the choice of k_{TF} is completely free: indeed, starting from Eq. 6.11 one may define a HF GKS scheme corresponding to $k_{\text{TF}} = 0$. Because k_{TF} enters (explicitly or implicitly) into both v_{xc}^{sx} and $v_x^{sx,\text{NL}}$ in Eq. 6.19, a cancellation effect ensures that the same ground state density and energy is reached, for the exact functionals.

For spectral properties extracted from the auxiliary KGS reference system, however, k_{TF} does play a role and should be chosen in order to produce a physically meaningful band structure. In practical calculations, k_{TF} can be determined from the electronic density at the Fermi level in metals (from an initial DFT calculation, or self-consistently)[120]. In insulators, where SEx GKS was first applied, this scheme cannot be applied since there is no density of states at the Fermi level. A usual choice is to define it from the average valence electron density[165].

6.2.4 From Screened Exchange generalized Kohn-Sham to Screened Exchange + Dynamical Mean-Field Theory

Once we have such a functional derivation, we may construct a spectral density functional in the same spirit as in DFT+DMFT [81], but starting from the generalized KS functional. In [168], the expression for the total energy within the standard DFT+DMFT case was shown to be

$$E = E_{\mathrm{DFT}} - \sum_l \varepsilon_l^{\mathrm{KS}} + \langle H_{\mathrm{KS}} \rangle + \langle (H_U - H_{dc}) \rangle \tag{6.24}$$

where $\sum_l \varepsilon_l^{\mathrm{KS}}$ is the sum of the occupied Kohn-Sham eigenvalues, $\langle H_{\mathrm{KS}} \rangle = \mathrm{Tr}\left[H_{\mathrm{KS}} \hat{G}\right]$, and H_{U} and H_{dc} denote the local interaction part of the Hamiltonian and the corresponding double counting term, respectively.

Instead of using the usual Kohn-Sham Hamiltonian for the construction of the one-body part, SEx+DMFT relies on the generalized Kohn-Sham reference system that includes the screened exchange potential. The generalization of (6.24) to the present case thus replaces the Kohn-Sham Hamiltonian H_{KS} in the expression for the energy by its non-local form, keeping track of the effective potential part:

$$E = E_{\mathrm{SEx-DFT}} - \sum_l \varepsilon_l^{\mathrm{SEx-KS}} + \langle \hat{\mathcal{O}} + \hat{v}_{\mathrm{eff}} \rangle + \langle H_U(V_{\mathrm{ee}}, \lambda_s, \omega_s) - H_{\mathrm{dc}} \rangle \tag{6.25}$$

Furthermore, the local interaction term is taken in the more general form of a dynamical interaction, thus corresponding to a local Hubbard term with *unscreened* interactions and local Einstein plasmons of energy ω_s coupling to the electronic density via the coupling strength λ_s.

6.2.5 In practice: one-shot Screened Exchange + Dynamical Mean-Field Theory

This concludes our description of the generalized Kohn-Sham interpretation of screened Exchange DMFT, resulting in particular in an energy functional expression. However, actually using the SEx GKS scheme greatly increases the computational cost compared to KS DFT: the difference is the same as using HF or hybrid functionals. Hence, a common approximation is to take the converged DFT density as a starting point, and then investigate spectral properties using the screened Exchange DMFT formalism[120]. This amounts to a one-shot screened Exchange-DFT+DMFT calculation that uses the DFT density as a starting point. The advantage of such an approach is obvious: numerically, this procedure allows us to avoid the expensive evaluation of non-local exchange terms within the self-consistency cycle of GKS theory.

Moreover, as is well-known, while severe deviations of the true spectrum from the Kohn-Sham spectrum are quite common, the ground state density obtained even from approximate DFT functionals is often a good representation of the true one. In the case of the *exact* DFT functional, this approach would also lead to the exact ground state density and energy, with additional improvements of the spectrum over standard Kohn-Sham DFT. Seidl *et al.*[165] themselves proposed a scheme adding a screened exchange perturbative term on top of the KS DFT eigenvalues, and showed that this is sufficient to improve on the spectral properties.

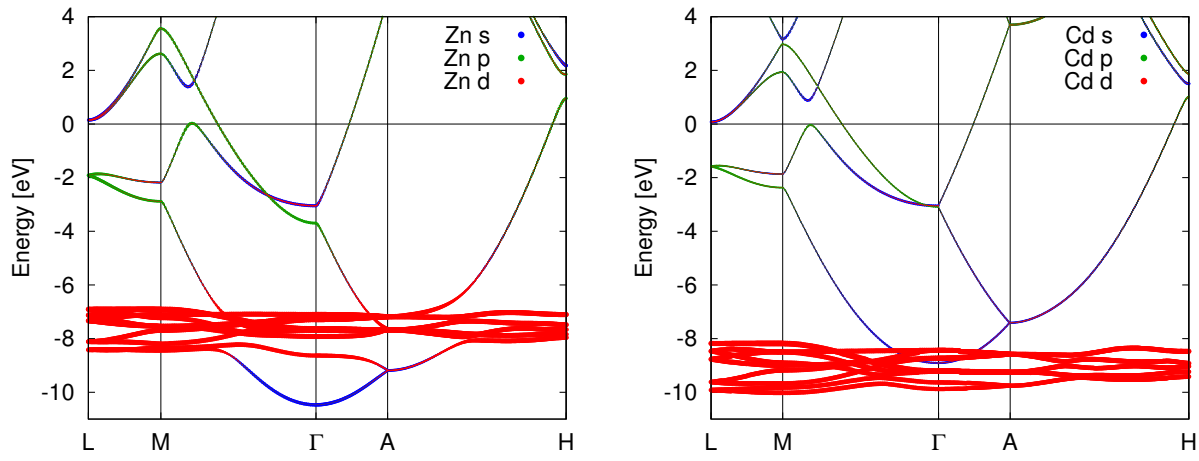

(a) Zn (b) Cd

Figure 6.1 – The band structure of elemental Zn and Cd calculated within DFT. The orbital character is indicated by the intensity of the different colors.

6.3 How should screened exchange Dynamical Mean Field Theory behave in weakly correlated materials?

Hamiltonians built as combinations of a DFT part and local Hubbard-type interaction terms trivially reduce to the DFT Kohn-Sham electronic structure when assuming that in weakly correlated materials the effective local interactions become negligible. The question of the recovery of the weakly interacting limit is, however, more interesting in the case of screened Exchange DMFT. While the static part of the effective local interaction may be assumed to lose its importance, band widening by the replacement of the DFT exchange correlation potential by the non-local exchange-correlation GW self-energy persists. On the other hand, plasmonic effects are also present in weakly correlated materials and continue to renormalize the low-energy band structure through electron-plasmon coupling. This raises the question of what the resulting spectra for weakly correlated materials look like in screened exchange + DMFT.

In Ref. [153], this question has been studied for early transition metal perovskites, where it was found that the band widening effect induced by non-local exchange and the electronic polaron effect counteract each other and tend to approximately cancel, thus resulting in a low-energy electronic structure close to the DFT Kohn-Sham band structure as long as static Hubbard interactions are disregarded. Here, we address this question in the case of the seemingly "simple" transition metals zinc and cadmium.

Both elements nominally display a d^{10} configuration, with fully occupied $3d$ orbitals in the case of Zn and $4d$ in the case of Cd, the dominantly d-derived bands being located several eV below the Fermi level. In Fig. 6.1a and Fig. 6.1b we show the band structure calculated within DFT for both materials. In the following we use the experimental crystal structure and lattice constants. DFT places the occupied d states at around -8 eV in Zn and -9 eV in Cd. The conducting states of these transition metals are formed by dispersive $4s(5s)$ in Zn(Cd) states around the Fermi level, that hybridize strongly with the p-manifold.

These facts raise the immediate expectation of negligibly small correlation effects on the occupied d shells. An effective Hubbard interaction calculated for the d-manifold within the constrained random phase approximation coincides with the fully screened interaction, since as a consequence of the complete filling of the d-shell there are no intra-d transitions to be cut out as opposed to an open shell system, where transitions inside the shell contribute to screening effects.

Figs. 6.2 and 6.3 display the local component of this fully screened interaction projected on the d-

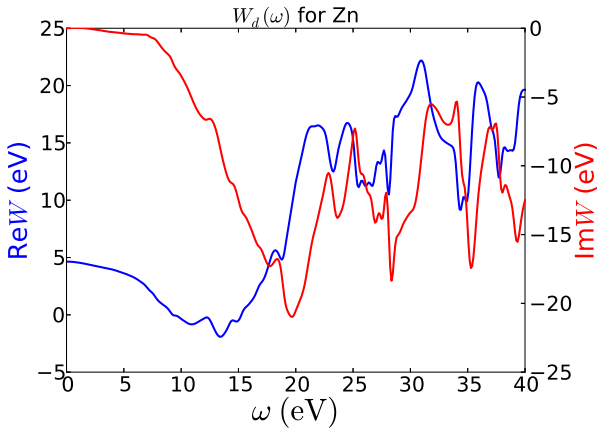

Figure 6.2 – The fully screened effective local Hubbard interaction on the $3d$ manifold for Zn.

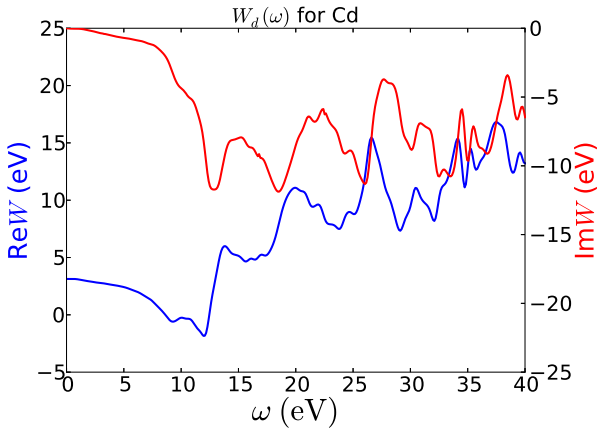

Figure 6.3 – The fully screened effective local Hubbard interaction on the $4d$ manifold for Cd.

manifold. The low-frequency limit approaches a value of 4.8 eV and 3.1 eV for Zn and Cd respectively. Even though this value is similar to their oxides, which are open shell systems, where correlations on the d states are significant, the high binding energy of these states far away from the Fermi level effectively prevents dynamical fluctuations. This suggests that screened exchange + DMFT should in fact reduce to screened exchange renormalized by the bosonic factor Z_B discussed above. Nevertheless, this does not mean that static effects of the interaction are properly treated in DFT. Even if this were the case, there is no reason that the DFT Kohn-Sham spectrum, being derived from an effective non-interacting system, provides an accurate description of the experimental situation.

Figs. 6.4 and 6.5 compare the experimental photoemission spectra [169, 170] from the literature to the density of states (DOS) derived from DFT and Hartree-Fock (HF) theory. The resulting discrepancy in terms of an underestimation of the binding energy of the d states in DFT of several eV had been noted in the literature before[171–173]: Norman *et al.* [171] discussed it in terms of a self-interaction error, proposing a correction in terms of an approximate substraction of self-interaction contributions contained in DFT [174]. Hartree-Fock calculations are, on the one hand, self-interaction free, but on the other hand – due to the absence of screening – widen all bands and place the d-bands far too low in energy, as can be seen in Figs. 6.4 and 6.5.

Since local dynamical correlations can be assumed to be small as discussed before, an improved

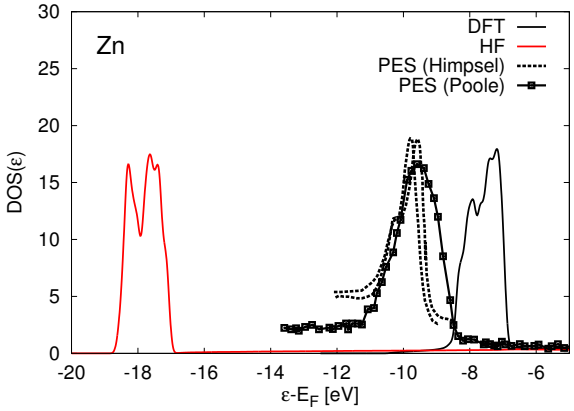

Figure 6.4 – The Density of States of elemental Zn calculated within Density Functional Theory (DFT, black solid line) and Hartree-Fock (HF, red solid line) in comparison with Photoemission experiments [169, 170] (dashed line, symbols). DFT calculations underestimate the binding energy of the Zn 3*d* states, while the HF overestimates the binding energy significantly (see explanation in the text).

treatment of the screened interaction *and* the self-interaction correction at the same time is likely to improve the shortcomings of Hartree-Fock (respectively DFT). Here we will discuss the two possible extensions of screened Exchange plus a bosonic renormalization factor Z_B and the GW approximation. The computationally cheaper option of screened exchange is including only static exchange contributions with a Yukawa-type interaction potential, and an effective renormalization Z_B which originates from the spectral weight transfer to plasmonic excitations. GW is computationally more demanding, but has the advantage of treating the dynamical part of the screening and correlation. Even though both methods include a self-interaction correction, the self-interaction contained in the Hartree term is not completely cancelled since the exchange contributions are derived from a screened interaction and not the bare one, as opposed to the Hartree term.

In Figs. 6.6 and 6.7 we show comparisons of the DOS of zinc and cadmium, calculated within DFT, screened Exchange($+Z_B$) and GW[175] to photoemission spectra. In the GW calculation we used $7 \times 7 \times 3$ k-points and 5 additional high-energy local orbitals. Interestingly, while in both systems the GW approximation provides a significant correction of the DFT Kohn-Sham spectrum in the right direction, but still underestimates the binding energy, the screened exchange scheme places the d-states too low in energy for Zn while providing a slightly better estimate than GW in Cd. The addition of the bosonic renormalization factor Z_B merely renormalizes the d bandwidth but keeps the average level position constant.

This raises the interesting question of which effects are missing in screened exchange and GW? The incomplete cancellation of the self-interaction in both approaches is expected to lead to an overall underestimation of the binding energy, since the additional unphysical interaction increases the energy of the d states. A more accurate estimate of this term would lead to an improvement of GW in both systems, but an even larger error of screened exchange in Zn. Another effect neglected in screened exchange is the Coulomb hole contribution: this term, discussed by Hedin as part of the "Coulomb hole screened exchange (COHSEX)" approximation (see 2.3.2) translates the fact that the presence of an electron at a position r pushes away charge at r (in the language of a lattice model, the charge-charge correlation function exhibits a reduction of the double occupancy), and the interaction of this effective positive charge with the electron presents an energy gain expressed in the form of an interaction of the electron with a "Coulomb hole". This term, contained in GW but not in screened exchange, also increases the binding energy.

This leads to the overall picture that screened exchange with the inclusion of the static corrections

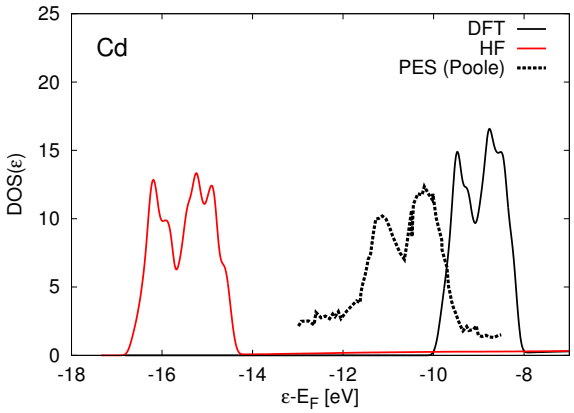

Figure 6.5 – The Density of States of elemental Cd calculated within Density Functional Theory (DFT, black solid line) and Hartree-Fock (HF, red solid line) in comparison with Photoemission experiments [169] (dashed line, symbols). DFT calculations underestimate the binding energy of the Cd $3d$ states, while the HF overestimates the binding energy significantly (see explanation in the text).

just discussed has a tendency to overestimate the binding energy in general, while GW underestimates it. The obvious difference between the two methods is the dynamical treatment of the screened interaction, which is treated more appropriately in GW, but it is not clear *a priori* whether the static approximation of the screened interaction or the approximative form of the screened interaction in terms of a Yukawa potential gives rise to the difference between screened exchange and GW.

The GW description of zinc and cadmium is close to the experiment. The remaining discrepancy to experiment is likely explained by remaining self-interaction contributions and/or missing self-consistency. Self-consistency (or quasi-particle self-consistency) has been investigated in the homogeneous electron gas [176] and various solid state systems [37] with different degrees of succes. These questions are left for future work.

6.4 Conclusion

In this chapter, we have reviewed and applied existing as well as novel approaches to obtain spectral properties of correlated electron materials. Guided by the need of a proper treatment of the long-ranged Coulomb interaction and non-local exchange effects we presented a lightweight version of the general GW+DMFT approach, the so-called screened exchange DMFT. It can be derived as a simplification to GW+DMFT in terms of a generalized screened exchange DFT scheme where local interactions are treated by dynamical DMFT.

We discussed the case of the elemental transition metals Zn and Cd, where strong local correlations are unimportant but the position of the occupied d manifold is sensitive to a proper treatment of screened exchange effects.

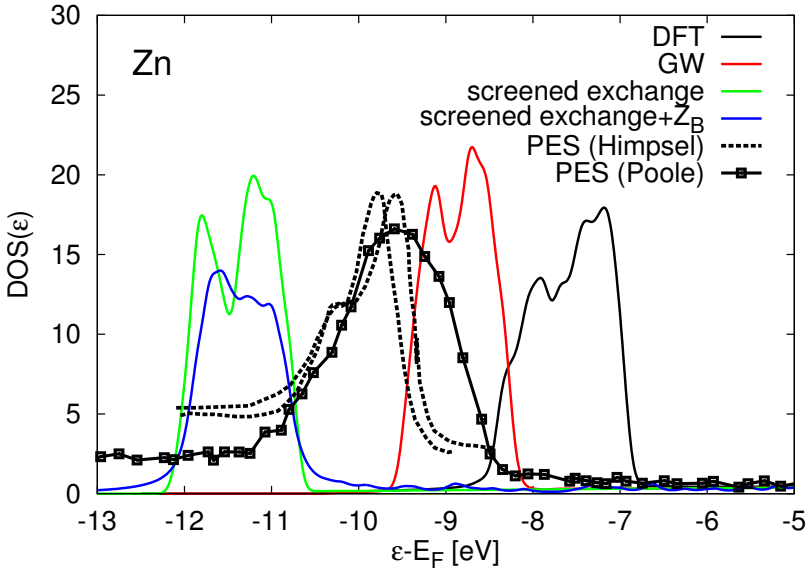

Figure 6.6 – The Density of States of elemental Zn calculated within different theoretical methods (solid lines), in comparison with Photoemission experiments [169, 170] (dashed line, symbols). Density Functional Theory (DFT) calculations significantly underestimate the binding energy of the Zn 3*d* states, while the GW approximation obtains a much better agreement. Screened exchange overestimates the binding energy significantly.

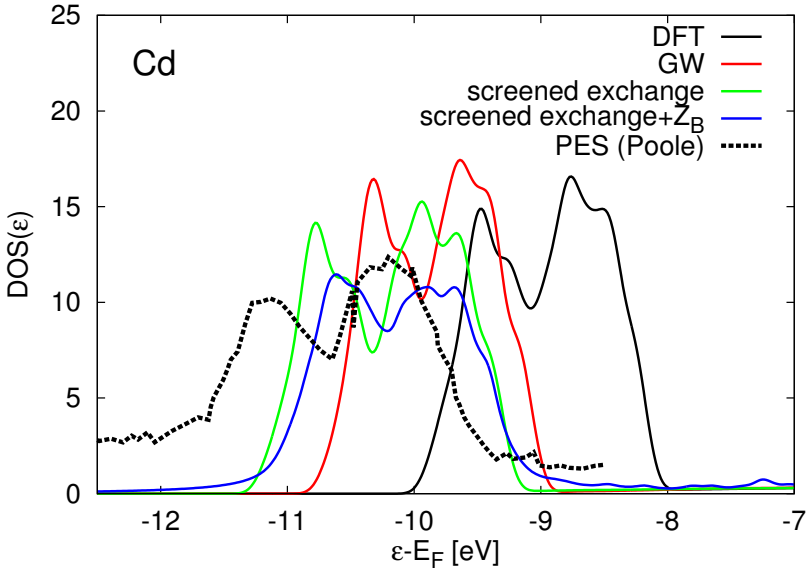

Figure 6.7 – The Density of States of elemental Cd calculated within different theoretical methods (solid lines), in comparison with Photoemission experiments [169] (dashed line). DFT calculations significantly underestimate the binding energy of the Cd 4*d* states, while the GW approximation and also screened exchange obtain a much better agreement.

Part III

Applications

Chapter 7

Vacancy formation energies in α-Fe

7.1 Introduction to iron

7.1.1 Iron in human technology

Iron (Fe) is the fourth most abundant element in the earth's crust, with 5.63% in weight. The only metal more abundant on earth is aluminum (Al), the second most abundant transition metal being titanium (0.56%). Because of its relatively high melting point of T_m=1811 K, other metals (in particular copper and its alloy, bronze) have been used in tools before long before mankind discovered techniques to smelt iron. On the other hand, aluminum is more abundant but only present in nature in oxidized form, often in low concentrations in rocks or clays. Chemical treatments to purify aluminum have only been discovered in 1825, very recently in human history.

Iron is thought to have first been used around 1400 B.C. in the near east, and has become more widespread in Europe and Asia after 1200 B.C. Iron and its carbon-doped cousin, steel, were poised to become the most heavily used metal over the following 3200 years, begin employed first in weapons, later in common tools, building structures, vehicles, etc. Iron and steel have undoubtably been one of the most icon materials of human technological development and manufacturing, only matched, perhaps, by oil and silicon in more recent technological revolutions.

Today, the annual iron ore production is estimated at over 3200 millions metric tons, in contrast with "only" about 5 million metric tons of aluminum. Most of this production is used in steels, often with a small percentage of dopants such as chromium, nickel or manganese that improve its mechanical properties (high-strength low-alloy steel) or its chemical properties (corrosion-resistant stainless steel).

In spite of its importance for technological applications, some of its basic properties, in particular its magnetism, remained hardly understood for a long time.

7.1.2 Phase diagram of iron

Fe comes in different phases depending on temperature and pressure (Fig. 7.1). The low-pressure, low-temperature α-phase (ferrite) crystallizes in a body-centered cubic (bcc) structure and is ferromagnetic, with a local moment of 2.22 μ_B/atom. The Curie temperature is T_c = 1043 K. At 1185 K, α-Fe undergoes a phase transition to a paramagnetic face-centered cubic (fcc) γ (also called austenite) phase, together with a local moments collapse[177]. γ-Fe has a complex magnetic structure[178, 179], with short-range order and magnetic frustration.

At even higher temperatures, Fe presents another transition back to another paramagnetic bcc phase, δ-Fe with an onset temperature of 1670 K. Anharmonic effects (like phonon-phonon interactions) are

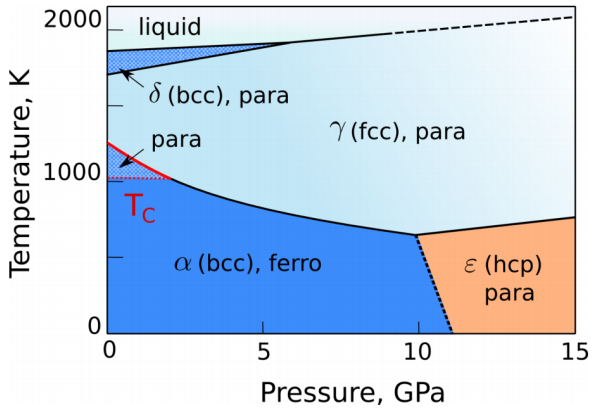

Figure 7.1 – Pressure-temperature phase diagram of Fe. Reproduced from Ref. [103].

thought to stabilize this phase[2, 180–183]. The melting point at atmospheric pressure is of 1811 K.

At higher pressures (about 13GPa at room temperature), α-Fe transforms into paramagnetic, hexagonal close-packed ε-Fe[184, 185]. It exhibits unconventional superconductivity between 13 GPa and 31 GPa[186], and is surprisingly paramagnetic even at low temperatures. Electronic correlations must be taken into account to understand the magnetic, conduction and structural properties of ε-Fe[105]. ε-Fe is, for obvious reasons, of limited interest for practical applications, but has received renewed interest in geology: it is one of the phases that may form the iron earth core. There, strong electronic correlations are key to understanding the magnetic properties as well[187, 188].

Doping C into metal Fe (to make steel) also changes its structure and physical properties. Depending on the carbon concentration, it allows a coexistence of α and γ Fe, as well as iron carbide FeC_3 (forming cast iron). Controlling the doping (in C and other metals) and the manufacturing process (rate of cooling, annealing...) allows to tune the mechanical properties: bulk modulus, hardness, yield).

7.1.3 *Ab initio* calculations of the properties of iron

Being one of the most used materials in today's technology, the different phases of Fe have been studied extensively with modern first principles calculation tools. In particular, its magnetism, conduction, phase stabilities, phase transitions and defect properties are all of interest. Typically used methods include DFT, its extensions like DFT+DMFT[84, 189, 190], as well as methods able to treat a larger number of atoms at the cost of lower precision such as molecular dynamics or the embedded atom method[191].

Obtaining reasonable results, let alone making quantitative predictions, with commonly available methods is no easy task. α-Fe at low temperatures is a fully polarized, rather weakly correlated ferromagnet, rather well described in LSDA or GGA DFT. This is, however, as easy as it gets. All the other usual phases: paramagnetic α-Fe, γ-Fe, ε-Fe display local moment physics[189], magnetic frustration[178] and/or non-Fermi liquid behavior[189]. All of them are significantly more strongly correlated, and only imperfectly described by KS DFT with common exchange-correlation potentials. To cite just one example, non-magnetic LDA or GGA calculations fail to account for the stability of bcc α-Fe[103] above T_c. Those phases are not quite exotic, however, being present at temperatures where iron (or steel) is typically used in real-world devices. The difficulty in simulating the paramagnetic states of magnetic materials (in particular iron and its alloys), and recent progress in this field, were recently reviewed by Abrikosov *et al.*[192] with an emphasis on spin states, phase stabilities and phase transitions, as well as point defects.

In the present chapter, parts of which are published in Ref. [106], we study more specifically the properties and, in particular, the formation energy of monovacancies in paramagnetic α-Fe. Next, we

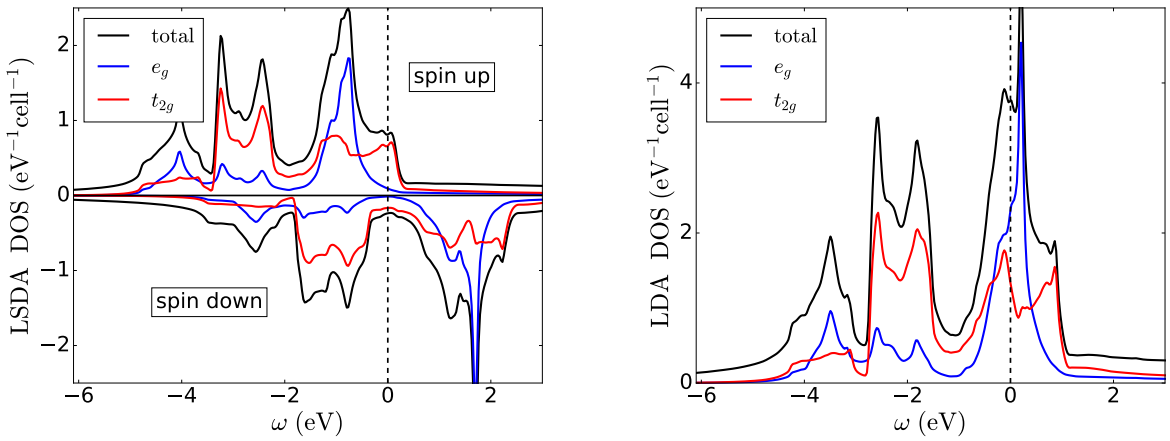

(a) Ferromagnetic LDA

(b) Nonmagnetic LDA

Figure 7.2 – Orbital-resolved density of states (DOS) of bcc Fe, calculated in ferromagnetic LSDA (left-hand panel) and nonmagnetic LDA (right-hand panel). In the ferromagnetic calculation, Fe is almost completely spin-polarized, and spin down electrons have mostly t_{2g} character. In the nonmagnetic calculation, the e_g partial DOS sums to 2.3 and t_{2g} partial DOS sums to 3.9 states per unit cell up to the Fermi level.

briefly discuss the electronic structure of α-Fe, before discussing the formation energy of vacancies.

7.2 Electronic structure of α-Fe

General remarks

Due to the bcc structure of Fe, the t_{2g} orbitals (d_{xy}, d_{xz} and d_{yz}) are pointing towards the nearest Fe atoms and have a large overlap with the corresponding t_{2g} orbitals. The e_g orbitals (d_{z^2} and $d_{x^2-y^2}$), on the other hand, are pointing away from the nearest neighbors, and have a smaller overlap. As a consequence, the electronic bands with e_g character have a smaller bandwidth those with t_{2g} character. Since the Fe d-shell is only partially filled, this means that the occupied part of the t_{2g} bands has a lower center of weight than the occupied part of the e_g bands even though, from an atomic point of view, the d orbitals all have the same energy level. The ground state has non-integer occupation of t_{2g} and e_g orbitals, with the former containing approximately 4 electrons and the latter approximately 3 (see Fig. 7.2).

The DFT density of states from spin-polarized LSDA and non-magnetic LDA calculations is shown in Fig. 7.2. As one can see in the left-hand panel (7.2a), spin-polarization of the d electrons is almost complete, with a total spin-moment per atom of 2.19 μ_B. The two spin down electrons have mostly (about 3/4) t_{2g} character. A dispersive s-band with onset at -8.3 eV that crosses the d-bands completes the picture. Even if non-magnetic LDA poorly describes the structural parameters of α-Fe, one can still gain some insights from such a calculation. The right-hand panel (7.2b) displays a high density of states at the Fermi level, due in particular to weakly dispersive (strongly localized) e_g states having a van Hove singularity near the Fermi level. Thus Fe fulfills the Stoner criterion[3] for ferromagnetism. On the other hand, such localized states are typically insufficiently described by DFT LDA, so it is no surprise that DFT gets the structural parameters of paramagnetic α-Fe wrong.

Charge self-consistent DFT+DMFT calculations further explain the difference in the physics of ferromagnetic and paramagnetic Fe. In Fig. 7.3, we display the self-energy of Fe e_g and t_{2g} states in both

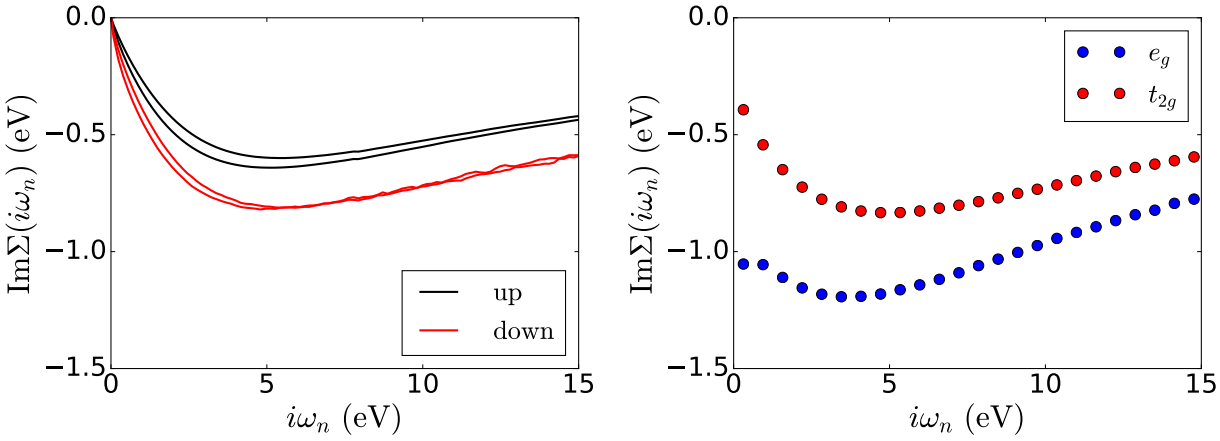

(a) Ferromagnetic

(b) Paramagnetic

Figure 7.3 – Imaginary part of the DFT+DMFT self-energy of α-Fe calculated in the ferromagnetic phase (left-hand panel) at inverse temperature $\beta = 40$ eV^{-1} and in the paramagnetic phase (right-hand panel) at inverse temperature $\beta = 10$ eV^{-1}. In the latter case, paramagnetism is enforced, since DFT+DMFT, as a local mean-field theory, overestimates the Curie temperature. In the ferromagnetic phase, e_g and t_{2g} orbitals have almost the same imaginary self-energy.

phases. While the ferromagnetic self-energy points to a weakly renormalized Fermi liquid ($Z \approx 0.7$ on spin down orbitals, 0.75 on spin up orbitals), the paramagnetic phase shows clearly non-Fermi liquid behavior, particularly the e_g states: the self-energy $\Sigma(i\omega_n)$ does not go to zero as $i\omega_n$ goes to zero. This can be understood in the following way: in the ferromagnetic phase, full spin-polarization does not leave much space for dynamical fluctuations. In the paramagnetic phase, on the other hand, local moments form and have many configurations to explore, allowing for stronger electronic correlations.

7.3 Monovacancies in α-Fe

7.3.1 State of the art from experiment and theory

Point defects, such as vacancies, play an important role for the electronic (conductivity, magnetism), mechanical (hardness, ductility) and thermodynamic (melting point) properties of materials. However, measuring the formation or migration energies of so seemingly simple defects is far from easy, since there are few experimental probes that couple to vacancies. The best available techniques are differential dilatometry[193] and positron annihilation spectroscopy[194]. Both suffer from large error bars, and strong sample dependence: the discrepancies between different measurements on one given material may be significant (see Table 7.1).

A further limit on experimental measurements is that they have to be performed at high enough temperatures: at low temperatures, the vacancy concentration is too low to be detected. This further complicates measurements on magnetic materials, like Fe. De facto, only the paramagnetic phase of α-Fe can be measured somewhat reliably[195]. Finally, the formation energy is typically obtained as a fitting parameter of a measured curve over a range of temperatures, never at a given temperature. The advantage is, however, that the formation energy is fitted separately from the formation entropy S^f_{vac}, as reported in Ref. [195]. All of this explains that only few measurements of the vacancy formation energy (E^f_{vac}) in iron have been reported, with relatively little agreement between groups (see table 7.1).

Therefore, *ab initio* theoretical calculations are an indispensable tool for developing a better under-

Method	E^f_{vac} (eV)	Uncertainty (eV)
Experiment (positron annihilation spectroscopy)		
Kim *et al.* (1978)[196] (PM)	1.4	±0.1
Matter *et al.* (1979)[197] (PM)	1.60	± 0.1
Schaefer *et al.* (1977)[198] (PM / FM)	1.53 / 1.60	±0.15
Schaefer *et al.* (1987)[199] (PM / FM)	1.74 / 1.81	±0.1
de Shepper *et al.* (1983)[195] (PM / FM)	1.79 / 2.0	±0.1

Table 7.1 – Vacancy formation energies from reported measurements. PM refers to the paramagnetic phase, FM to the ferromagnetic one. FM values are in fact inferred from the PM values, using additional approximations.

standing of the defect properties of materials[200]. Early DFT LDA calculations have predicted formation energies of vacancies in simple metals in good agreement with experiment[201, 202]. Despite a large body of successful calculations, it has later been recognized that the good agreement with experiment could often be the effect of the cancellation of errors in the exchange and correlation parts of the density functional [180]. Indeed, as has been discussed by Ruban [203], despite the structural simplicity of vacancies, their energetics is still one of the least reliable physical properties determined in first-principles calculations.

In the more complex transition metals, where the open d shells are often poorly described in LDA or GGA, the quality of results of DFT calculations for point defect properties is rather unpredictable and strongly material-dependent. There have been several attempts to improve the available functionals (see, e.g. Refs. [182, 204–206]). It was noticed that the predicted vacancy formation energies seem to be especially poor for $3d$ transition metals, for which many-body effects are fairly important, in particular in the paramagnetic state and body-centered cubic crystal structure[207]. Likewise, DFT has limitations for point defect calculations in correlated lanthanide or actinide oxides with $4f$ or $5f$ electrons, for example in the case of uranium oxides used in the nuclear industry[208].

The paramagnetic phase of α-Fe, as discussed above, is challenging for DFT. If basic structural parameters cannot be obtained accurately, what can one expect for point defects? Indeed, extensive DFT calculations of α-Fe [209–220] predict a monovacancy formation energy about 30 to 40 % higher than the measured values, with significant variations depending on the DFT implementation used (see table 7.2). Such comparison between theory and experiment is, of course, of limited meaning since it concerns two different phases (ferromagnetic and paramagnetic).

Just as DMFT corrections to DFT have helped to better understand the electronic and structural properties of α and ε-Fe[103, 105, 187], it is likely that an explicit treatment of many-body effects within DMFT will also correct the severe problems of DFT in describing point defects in paramagnetic α-Fe.

Hence, in the present work we have developed a state-of-the-art DFT+DMFT method [78, 81, 221] into a scheme for studying vacancy properties. We have applied this technique to a single vacancy in paramagnetic α-Fe. We have computed the electronic structure around the vacancy as well as the vacancy's formation energy, taking into account local lattice distortions around the defect. Compared to ferromagnetic DFT calculations, a significant reduction of the theoretical formation energy is obtained, with calculated values in remarkable agreement with experimental estimates [195–199]. We trace back this reduction to rather subtle effects of the vacancy on the local density of states and hybridization with its nearest neighbors.

7.3.2 Methods

We model a single vacancy in bcc Fe using the $2 \times 2 \times 2$ and $3 \times 3 \times 3$ cubic supercells represented in Fig. 7.4, with the vacancy placed at the origin of the supercells. The vacancy formation energy is

Reference	Method	Relaxation	E^f_{vac} (eV)
this work	FP LAPW GGA PBE	position / none	2.32 / 2.51
[210]	FP LMTO GGA	full / volume	2.18 / 2.60
[212]	FP KKR in GGA PW91	none	2.44
[219]	PAW GGA PW91	full	2.16
[218]	PAW GGA	full / position	2.17 / 2.17
[216]	PAW GGA PBE	full	2.15
[217]	PAW GGA	position	2.16
[217]	US-PP GGA	position	2.15
[211]	US-PP GGA PW92	full / volume / none	1.95 / 1.94 / 2.24
[214]	US-PP GGA	none	2.04
[215]	SIESTA method GGA PBE	full	2.07
[209]	LSGF ASA LDA	volume	2.25

Table 7.2 – DFT results for the vacancy formation energies for iron. All results above are for the ferromagnetic (FM) phase. The results are sorted by the method used (with decreasing accuracy of the basis set from top to bottom.) There are significant variations depending on the method, ultrasoft pseudopotential calculations reporting values significantly smaller than all-electron full potential ones.

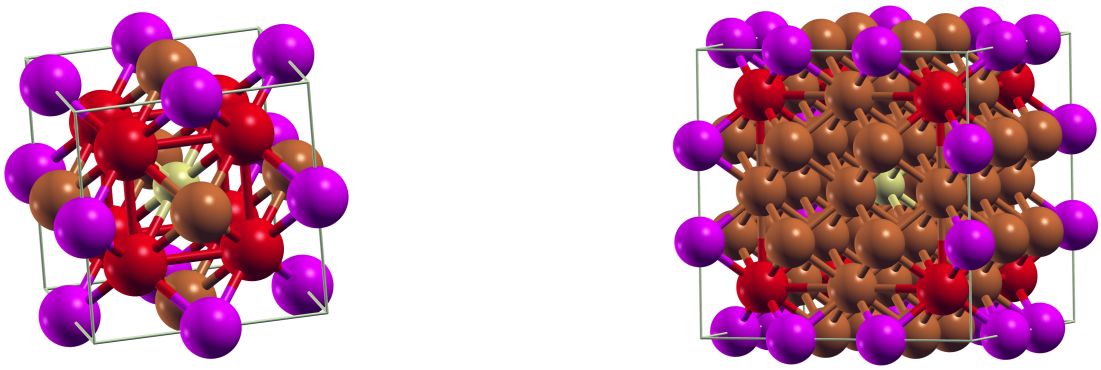

(a) $2 \times 2 \times 2$ supercell

(b) $3 \times 3 \times 3$ supercell

Figure 7.4 – The $2 \times 2 \times 2$ and $3 \times 3 \times 3$ supercells with the vacancy in the corner. Different colors indicate the atom nearest to the vacancy (red), the second nearest (purple), and the furthest (the central atom, yellow). Generated with XCrySDen [222]

calculated from the supercell total energy using the standard formula

$$E^f_{\text{vac}} = E^{\text{vac}}(N-1) - \frac{N-1}{N} E^{\text{no vac}}(N), \tag{7.1}$$

where N is the number of atoms in the ideal supercell, $E^{\text{no vac}}(N)$ is the total energy of the ideal supercell containing N atoms and no vacancy, and $E^{\text{vac}}(N-1)$ is the total energy of the same supercell with a vacancy (hence $N-1$ atoms). N is 16 in the $2\times2\times2$ supercell and 54 in the $3\times3\times3$ supercell, corresponding to vacancy concentrations of 6.25% and 1.85%, respectively.

The DFT+DMFT method had hitherto rarely been used to compute point defect properties, due to the heavy computational load when working with supercells. The calculations in the present work were rather heavy (two to three weeks on 100 cores to obtain a reliable total energy for one set of parameters), but have become possible thanks to recent developments in quantum impurity solvers. We used a continuous-time quantum Monte-Carlo (CTQMC) hybridization expansion algorithm [57] in the segment representation for the solution of the local impurity problems (see Chap. 5).

The computational cost of performing DFT+DMFT calculations in larger cells (which is necessary to treat reasonably low concentrations of vacancies) was for a long time a bottleneck to performing such calculations. In the last few years, the effect of oxygen vacancies on the magnetism and photoemission spectra in oxides has been investigated using DFT+DMFT in supercells. Lechermann *et al.* have reported about the effect of vacancies on magnetism within DFT+DMFT[223, 224]. They found that, for instance, the combined presence of oxygen vacancies at the $LaAlO_3/SrTiO_3$ interface *and* local many-body physics explains the stabilization of interface ferromagnetism. In the well-known "drosophila" of correlated materials, $SrVO_3$, Backes *et al.*[225] found that oxygen vacancies play an important (if not dominant) role in explaining the photoemission peak at -1 eV, sometimes assigned to a lower Hubbard band.

7.3.3 Technicalities

The on-site density-density interaction between the $3d$ is parametrized by the Slater parameter $F_0 = U = 4.3$ eV and the Hund's rule coupling $J_H = 1.0$ eV that were previously used in the DFT+DMFT calculations of α and ϵ-Fe of Ref. [105]. The same work reproduced almost exactly the experimental lattice parameter of 2.86 Å, hence we perform our DFT+DMFT calculations at the experimental volume. Other DFT calculations were performed at the corresponding theoretical volume. All DFT+DMFT calculations were performed at the electronic temperature of 1162K, corresponding to β =10 eV^{-1}.

We use a k-point mesh with $8\times8\times8$ points for the 16 atom supercell, and $4\times4\times4$ points for the 54 atom supercell. Convergence with respect to calculation parameters (the k-point mesh density, supercell size and size of the functions basis) has been verified within DFT. In particular, using a larger $4\times4\times4$ (128 atoms) supercell is not useful and leads to the same results.

The DFT+DMFT Hamiltonian is parameterized with the density-density interaction Hamiltonian of Eq. 5.8 for the full d-shell (see Chap. 5).

We use the around mean-field approximation of Eq. 4.15 for the double-counting correction H_{DC}[75, 226]. Finally, the interaction energy is computed according to Eq. 4.24.

About 15 iterations are needed to reach convergence in the DFT+DMFT cycle. An averaging of the total energy values over further iterations is required to obtain precise enough values. In practice, at least 50 more cycles are needed. The error bars shown in table 7.3 and Fig. 7.5 are computed as the empirical standard deviation over these iterations. This uncertainty increases with the supercell size. Indeed, for each impurity site small fluctuations around the equilibrium value of the Hubbard interaction energy exist, and are multiplied by the number of atoms in the supercell.

The $2\times2\times2$ and $3\times3\times3$ supercells with a vacancy have an overall cubic symmetry. However, the presence of the vacancy still breaks the on-site cubic point group symmetries for all iron atoms apart from the central one. For those atoms the Wien2k code uses local coordinate frames chosen in such a way as to have the highest possible on-site symmetry. Subsequently, our impurity problems are also solved

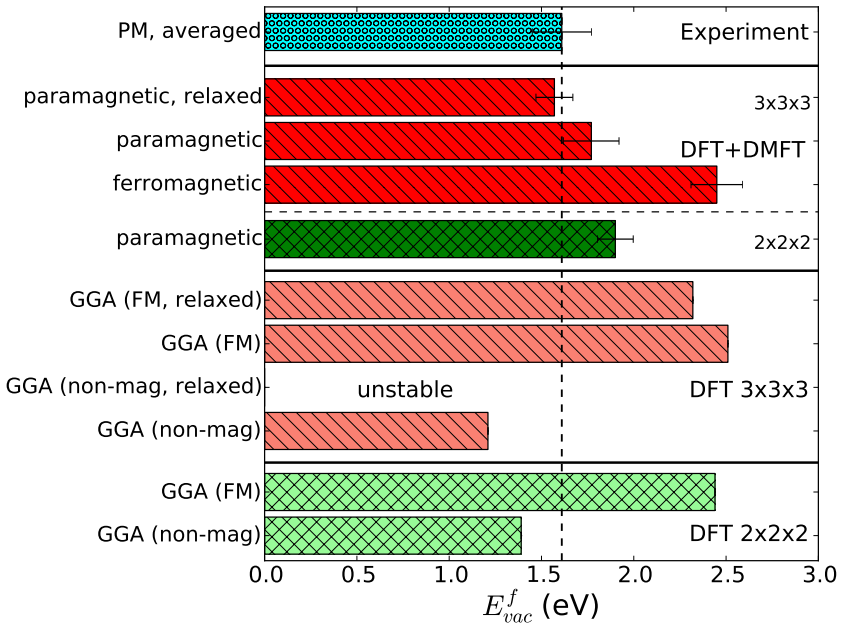

Figure 7.5 – Vacancy formation energies calculated by different methods (GGA and DFT+DMFT) in the different setups: small ($2 \times 2 \times 2$) and large ($3 \times 3 \times 3$) supercell, relaxed or not, non-magnetic, paramagnetic (PM) or ferromagnetic (FM). Calculations are performed at the equilibrium volume for the relevant setup. The average of experimental values is shown for comparison[195–199]

in these local coordinate frames. Hence, a corresponding rotation back to the reference frame should be applied to the resulting self-energies, if one wishes to compare them with the self-energy of perfect bcc Fe. The latter is, of course, obtained for the standard coordinate frame with x, y, and z axises along the cube edges. However, because we are using a density-density Hamiltonian instead of the full rotationally-invariant one, the self-energies obtained for those local frames are still somewhat different from that of perfect bcc iron even after the inverse rotation. Hence, in our calculations of the ideal supercells (without vacancies) we employed the same local coordinate frames as for the supercells with vacancy in order to avoid spurious contributions of those rotations to the vacancy formation energy. Furthermore, we verified that the off-diagonal elements in the Green's functions stay small, so that we could neglect them.

7.4 Results

7.4.1 Vacancy formation energy E^f_{vac}

The vacancy formation energies obtained within DFT+DMFT together with different DFT results and experimental values are shown in Fig. 7.5, and also summarized more extensively in table 7.3. The resulting value for E^f_{vac} in DFT+DMFT is 1.77 eV for the unrelaxed 54-atom supercell with lattice relaxations reducing it further to $E^f_{\mathrm{vac}} = 1.56 \pm 0.13$eV, in excellent agreement with the experimental average value of about 1.6 eV. We also calculated E^f_{vac} within DFT+DMFT for the unrelaxed ferromagnetic phase obtaining a higher value of 2.45±0.15eV. Experiments indeed seem to confirm that E^f_{vac} in the ferromagnetic phase should be larger than in the nonmagnetic one[195, 199], though direct low-temperature measurements of E^f_{vac} in the ferromagnetic phase with positron annihilation spectroscopy are notoriously difficult.

DFT (GGA) calculations for ferromagnetic bcc Fe predict a significantly larger value E^f_{vac} of 2.51

Method	E^f_{vac} (eV)	Uncertainty (eV)
$2 \times 2 \times 2$ supercell		
GGA (NM, exp vol)	3.46	$< 10^{-2}$
GGA (NM, theo. vol)	1.39	$< 10^{-2}$
GGA (FM, exp vol)	2.50	$< 10^{-2}$
GGA (FM, theo. vol)	2.44	$< 10^{-2}$
DFT+DMFT	1.90	± 0.097
$3 \times 3 \times 3$ supercell		
GGA (NM, exp vol)	1.51	$< 10^{-2}$
GGA (NM, theo. vol)	1.21	$< 10^{-2}$
GGA (NM, relaxed)	unstable	-
GGA (FM, exp vol)	2.71	$< 10^{-2}$
GGA (FM, exp vol, relaxed)	2.50	$< 10^{-2}$
GGA (FM, theo. vol)	2.51	$< 10^{-2}$
GGA (FM, theo. vol, relaxed)	2.32	$< 10^{-2}$
DFT+DMFT (PM, unrelaxed)	1.77	± 0.14
DFT+DMFT (PM, relaxed in FM GGA)	1.66	± 0.15
DFT+DMFT (PM, relaxed in DMFT)	1.56	± 0.13
DFT+DMFT (FM DMFT, unrelaxed)	2.45	± 0.15

Table 7.3 – Vacancy formation energies computed this work. The statistical uncertainty shown is the empirical standard deviation of the value over the last 50 iterations. Different calculation setups are shown: ferromagnetic (FM), paramagnetic (PM) or nonmagnetic (NM), experimental volume or DFT theoretical volume, relaxed or unrelaxed.

and 2.32 eV for an unrelaxed and a fully relaxed cell, respectively. Hence, one can see that many-body effects included within DMFT reduce E^f_{vac} for the paramagnetic phase by about 0.7 eV. The impact of correlation effects for ferromagnetic α-Fe is much less significant, in agreement with the predicted suppression of dynamic correlations in this phase[105] (see also Fig. 7.3). The vacancy formation energies obtained with nonmagnetic DFT calculations are even lower than the measured values, with $E^f_{\text{vac}} \approx 1.5$eV in unrelaxed GGA. They have, however, very little physical meaning: DFT in general fails dramatically for the paramagnetic phase, which is reflected by the fact that $\alpha-$Fe is not dynamically stable and the predicted lattice parameter would be significantly smaller in nonmagnetic DFT. Hence, using our relaxed positions in a nonmagnetic DFT calculation gives an (unphysical) negative vacancy formation energy. Thus, the strongly reduced value of E^f_{vac} in nonmagnetic DFT calculations compared to ferromagnetic ones may be due to a spurious cancellation of errors.

7.4.2 Discussion

The total energy in DFT+DMFT, given in Eq. 4.22, can alternatively be written

$$E^{\text{tot}}_{\text{DMFT}} = \text{Tr}(\hat{H}^{\text{KS}}_{\mathbf{k}} \hat{N}^{\text{DMFT}}_{\mathbf{k}}) + E[\rho^{\text{DMFT}}] + (\langle H_U \rangle - E_{\text{DC}}) \tag{7.2}$$

where $\hat{N}^{\text{DMFT}}_{\mathbf{k}}$ is the density matrix at crystal momentum $\mathbf{k}$, $\hat{H}^{\text{KS}}_{\mathbf{k}}$ the corresponding Kohn-Sham LDA Hamiltonian and $E[\rho^{\text{DMFT}}]$ only depends explicitly on the charge density. $\langle H_U \rangle = \frac{1}{2} \sum_{mm'} U_{mm'} \langle n_m n_{m'} \rangle$ is the Coulomb interaction between Fe $3d$ electrons (m and m' are orbital indices and $U_{mm'}$ is the density-density Coulomb matrix, see Chap. 5), and E_{DC} is the double-counting term that estimates the energy already present in LDA. When one removes an atom from the cell to create a vacancy, all three terms in Eq. (7.2) change. Figure 7.6 shows the difference in the third term, $E^{\text{int}} = \langle H_U \rangle - E_{\text{DC}}$, for each respective atom in the supercell before and after removing an atom. Summing this up and taking into account the multiplicity of the atoms in the cell yields a change $\Delta E^{\text{int}} \approx$ -1.6 eV, that is compensated by a larger change in $E[\rho^{\text{DMFT}}]$ due to a redistribution of the charge density, as wavefunctions from DFT+DMFT are more localized. The contributions from the second and third coordination shells compensate one another

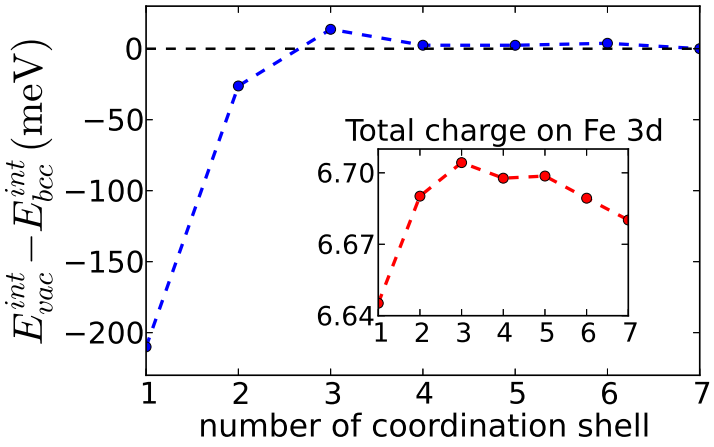

Figure 7.6 – Difference in the interaction energy per atom, before and after adding a vacancy. Inset : Fe $3d$ charge in the cell with one vacancy.

in E^{int}, so that the net change in the interaction energy only comes from the first nearest neighbor. This is due to efficient metallic screening, and is in good agreement with embedded atom method calculations of iron vacancies near the surface[227] that show that the vacancy formation energy becomes equal to the bulk value for the vacancy located in the third layer or deeper.

The self-energy of the vacancy's first coordination shell shows a significant difference from the bulk bcc-Fe self-energy, as shown in Fig. 7.7 (a) and (b). t_{2g} states, but also e_g states to a lesser extent, become more strongly correlated (less coherent) with a larger $\text{Im}\Sigma(i\omega)$. A larger absolute value of the imaginary part of the self-energy at low frequencies means reduced quasi-particle lifetimes, equivalent to stronger dynamic correlations. This difference almost vanishes for the self-energy of the atoms further away than the nearest neighbor, in agreement with the variation of the interaction energy shown in Fig. 7.6. Stronger correlations on the atoms near the vacancy imply that a more accurate description of the $3d$ electrons of the Fe atoms in DFT+DMFT is crucial, not only for predicting the crystal structure, but especially for estimating the energetics of the vacancy, which eventually leads to a smaller formation energy. Note that the self-energies are slightly atom-dependent even in the absence of a vacancy in our calculations, due to an artificial symmetry-breaking in the supercell in DFT calculations and the non-rotational invariance of the density-density Hubbard Hamiltonian. However, we compare self-energies and interaction energies in a consistent, atom-to-atom way.

The enhancement of the nearest-neighbor self-energy can be traced back to a change in the hybridization function. As can be seen in Figure 7.8b, the imaginary-frequency hybridization function, in particular for the t_{2g} states, is reduced at low frequencies for the atom near the vacancy. This reduction is due to an increase in the corresponding t_{2g} partial density of states (DOS) in the vicinity of the Fermi level, E_F, as one can see in Fig. 7.8a. A larger DOS at E_F induces a suppression of low-energy hopping leading to stronger correlation[187, 228]: at the first iteration of DMFT, $\text{Im}\Delta(i0^+) = -\pi\rho_F / \left[\text{Re}G_{\text{loc}}(i0^+)^2 + (\pi\rho_F)^2\right] \approx -1/(\pi\rho_F)$, with ρ_F the LDA DOS. The enhancement of the nearest-neighbor e_g self-energy is smaller and the corresponding DOS at E_F even decreases compared to the bulk case. This decrease in the value the of DOS exactly at E_F is compensated by an overall narrowing of the e_g peak in the vicinity of E_F, see Fig. 7.8a (see also Fig. 7.9 for the full partial densities of states). Hence, the resulting hybridization function for e_g is still suppressed starting from the second Matsubara frequency.

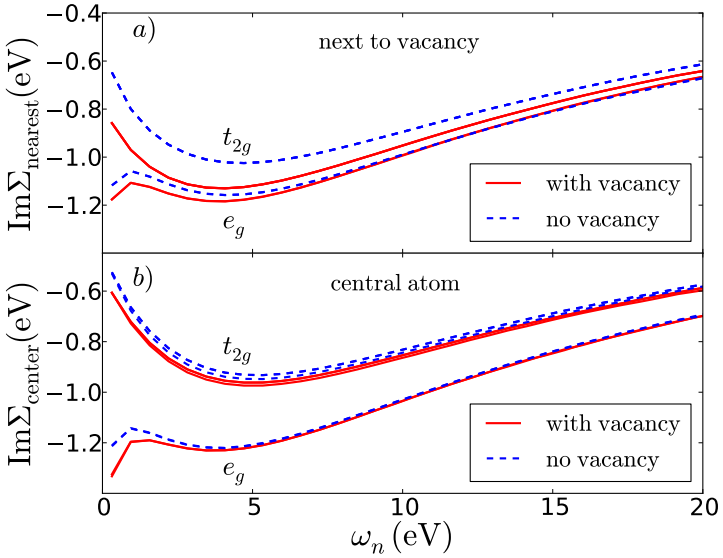

Figure 7.7 – Imaginary part of the Matsubara self-energies for a) the vacancy nearest neighbor and b) central atom in the $3 \times 3 \times 3$ supercell with a vacancy present (red, full) or without it (blue, dashed). Correlations become stronger on the atom nearest to the vacancy while the difference between e_g and t_{2g} is strongly reduced.

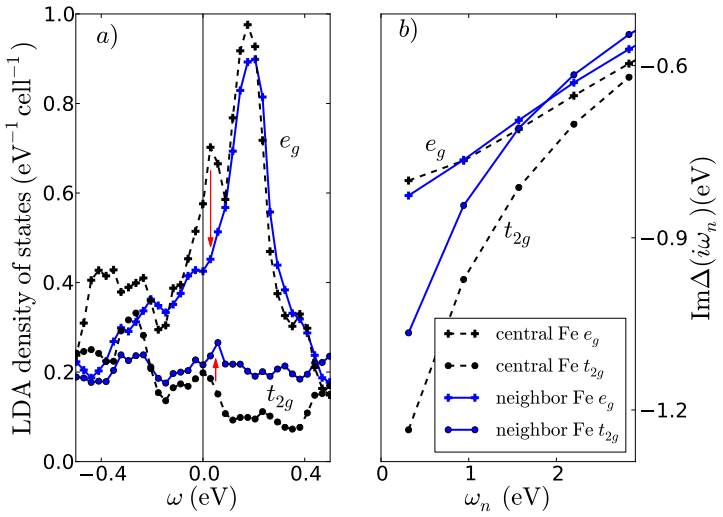

Figure 7.8 – a) LDA density of states around the Fermi level and b) Hybridization function on the Matsubara axis for the nearest neighbors (blue, full) to the vacancy, and for the central atom (black, dashed).

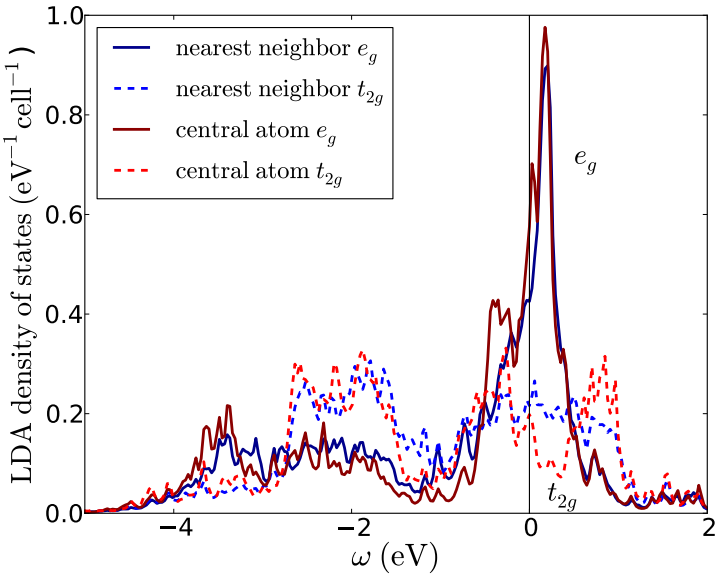

Figure 7.9 – Partial density of states of the e_g (full line) and t_{2g} (dashed line) orbitals on the first nearest neighbor atom to the vacancy (blue) and on the central atom (red). Away from the Fermi level, the difference in the partial DOS between both atoms is small.

7.4.3 Importance of local atomic relaxations

Next, we calculated the relaxed atomic positions in DFT+DMFT around the vacancy. Computing atomic forces in DFT+DMFT is rather complicated[229], so we obtained the relaxed atomic positions by shifting the atoms around their equilibrium position and minimizing the total energies. We performed a relaxation of the atoms around the vacancy in two steps in order to reduce the computational effort. We first obtained a fully relaxed structure in spin-polarized GGA (at its corresponding theoretical volume, computing atomic forces), to obtain an initial guess of the atomic positions.

In this calculation, we observe a shift of the first coordination shell towards the vacancy by about 4%, and a shift of the second coordination shell away from the vacancy by about 1.5%, while all the other atoms do not move significantly, in agreement with previous calculations[211]. In the second step, the positions of the two first nearest neighbors were relaxed within DFT+DMFT. In Fig. 7.10, we show the total energy (minus an offset depending on the method used, GGA or DFT+DMFT, for easier representation) of the supercell as a function of the relaxed position of the nearest and second nearest neighbor of the vacancy. Each site was moved independently, preserving the symmetry of the cell, while the positions of others were fixed at their fractional GGA values.

We obtain the following results: in DFT+DMFT, for paramagnetic α-Fe, the first nearest neighbor relaxes by 5.7% towards the vacancy while the second nearest neighbor relaxes away from it by 0.7%. One sees that many-body effects have a significant impact on the nearest-neighbor relaxation, enhancing the shift away from the unrelaxed position by almost 50%. Overall, relaxing the two first coordination shells in full DFT+DMFT reduces the vacancy formation energy by 0.21 eV.

7.5 Conclusion

We have shown that local many-body effects are crucial for explaining a relatively low vacancy formation energy in α-Fe. The presence of a vacancy induces rather subtle changes in the local electronic structure of its surroundings, leading to a moderate increase in the strength of correlations at neighboring sites. This moderate increase has, however, a very significant impact on the vacancy energetics.

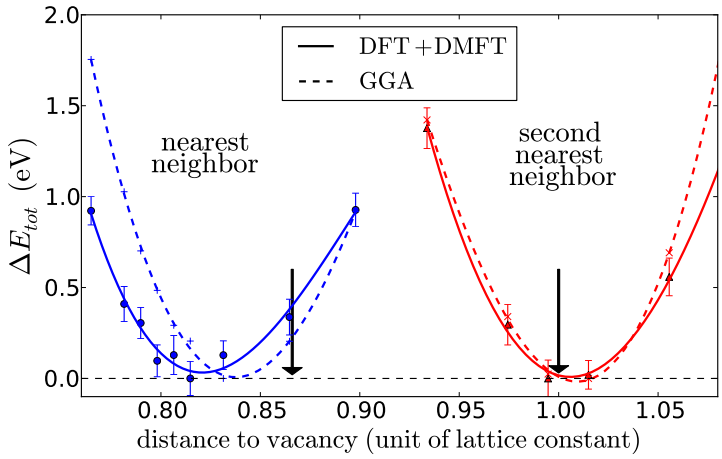

Figure 7.10 – Total energy vs distance to the vacancy (as fraction of the lattice parameter) for the first nearest neighbor (blue) and the second nearest neighbor atom (red), in DFT+DMFT (full line) and GGA (dashed line). The black arrows show the position of the atoms in the unrelaxed bcc supercell. The points denote the calculated values, while the lines are obtained by a cubic fitting of these points.

When the effect of local relaxations is consistently included, the calculated vacancy formation energy in paramagnetic α-Fe is reduced by about 0.7 eV, or about 30% compared to the corresponding value in the ferromagnetic phase and is in excellent agreement with experiment. The predicted magnitude of nearest-neighbor relaxations is about 50% larger compared to the one obtained within DFT.

This remarkable sensitivity to correlation effects is most probably pertinent to other types of defects in iron that are of crucial importance for mechanical properties and thermodynamics of steels, e.g. interstitial sites, stacking faults and dislocations. It seems plausible that the same kind of effects should also be considered in other strongly correlated materials.

Finally, this is a proof of principle that total energy calculations can be performed with reasonable precision in supercells with DFT+DMFT, in somewhat long but not prohibitive computation time. This would have been much more complicated even a few years ago, as quantum impurity solvers have made tremendous progress. The present calculation scheme could probably still be refined, considering that most of the important physics is happening on the vacancy's nearest neighbor site. A much less expensive approach would be to freeze the DMFT loop on the atoms far away from the vacancy, where a perfect bcc self-energy is a very good approximation.

Chapter 8

Epitaxially stabilized phases of VO_2: the B phases

In this chapter, we study the reported phase transition in the metastable B phase of VO_2. We first give an overview of the experimental and theoretical state of the art on VO_2 in section 8.1. We then discuss recent measurements on the B phase[230, 231] in sections 8.2 and 8.3. Next, we show how a simplified form of DFT+CDMFT accounts for the measured bad metal to insulator transition in this phase in sections 8.4 and 8.5. Finally, motivated by a recent publication demonstrating the importance of oxygen vacancies for understanding the electronic structure of $SrVO_3$[225], we investigate the possible effects of the presence of oxygen vacancies on the spectra of VO_2 in section 8.6.

8.1 Introduction to VO_2: the well-known rutile and M_1 phases

8.1.1 General remarks

Vanadium dioxide (or VO_2) is a $3d$ transition metal oxide with electronic configuration $3d^1$ that comes in many different phases, depending on temperature, doping and stress. It is probably best known for its extensively studied insulator to metal transition as temperature is increased above $T_c = 340$ K[232]. Indeed, the proximity of this phase transition to standard room temperature, together with its ultrashort timescale and sensitivity to tuning by doping, is one of the reasons why VO_2 is considered a promising material for electronic devices and applications[233]. Recently, VO_2 has made headlines due to a severe breakdown of the Wiedemann-Franz law in its high-temperature phase[234], suggesting possible uses as a thermoelectric material. Again, the proximity of the phase transition to room temperature is critical.

The two best known phases of VO_2 are the high-temperature tetragonal (rutile) R phase, and the low-temperature monoclinic M_1 phase. VO_2 (R) is a (bad) metal, with fairly short-lived quasi-particles[235]. It has space group No. 136 ($P4_2/mmnm$) (see Fig. 8.1). At $T_c = 340$ K, VO_2 goes through a first-order structural transition whereby two nearest V atoms along the rutile c axis dimerize, and the resulting dimers are tilted, forming zig-zag dimer chains. This phase is called the monoclinic M_1 phase of VO_2 (see Fig. 8.1). Concurrently, the material undergoes a Mott-Peierls metal to insulator transition (MIT), with the resistivity changing by two orders of magnitude. Because of the doubling of the unit cell, a Peierls mechanism has been proposed as an explanation for the MIT. The question of "the chicken or the egg", or which of the structural and electronic transition causes the other, has been debated but has not been completely settled yet[236–239].

A qualitative but still very relevant description of the electronic structures of VO_2 was given early on by Goodenough[241, 242]. The five V $3d$ orbitals are split by the cubic component of the crystal field into two e_g orbitals and three lower energy t_{2g} orbitals. The actual symmetry on a V site is in fact

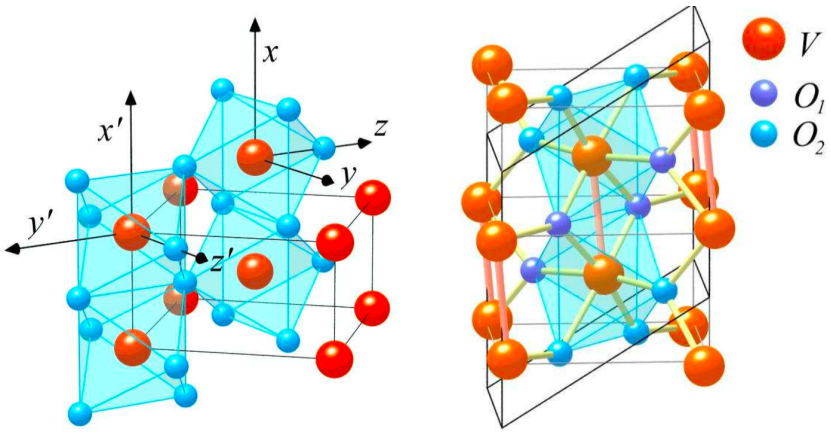

Figure 8.1 – Crystal structure of VO_2 (R) (left panel) and VO_2 (M_1) (right panel). To form the M_1 phase, consider a double unit cell of the rutile phase and form tilted dimers along the c axis. The resulting monoclinic unit cell is twice as large. Reproduced from [240].

lower than cubic, so that the e_g orbitals are further split into two non-degenerate orbitals, and the t_{2g} orbitals are split into a more stable a_{1g} orbital pointing along the c axis and two less stable e_g^π orbitals. According to Goodenough's analysis, both the a_{1g} and e_g^π states are partly filled in the metallic rutile phase, VO_2 (R). At lower temperatures in the M_1 phase, the physics of the dimer become important. The intra-dimer hopping between the a_{1g} orbitals of two neighboring V ions splits the a_{1g} band in two, stabilizing a bonding state. At the same time, the tilting of the dimers increases hybridization between the O $2p$ and the V e_g^π orbitals, pushing the e_g^π states to higher energies. The aggregate effect of the distortion is to stabilize an isolated bonding a_{1g} state, separated from the other bands. As the total occupancy per V remains unity, this explains the insulating state. Hence, in Goodenough's view, VO_2 is a band insulator showing a Peierls transition.

On the other hand, Zylbersztejn and Mott[243] proposed an explanation for the MIT of VO_2 that emphasizes the importance of correlations in the material. In their view, it is the Coulomb repulsion between electrons that freezes them in place, forming a Mott insulator. To this day, the Peierls or Mott nature of the insulating phase of VO_2 remains unsettled. Experiments and calculations over the last 15 years suggest that both aspects are needed to completely understand the MIT of VO_2.

VO_2 has, in fact, not one but several insulating phases. Uniaxial strain or doping with Cr, Fe, Al or Ga stabilizes another monoclinic phase, VO_2 (M_2)[244, 245], where one half of the V ion pairs dimerize (but do not tilt) and the other half of V pairs tilt (but do not dimerize). Yet another insulating phase, VO_2 (T), has triclinic symmetry and is an intermediate phase between M_1 and M_2, where all V pairs are tilted (though at different degrees) but only half dimerize. The existence of several insulating phases generates some complexity but actually provides useful informations on the mechanisms of the MIT. Indeed, it allows to partly decouple the lattice and electronic transitions. All three insulating phases have very similar values of the insulating gap[246] (about 0.6 eV), similar free energies[237, 244] and revert to the rutile phase at high temperatures (though VO_2 (T) transits through the M_2 phase). There are, however, also differences from the electronic point of view. V ions in VO_2 (M_1) have been shown in NMR experiments to be nonmagnetic (S=0), consistent with the band picture. In the M_2 phase, on the other hand, dimerized V ions are nonmagnetic but the non-dimerized tilted V chains form local moments ($S = 1/2$) with antiferromagnetic coupling[244]. This is more in line with the physics of a Mott insulator.

Other (less stable) polymorphic forms of VO_2 can be stabilized as nano powders or thin films. This is the case for VO_2 (A) [247] and VO_2 (B) [248]. VO_2 (B), in particular, is attracting much attention in the chemistry community because it is considered a promising cathode material for new generation batteries[249]. Thermal annealing on powders causes both materials to revert to the rutile phase[250]. They have recently been grown epitaxially as thin films over a $SrTiO_3$ substrate with a pulsed laser

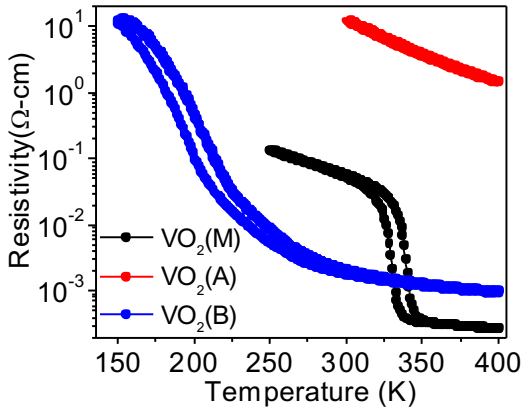

Figure 8.2 – Resistivity of the M_1, R (black line, above 340K), A and B phases of thin films of VO_2 grown on $SrTiO_3$. The MIT from M_1 to R is both wider (occuring over a 10 K range) and lesser (the resistivity changes by only two orders of magnitude) than can be observed in single crystal VO_2. Reproduced from [230].

deposition technique by Srivastava *et al.*[230]. The oxygen pressure and laser pulse frequency determine which phase is deposited. In their work, VO_2 (B) was shown to go from a bad metal high-temperature (HT) phase, with conductivity 10 times lower than the rutile phase, to a low-temperature (LT) insulating phase over a range of 100 K when temperature is lowered below about 250 K (see Fig. 8.2). VO_2 (B) crystallizes in a monoclinic structure with lower symmetry than VO_2 (M_1), similar to VO_2 (M_2). This was shown to be linked to a structural transition preserving the symmetry where half of the V ions form dimers in the LT phase. In this chapter, we study the electronic structure and phase transition of VO_2 (B). In what follows, for simplicity, we shall label the low-temperature phase of VO_2 (B) as LT and the high-temperature phase of VO_2 (B) as HT.

8.1.2 VO_2 as seen by experiments

Since the original publication on the MIT of VO_2 in 1959[232], this material has attracted much attention from the solid state physics community. In particular, the advent of modern electronic structure codes in the 1990's has initiated a renewed interest from the experimental and theoretical communities to try and explain the nature of the MIT transition. In this section, we briefly review some key experimental findings on VO_2.

Many photoemission spectroscopy (PES) experiments have been carried out on VO_2, using single crystals or thin films and at different photon energies[230, 251–261]. We display a few examples of photoemission spectra in Fig. 8.3. One may observe that, while all VO_2 (M_1) spectra have a proper PES peak at around -0.9 eV, the picture is not so clear in the metallic R phase. Indeed, while some groups observe a clear quasi-particle peak at the Fermi level, others measure a superposition of several peaks or indeed mainly incoherent spectra. Such is the case, in particular, in recent measurements made on epitaxially grown thin films.

PES experiments give us several pieces of information on the phase transition. Okazaki *et al.*[253] noted that the self-energy in the metallic rutile phase is **k**-dependent and explained this by ferromagnetic fluctuations mediated by the Hund's coupling between the d orbitals, a view rather in agreement with the Zylbersztejn and Mott picture of the phase transition. The temperature dependence of the V $3d$ band width in the insulating phase is attributed to a strong electron-phonon coupling. They also concluded that electrons in the rutile phase are actually more localized than in the insulating M_1 phase. Haverkort *et al.*[257], on the other hand, pointed out the importance of orbital polarization across the transition:

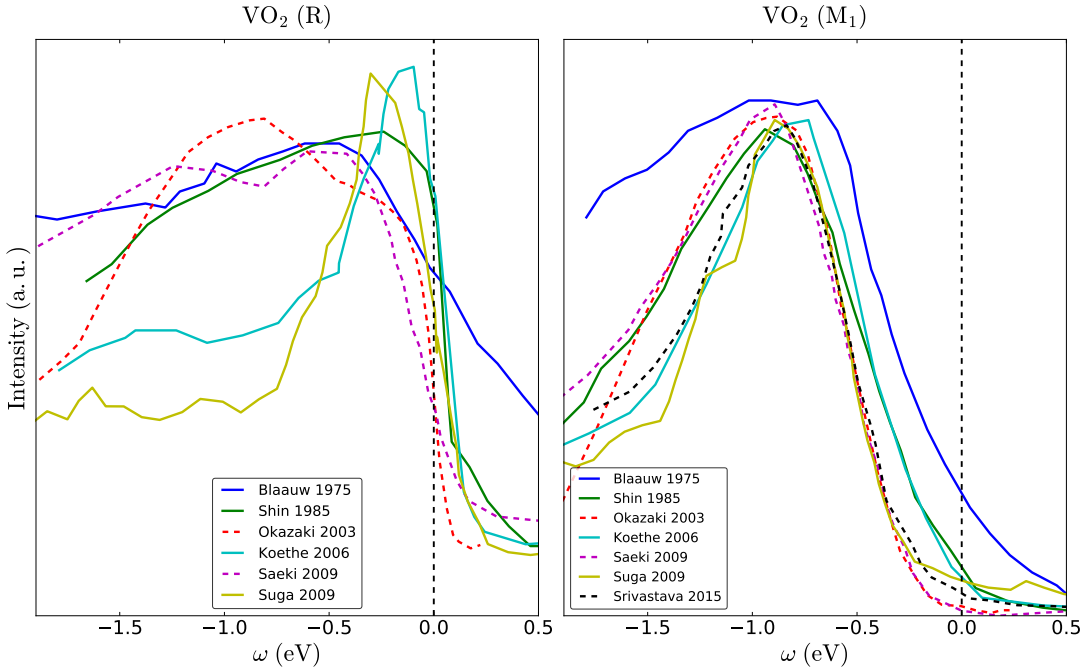

Figure 8.3 – Valence band photoemission spectra of VO_2 (R) and VO_2 (M_1). Full lines indicate measurements on "bulk" samples, and broken lines measurements on thin films. While the measurements on the M_1 phase consistently show a single peak centered around -0.9 eV, measurements on the metallic R phase are not so consistent and tend to display secondary peaks, in particular on thin films. Data from [230, 251–256] (in chronological order).

they confirmed experimentally the idea advanced by Goodenough that the rutile phase has partially filled e_g^π and a_{1g} bands, while the M_1 phase has one completely filled a_{1g} band. This importance of orbital polarization was further strengthened in a recent experiment by Aetukuri *et al.*[262]. In their work, the strain on VO_2 thin films was tailored by inserting a RuO_2 layer with varying thickness between the substrate TiO_2 and VO_2. By changing the strain, they were able to shift the energetic levels of the different orbitals and thus engineer the onset temperature of the MIT. Koethe *et al.*[254] expanded on this work[257] and concluded that a dimer model accounts for the **k**-dependence of the self-energy. Suga *et al.*[255] confirmed the proposal of [96] that the PES peak at -0.9 eV in the M_1 phase is a coherent peak corresponding to a dispersive electronic band, not an incoherent peak corresponding to a lower Hubbard band. Eguchi *et al.*[259], however, favor a Mott-Hubbard transition picture. Saeki *et al.*[256] performed angle-resolved PES on VO_2 (R) and found two electron pockets with different masses at the center of the Brillouin zone.

All this means there is conclusive evidence for the importance of both Peierls and Mott physics in the R–M_1 phase transition. Recent experiments on more exotic metallic phases of VO_2 further complicate the picture.

Recent femtosecond time-resolved PES[260] and electron diffraction[263] measurements reported a metastable, relatively long-lived metallic state upon photoexcitation of VO_2 (M_1). Because the transition to this metallic state is significantly faster than the structural transition and the thermalization time is much shorter than the reversal to the insulating ground state, this demonstrates that an out-of-equilibrium but metastable metallic state with M_1 structure is possible. Arcangeletti *et al.*[264] stabilized an ambient temperature metallic phase with monoclinic symmetry at high pressures. More surprisingly, it has been suggested that these high pressure and out-of-equilibrium metallic monoclinic phases are of similar nature, and are also comparable to an intermediate metallic phase measured within the transition temperature range in thin films[261]. Finally, it appears that creating oxygen vacancies can strongly affect the phase transition, as is visible in two recent experiments. Jeong *et al.*[265] demonstrated that a suppression of the MIT and metallization of the monoclinic phase by gating-induced oxygen vacancy creation is possible. Similarly, Zhang *et al.*[266] stabilized a metallic rutile phase down to 1.8 K after creating oxygen vacancies by annealing thin films at low oxygen partial pressure.

The R to M_1 MIT has been studied for longer, and much more extensively, than the transition of VO_2 (B) displayed in Fig. 8.2. Indeed, as of today, VO_2 (B) has been mostly studied by the chemistry community from the point of view of film and nanocrystal growth, and the electronic and structural properties thereof[230, 248, 249, 267, 268]. Oka *et al.*[248] measured the structural parameters across the transition. They also performed magnetic susceptibility, finding a dip in the susceptibility below 300 K followed by a renewed increase below 200 K, and nuclear magnetic resonance, finding a positive knight shift characteristic of a singlet spin state, to demonstrate the formation of bonding dimers in half the V pairs. The susceptibility measurements are qualitatively similar to those on the M_2 phase[244], though the drop is much sharper in the latter.

A recent publication by Lourembam *et al.*[269] extensively studies both phase transitions (M_1 to R and B low-temperature to high-temperature) using terahertz spectropscopy. In this work, the authors measure the complex optical conductivity in the THz range and extract the plasma frequency ω_p and free carrier scattering rate γ by fitting the measured data to a Drude model. In VO_2 (B), they find an onset of the phase transition at 240 K and a near saturation of ω_p and γ above 280 K, linked to a lower activation energy of the dc conductivity. In VO_2 (M_1), a Drude-Smith model, taking into account charge localization, is shown to be necessary to to fit the complex conductivities. This is, the authors argue, consistent with the picture of a MIT in VO_2 (M_1) to (R) taking place by percolation, with metallic domains nucleating in the insulating phase, as described by Qazilbash *et al.*[235]. On the other hand, this suggests that the VO_2 (B) LT to HT transition does not follow such a percolation mechanism. Furthermore, the authors argue that the lower inter-axial angle β of VO_2 (B) (as compared to M_1) facilitates the formation of defects and impurities in epitaxially grown films.

In a follow-up to this first publication[269], Lourembam *et al.* show that, similarly to what has been observed in VO_2 (M_1)[260, 263], photoinduced electrons can stabilize an out-of-equilibrium but long-lived metallic state in the LT phase of VO_2 (B)[270].

We conclude this brief overview of experimental results by pointing out that based on experiments published so far, the phase transitions of VO_2 cannot be understood in a purely Peierls or Mott physics picture. Rather, the two aspects should be treated on equal footing, for example in a correlation-assisted Peierls transition. In the following section, we discuss how *ab initio* or model-based calculations account for the electronic structure of the different phases of VO_2.

8.1.3 The band picture: VO_2 from Density Functional Theory to the GW approximation

With the development of modern DFT codes since the 1990's, and after having been studied mostly by experiments or more phenomenological theories, VO_2 has been the subject of several ab initio calculations aiming at understanding its conductive properties and phase stability.

The KS band structure from DFT calculations using the LDA or GGA exchange-correlation potentials does not reproduce the experimental gap of about 0.6 eV in the insulating M_1 and M_2 phases[236, 240]. Instead, DFT predicts a small overlap between the bonding a_{1g} states and the e_g^π states (that is to say a "negative" gap of ≈ -0.05 eV). This result has led to a longstanding controversy. For proponents of the band picture and Peierls transition, this reflects the well known and systematic tendency of LDA and GGA DFT to underestimate band gaps, and even artificially closing band gaps in small gap semiconductors like Ge. The underlying idea is that the different phases of the materials are well described by LDA and GGA DFT, and the band gap problem is but an unphysical artifact of the calculation method.

More recently, DFT calculations have been performed with the HES hybrid exchange-correlation functionals[271–273]. On the one hand, these calculations correctly open the band gap observed in the M_1 and M_2 phases, though the value is overestimated, at about 1.1 eV. In the case of the M_2 phase, antiferromagnetic calculations are needed to account for the non-dimerized, antiferromagnetic zig-zag chains. This result is supposed to confirm that VO_2 is properly described by a band picture, as the authors of Ref. [271] argue. On the other hand, the same hybrid functionals fail at predicting the correct non-magnetic ground state of VO_2 (M_1)[272, 273]. They also predict a ferromagnetic insulating ground state for VO_2 (R), but this is less critical: there are indeed signs of ferromagnetic fluctuations in this phase[253] and the Curie temperature would be well below the MIT temperature. Still, no known exchange-correlation potential predicts simultaneously the quasi-particle spectrum and the respective phase stabilities. The same remarks apply to DFT+U calculations[273, 274].

To go beyond the KS DFT picture, and take into account non-local self-energy effects, a simple model GW scheme[275] and, more recently, self-consistent GW calculations without further approximations[276, 277] have been reported. Both groups[276, 277] found that some level of self-consistency in the GW calculation is necessary to obtain reasonable spectra, and that one-shot G_0W_0 calculations on top of LDA are not sufficient. Moreover, the off-diagonal elements of the GW self-energy are important[277]. This suggests that the physics of VO_2 is indeed much more complex than that of a "simple" small gap semiconductor whose band gap is underestimated in DFT[236, 240].

8.1.4 Correlations in VO_2: Density Functional Theory + (Cluster) Dynamical Mean-Field Theory

In order to better understand the strong correlations in VO_2, several attempts have been made to apply the DFT+DMFT method to its phase transition. While local correlations are thought to be strong in rutile VO_2, there exists overwhelming experimental proof that the dimer physics is crucial for (though not sufficient to explain) the electronic structure of the M_1 and M_2 phases. Therefore, it was realized early on that any DMFT calculation of VO_2 should be performed in its cluster extension (or CDMFT), allowing at least an off-diagonal self-energy element between the dimer a_{1g} states[96]. This approach was shown to be sufficient to describe the spectral properties of VO_2 (R) and (M_1) on an equal footing. More importantly, it illustrated how the Peierls and Mott physics can overlap when local Coulomb interactions contribute to push electrons in the dimer bonding state to minimize the interaction energy.

In a series of publications[278–281], Tomczak *et al.* expanded and refined the initial work by Biermann *et al.*[96]. In particular, the authors demonstrated that in the M_1 phase, since the intra-dimer self-energy elements are essentially real and static, the electronic structure is well reproduced by adding off-diagonal matrix elements (or "scissors operators") on the Kohn-Sham Hamiltonian. The values of the relevant matrix elements are calculated from a simpler system, the Hubbard dimer.

Several other calculations using DFT+CDMFT on VO_2 followed. Lazarovits *et al.*[282] showed how uniaxial strain stabilizes the metallic phase, by enhancing the bonding-antibonding splitting but simultaneously stabilizing the e_g^π orbitals and enhancing the a_{1g} bandwidth. Belozerov *et al.*[283], in a publication extending the work by Biermann *et al.*[96], where intra dimer Coulomb interactions are taken into account (as in the extended Hubbard model), confirmed the results of the calculations by Tomczak *et al.*

More recently, motivated by the experimental observation of metastable metallic phases of VO_2[260, 263], out-of-equilibrium quantum Boltzmann equation[284] and high-temperature DFT+CDMFT[238] calculations have been performed. In the former[284], He *et al.* theoretically confirmed the existence of a long-lived metastable metallic state in the M_1 phase upon photoexcitation. In the latter[238], Brito *et al.* treated the electronic structures of the R, M_1 and M_2 phases on the same footing and reproduce the respective metallic and insulating states. Furthermore, they found a metallic state in the M_1 phase when the electronic temperature is high (900 K), in agreement with the photoexcitation of the electrons.

Finally, Nareja *et al.* proposed another perspective on the problem of the phase transition in presence of strong correlations and dimer physics[239]. They calculated $(U - T)$ and $(t - U)$ phase diagrams of a dimer Hubbard model (where T is the temperature, U the local Coulomb interaction, and t the intra-dimer hopping). With this, they reproduced the Coulomb-assisted MIT of the dimers with the formation of singlet states. However, the validity of the analogy with the physics of VO_2 is debatable, since their model essentially represents a single-band problem containing only the a_{1g} band (with dimers) while the importance of the e_g^π orbitals in VO_2 is well-known.

8.2 Recent measurements on VO_2 (B)

Pal *et al.*[231] recently performed further PES and optical conductivity measurements on thin films of VO_2 (B), in continuation of Ref. [230]. The theoretical work presented in this chapter was prepared together with B. Pal, D.D. Sarma *et al.*, to try explain their measurements from electronic structure calculations.

In Fig. 8.4 we display the photoelectron spectra of the VO_2 (B) HT and LT phases. The lineshapes are similar, with slightly more intensity at the Fermi level in the (nominally metallic) HT phase. Both spectra suggest a dominant peak centered around 0.4 eV binding energy. Comparing this data to Fig. 8.3, the LT phase seems less clearly insulating than the M_1 phase, and the HT phase less metallic than the R phase. The difference between both B phases is no longer easily visible in the core state photoelectron spectra of Fig. 8.5 (for the B phase and the R to M_1 phase transition).

Finally, let us go back to the resistivity measurements of Fig. 8.2. The change in resistivity through the transition is rather large. Being four orders of magnitude, it is comparable to what can be obtained in good single crystals of VO_2 (R), and much larger than the change in resistivity reported on the R to M_1 transition in samples of the same set. However, the lowest resistivity reached for the HT phase is almost an order of magnitude larger than the resistivity of the VO_2 (R) thin films, and we know that the rutile phase is itself rather a bad metal.

These experimental findings seem contradictory. They suggest a material going through a structural transition with a large change in resistivity, while on the other hand its photoelectron spectrum is largely unchanged. In the calculations discussed below, we use a DFT+DMFT scheme to understand how these measurements can be reconciled.

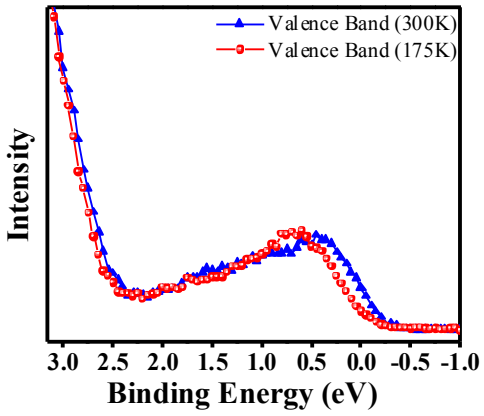

(a) Full range

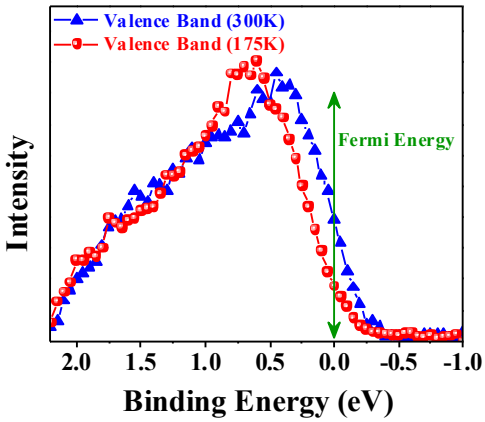

(b) Zoom on 3*d* states

Figure 8.4 – Photoelectron spectrum of VO_2 (B). The lineshape is very similar, with a slightly upward shift of the peak in the HT phase. From Ref. [231].

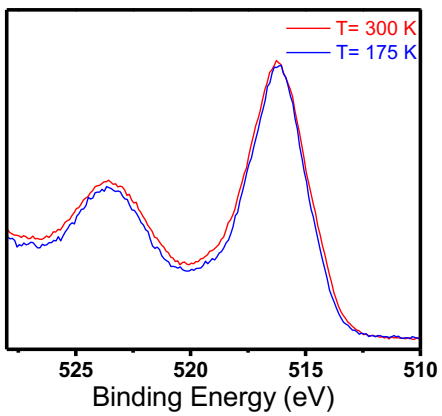

(a) VO_2 (B) HT (red) and LT (blue) phases

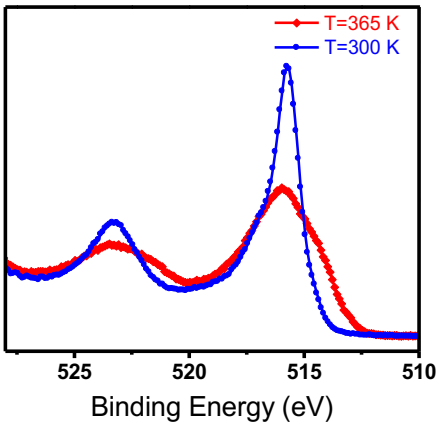

(b) VO_2 R (red) and M_1 (blue) phases

Figure 8.5 – Core state (V 2*p*) photoelectron spectra of (a) VO_2 (B) and (b) of VO_2 (R) and (M_1). The low binding energy shoulders can be associated to charge fluctuations in the valence band (see also [259]). Again, there is little sign of a drastic phase transition in the valence states (contrary to the R to M_1 transition). In the R to M_1 transition, it appears that the non-local screening channel is free in the HT R phase but blocked in the LT M_1 phase, but that there is little change in the available screening channels through the B phase transition. From Ref. [231]

8.3 Crystal structures of VO_2 (B)

For the sake of clarity, we present here the crystal structures used in our calculations. We remind that VO_2 (B) has the space group 12 (C_2/m). The (small) difference between the HT and LT phases is in the lattice constants and atom positions, as given in Tables 8.1, 8.2 and 8.3. All atoms have multiplicity 2 (by symmetry) in the primitive unit cell, and multiplicity 6 in the conventional unit cell (as in Fig. 8.1).

	a	b	c	α	β	γ
HT	12.09	11.92	3.70	90°	90°	148.9°
LT	12.15	11.89	3.72	90°	90°	149.4°

Table 8.1 – Experimental lattice parameters of the conventional unit cell of VO_2 (B). The lengths are in Å. From Ref. [230].

Atom	x	y	z
V_1	0.9204	0.7214	0
	0.0796	0.2786	0
V_2	0.4150	0.3145	0
	0.5850	0.6855	0
O_1	0.1405	0.0006	0
	0.8595	0.9994	0
O_2	0.6098	0.3436	0
	0.3902	0.6564	0
O_3	0.7064	0.6496	0
	0.2936	0.3504	0
O_4	0.7016	0.6928	0
	0.9284	0.3072	0

Table 8.2 – Atomic positions in VO_2 (B) HT.

Atom	x	y	z
V_1	0.9285	0.7249	0
	0.0715	0.2751	0
V_2	0.4241	0.3281	0
	0.5759	0.6719	0
O_1	0.1432	0.9944	0
	0.8568	0.0056	0
O_2	0.6174	0.3502	0
	0.3826	0.6498	0
O_3	0.7144	0.6545	0
	0.2856	0.3455	0
O_4	0.0746	0.6792	0
	0.9254	0.3208	0

Table 8.3 – Atomic positions in VO_2 (B) LT.

Table 8.4 – Experimental atomic positions in the conventional unit cell of VO_2 (B) LT and HT (as fraction of the lattice parameters in the primitive cell). In addition, an atom at coordinates $(x, y, 0)$ has equivalent positions at $(x + \frac{1}{2}, y, \frac{1}{2})$ and $(x, y, 1)$. From Ref. [230]

The distance between two V_2 atoms is 2.867 Å in the HT phase and 2.6072 Å in the LT phase (forming a dimer). In contrast, the nearest vanadium atom for a given V_1 is a V_2 atom, at a distance of about 3 Å.

8.4 Methods

As discussed above, single-site DMFT calculations alone do not account for the MIT of VO_2 R to M_1. A cluster extension has to be used to obtain the intra-dimer self-energy term that, supported by local Coulomb interactions, opens a gap. In the LT phase of VO_2 (B), dimer effects are expected to be important as well: the large change in resistivity goes together with a dimer formation on one of two inequivalent V pairs.

For simplicity, and following the observation that the intra-dimer self-energy is well approximated by a real and static term, we use in this work only single-site DMFT and mimic the effect of dimerization

by a "scissor operator", as discussed by Tomczak *et al.*[279]. Namely, the bonding-antibonding splitting is given by its limit in the isolated dimer:

$$\Delta_{bab} = -2t + \sqrt{16t^2 + U^2} \tag{8.1}$$

where t is the intra-dimer hopping and U the local Coulomb interaction. This corresponds to adding an off-diagonal self-energy term on the Kohn-Sham Hamiltonian, between the respective a_{1g} states of the dimer, with the value

$$\Sigma_{a_{1g}-a_{1g}} = -\frac{1}{2}\sqrt{16t^2 + U^2}$$

In the present work, we use this approach, which we may call "DFT+Σ_{dimer}+DMFT". It is of course an approximation, but it accounts for much of the physics of VO_2, as previously noted.

Our DMFT calculations, except otherwise noted:

- run at an electronic temperature of $\beta = 40$ eV^{-1} (corresponding to room temperature)
- use the Hubbard-Kanamori parameterization of the interaction Hamiltonian in the impurity model:

$$H_U = \sum_m \mathcal{U} n_{m\uparrow} n_{m\downarrow} + \sum_{\sigma, m>m'} (\mathcal{U} - 2\mathcal{J})\, n_{m\bar{\sigma}} n_{m'\sigma} + (\mathcal{U} - 3\mathcal{J})\, n_{m\sigma} n_{m'\sigma} \tag{8.2}$$

  where $\bar{\sigma}$ is the opposite spin of σ. This allows us to use the much faster segment picture in the CTQMC hybridization-expansion solver (see Chap. 5)
- include only the t_{2g} states as correlated in DMFT: the e_g states are treated within DFT LDA.

Some exceptions appear below, but are clearly labeled as such.

The monoclinic phases of VO_2 have a low-symmetry distorted structure, and a rotation of the axes may be needed to obtain the correct coordinate systems t_{2g} and e_g orbitals on a V atom. Moreover, the octahedra surrounding a V atom are distorted, which tends to create off-diagonal elements on the local density matrix, Hamiltonian and Green's functions. This is particularly the case in the B phase. To avoid taking into account off-diagonal elements in the CTQMC solver, we perform a rotation in the basis of d orbitals that minimizes these off-diagonal elements. This rotation is chosen in the following way: we first compute the local (i.e. projected and **k**-summed) Kohn-Sham Hamiltonian $H_{1\text{el}}$ on each inequivalent V site. We then diagonalize $H_{1\text{el}}$ and use the corresponding rotation to compute a new set of Wannier functions and projectors. This does not make the off-diagonal elements disappear completely. Indeed, unless imposed by symmetries (say, in cubic symmetry), there is generally no rotation that makes the off-diagonal elements in the Green's function vanish at all frequencies. Still, in practice, the density matrices and hybridization functions constructed with this choice of basis have off-diagonal elements smaller than the diagonal parts by about an order of magnitude. Hence, in a first approximation, we neglect them here.

8.5 Calculated electronic structure of VO_2

8.5.1 Electronic structure within the local density approximation

In this section, we first summarize a few results from DFT LDA calculations on VO_2 B, as well as the R and M_1 phases for comparison. These calculations are important as they are used as a starting point for our DFT+DMFT calculations.

In Fig. 8.6, we show the atom-resolved LDA DOS of the HT and LT phases of VO_2 (B), in a window containing O $2p$ and V $3d$ states. The O $2p$ states span an energy range from -7.5 to -2.5 eV, and the V $3d$ states range from -0.5 to 5 eV. Excited states above 6 eV are delocalized states with mixed O $3s$ and V $4p$ character. The metallic HT phase has a larger DOS at the Fermi level than the LT phase, which displays peaks slightly below and above the Fermi level.

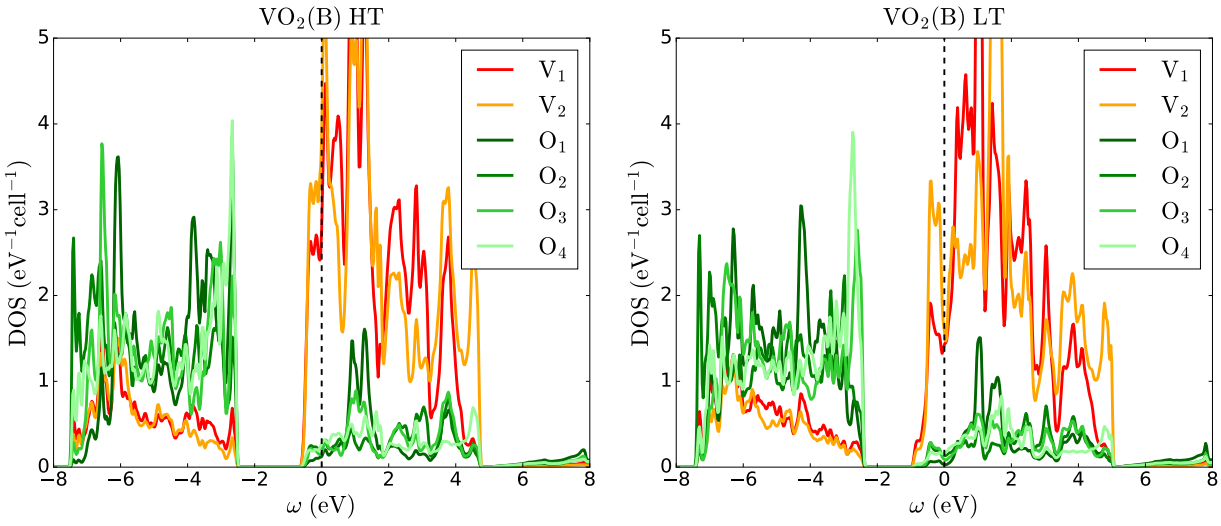

(a) VO_2 (B) HT (b) VO_2 (B) LT

Figure 8.6 – Atom-resolved partial LDA density of states for VO_2 (B) in the HT and LT phases.

We zoom in and show the orbital-resolved partial DOS of the V $3d$ states in the HT and LT phase in Fig. 8.7 and Fig. 8.8, respectively. In both phases, the separation between t_{2g} and e_g states is only approximate, with a boundary roughly around 1.9 eV but some overlap of e_g and e_g^π orbitals. This is the result of the important distortion of the cell and of the O octahedra surrounding the V atoms, and of the fact that the vanadium atoms (especially V_1) are not well centered in their respective octahedra. There are also significant differences between both phases. In the HT phase, the occupied states have mixed a_{1g} and e_g^π orbital character. The a_{1g} states are almost divided into two peaks at 0 eV and 1.1 eV, suggesting there is also some dimer bonding.

In the LT phase, on the other hand, there is a rather strong orbital-polarization of the occupied states. The non-dimerized V_1 atom has an almost half-filled, dispersive a_{1g} band at the Fermi level, and the e_g^πbands are mostly centered around 1 eV. The dimerized V_2 atom, however, a prominent peak of mostly a_{1g} character below the Fermi level takes almost one electron. The a_{1g} band of V_2 is in fact split into a first peak at -0.3 eV and a second peak 1.6 eV, corresponding respectively to the bonding and anti-bonding states of the dimer formed by two V_2 atoms. The difference in energy between these two peaks gives the order of magnitude of the intra-dimer hopping t (or more precisely, $2t$).

In Fig. 8.9, we show the LDA density of states (DOS) on VO_2 R and M_1 for comparison. Here, the t_{2g} and e_g states are barely, but clearly separated: the boundary is around 2.3 eV. Within LDA, the t_{2g} orbitals are almost equally occupied in the R phase, though the a_{1g} state is slightly lower in energy (this can be seen by computing the projected local Hamiltonian or by taking the center of mass of the partial density of states). The DOS of VO_2 (R) is similar to the partial DOS on atoms V_1 and V_2 of the HT B phase, and to the partial DOS of V_1 of the LT B phase. In the M_1 phase, however, there is a fairly strong orbital polarization, the a_{1g} state taking most of the V d^1 electron. The a_{1g} band is split into a bonding and anti-bonding states, similarly to V_2 in the LT B phase. The M_1 phase according to LDA is metallic, with some spectral weight from all three t_{2g} orbitals remaining at the Fermi level. However, it is clearly apparent that little more is needed to push the bonding a_{1g} state completely below the Fermi level and the e_g^π states, giving a band insulator.

Finally, Fig. 8.10 displays the LDA band structure of VO_2 B along a path in the Brillouin zone. In terms of LDA bands, we can see that the HT phase has 4 bands crossing the Fermi level, with a 5^{th} band in close vicinity to E_F. The separation between t_{2g} and e_g states is also more pronounced in the band structure than in the DOS: bands are touching but relatively disentangled with a boundary at about 1.75

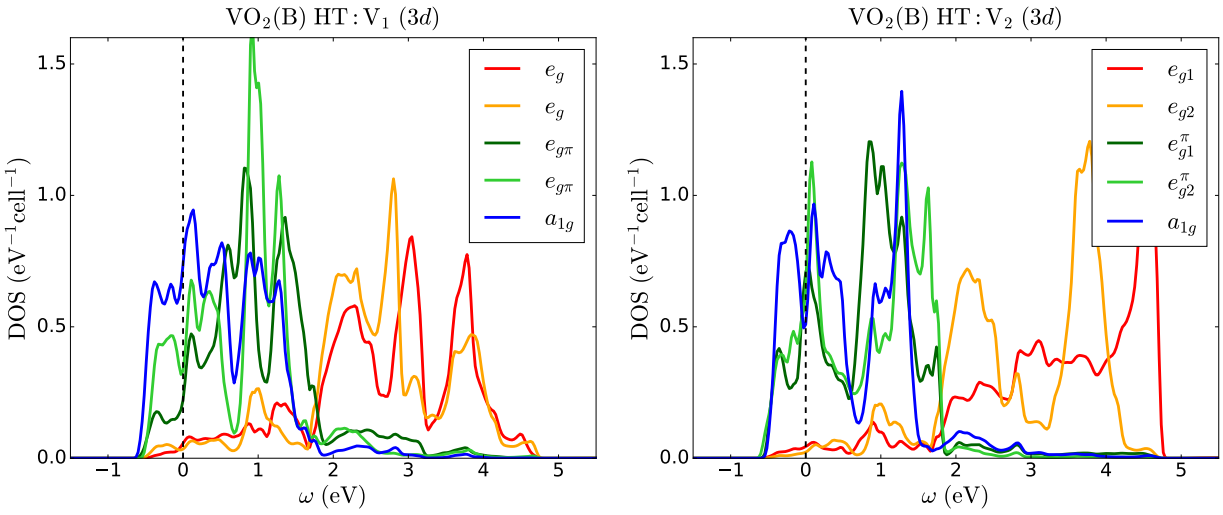

(a) VO_2 (B) HT V_1 (b) VO_2 (B) HT V_2

Figure 8.7 – Partial LDA density of states for $3d$ states of inequivalent atoms V_1 and V_2 (dimerized) in high-temperature (HT) VO_2 (B). Atom 2 (right-hand panel) displays a nascent splitting between bonding and anti-bonding a_{1g} states, but the effect is less pronounced compared to what is seen in the LT phase (Fig. 8.8b)

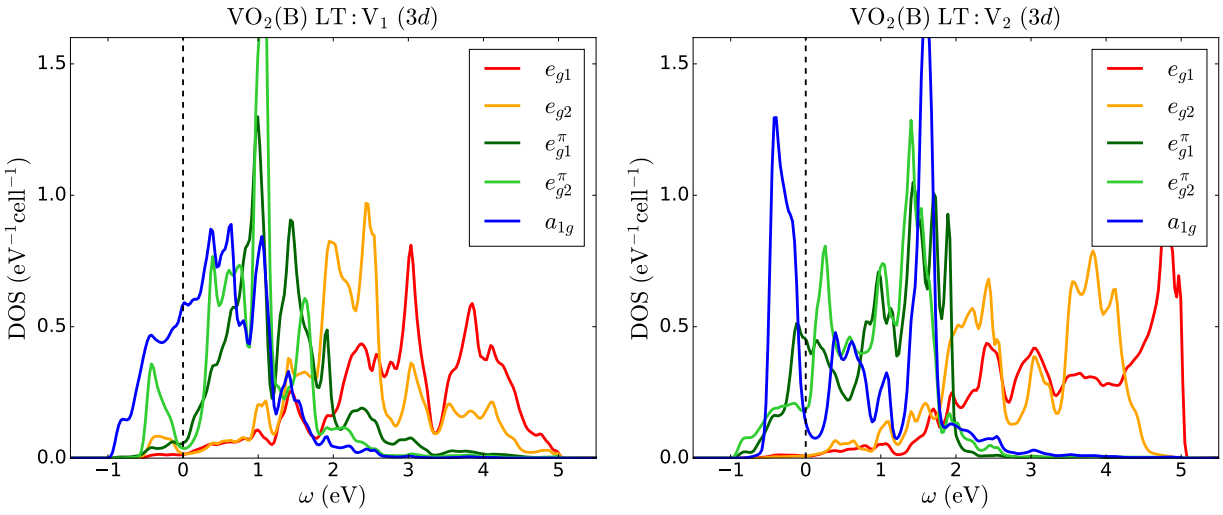

(a) VO_2 (B) LT V_1 (b) VO_2 (B) LT V_2 (dimerized)

Figure 8.8 – Partial LDA density of states for $3d$ states of inequivalent atoms V_1 and V_2 (dimerized) in low-temperature (LT) VO_2 (B).

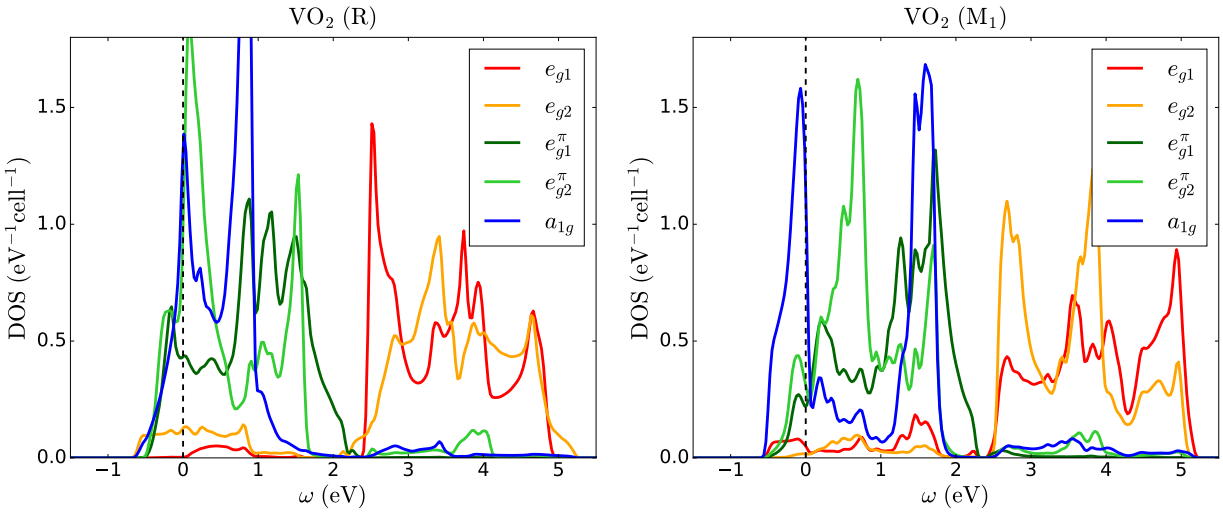

(a) VO_2 (R) (b) VO_2 (M1)

Figure 8.9 – Partial LDA density of states for $3d$ states of the rutile (R) and monoclinic (M_1) phases of VO_2. The rutile density of states is multiplied by two, for easier comparison: the unit cell is half that of the M_1 phase.

eV. In the LT phase, one of these four bands completely drops below the Fermi level (this is the dimer bonding state), leaving 3 bands crossing it.

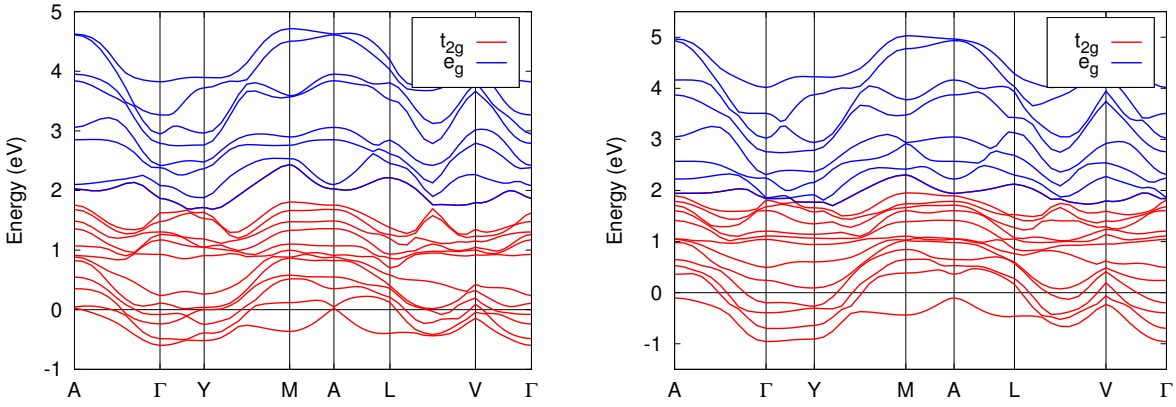

(a) VO_2 (B) HT (b) VO_2 (B) LT

Figure 8.10 – LDA band structure of VO_2 (B) in its HT and LT phases. t_{2g}-dominated bands are depicted in red, bands of dominant e_g character in blue.

8.5.2 Electronic structure within the Density Functional Theory + Dynamical Mean-Field Theory + Σ_{dimer} scheme

Here, we first present our results using the same values of $U = 4$ eV and $J_H = 0.68$ eV as used in previous reports on VO_2[96, 278, 283]. In section 8.5.3, we discuss the validity of this choice of parameters and compare them to values calculated in the constrained random phase approximation.

Self-energies

Fig. 8.11 shows the local self-energy for the R and M_1 phases. One can see that the rutile phase is a rather strongly renormalized Fermi liquid, with a quasi-particle renormalization factor of $Z \approx 0.3$ on the most occupied a_{1g} orbital and $Z \approx 0.5$ on the less occupied e_g^π orbitals. On the other hand, the imaginary part of the self-energy in the M_1 phase is small and quasi-static, demonstrating weak correlations. This is no surprise, since the complete filling of the dimer singlet state makes this phase essentially a band insulator.

The self-energies should be compared with those of the HT and LT phases of VO_2 (B), displayed in Fig. 8.12. The HT phase is very similar to the rutile phase, as expected from the similarity of the DFT DOS in Fig. 8.9a and 8.7. The magnitude of the imaginary self-energies and quasi-particle renormalization factors are about the same, and there is little difference between the two inequivalent atoms. The picture is very different in the LT phase. There, the dimerized atom 2 has a local self-energy close to the one calculated in the M_1 phase. Again, the dimerized atom behaves like a band insulator with weak correlations.

What is more interesting is what happens to non-dimerized atom V_1. On this atom, the self-energy of the a_{1g} orbital (the one that is occupied) develops a non-Fermi liquid, pole-like structure. Importantly, this is also an effect of the dimer physics. Indeed, in DFT+DMFT calculations of the LT phase without the Σ_{dimer} term, we obtain a weakly renormalized Fermi liquid (more weakly, in fact, that the HT phase). In other words, it is the freezing of the electron of V_2 in the a_{1g} dimer singlet state that forbids the hopping of the electrons on V_1 to neighboring V_2 sites, and thus favors their localization.

In Fig. 8.13 and 8.14, we obtained the real-frequency self energy of the two B phases, by using the maximum entropy analytical continuation (Bryan's maxent) algorithm [69]. Again, we see in the LT phase that the self-energy of all orbitals but the a_{1g} orbital of the non-dimerized atom are roughly equal to a constant shift. That last a_{1g} orbital, on the other hand, shows all the signs of a strongly correlated

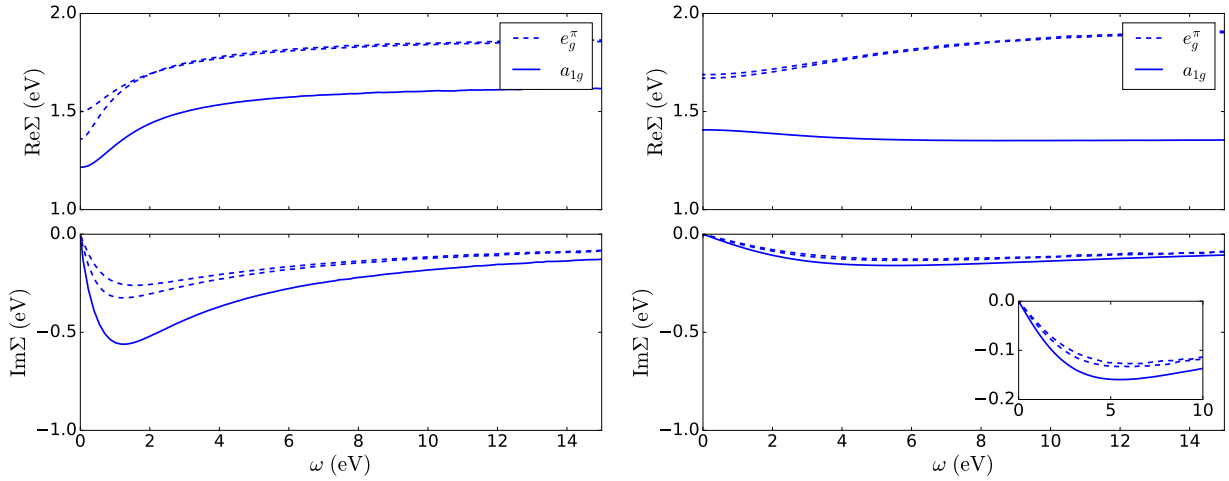

(a) VO_2 (R) (b) VO_2 (M_1) (dimerized)

Figure 8.11 – Real (upper panel) and imaginary (lower panel) part of the local DFT+DMFT self-energy on the V t_{2g} states of VO_2 (R) and VO_2 (M_1). Inset: zoom on the imaginary part of Σ in VO_2 (M_1). The full line (resp. broken line) corresponds to the self-energy of the lower-energy a_{1g} (resp. higher-energy e_g^π) states.

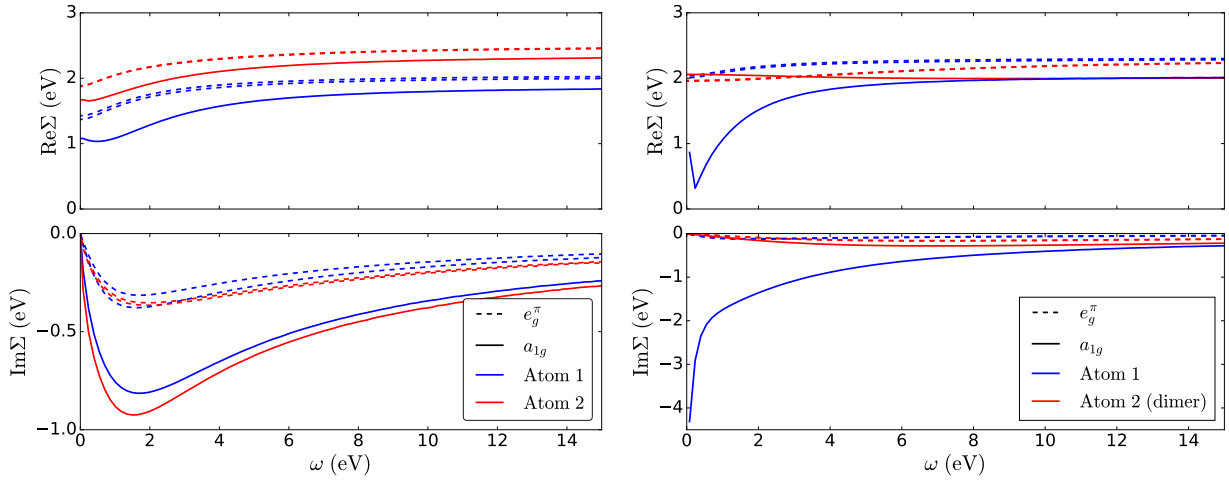

(a) VO_2 (B) HT (b) VO_2 (B) LT (dimerized)

Figure 8.12 – Real (upper panel) and imaginary (lower panel) part of the local DFT+DMFT self-energy on the V t_{2g} states of VO_2 (B) in the HT and LT phases. Blue and red are used for the two inequivalent V atoms. The full line (resp. broken line) corresponds to the self-energy of the lower-energy a_{1g} (resp. higher-energy e_g^π) states. Note the pole in the V_1 a_{1g} self-energy in the LT phase.

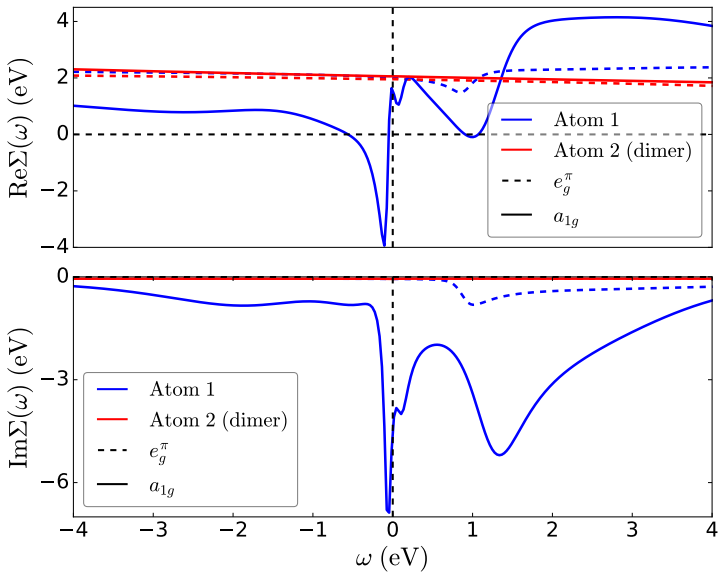

Figure 8.13 – Real (upper panel) and imaginary (lower panel) part of the real-frequency, local DFT+DMFT self-energy of the V t_{2g} states of VO_2 (B) in the LT phase. Blue and red are used for the two inequivalent V atoms. The full line (resp. broken line) corresponds to the self-energy of the lower-energy a_{1g} (resp. higher-energy e_g^π) states.

orbital. In the HT phase, we have a Fermi liquid self-energy with prominent features around -1.5 eV and 1.5eV, the a_{1g} orbital being more strongly correlated.

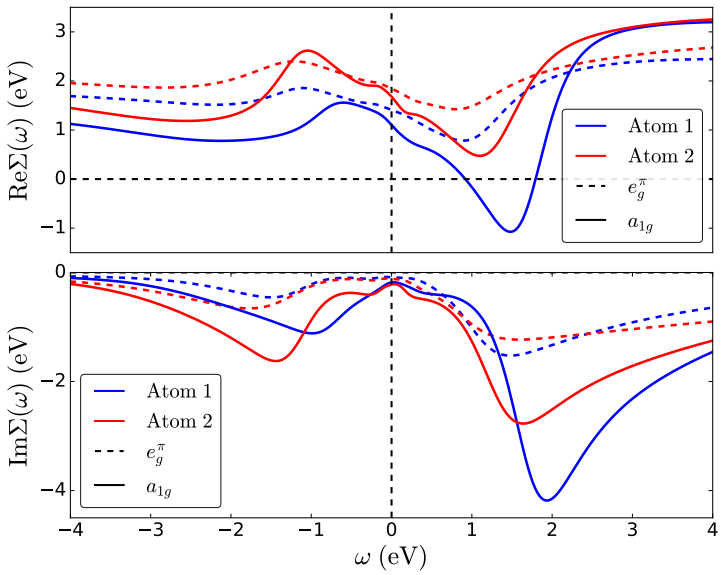

Figure 8.14 – Real (upper panel) and imaginary (lower panel) part of the real-frequency, local DFT+DMFT self-energy of the V t_{2g} states of VO_2 (B) in the HT phase. Blue and red are used for the two inequivalent V atoms. The full line (resp. broken line) corresponds to the self-energy of the lower-energy a_{1g} (resp. higher-energy e_g^π) states.

Spectral functions

We used these real-frequency self-energies to obtain the real-frequency Green's functions, and the corresponding spectral functions as $A(\omega) = -\frac{1}{\pi}\mathrm{Im}G(\omega)$. In Fig. 8.15, we show the total local (**k**-summed) spectral function of t_{2g} states in the VO_2 R, M_1[1], B (HT) and B (LT) phases.

In Fig. 8.16 and Fig. 8.17, we show the same spectral functions in a reduced energy window and in an orbitally-resolved way.

In VO_2 (R) (see Fig. 8.16a), both the a_{1g} and e_g^π states are partly filled, in agreement with Ref. [257], though we find a quantitatively stronger orbital-polarization towards a_{1g} than they measured. The a_{1g} orbital has a lower Hubbard band at -1.2 eV, and an upper Hubbard band at 3 eV. All t_{2g} orbitals contribute to a strong quasi-particle peak. This description is consistent with the strongly renormalized metal picture observed in spectroscopy.

In VO_2 (M_1) (see Fig. 8.16b), the e_g^π states are around the same level they are in DFT (and empty), and the enhanced bonding-antibonding splitting pushes the bonding a_{1g} states well below the Fermi level. This opens a gap of about 0.5 eV between the bonding a_{1g} state and the e_g^π states.

Several bands contribute to a strong quasi-particle peak at the Fermi level in the VO_2 (B) HT phase (see Fig. 8.17a), and the a_{1g} orbitals (but not the e_g^π ones) contribute to a nascent Hubbard band around -1.5 eV. This Hubbard band develops into a fully fledged peak only with higher values of U: the HT phase appears to be slightly *less* correlated than the rutile phase. Generally, though, whether we judge from the self-energy or from the spectral function, the HT phase seems to behave similarly to the rutile phase.

The VO_2 (B) LT phase (see Fig. 8.17b) is more complex, due to the interplay of dimer and local correlation physics. We make two observations. First, there are two peaks around -1 eV to -2 eV in the spectral function: one of roughly Lorentzian shape, and another displaying more structures. These peaks

[1]For technical reasons, in the M_1 phase we directly performed analytical continuation on the spectral function, rather than on the self-energy.

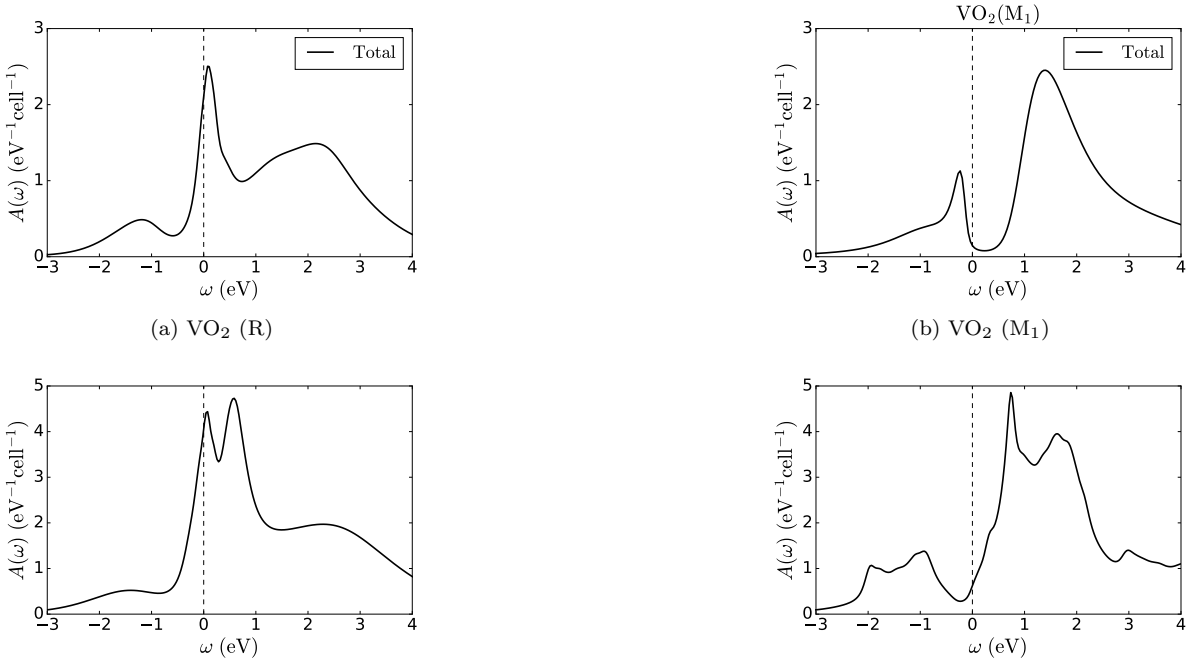

(a) VO_2 (R)

(b) VO_2 (M_1)

(c) VO_2 (B) HT

(d) VO_2 (B) LT

Figure 8.15 – Total spectral function computed within DFT+DMFT for the V t_{2g} states of VO_2 R, M_1 and B in the HT and LT phases.

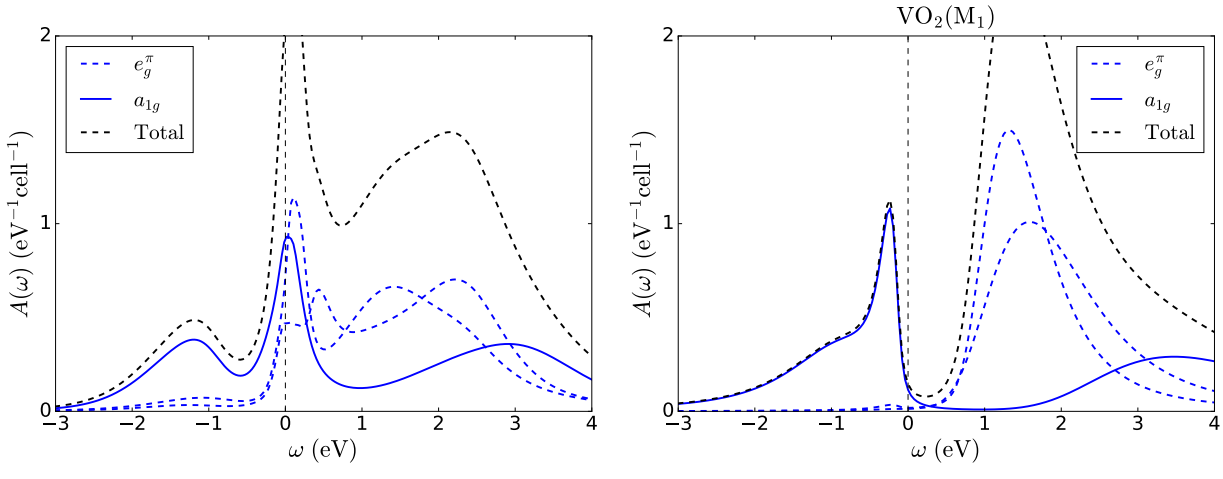

(a) VO_2 (R)

(b) VO_2 (M_1) (dimerized)

Figure 8.16 – Orbital-resolved spectral function computed within DFT+DMFT for the V t_{2g} states of VO_2 (R) and VO_2 (M_1). The total spectral function is overlain (black broken line).

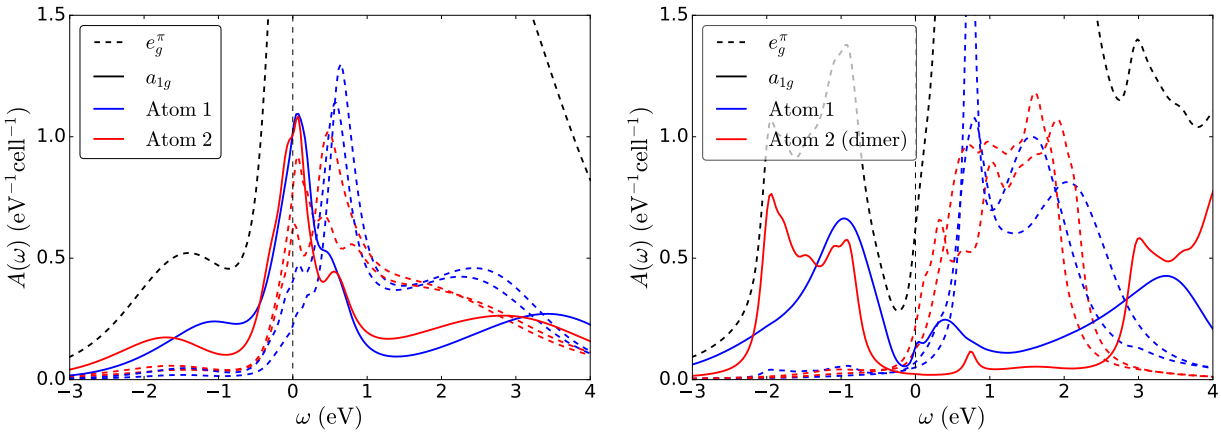

(a) VO_2 (B) HT

(b) VO_2 (B) LT (dimerized)

Figure 8.17 – Orbital-resolved spectral function computed within DFT+DMFT for the V t_{2g} states of VO_2 (B) in the HT and LT phases. The total spectral function is overlain (black broken line).

are of different natures: the first (corresponding to the lower Hubbard band of V_1) is a non-dispersive, incoherent peak, while the other (corresponding to the bonding a_{1g} state of the dimer formed by V_2) is a dispersive band below the Fermi level. A pseudogap of about 0.3 eV forms between the lower Hubbard band of V_1 and the e_g^π states of V_2. A little spectral weight, belonging to the remaining quasi-particle peak of the V_1 a_{1g} orbital, remains at the Fermi level.

Second, comparing the spectral function 8.17b to the DFT DOS 8.8a where the occupied states have some e_g^π character, we see that the combined effect of the dimer bonding on V_2 and local correlations on both atoms stabilizes the a_{1g} state with respect to the e_g^π states on V_1. This enhanced orbital-polarization and suppressed hopping to the dimer V_2 favors a Mott transition of V_1.

In Fig. 8.18 and 8.19, we display the momentum-resolved spectral functions of the HT and LT phases, respectively. In the HT phase, this confirms the picture of three t_{2g} bands crossing the Fermi level. The case of the LT phase is, again, more interesting, because it emphasizes the difference between atoms V_1 and V_2: the momentum-resolved spectral function makes the nature of the insulating LT phase clearer than the **k**-summed one. In particular, we can clearly see how the bonding a_{1g} state of atom V_2 forms a dispersive band below the Fermi level, while the V_1 atom a_{1g} band forms a mostly incoherent lower Hubbard band (around -1.2 eV) and upper Hubbard band (around 3 eV). A strong peak around 0.8 eV, also visible in the **k**-summed spectral function and in the HT phase to some extent, has mainly V_1 e_g^π character. The hybridization between the two atoms restores some itinerant character of the a_{1g} states of V_1.

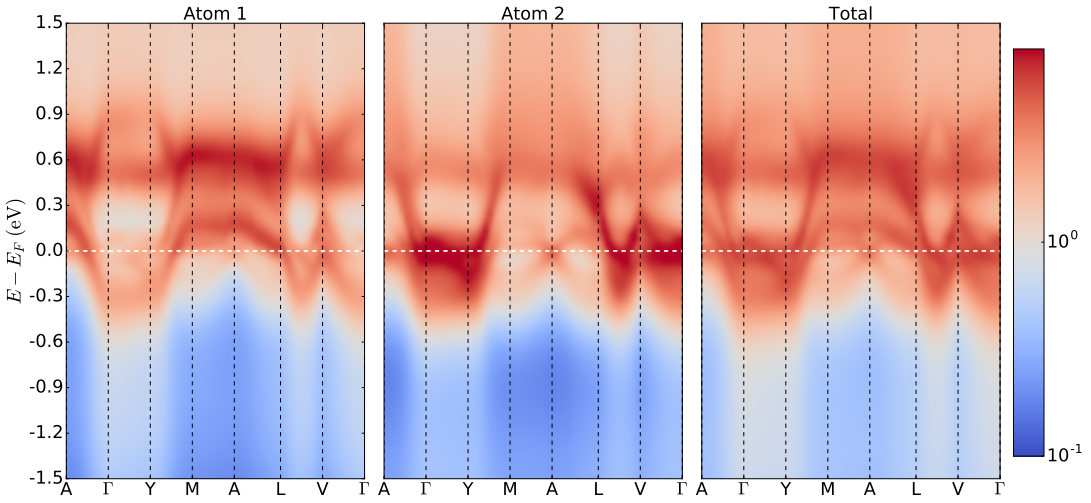

Figure 8.18 – Momentum-resolved spectral function in the HT phase of VO_2 (B). Left panel: spectral function of atom V_1. Middle panel: spectral function of atom V_2. Right panel: total spectral function.

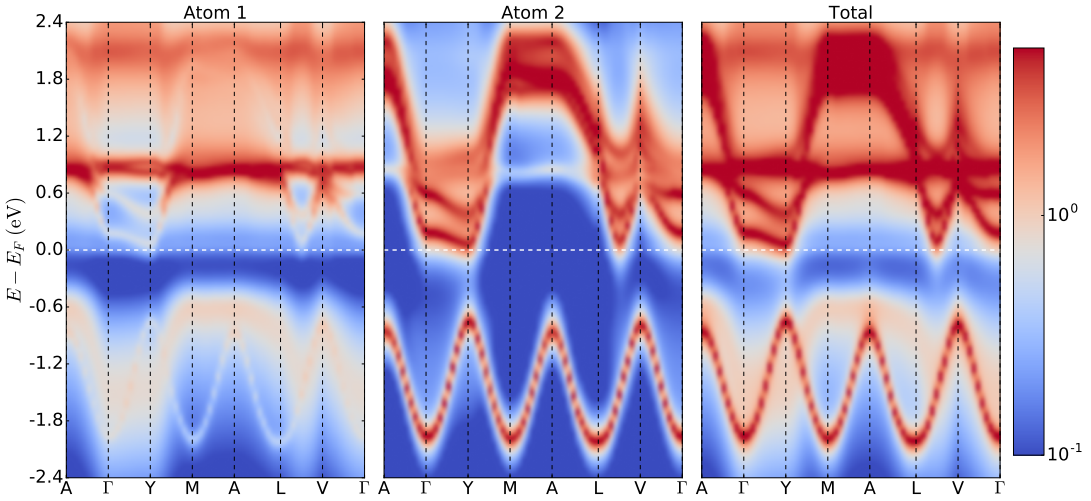

Figure 8.19 – Momentum-resolved spectral function in the LT phase of VO_2 (B). Left panel: spectral function of atom V_1. Middle panel: spectral function of atom V_2. Right panel: total spectral function. The different nature of the insulating character on atoms V_1 and V_2 appears clearly.

The orbital-polarization (or absence thereof) appears to be important to explain the physics of VO_2, and also represents a useful sanity check against experiment. The respective fillings of the a_{1g} and e_g^π orbitals in the four phases, obtained within LDA and DFT+DMFT ($+\Sigma_{\text{dimer}}$ in the M_1 and LT phases) are summarized in Table 8.5.

Phase	Method	Filling V_1		Filling V_2	
		a_{1g}	e_g^π	a_{1g}	e_g^π
VO_2 (B) HT	DFT+DMFT	0.69	0.33	0.60	0.42
	LDA	0.47	0.39	0.51	0.58
VO_2 (B) LT	DFT+$\Sigma_{\text{dimer}}+DMFT$	0.92	0.10	0.92	0.09
	LDA	0.51	0.21	0.75	0.49
VO_2 (M_1)	DFT+$\Sigma_{\text{dimer}}+DMFT$	0.98	0.02		
	LDA	0.75	0.24		
	Haverkort *et al.* [257]	0.81	0.19		
VO_2 (R)	DFT+DMFT	0.60	0.40		
	LDA	0.45	0.55		
	Haverkort *et al.* [257]	0.33	0.67		

Table 8.5 – Occupation of orbitals, calculated within LDA and DFT+$\Sigma_{\text{dimer}}+DMFT$. The column e_g^π contains the total filling of the two higher-lying t_{2g} states.

Our DFT+$\Sigma_{\text{dimer}}+DMFT$ calculations explain the electronic transition observed in VO_2 (B). Moreover, the same choice of method and parameters also provides a good description of the R and M_1 phases. We understand why the resistivity goes through a large transition (Fig. 8.2), though it is not yet clear why the resistivity of the HT phase is significantly higher than that of the rutile phase. Importantly, antiferromagnetic ordering of the non-dimerized atom chains is not needed to make the LT phase insulating, characteristically of a Mott transition. In Fig. 8.20, we compare our calculated spectral function with the photoemission spectra of Fig. 8.4. Up to a shift of the peak in the LT phase, that could be partly explained by an error in determining the chemical potential within the pseudogap, the general shape of the calculated and measured spectral functions in reasonable agreement.

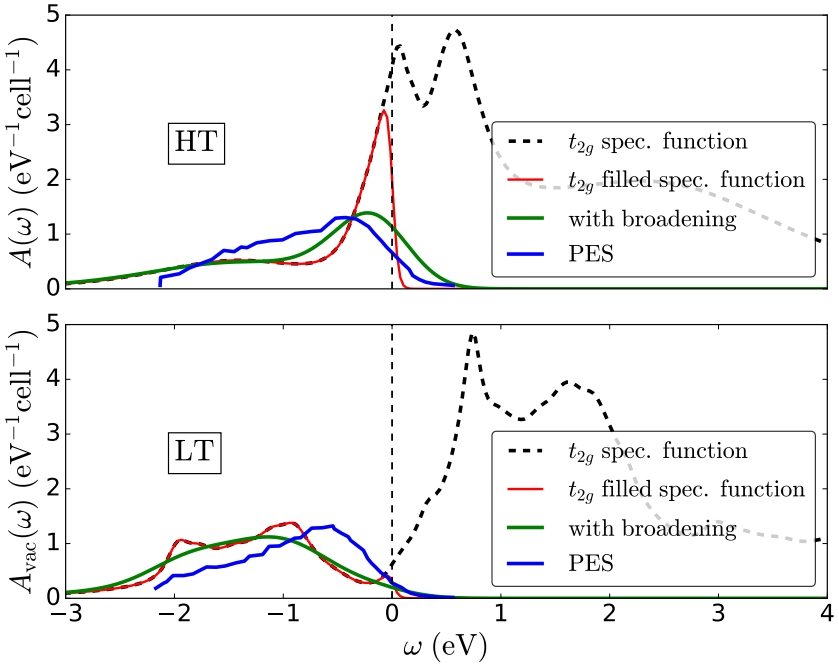

Figure 8.20 – Total spectral function of VO_2 (B) as computed within DFT+DMFT (black broken line), multiplied by the Fermi function (red line) and broadened by a gaussian with $\sigma = 0.3$ (green line), compared to the PES of Fig. 8.4 (blue line), in the HT (upper panel) and LT (lower panel) phases.

8.5.3 What about U in VO_2?

An important parameter of our DMFT calculations are the Coulomb interaction parameter U and Hund's coupling J_H. What are reasonable values for these parameters, and can we determine them from first principles?

Our cRPA calculations

We performed cRPA calculations on VO_2 (R) using the implementation by Vaugier *et al.*[119, 139]. Calculations for the monoclinic phases were not accessible, for technical reasons. However, since the energetic positions of the relevant bands (O $2p$, V $3d$ t_{2g} and e_g, and higher energy excited levels) are comparable in the rutile and monoclinic phases, it is reasonable to think that calculations on these other phases would yield similar results. We used a $7 \times 7 \times 11$ discretized Brillouin zone mesh and a cutoff at 7 Ry on the excited states to compute the polarization, which was sufficient to converge the values of U and J_H.

The results of our cRPA calculations are displayed in Table 8.6. For a t_{2g} model and with the usual parameterization of the Hubbard-Kanamori Hamiltonian (8.2), this suggests to use

$$\mathcal{U} = 2.6 \text{ eV}$$
$$\mathcal{J} = 0.4 \text{ eV}$$

These numbers are based on the average direct and exchange terms of the full $U_{m_1m_2m_3m_4}$ matrix, following Eq. 5.19 and 5.20. In reality, the a_{1g} orbital has a significantly larger value of the direct interaction U_{mmmm}. This is due to the a_{1g} orbital being more localized, not to a reduced screening: the bare Coulomb matrix element is also larger, in the same proportions. Since it is also at a lower energy

than the e_g^π states due to the crystal field splitting, and consequently the most occupied orbital, it may be better to use the larger resulting F^0, leading to

$$\mathcal{U} = 2.8 \text{ eV}$$
$$\mathcal{J} = 0.4 \text{ eV}$$

Whichever choice we make, these values are significantly smaller than the values used in most previous DMFT calculations on VO_2[96, 238, 278, 279, 283]. This raises the question of whether these smaller values can account for the insulating state of the M_1, M_2 and B (LT) phases.

For the sake of completeness, we also computed the values in a $d-d$ model and in a $dp-dp$ model (see section 4.3 for the definition of these models).

$t_{2g}-t_{2g}$ model			
$\mathcal{U}^{\text{bare}}$	$\mathcal{U}$	$\mathcal{J}^{\text{bare}}$	$\mathcal{J}$
14.4	2.6	0.5	0.4
U^{bare}	U	J_H^{bare}	J_H
13.7	2.0	0.7	0.5
$t_{2g}-t_{2g}$ model ($\mathcal{U}$ from a_{1g} orbital)			
$\mathcal{U}^{\text{bare}}$	$\mathcal{U}$	$\mathcal{J}^{\text{bare}}$	$\mathcal{J}$
15.8	2.8	0.5	0.4
U^{bare}	U	J_H^{bare}	J_H
15.1	2.3	0.7	0.5
$d-d$ model			
U^{bare}	U	J_H^{bare}	J_H
16.3	2.8	0.6	0.4
$dp-dp$ model			
U_{dd}^{bare}	U_{dd}	$J_H^{\text{bare},dd}$	J_H^{dd}
20.2	11.9	0.8	0.7
U_{dp}^{bare}	U_{dp}	U_{pp}^{bare}	U_{pp}
7.5	4.1	19.5	9.9

Table 8.6 – Parameters (in eV) of the interaction Hamiltonian VO_2 (R) calculated in a $t_{2g}-t_{2g}$ model, a $d-d$ model and a $dp-dp$ model. Here, $\mathcal{U}$ and $\mathcal{J}$ denote the parameters of the t_{2g} Hubbard-Kanamori Hamiltonian, while $U = F^0$ denotes the monopole part of the Slater interaction Hamiltonian and $J_H = (F^2 + F^4)/14$.

Comparison with reported values

In the DFT+CDMFT calculations of VO_2 reported in the literature[96, 238, 278–283], different values of U and J_H have been used. However, surprisingly for a material as iconic as VO_2, we found rather few *ab initio* calculations of the Coulomb parameters. Early constrained LDA calculations reported larger values of U, of the order of 4 eV and equal in the R and M_1 phases, in the context of DFT+U calculations[274, 285].

A value of $U = 2.7$ eV in the t_{2g} subspace was reported by Casula *et al.*[115] in a work comparing the values for different oxides. This value was obtained with the same code as used in this work, so it is not surprising that we find a similar value for a $t_{2g}-t_{2g}$ model.

Shih *et al.*[286] performed the most detailed cRPA calculation of VO_2 reported so far, to the best of our knowledge. They found a surprisingly small value of $U = 1.12$ eV in the rutile phase and $U = 2.61$ eV

in the M_1 phase in a $d-d$ model, where their maximally localized Wannier functions are constructed using all the d orbitals and transitions within the d states are excluded. After removing residual metallic screening due to the $p-d$ hybridization, they obtain larger values of respectively 3.12 eV and 3.45 eV. The exchange J_H is found to be around 0.6 eV in all cases. The difficulty of consistently determining the Coulomb parameters in oxides, in particular in the full d shell where the e_g states are strongly hybridizing with the O $2p$ states, remains a bottleneck. A scheme taking into account $p-d$ Coulomb interactions has been proposed by Seth *et al.*[287].

However, we rather disagree with the approach used by Shih *et al.* in their work, because VO_2 hosts only one electron in the V d orbitals and has well-separated t_{2g} and e_g states: the physics should be determined by the t_{2g} states only. It is known[119], but rarely discussed, that the values of U and J_H to be used in a DFT+DMFT calculation are not universally defined for the material, but actually depend strongly on the exact definition of the low energy space where the DMFT calculations are performed. In particular, the interaction Hamiltonian is different for a calculation in the t_{2g} subspace and in the full d space. More critically, for a given material and subset of orbitals, quite different values can be obtained for different projection schemes (e.g. Wannier functions constructed in a small or large energy window).

Dynamical Mean-Field Theory calculations with the cRPA U and J_H

We performed the same calculations reported above, this time using our calculated values of U and J (or rather, Kanamori $\mathcal{U}$ and $\mathcal{J}$). In the R and M_1 phases, the results are comparable to the ones described in the previous section: a rather strongly renormalized metallic R phase, and a band insulating M_1 phase, where the band gap is about 0.5 eV and opens between the a_{1g} bonding state and the e_g^π states.

We display the orbital-resolved spectral function of the R, M_1, B HT and LT phases calculated with DFT+Σ_{dimer}+DMFT with the values of $\mathcal{U}=2.8$ eV and $\mathcal{J}=0.4$ eV from cRPA (Table 8.6) in Fig. 8.21. Using these values, not much is changed in the R and M_1 phases: in the former, the Hubbard peaks are less marked and the quasi-particle peak stronger (corresponding to a larger value of $Z\approx 0.45$ instead of 0.3). In the latter, a gap opens and the a_{1g} anti-bonding state is at a lower energy. In the HT phase, similarly to the R phase, the Hubbard peaks are slightly weaker than in the calculation using $\mathcal{U}=4$ eV and $\mathcal{J}=0.68$ eV, but there is no important qualitative difference. However, the smaller values of $\mathcal{U}$ and $\mathcal{J}$ fail to open a gap in the LT phase. Indeed, we see that a strong quasi-particle peak remains on the a_{1g} orbital of the non-dimerized atom V_1 in the LT phase, with a quasi-particle renormalization factor $Z\approx 0.15$.

Taking into account the dynamical character of the effective screened Coulomb interaction $\mathcal{U}(\omega)$ (as discussed in Chapter 6), the additional hopping renormalization could possibly be sufficient to cause the Mott transition on this orbital. This is one aspect of the physics of VO_2 that we would like to further investigate.

8.6 The physics of oxygen vacancies in VO_2

In a recent publication, Backes *et al.*[225] demonstrated that oxygen vacancies participate strongly in what was thought to be the lower Hubbard band of $SrVO_3$, observed in PES. The same phenomenon could possibly be observed in other oxides, including VO_2. In this section, we study the hypothetical properties of vacancies in the R, M_1 and B phases of VO_2. In particular, we discuss on which site such vacancies would form, and what the spectral signature could be.

8.6.1 Motivation

The creation of oxygen vacancies by UV or X-ray exposition in d^0 transition metal oxides has been observed and discussed by several groups[288–290]. In Ref. [225], the authors show that oxygen vacancies in the correlated d^1 oxide $SrVO_3$ cause a peak of e_g character in the DOS at about -1.5 eV binding

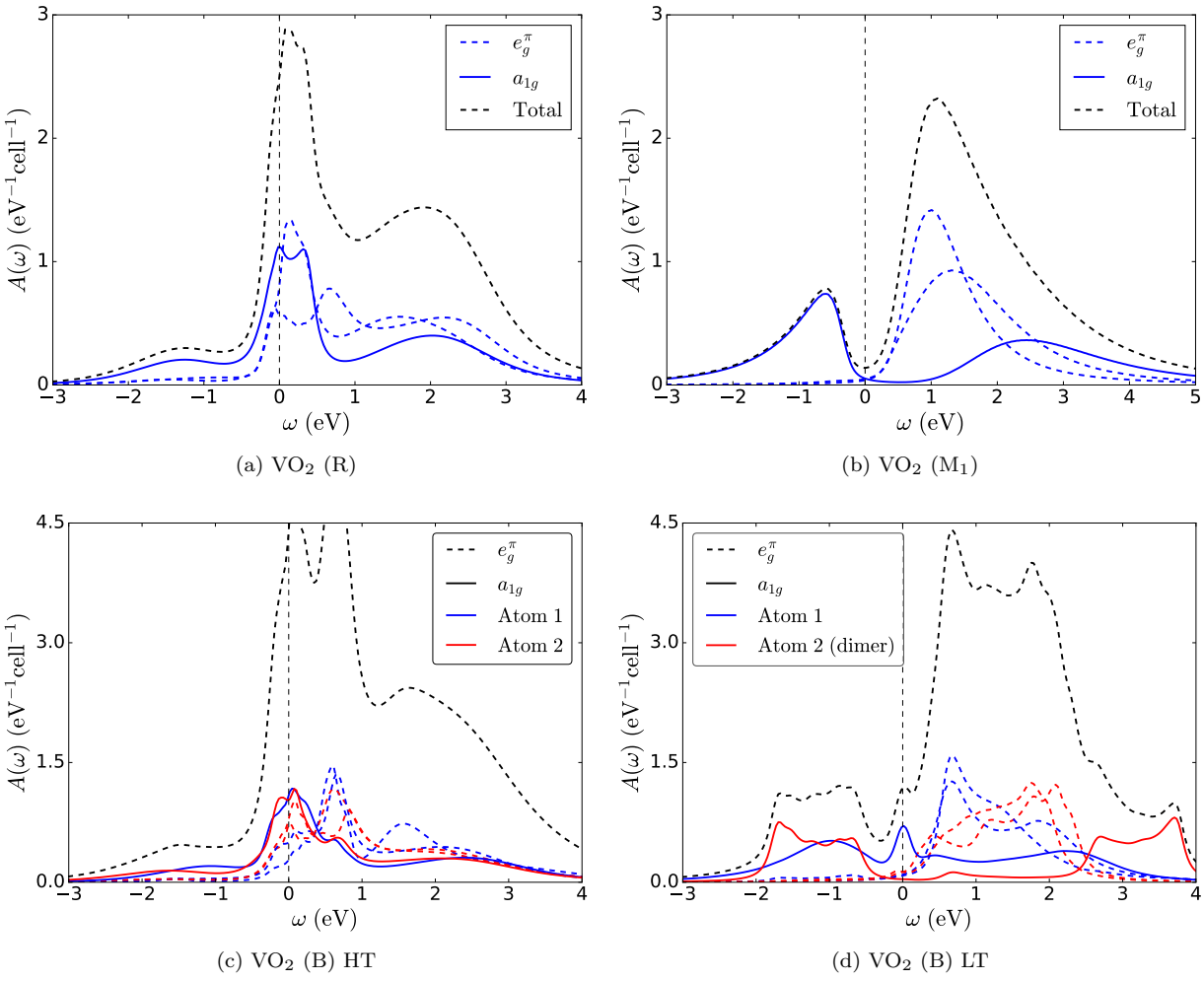

(a) VO_2 (R)

(b) VO_2 (M_1)

(c) VO_2 (B) HT

(d) VO_2 (B) LT

Figure 8.21 – Orbital-resolved spectral function of VO_2 R, M_1, B HT and B LT, calculated within DFT+Σ_{dimer}+DMFT with the cRPA values of $\mathcal{U} = 2.8$ eV and $\mathcal{J} = 0.4$ eV. Note the quasi-particle peak stemming from the non-dimerized atom V_1 in the LT phase (8.21d)

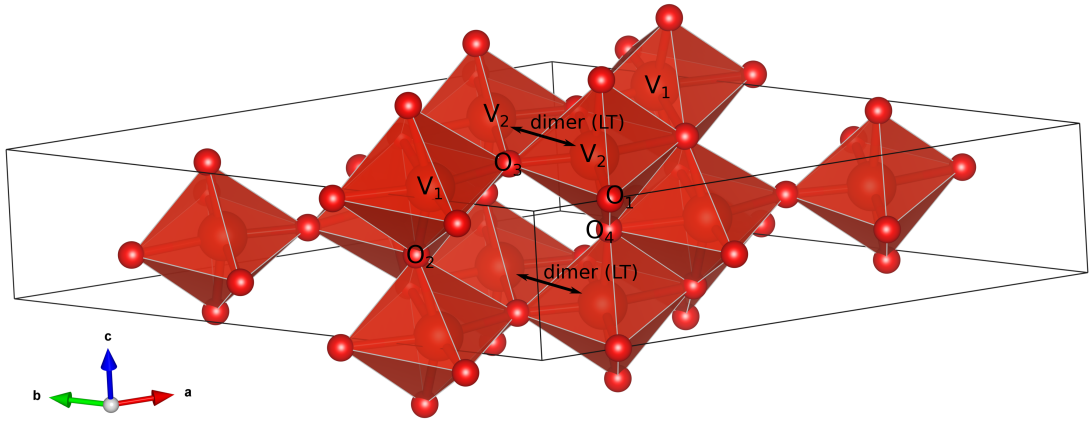

Figure 8.22 – Conventional unit cell of VO_2 (B). One conventional unit cell contains three formula units. The two inequivalent V and four inequivalent O atoms are labeled. Note the qualitative difference between O_1 and O_3 on the one hand (at the touching point of three octahedra in the same plane, at the *c*-direction tip of none), and O_2 and O_4 on the other hand (at the *c*-direction tip of the touching octahedra of two equivalent V_1 and V_2 atoms, respectively).

energy. In DFT+DMFT calculations, they show that electronic correlation effects do not qualitatively modify these vacancy states, only broadening them to some degree, and that the vacancy's effect on the lower Hubbard band in that material is only to widen it. Moreover, using photoemission spectroscopy, the authors suggest that the quasi-particle peak is hardly changed by the creation of oxygen vacancies (monitored in real time by a growing satellite peak between -1 and -1.5 eV in $SrVO_3$ and $SrTiO_3$). This suggests that oxygen vacancies form localized electronic states rather than doping the t_{2g} conduction band.

Finally, the authors suggest that similar effects may be visible in other correlated transition metal oxides. The difficulty to observe such effects lies in the fact that the vacancy states are typically around the same energies where lower Hubbard bands are expected, which may explain that this question has not been studied more extensively until now.

We speculate that the question may be even more relevant here. Indeed, the samples are grown on a substrate, where the lattice mismatch may generate substantial strain at the interface, thus favoring the formation of defects compared to the perfect crystal. Moreover, as the B phase of VO_2 is only metastable, it would not be a surprise if this particular phase had a rather higher concentration of point defects.

Finally, we would like to investigate whether the presence of vacancies could explain the qualitative difference in photoemission spectra on thin films and single crystals of VO_2 (R), as shown in Fig. 8.3. In other words, are Okazaki *et al.* observing a large vacancy concentration contributing to a peak at -1 eV in the thin films of rutile VO_2, or do they see a magnified Hubbard band at the surface?

8.6.2 Possible configurations of vacancies in VO_2

First, let us analyze the possible configurations for an oxygen vacancy in VO_2. As described in Table 8.2 and 8.3, there are four (inequivalent) possible positions to introduce such a vacancy. We shall denote these four positions as "position 1,2,3,4", respectively, in agreement with the labeling of inequivalent oxygen atoms in the aforementioned tables (see crystal structure in Fig. 8.22).

When an oxygen vacancy is created in VO_2, two additional electrons are donated to the unit cell (because the oxygens are nominally in a O^{2-} state). These electrons are naturally distributed on the vanadium atoms (that are nominally in a d^1, or V^{4+} state in VO_2). We studied the whereabouts of these

electrons when a single O atom is removed in the primitive cell using DFT. The corresponding atom- and orbital-resolved DOS are shown in Fig. 8.23 and Fig. 8.24 for the HT and LT phases, respectively. Note that the creation of a vacancy breaks the symmetry of the cell, so that there are now four inequivalent V atoms. Here, we show the orbital-projected partial DOS on all four inequivalent V atoms, for the four possible positions of a vacancy. In the figure, "inequivalent atom 1 and 2" refers to the two previously equivalent V_1 atoms, and "inequivalent atom 3 and 4" refers to the two previously equivalent V_2 atoms.

It appears that the effect of creating an O vacancy causes the e_g states of the nearest neighbor V atom(s) to drop to much lower energies, while the filling of the t_{2g} states is to a large extent unchanged. This does not come as a surprise: the e_g orbitals are pushed to higher energies by the crystal / ligand field precisely because they are pointing towards the oxygen atoms of the octahedra, contrary to the t_{2g} orbitals. Removing one of these oxygen atoms is thus bound to partially stabilize the e_g states. As mentioned in Ref. [225], this fact has been discussed in the case of oxygen vacancies in $SrTiO_3$[223, 291–293].

Based on the DOS of Fig. 8.23 and 8.24, we observe that there is a qualitative difference between the vacancy positions 1 and 3 on the one hand, and the positions 2 and 4 on the other hand. In the former case, the stabilized e_g state becomes approximately degenerate with the t_{2g} states around the Fermi level. In the latter case, a clear and sharp peak of predominantly e_g character is formed at around -1 eV binding energy, corresponding to a completely filled band holding two electrons in the band picture. This difference is not a coincidence. Indeed, the oxygen atoms O_1 and O_3 on the one hand and O_2 and O_4 on the other hand are in a rather different environment.

More specifically, O_2 is located at the tip shared by two equivalent octahedra surrounding the vanadium atom V_1, along the c axis of the conventional monoclinic cell (out of the plane containing the dimer bonds, see Fig. 8.1). O_4 is in a similar position, but near V_2. In contrast, O_1 and O_3 are located on the other vertices of the octahedra, in the ab plane of the conventional monoclinic cell, orthogonal to the c axis and containing the dimers. Moreover, O_1 and O_3 have more nearest V neighbors (respectively 3) than O_2 and O_4, so that the two electrons they donate when a vacancy is created is distributed more evenly over the surrounding V atoms.

This difference is not only visible in the spectral properties, but also in the respective formation energies of vacancies in these four positions. Here, we do not compute the total formation energy of these vacancies (doing so would require to estimate the formation energy of an O_2 molecule) but simply compare the DFT total energies of a unit cell with one vacancy present in the four configurations. The results are summarized in Tables 8.7 and 8.8. Vacancies on O_2 and O_4 are significantly more stable than vacancies on O_1 and O_3. Consequently is seems likely that, if vacancies are induced by strain in the thin films or irradiation in the PES experiment (as discussed in Ref. [225]), those vacancies would rather migrate to the O_2 and O_4 sites. Of course this supposes that the migration energy is not too high so that the migration of vacancies can happen, which we do not investigate here any further.

In VO_2 (M_1), where symmetry is higher, there are only two inequivalent O positions. The formation energy for vacancies on these two sites only differ by about 0.06 eV. In VO_2 (R), all O positions are equivalent by symmetry.

vac. position	E^f_{vac} (LDA)	E^f_{vac} (GGA)	nearest V	direction
1	0.92	1.09	V_1 and V_2	ab plane
2	0.24	0.20	V_1	c axis
3	0.66	0.65	V_1 and V_2	ab plane
4	0	0	V_2	c axis

Table 8.7 – Summary of the *relative* values of the vacancy formation energies E^f_{vac} (in eV. Reference point: formation energy at O_4), index of nearest V atom, and orientation with respect to it for the four different vacancy sites in the HT phase.

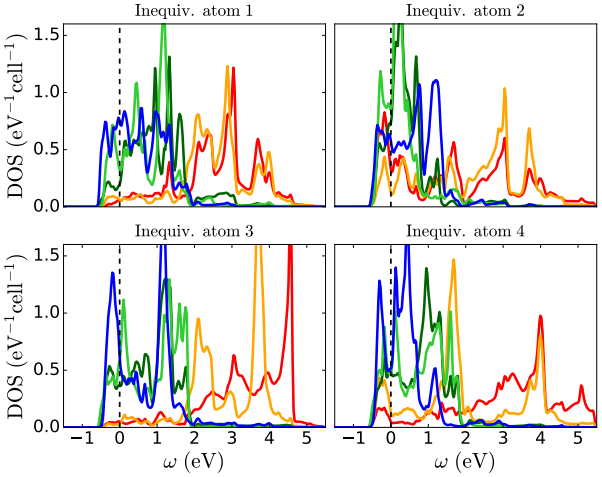

(a) VO_2 (B) HT with O vacancy in position 1

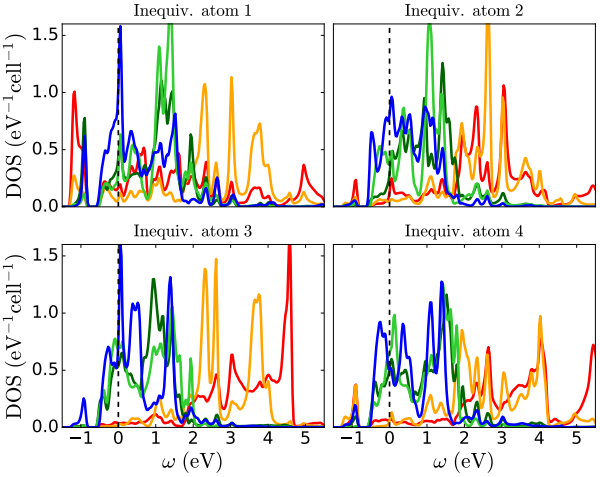

(b) VO_2 (B) HT with O vacancy in position 2

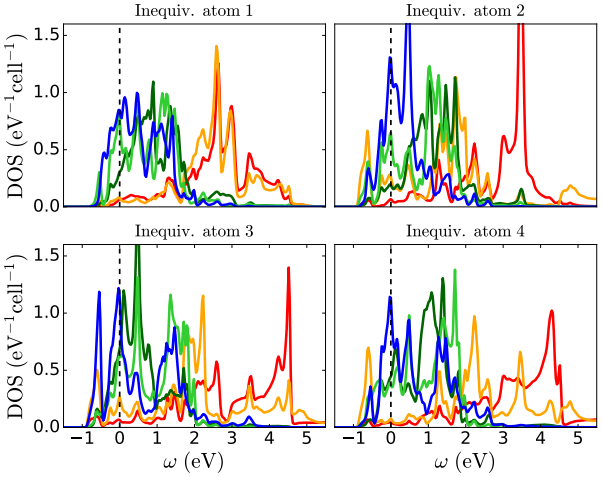

(c) VO_2 (B) HT with O vacancy in position 3

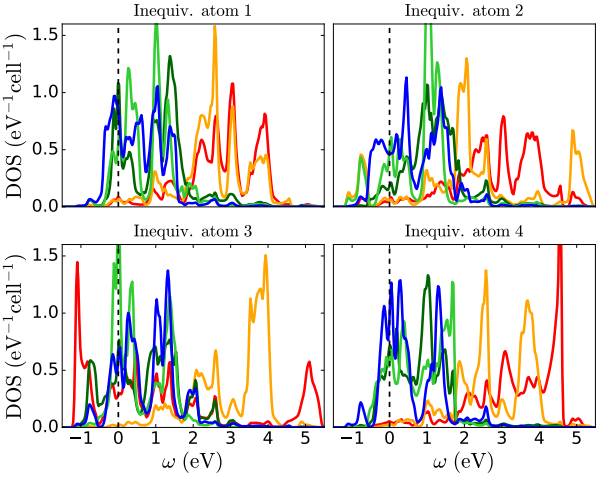

(d) VO_2 (B) HT with O vacancy in position 4

Figure 8.23 – Partial density of states of VO_2 (B) HT in the presence of an oxygen vacancy in position O_1, O_2, O_3 or O_4, resolved on the four inequivalent vanadium sites (the vacancy breaks the symmetry). For a vacancy in position O_2 (respectively O_4), the nearest V_1 (respectively V_2) atoms capture its electrons in the d_{z^2} (e_g) orbital. The color code is the same as in Fig. 8.7 to 8.9, with states of dominant e_g character shown in red and orange and states of dominant t_{2g} character shown in blue (a_{1g}) and green (e_g^π).

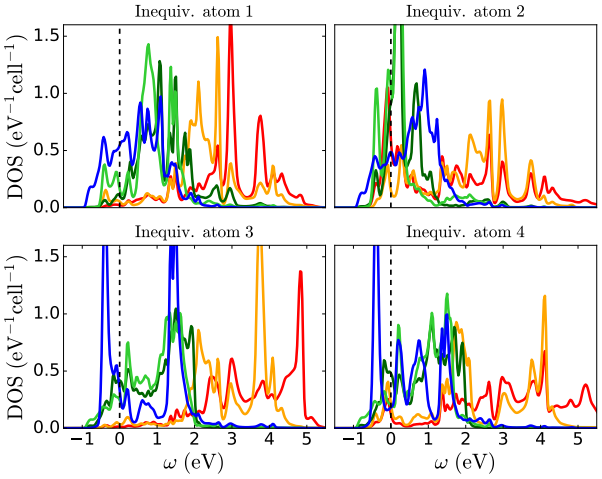

(a) VO_2 (B) LT with O vacancy in position 1

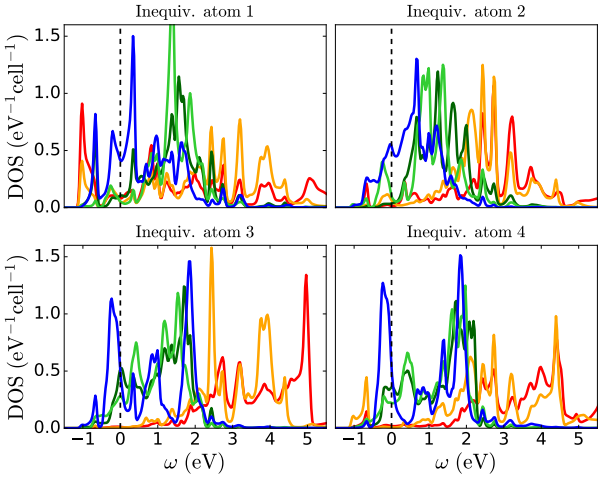

(b) VO_2 (B) LT with O vacancy in position 2

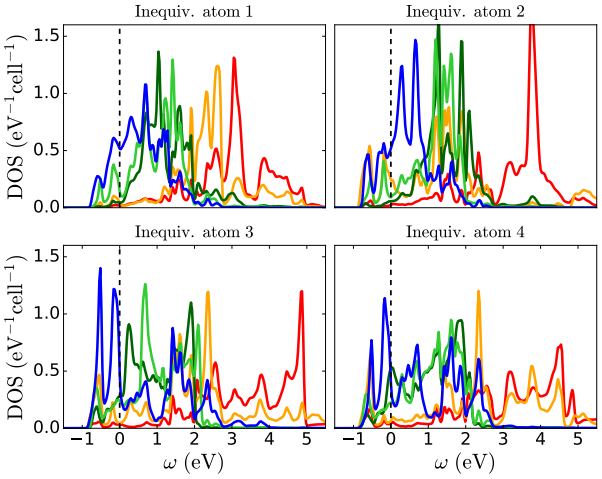

(c) VO_2 (B) LT with O vacancy in position 3

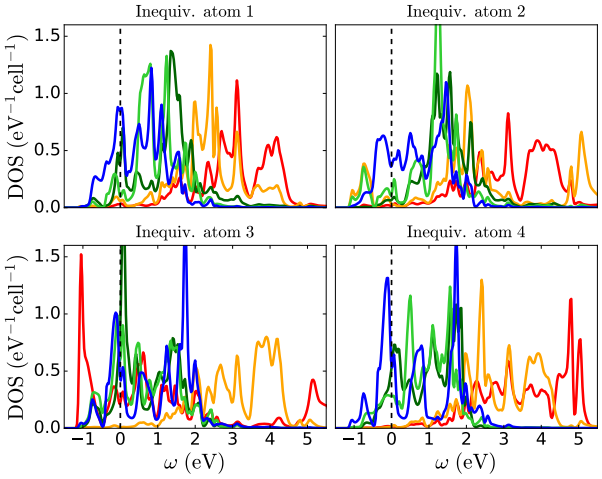

(d) VO_2 (B) LT with O vacancy in position 4

Figure 8.24 – Same as Fig. 8.23, but for the VO_2 (B) LT phase. The color code is the same as in Fig. 8.7 to 8.9, with states of dominant e_g character shown in red and orange and states of dominant t_{2g} character shown in blue (a_{1g}) and green (e_g^{π}).

vac. position	E^f_{vac} (LDA)	E^f_{vac} (GGA)	nearest V	direction
1	0.97	1.11	V_1 and V_2	*ab* plane
2	0.23	0.18	V_1	*c* axis
3	0.51	0.46	V_1 and V_2	*ab* plane
4	0	0	V_2	*c* axis

Table 8.8 – Summary of the *relative* values of the vacancy formation energies E^f_{vac} (in eV. Reference point: formation energy at O_4), index of nearest V atom, and orientation with respect to it for the four different vacancy sites in the LT phase.

8.6.3 Effect of vacancies on the photoemission spectra

In this section, we study the effect of oxygen vacancies on the spectral function in VO_2. We use a simple approximation where a vacancy correction is added to the spectral functions shown above (Fig. 8.16 and 8.17).

Based on the remarks above (oxygen vacancies in the positions 1 and 3 have significantly higher formation energy than in position 2 and 4), we only consider the effect of oxygen vacancies in positions 2 and 4. In VO_2 (M_1) we consider both positions on an equal footing, and the rutile phase has only one position available.

Fig. 8.25 displays the total DFT DOS of VO_2 (B) without vacancies, the same DOS averaged for one vacancy per unit cell in position 2 or 4, and the additional peak of e_g character around -1 eV corresponding to the vacancy states. Fig. 8.26 displays the same for the R and M_1 phases. Note that in the rutile phase, contrary to the B and M_1 phases, spectral weight is displaced below the t_{2g} states of the perfect cell, but without creating a well separated peak. This can be understood in the following way: in the R phase, any given oxygen atom is at the tip of three octahedra, with two different orientations and at the same distance of the corresponding vanadium atoms (see Fig. 8.27a). Therefore, the structure is less favorable for distributing the electron over the nearest d_{z^2} orbitals, as happens in the B phase. The same argument holds for the structure of the M_1 phase, but the octahedra are distorted so that a given oxygen atom has one neighboring V closer than the others (see Fig. 8.27b).

It is this additional spectral weight at the lower edge of the *d* states, depicted as a blue broken line in Fig. 8.25 and 8.26, that we now add to the previously calculated spectral functions, and compare to the experimentally measured spectra.

Therefore, our simple approximation for including the effect of oxygen vacancies on the spectral function can be written as

$$A_{\text{DMFT+vac}}(\omega) = \alpha_1 \left[A_{\text{DMFT}}(\omega) + \alpha_2 A_{\text{vac}}(\omega)\right] \tag{8.3}$$

where α_2 is chosen such that a vacancy concentration of 1/16 is obtained (i.e. one out of 16 oxygen atoms is missing), and α_1 normalizes the spectral function to ensure a consistent comparison of the different quantities. As a reference, Zhang *et al.*[266] have reported a metastable oxygen vacancy concentration of 10%, higher than we use here, by annealing under low oxygen pressure.

The corresponding spectra are shown in Fig. 8.28 and 8.29. More precisely, in the upper panels we show the total spectral function of t_{2g} states, multiplied by a Fermi occupation factor (with $\beta = 40\ \text{eV}^{-1}$), and broadened to mimic the finite experimental resolution. For the rutile and M_1 phases, the broadening is obtained by a convolution with a gaussian with standard deviation $\sigma = 0.1$ eV. For the B phases, we use a larger standard deviation $\sigma = 0.3$ eV, as the PES measurements of Ref. [231] (and Fig. 8.4) have lower resolution.

In VO_2 (R), the calculated spectral function agrees surprisingly well with the PES of Koethe *et al.*[254]. Their measurements showed a strong quasi-particle peak at the Fermi level. However, they do not explain the secondary peak seen in thin films in the experiments by Okazaki *et al.*[253] and Saeki

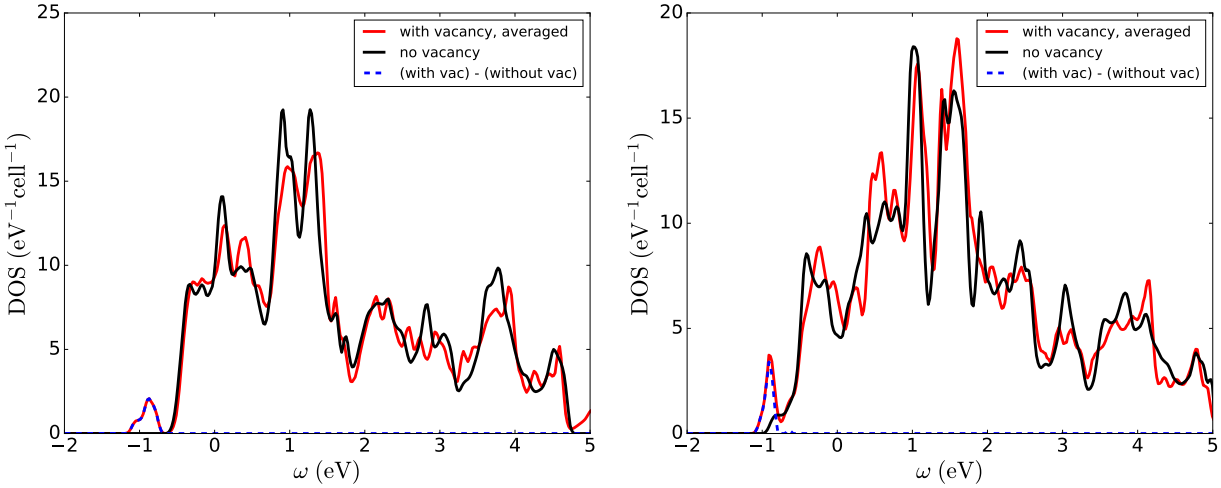

(a) VO_2 (B) HT DOS with vacancies

(b) VO_2 (B) LT DOS with vacancies

Figure 8.25 – LDA density of states for $3d$ states in VO_2 (B) without vacancies (perfect cell) and with one O vacancy (average over positions 2 and 4 in a four times larger supercell). In particular, spectral weight corresponding to V e_g states is pulled down to around -1 eV when an oxygen vacancy is introduced (blue dotted line). The vacancy concentration is of 1/16. The additional peak in the DOS at -1 eV contains the 2 electrons that are donated when an O vacancy is created. For better readability, we only show the difference in the energy range around -1 eV, corresponding to e_g spectral weight pulled down when a vacancy is created.

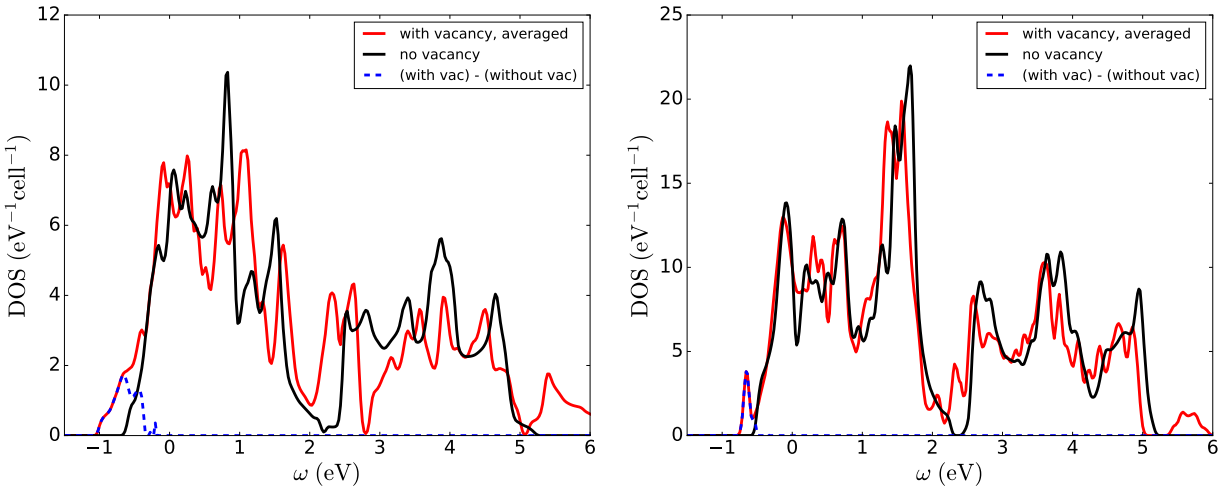

(a) VO_2 (R) DOS with vacancies

(b) VO_2 (M_1) DOS with vacancies

Figure 8.26 – LDA density of states for $3d$ states in VO_2 (R) and VO_2 (M_1) without vacancies (perfect cell) and with one O vacancy (average over all possible positions). In particular, spectral weight corresponding to V e_g states is pulled down to around -1 eV when an oxygen vacancy is introduced (blue dotted line). This mechanism works does not work as well in the more symmetric rutile phase: no completely separate peak is created. For better readability, we only show the difference in the energy range around -1 eV, corresponding to e_g spectral weight pulled down when a vacancy is created. (For consistent plotting, we double the VO_2 (R) unit cell in order to have 4 V and 8 O atoms in the unit cell.)

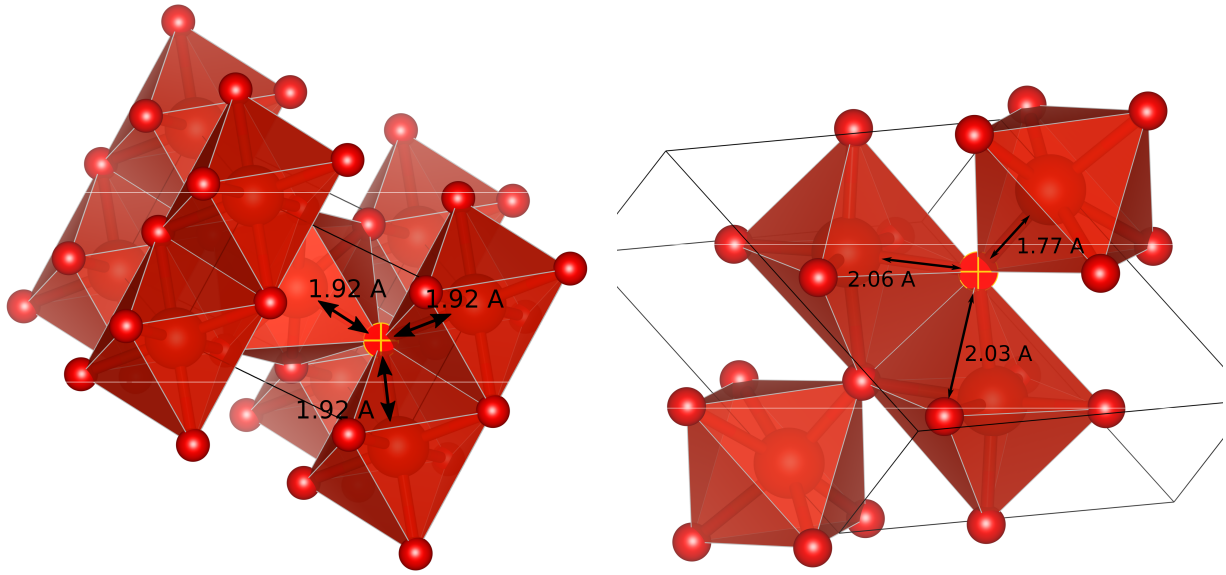

(a) VO_2 (R) (b) VO_2 (M_1)

Figure 8.27 – Local environment and distance to the nearest V atoms (in Å) for a given oxygen atom in the rutile and M_1 phases. The small spheres at the tips of the octahedra are oxygen atoms, the larger spheres within the octahedra are the vanadium atoms.

et al.[256]. This raises the question whether this peak corresponds to a lower Hubbard band or vacancy states.

We observe that the lower Hubbard band in our calculations is centered around -1 eV, just like the peak measured by Okazaki *et al.* However, the lower Hubbard band should contribute a weaker peak than the quasi-particle one. On the other hand, the oxygen vacancy peak in the rutile phase is at lower binding energy (0.5 eV) than in the B phase (1 eV) (see Fig. 8.26a). It may contribute to the measured secondary peak, but the incoherent character seems dominant (see lower panel of Fig. 8.28a). With this observation we cannot exlude or confirm the presence of oxygen vacancies in the experiment, but it seems more likely that enhanced correlations of surface states (due to reduced screening and hopping) are reinforcing the Hubbard band. In the M_1 phase (Fig. 8.28b), the O vacancy states at -0.7 eV are close to the a_{1g} bonding state, so that the presence of vacancies does not qualitatively change the spectrum.

In the LT phase of VO_2 (B), similarly to the M_1 phase, the oxygen vacancy states are found at approximately the same energy as the bonding state and lower Hubbard band (see Fig 8.29b). This means that separating the contributions in a **k**-summed spectral function is difficult. A momentum-resolved PES experiment, on the other hand, could possibly discriminate the non-dispersive oxygen vacancy state from the broader V_1 Hubbard band and the itinerant V_2 bonding band.

In the HT phase, the vacancy peak is separated from the quasi-particle peak by about 1 eV (see Fig 8.29a). Moreover, the lower Hubbard band is much weaker than in the rutile phase. Again, the presence of vacancies is consistent with the measured spectrum, and could help explaining the asymmetric shape of the experimental PES. The energy resolution of the photoemission spectrum in Fig. 8.4 is not sufficient to clearly separate the contributions from both peaks, and a measurement with higher energy resolution would be useful to confirm the hypothesis of oxygen vacancies in VO_2 thin films. If two clearly separate peaks can be measured, this would strongly hint at the presence of vacancies.

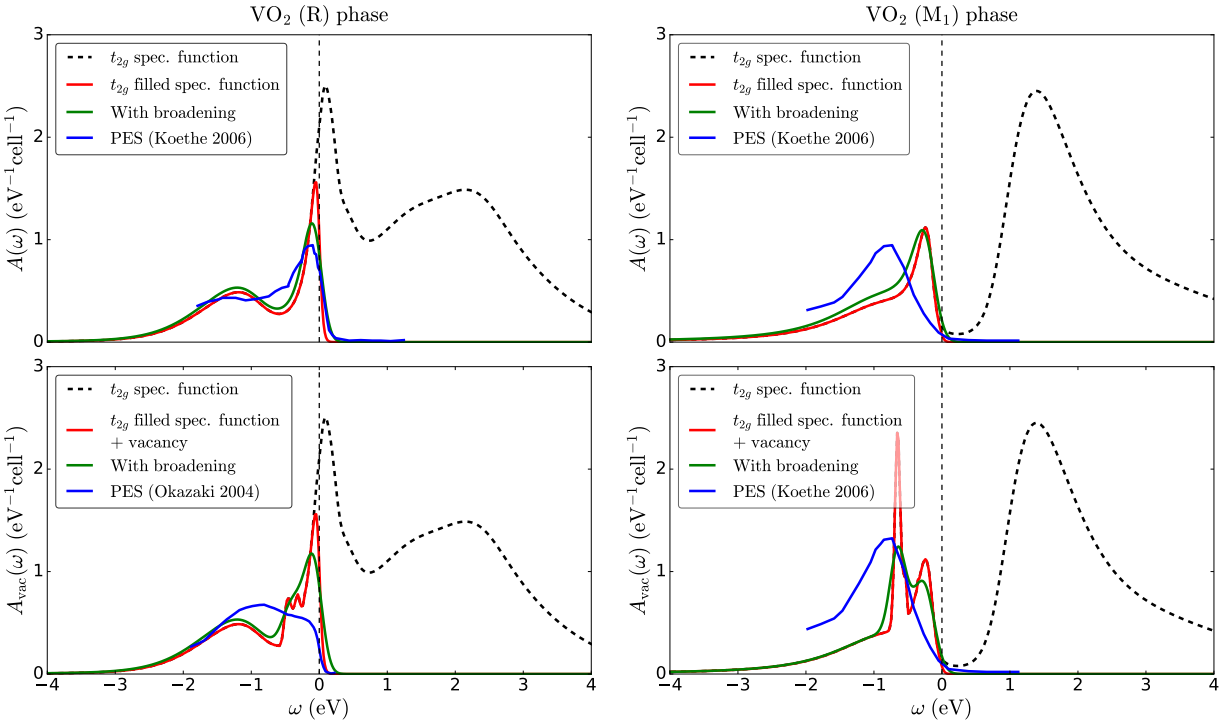

(a) VO_2 (R) (b) VO_2 (M_1) (dimerized)

Figure 8.28 – Total spectral function computed within DFT+DMFT for the V t_{2g} states of VO_2 (R) and VO_2 (R) and occupied part thereof, with and without a broadening of 0.1 eV. The upper panel shows the quantities in a perfect unit cell, while in the lower panel an additional peak due to vacancy states (see Fig. 8.26) is added to the spectral function to simulate the presence of oxygen vacancies. The photoemission spectrum (blue line) correspond to the measurement by Koethe *et al.*[254] and Okazaki *et al.*[253].

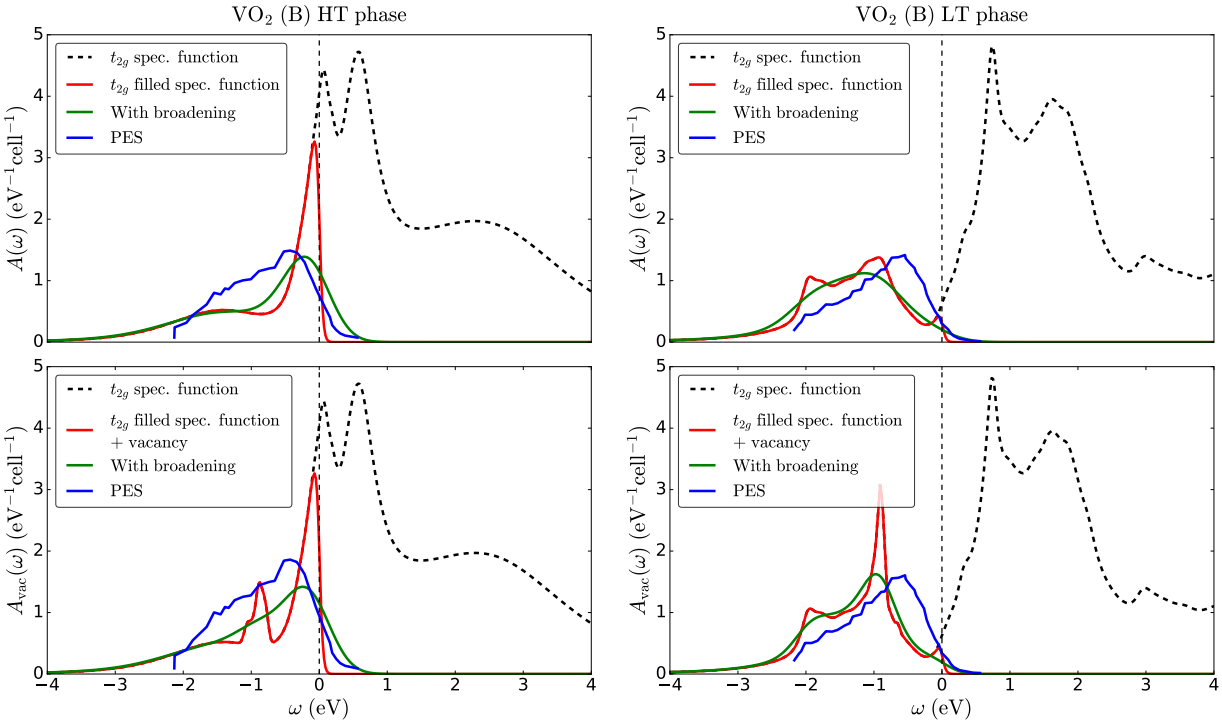

(a) VO_2 (B) HT (b) VO_2 (B) LT (dimerized)

Figure 8.29 – Total spectral function computed within DFT+DMFT for the V t_{2g} states of VO_2 (B) in the HT and LT phases and occupied part thereof, with and without a broadening of 0.3 eV corresponding to the experimental resolution. The upper panel shows the quantities in a perfect unit cell, while in the lower panel an additional peak around -1 eV (see Fig. 8.25) is added to the spectral function. The photoemission curve (blue line) corresponds to the measurement by Pal *et al.*[231].

8.7 Conclusion

In this chapter, we have shown that a unified framework using DFT+DMFT with an additional static intra-dimer self-energy on the dimerized V atoms reproduces both the VO_2 rutile to M_1 and the VO_2 (B) high temperature to low temperature bad metal to insulator transitions. We found that the VO_2 (B) HT to LT transition is similar, from the electronic point of view, to the rutile to M_2 transition, with half the V pairs forming dimers and a filled band below the Fermi level, thus causing the other half to become orbital-polarized and undergo a Mott transition. This observation is in agreement with the qualitatively similar magnetic susceptibility measurements in the B and R to M_2 transitions[244, 248].

Our results indicates that the different phases of VO_2, with their subtle but physically significant structural differences, should be described on the same footing, including both dimer physics and correlation effects. There are, however, some differences between the two aforementioned phase transitions: the R to M_2 transition happens sharply over a few K with a change of crystal structure, while the B transition occurs over a range of over 100 K and conserves the space group. The present calculations do not allow us to understand this difference.

We also investigated effects of oxygen vacancies in VO_2 on the electronic structure. We have shown that in the B phase, the preferred configuration for an O vacancy is at the tip pointing along the c axis of the octahedron surrounding the V atoms. In this configuration, the (e_g) d_{z^2} orbital is pulled down in energy, creating a localized bound state 1 eV below the Fermi level. In the insulating M_1 and LT phases, these states are roughly at the same binding energy as the bonding states or lower Hubbard bands. We suggest that photoemission spectroscopy measurements with a higher energy resolution than the ones recently reported on VO_2 (B) should allow to confirm or invalidate the presence of vacancies under photo-excitation in the metallic HT phase.

From a methodological point of view, the DFT+CDMFT method has already been shown to provide a sufficient description of both aspects: here, we followed the calculations of Tomczak *et al.*[278–281] on the M_1 phase and showed that a simplified scheme combining DFT+DMFT with an additional intra-dimer static self-energy is sufficient to describe the more complex B phase, and has the advantage of reduced computational cost. In the future, it would be interesting to use this comparably lightweight computational scheme to assess the properties of larger supercells. This could allow us to study point defects (e.g. oxygen vacancies) with a full DMFT treatment of the d states, strained or epitaxially grown samples or even doped ones.

Finally, we have observed that the values of the Coulomb interaction parameter $\mathcal{U}$ and of the Hund's rule coupling $\mathcal{J}$ calculated in cRPA are too small to explain the opening of a gap in the VO_2 B LT phase. Drawing on the ideas discussed in Chapter 6, it would be interesting to know if the neglect of dynamical interactions in the present calculations is sufficient to explain this discrepancy.

Chapter 9

Hard magnets & Crystal-Field calculations

In the present chapter, we discuss crystal-field parameter calculations from first principles. In section 9.1, we give a general introduction to crystal-field interactions: their physical effects, parameterization and derivation. In section 9.2, we give a brief introduction to hard magnetic materials, and the importance of crystal-field interactions in these materials. In section 9.3, we provide a brief summary of previous theoretical approaches to calculations of crystal-field parameters in rare-earth ions. Next, in section 9.4 we propose a technique to obtain crystal-field parameters from first principles in an important subgroup of hard magnets, namely rare-earth intermetallics. Finally, in section 9.5 we apply our method and discuss the results on compounds of the $R\mathrm{Fe}_{12}$ family. This chapter presents and extends the work published in Ref. [294].

9.1 Introduction to Crystal-Field theory

9.1.1 Generalities

In a spherically symmetric environment (e.g. in an isolated atom or ion), the energy levels of the orbitals with a given principal and orbital quantum number are degenerate. For instance, if we neglect the (in that case weak) spin-orbit coupling, the d orbitals of an isolated Fe atom with magnetic quantum number $m = -2$ to 2 have the same energy and occupation (so that the charge on the atom is spherically symmetric, as well). However, this breaks down for atoms embedded in a crystal. An atom embedded in a crystal is in an environment with reduced symmetry.

In the perovskite-type oxide SrVO_3, for instance, a given V atom is surrounded by an octahedron of ligands (O ions). This breaks the degeneracy of the d orbitals, separating the five d states into two higher-energy e_g states and three lower-energy t_{2g} states, while keeping the average level of all d orbitals the same (see Fig. 9.1). In this case the complex harmonics are not eigenfunctions of the Hamiltonian any more. Instead, one typically uses real or cubic harmonics, obtained as linear combinations of the complex harmonics: d_{z^2} and $d_{x^2-y^2}$ for the e_g orbitals and d_{xy}, d_{xz} and d_{yz} for the t_{2g} orbitals. The lifting of the degeneracy stems from the fact that the t_{2g} orbitals are pointing away from the neighboring ligands "as much as possible", as seen in Fig. 9.2. In contrast, the e_g states are pointing towards the neighboring oxygen atoms: they are at the same time pushed away by the electrostatic interaction and hybridize with the occupied ligand p states, forming bonding and anti-bonding states. The resulting bonding states have mostly oxygen character and are usually filled, while the anti-bonding states have mostly e_g character and are found at higher energies.

The number of degenerate "subshells" of a given set of orbitals (e.g. p, d or f orbitals), and the number

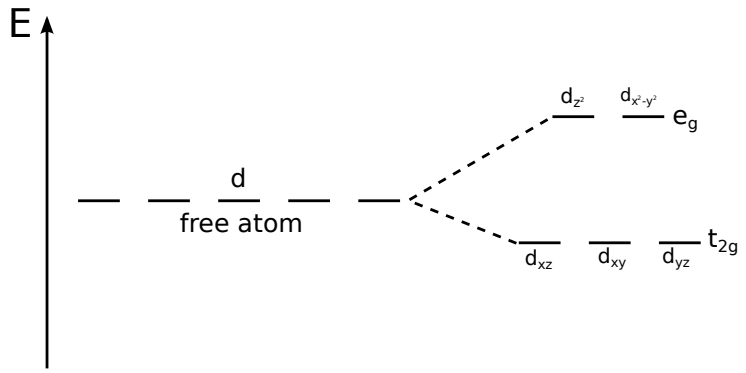

Figure 9.1 – Splitting of the 5 degenerate d orbitals into e_g and t_{2g} states by the crystal-field.

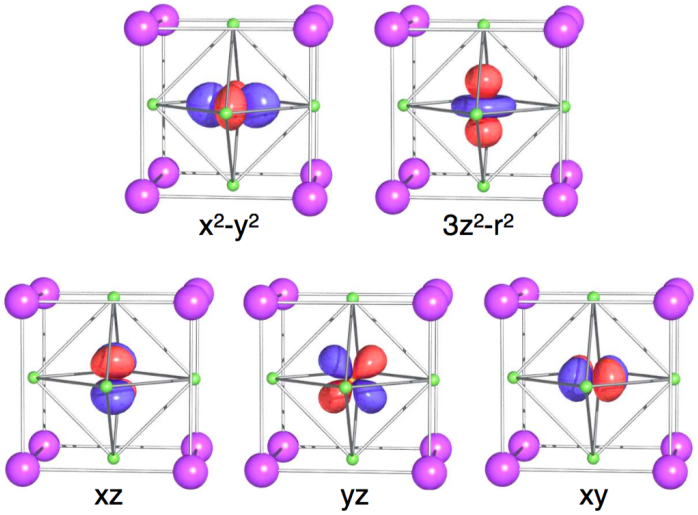

Figure 9.2 – Cubic harmonics in a perovskite. The e_g states (upper 2 orbitals) point to the nearest oxygen atoms, the t_{2g} states (lower 3 orbitals) point away from them. Reproduced from [295].

of degenerate orbitals therein, is almost entirely determined by the local symmetry or point group. There can be additional "accidental" degeneracies, but the local point group determines the minimal symmetry of the orbitals' degeneracy. Apart from this, the amplitude and the sign of the splitting(s) depend on a multitude of parameters, including the nature of the reference atom, its oxidation state, the nature of its neighbors and the distance to them.

This phenomenon, namely the lifting of degeneracy of p, or more usually d and f orbitals of atoms in molecules and crystals, is commonly known as crystal-field (CF) theory. The study of crystal-fields is a longstanding problem of quantum chemistry (like the more general problem of the electronic structure of materials). The early work on CF theory goes back to the early days of quantum physics, with works by Bethe[296] and van Vleck[297]. CF theory was combined with molecular orbital theory (a quantum chemistry theory) to form ligand field theory[298], which models the bonding of a metal ion with its ligands. The word "ligand" refers to ions or molecules that bond to a central metal atom in organic and inorganic chemistry. Typical ligands are nonmetals and halogens, or molecules formed by them. The term of ligand field theory is often used instead of CF theory, especially since the most dramatic CF splittings tend to be observed in molecules or materials made of transition metals and such ligands. However, the concept of CF theory is not limited to this case. For instance, as we discuss later in this chapter, even small CF splittings in intermetallic materials can have important physical effects.

9.1.2 Physical effects due to crystal-field splittings

The magnitude of crystal-field splittings can vary significantly. The largest ones are obtained, for instance, in transition metal oxides, where the energy difference between t_{2g} and e_g levels can reach several eV. Splittings within the t_{2g} subspace in oxides with reduced local symmetry, or $t_{2g} - e_g$ splittings in pure transition metals are typically of the order of a few 100 meV, but the CF splitting on rare-earth sites in rare-earth intermetallics (which we discuss more specifically in the present chapter) can be as small as a few meV.

The value of the crystal-field splitting in materials, both in absolute value and with respect to other relevant quantities, is of crucial importance for determining spectral and ground state properties in molecules, oxides and pure metals. In pigments consisting of transition metal oxides, the color is determined both by the charge transfer transitions (i.e. transitions from the ligand to the metallic cation) and transitions between the metal's d orbitals, split by the crystal-field[299, 300]. The same holds in active laser materials, where crystal-field levels can be tuned for optimal optical transitions[301]. These are but two examples where the crystal-field levels determine the spectral properties.

To illustrate how the crystal-field splitting also determines the ground state properties, let us give the example of the high-spin state in transition metal oxides. In an isolated atom, the occupation of the orbitals for a given number of electrons is given by Hund's rules[302, 303]. First, to minimize the electrostatic electron-electron interaction, one maximizes the total spin moment S while respecting the Pauli principle, then the total orbital angular momentum L while respecting the previous constraint. Finally, owing to the spin-orbit (SO) interaction, the spin and orbital angular momentums combine to form a total angular momentum $\boldsymbol{J} = \boldsymbol{S} + \boldsymbol{L}$ with an associated quantum number J: such that $J = L - S$ for less than half-filled shells, or $J = |L + S|$ for more than half-filled shells (for exactly half-filled shells, $L = 0$ so $J = S$). This two-step procedure is based on the fact that the spin-orbit interaction is of much smaller amplitude than the Coulomb interaction.

In a crystal, the breaking of the degeneracy by the crystal-field must be considered on top of these two interaction terms. This can have many different effects, because the CF splitting can take all kind of values with respect to the on-site Coulomb and SO interactions.

- $H_{\mathrm{CF}} > H_{e-e} > H_{\mathrm{SO}}$ in nearly empty or nearly filled transition metal oxides (e.g. $SrVO_3$)
- $H_{e-e} > H_{\mathrm{CF}} > H_{\mathrm{SO}}$ in nearly half-filled transition metals (e.g. elemental Fe)
- $H_{e-e} > H_{\mathrm{SO}} > H_{\mathrm{CF}}$ in rare-earth intermetallics (e.g. $NdFe_{12}$, see next section)

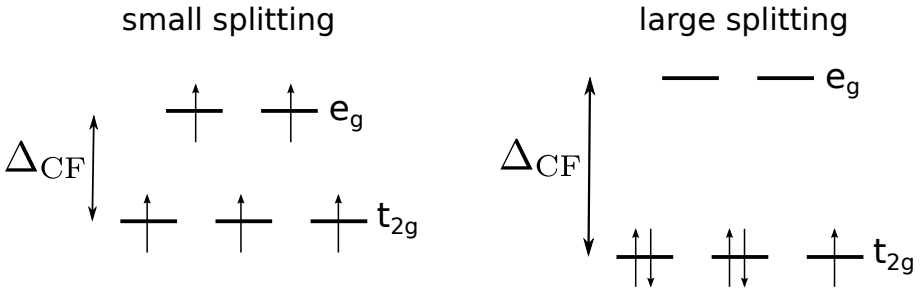

Figure 9.3 – High-spin and low-spin configuration of a set of d orbitals with 5 electrons.

Of course, the most complex effects are observed when the CF term is of similar order of magnitude as one of the other terms. This is illustrated in Fig. 9.3, showing a high to low spin transition in a transition metal with 5 electrons. With an intermediate CF splitting, the electrons minimize the total energy by spreading over the orbitals, and the resulting total spin moment S is large. Inversely, if the CF splitting between orbitals is large enough, the electrons minimize their energy by aggregating in the low-energy states, even though this increases the on-site Coulomb interaction. By doing this, the total spin moment S is reduced. $LaCoO_3$ is an example of a material going through a metal to insulator transition above 400 K, associated with a transition from low to intermediate spin state at 90 K[304].

In the rest of the chapter, we focus on the opposite limiting case: we will consider rare-earth intermetallics where the crystal-field splitting is the smallest energy scale.

9.1.3 Crystal-field parameters: notation and symmetry

Here we introduce some commonly used notations for crystal-field parameters (CFP). For a more extensive discussion, we refer the reader to Refs. [305–307].

The local Hamiltonian of a rare-earth or transition metal ion with a partially-filled d or f shell subject to the exchange field created by the rest of the lattice and to a crystal-field potential reads

$$H = H_{\text{1el}} + H_U = E_0 + \lambda \hat{L} \cdot \hat{S} + 2\mu_B B_{\text{ex}} \hat{S}_a + H_{\text{CF}} + H_U \tag{9.1}$$

where the one-electron part of the Hamiltonian corresponds to the first four terms on the right-hand side, namely, a uniform shift, spin-orbit, exchange-field, and crystal-field terms. $\hat{S}_a$ is the in-plane or ouf-of-plane spin operator, corresponding to the case where B_{ex} is along x or z, respectively. $\hat{H}_U$ represents the atomic (local) electron-electron Coulomb repulsion term of the many-body Hamiltonian. The crystal-field term $\hat{H}_{\text{CF}}$ is defined as the non-spherically symmetric part of the one-electron Hamiltonian. The corresponding non-spherical part $V_{ns}(\hat{\mathbf{r}})$ of the one-electron potential can be expanded into spherical harmonics as follows:

$$V_{ns}(\hat{\mathbf{r}}) = \sum_{k=1}^{\infty} \sum_{q=-k}^{k} A_k^q r^k Y_{kq}(\hat{\mathbf{r}}). \tag{9.2}$$

where $Y_{kq}(\hat{\mathbf{r}})$ is the spherical harmonic function with total angular moment k and projected angular moment q. The CF Hamiltonian is then defined as

$$H_{\text{CF}} = \int d\mathbf{r} V_{ns}(\mathbf{r}) \Psi(\hat{\mathbf{r}})^\dagger \Psi(\hat{\mathbf{r}}) \tag{9.3}$$

where $\Psi^\dagger(\mathbf{r})$ and $\Psi(\mathbf{r})$ are respectively the operators creating and removing an electron at $\mathbf{r}$ in real space. The matrix elements of $V_{ns}(\mathbf{r})$ between $4f$ orbitals define H_{CF}. Due to the properties of the spherical harmonics, only A_k^q for $k \leq 2l$, i.e. $k \leq 6$ in the case of an f shell or $k \leq 4$ in the case of a d shell, can contribute to H_{CF}. For historic reasons, several conventions exist for the parameterization of H_{CF},

leading to a rather confusing variety of definitions for the crystal-field parameters. One of the earlier parameterizations involves the Stevens operator equivalents[308] $\hat{O}_k^q$: $(\hat{O}_k^q)_{kq}$ are operators acting on the atomic (e.g. $3d$ or $4f$) states, obtained by taking the Cartesian expression or the tesseral harmonic functions and replacing each coordinate x, y or z by the corresponding component of the total angular momentum $\hat{\boldsymbol{J}}$: $\hat{J}_x$, $\hat{J}_y$ or $\hat{J}_z$, allowing for the commutation relations the angular moment operators. Using the Stevens operator equivalents, H_{CF} is decomposed as follows

$$H_{\mathrm{CF}} = \sum_{kq} A_k^q \langle r^k \rangle \Theta_k(J) \hat{O}_k^q \tag{9.4}$$

where $A_k^q\langle r^k\rangle$ are the crystal-field parameters for given k and q, $\Theta_k(J)$ is the Stevens factor for a given ground state multiplet defined by the quantum number J. $\Theta_k(J)$ for k =2, 4, and 6 are often designated by α_J, β_J, and γ_J, respectively. Note that the implied factorization $A_k^q\langle r^k\rangle$ is only valid for an atom surrounded by point charges[309], a rather crude model: the notation, however, continues to be used in the community. The Stevens operator equivalents are more convenient for analytical calculations and somewhat outdated, but they are still extensively used in the literature. For numerical calculations it is more convenient to express H_{CF} in terms of Wybourne's[310] spherical tensor operators $\hat{C}_k^q$:

$$H_{\mathrm{CF}} = \sum_{kq} B_k^q \hat{C}_k^q \tag{9.5}$$

where $\hat{C}_k^q$ are defined by

$$C_k^q(\hat{\mathbf{r}}) = \sqrt{4\pi/(2k+1)} Y_{kq}(\hat{\mathbf{r}})$$

Moreover, the CFP can be made real by employing the Hermitian combination of Wybourne's operators $\hat{T}_k^q$ defined by

$$\hat{T}_k^0 = \hat{C}_k^0 \text{ and } \hat{T}_k^{\pm|q|} = \sqrt{\pm 1}\left[\hat{C}_l^{-|q|} \pm (-1)^{|q|}\hat{C}_k^{|q|}\right]$$

H_{CF} can then be expressed as

$$H_{\mathrm{CF}} = \sum_{kq} L_k^q \hat{T}_k^q \tag{9.6}$$

with a set of real parameters L_k^q. L_k^q are linked to the Stevens CFP $A_k^q\langle r^l\rangle$ by a set of positive prefactors $\lambda_{kq} = A_k^q\langle r^k\rangle / L_k^q$. For a more extensive discussion of CFP conventions see, e.g., Refs. [305–307]. Note that to simplify the notations, we have not introduced a spin label to the CF parameters in Eqs. 9.5 and 9.6. In reality, the CFP can be spin-dependent. More specifically, the electrostatic contribution is of course identical for up and down spins on the atom, but the effect of hybridization is in general spin-dependent if the sub-lattice is spin-polarized. We found that taking into account this spin-dependence of CFP improves the fit for spin-polarized H_{1el}.

The number of a priori non-zero CF parameters $A_k^q\langle r^k\rangle$ is constrained by the point-group symmetry of a given rare-earth site. In particular, in the presence of inversion symmetry, $V_{ns}(\hat{\mathbf{r}}) = V_{ns}(-\hat{\mathbf{r}})$, only $A_k^q\langle r^k\rangle$ for even k can be nonzero (cf. eq. 9.2). Other point-group symmetries further reduce the number of relevant $A_k^q\langle r^k\rangle$.

9.2 Hard magnets and the importance of crystal-field effects

Hard-magnetic rare-earth intermetallics represent an outstanding example of the importance of crystal-field effects for functional properties of materials. As these materials are the main focus of the present chapter, we briefly summarize here their principal properties and introduce key quantities characterizing the hard-magnetic behavior.

Permanent magnets are a key component of modern electronic devices, ranging from electrical motors to medical imaging. Making a good permanent magnet, however, is more challenging than making a simple ferromagnet. Indeed, regular ferromagnets like iron have little magnetic anisotropy and spontaneously

demagnetize under their own demagnetizing field, unless made in unwieldy shapes (e.g. needles). An important breakthrough in the quest for high-performance permanent magnets was the discovery of rare-earth intermetallic magnets, starting with $SmCo_5$ in 1966[311]. Since its discovery in 1982, the champion of hard magnets has been $Nd_2Fe_{14}B$[312]. Most rare-earths are expensive and strategically important, however, so that it has become important to find alternative compositions or at least materials with a reduced rare-earth concentration[313]. More recently, rare-earth iron-based hard magnets $RFe_{12}X$ with the $ThMn_{12}$ structure such as $NdFe_{12}N$ have been under renewed scrutiny[314–318].

The main physical ingredients for a rare-earth hard magnet are the high magnetic anisotropy energy provided by rare-earth ions combined with the high magnetization and Curie temperature from the transition metal sub-lattice, typically composed of Fe or Co atoms[313, 319, 320]. The $3d$ transition metal atoms carry little anisotropy: because of their rather small spin-orbit coupling, their magnetization direction is approximately fixed by that of the rare-earth ion through an exchange coupling. Their anisotropy is not, in fact, completely negligible, in particular in non-cubic or distorted structures[321]. Here, however, we rather focus on the rare-earth contribution to the anisotropy. As mentioned above, most rare-earth elements, especially heavy rare-earth elements, are very expensive. Moreover, the magnetic moment of heavy rare-earth is normally anti-parallel to the transition-metal one reducing the net magnetization[313]. Hence, one advantage of new compounds like $RFe_{12}X$ is a reduced rare-earth concentration. In turn, a higher Fe concentration is favorable for achieving a large magnetization and Curie temperature, which is another advantage of $RFe_{12}X$ compounds. However, this reduced rare-earth concentration means each rare-earth ion must contribute a strong magnetic anisotropy to keep the overall magnetic hardness. Another remaining bottleneck is that $RFe_{12}X$ compounds are usually not stable: at least one of the Fe atoms must be substituted by another transition metal (Ti, for instance), thus loosing some magnetization[322]. Thin films of $RFe_{12}X$ have, however, been obtained using epitaxial growth[317].

Additional small doping of light elements is also found to strongly modify the anisotropy by affecting the rare-earth CF splitting [316, 323]. They also modify the structural stability: doping boron makes the $Nd_2Fe_{14}B$ phase more stable, while interstitial nitrogen has only a minor effect on the structural stability.

The preferred magnetization direction (in-plane or out-of-plane) of a given rare-earth ion is determined by the interplay between the crystal-field (CF) splitting and spin-orbit (SO) interactions. To first order, the crystalline magnetic anisotropy energy is given by:

$$E_A \approx K_1 \sin^2\theta$$

where θ is the angle between the magnetization and the easy axis, and

$$K_1 = -3J(J - \frac{1}{2})\alpha_J A_2^0 \langle r^2 \rangle n_R \tag{9.7}$$

where J is the total angular momentum for the rare-earth $4f$ shell and n_R the concentration of rare-earth atoms (in atoms per volume unit).

This result of perturbation theory (where the crystal-field is the small perturbation parameter) can be understood qualitatively in the following way[319, 324]: In trivalent rare-earths of the first or third quarter of the $4f$ series (Ce^{3+}, Pr^{3+}, Nd^{3+}, Tb^{3+}, Dy^{3+}, Ho^{3+}), atomic eigenstates with a given orientation of the magnetic moment are associated with an oblate (or "flat") charge distribution (see Fig. 9.4). Conversely, if the environment of the ion favors an anisotropic $4f$ charge density, this constrains the magnetization: out-of-plane for an oblate or in-plane for an prolate ("elongated" charge distribution) distribution. The opposite effect happens in the second and fourth quarter of the $4f$ series (Sm^{3+}, Er^{3+}, Tm^{3+}, Yb^{3+}). The Stevens factor α_J encodes this, taking negative and positive values respectively for the former and the latter ions.

Note that, because the crystal-field splitting is the smallest energy scale in this case, it leads to radically different effects from the low to high-spin transition in transition metals (Fig. 9.3). This epitomizes how even small effects in the electronic structure, with couplings of the order of a few meV, can have sizable macroscopic effects and technological consequences.

This simple picture also explains why different light element dopants, depending on the charge they

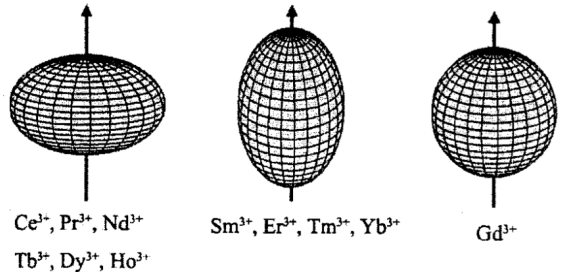

Figure 9.4 – Shape of $4f$ shells of different rare-earth ions, depending on the electron-count. Sm, Er, Tm and Yb have positive α_J, in Gd $\alpha_J = 0$, and it is negative in the other lanthanides. Reproduced from Ref. [324]

take in the crystal and the nature of their (possible) bonding with the rare-earth, can have opposite effects on the anisotropy (see Ref. [316] and section 9.5 below).

9.3 Determining the crystal-field parameters

Hereafter, when discussing CFP calculations, we focus on the particular case of rare-earth based elements (intermetallics or oxides). The same methods should not be expected to work in transition metal compounds.

9.3.1 Calculating crystal-field parameters

Considering the importance of crystal-field splittings for the physical properties of materials, it is hardly surprising that considerable effort was spent both by theoretical chemists and condensed matter physicists to determine the exact values of CF parameters. The simple point charge model[309] describes, as its name indicates, an atom surrounded by point charges representing its neighbors. If the position and valence of the ligands are known, this is enough to determine the CF Hamiltonian. The approximation is quite drastic since all hybridization and screening effects are neglected.

More sophisticated models have been developed and widely used since the 60's, such as the superposition model[305] or the overlap model[325]. However, such models, which are extensively discussed in Ref. [307], are intrinsically semi-empirical and require external information such as the ligands positions and effective charge to give reasonable results. In other words, some experimental input is needed to make these models work. Such experimental information is readily available for large band-gap insulators, where the CFP can be extracted from measurements of dipole-forbidden optical transitions between f-states[326]. In the case of rare-earth intermetallics, where the $f-f$ transitions are hidden by the optical response of conduction electrons, inelastic neutron spectroscopy can be used to determine CFP[327–331]. However, the results are more ambiguous as one needs to sort out the contributions of phonons and the effect of inter-site exchange interactions (moreover, neutron data are usually less sharp than optical measurements).

9.3.2 Crystal-field parameters from first principles using Density Functional Theory

In contrast, *ab initio* calculations do not rely on experimental input and can have truly predictive power. With the development of modern DFT codes since the 80's, such calculations have been applied to compute CFP[318, 332–341]. First-principles techniques for computing the CF parameters can be separated

into two main approaches. The first one [318, 333–338] consists in extracting the nonspherical Kohn-Sham potential V_{lm} and the $4f$ charge density ρ_{4f} around the rare-earth site and then computing the corresponding crystal-field parameter as

$$B_{lm} \propto \int_0^{+\infty} \rho_{4f}(\mathbf{r}) \mathrm{V}_{lm}(\mathbf{r}) \mathbf{r}^2 d^3\boldsymbol{r} \tag{9.8}$$

Since density functional theory (DFT) with usual local or semi-local exchange-correlation functionals (LDA or GGA) is not able to fully capture the physics of partially-filled localized $4f$ shells, one has to impose their localization by, for example, treating the $4f$ orbitals as semi-core states.

In the second more recent approach, the $4f$ states are represented by projective Wannier functions[340–342], while the charge density and, correspondingly, the Kohn-Sham potential are generated by self-consistent DFT calculations with $4f$ states treated as semi-core. In this case, the CFP are obtained by fitting the projected Kohn-Sham eigenvalues. One consequence is that, similarly to band gaps in semiconductors, a systematic error may be introduced as the (auxiliary) Kohn-Sham eigenvalues are identified to the excitation energies of the real system. Moreover, in Ref. [341], an additional *ad hoc* parameter is used to correct the charge transfer energy between $4f$ and conduction bands.

Overall, *ab initio* calculations of CFP for rare-earth ions remain a formidable theoretical problem, due to generally small values of those CFP and their extreme sensitivity to computational details. The main weak point of previously proposed DFT-based approaches is that they are not able to correctly treat the localized valence $4f$ states. Hence, the charge density is derived under the drastic approximation of treating them as fully localized core states, spherically-averaged inside the atomic sphere. The DFT+U method provides a more realistic treatment for the $4f$ density in the limit of strong ordered magnetism. However, it is not able to capture the true quasi-atomic (multiplet) nature of rare-earth shells in the paramagnetic or partially-polarized state.

We note that different techniques are used in quantum chemistry, in the context of calculating crystal-field splittings in molecules or complexes[343, 344]. While conceptually similar to techniques used in solid state physics, their techniques cannot be directly used in periodic but infinite crystals, so we do not further discuss them here.

9.3.3 Crystal-field parameters and the self-interaction problem

The non-spherical $4f$ charge density $\rho_{4f}(\mathbf{r})$ of the rare-earth ion includes an unphysical contribution to the CFP stemming from the local-density-approximation (LDA) self-interaction error. Indeed, the differential occupation of f orbitals and the resulting non-spherical charge density feeds back into the Kohn-Sham potential. This is problematic, since the CFP felt by the atom should not depend on its occupancy.

The self-interaction problem in the context of CF calculations of $4f$ elements was studied by Brooks *et al.*[345]. The authors interpreted crystal-field excitations of the rare-earth electrons in terms of quasi-particle excitations and proposed a constrained variational scheme to determine the spin Hamiltonian in rare-earth compounds from LDA total energy calculations.

In CFP calculations based on Eq. 9.8, the self-interaction problem is usually corrected by spherically-averaging the $4f$ charge density. In practical DFT implementations, this means approximations must be made, for instance treating the $4f$ electrons as core rather than valence states, and approximating the long-range "tails" of $\rho_{4f}(\mathbf{r})$, as discussed in Refs. [318, 339].

9.4 Density Functional Theory + Hubbard I approach to crystal-field parameters: eliminating the self-interaction error by averaging over the ground state multiplet

9.4.1 Numerical approach

We propose an approach to *ab initio* CFP calculations based on charge self-consistent DFT+DMFT, treating the local many-body problem for the $4f$ shell in the quasi-atomic (Hubbard-I) approximation (see section 5.2.1). While this approach of using DFT+DMFT with the Hubbard I approximation, which we may call DFT+Hub-I, is rather simple and computationally efficient, it was shown to capture not only the $4f$ multiplet structure in the paramagnetic state[108, 141, 346, 347], but also the $4f$–conduction band exchange interaction and the resulting exchange splitting of the Fermi-surface[141]. Locht *et al.*[108] recently benchmarked the Hubbard I approximation by studying a wide range of properties of rare-earth metals: lattice parameters, bulk moduli, photoemission spectra, magnetic ground state properties and intersite exchange parameters, finding good agreement with experimental data. Moreover, in the present context of CFP calculations, this scheme provides a rather natural way of averaging the $4f$ partial charge density to reduce the self-interaction error discussed in section 9.3.3 from the CF Hamiltonian.

In the Hubbard-I approximation the hybridization function is neglected and solving of the DMFT impurity problem is reduced to the diagonalization of the atomic Hamiltonian (9.1), see section 5.2.1. The one-electron part H_{1el} thereof is then given by[107]

$$H_{\mathrm{1el}} = -\mu + \langle H^{ff} \rangle - \Sigma_{\mathrm{DC}} \tag{9.9}$$

where μ is the chemical potential, $\langle H^{ff} \rangle$ is the Kohn-Sham Hamiltonian projected to the basis of $4f$ Wannier orbitals and summed over the Brillouin zone, Σ_{DC} is the double counting correction term for which we employ the "frozen integer" or nominal limit[107, 348], best adapted with the Hubbard I approximation.

Self-consistent DFT+Hub-I calculations produce a non-spherical one-electron Kohn-Sham potential (9.2), that includes several non-spherical contributions acting on $4f$ states: the long-range electrostatic (Madelung) interaction, as well as the LDA exchange-correlation potential due to conduction electrons and $4f$ states themselves. As mentioned in section 9.3, this last "intra-$4f$ shell" contribution to the exchange-correlation potential should be removed within DFT+Hub-I, since the on-site interaction H_U between $4f$ states is already treated within DMFT. Hence, the "intra-$4f$ shell" contribution in the one-electron part H_{1el} of (9.1) due to LDA is counted twice and should be removed by a double-counting correction. Moreover, this contribution includes the LDA self-interaction error for localized states directly impacting CFP: for low-lying CF levels, the self-interaction error will be larger than for less occupied excited CF states.

In order to reduce the self-interaction error from CFP we enforce uniform occupancy of all states within the $4f$ ground state multiplet in our charge self-consistent DFT+Hub-I calculations. For this, we define the imaginary-frequency atomic (Hubbard-I) Green's function at the fermionic Matsubara frequency $\omega_n = (2n+1)\pi T$, where T is the temperature, as follows:

$$G^{\mathrm{at}}_{mm'}(i\omega_n) = \frac{1}{M} \sum_{\substack{n \in \mathrm{GSM} \\ n' \notin \mathrm{GSM}}} \left(\frac{\langle n|f_m|n'\rangle\langle n'|f^\dagger_{m'}|n\rangle}{i\omega_n - E_n + E_{n'}} + \frac{\langle n'|f_m|n\rangle\langle n|f^\dagger_{m'}|n'\rangle}{i\omega_n + E_n - E_{n'}} \right) \tag{9.10}$$

where the eigenstates $|\gamma\rangle$ and $|\delta\rangle$ with eigenenergies E_γ and E_δ are obtained by diagonalization of Eq. **??** and belong to the ground-state multiplet (GSM) and excited multiplets respectively, a and b label $4f$ orbitals, M is the degeneracy of the GSM. In other words, to obtain Eq. 9.10 we substitute the standard Boltzmann weight $X_\gamma = e^{-E_\gamma/T}/Z$, where Z is the partition function, with the uniform weight $\tilde{X}_\gamma = 1/M$ for the GSM and $\tilde{X}_\delta = 0$ for exited multiplets in the spectral representation of the Green's

function [1][2]. In practice, the degeneracy of the ground state multiplet M is chosen to be the same as for the corresponding free ion, hence, it is given by Hund's rules. Therefore, $M = 10$ for Nd and $M = 6$ for Sm. This leads to a spherically-averaged contribution from the $4f$ orbitals, both inside and outside the rare-earth atomic sphere, while non-spherical contributions from other states are taken into account. Conceptually speaking, our approach amounts to replacing in Eq. 9.9 the double-counting correction by a term that enforces equal occupancy of the ground state multiplet:

$$H_{\text{1el}} = -\mu + \langle H^{ff} \rangle - \Sigma_{\text{DC}} - v_{\text{KS}}\left[\rho_{spd} + \rho_{4f}\right] + v_{\text{KS}}\left[\rho_{spd} + \bar{\rho}_{4f}\right] \tag{9.11}$$

where $v_{\text{KS}}[\rho]$ is the Kohn-Sham potential ($v_{\text{KS}} = v_{\text{Hartree}} + v_{xc}$) acting on density ρ. ρ_{4f} designates the projected electronic density belonging to the rare-earth's $4f$ orbitals, $\bar{\rho}_{4f}$ is the same density, spherically averaged, and ρ_{spd} designates all the remaining density, belonging to all atoms' s, p and d orbitals.

The same approach is used in the spin-polarized DFT+Hub-I calculations: in this case the exchange splitting is also removed within the ground state multiplet. However, we found that this averaging is not sufficient, since the value of the exchange field within our DFT+Hub-I iterations may become larger than the inter-multiplet splitting. Hence we also remove the $4f$ spin polarization from the resulting DFT+Hub-I density matrix. For a given $\mathbf{k}$-point the "averaged" density matrix $\tilde{N}^{\mathbf{k}}$ in the Bloch basis reads

$$\tilde{N}^{\mathbf{k}} = N^{\mathbf{k}} + \frac{1}{2} P^{\dagger}(\mathbf{k}) \left(T n^{ff}(\mathbf{k}) T^{\dagger} - n^{ff}(\mathbf{k}) \right) P(\mathbf{k}) \tag{9.12}$$

where $N^{\mathbf{k}}$ is the density matrix in the Bloch basis calculated as described in chapter 4.1, section 4.1.3 and in Refs. [78, 86, 349]. $P(\mathbf{k})$ is the projector[80, 349] between the spaces of Wannier and Bloch functions, $n^{ff}(\mathbf{k})$ is the density matrix in the Wannier basis, T is the time-reversal operator. The averaged density matrix $\tilde{N}^{\mathbf{k}}$ is then used to recalculate the electron density at the next DFT iteration as described in section 4.1.3. The contribution of $4f$ states to the spin density and LSDA exchange field is thus suppressed. The resulting exchange field is due to the polarization of the transition-metal sub-lattice, as expected for rare-earth intermetallics. In contrast, direct spin-polarized DFT+Hub-I calculations without the averaging would lead to a large unphysical exchange field on rare-earth sites due to the magnetization density of $4f$ electrons themselves.

Having converged DFT+Hub-I calculations, we extract the set of parameters L_k^q defined in Eq. 9.6 (or equivalently, $A_k^q \langle r^k \rangle$), as well as B_{ex} and λ, by a least-square fit of the *ab initio* Hamiltonian H_{1el} defined in Eq. 9.1 and obtained within DFT+Hub-I (see below).

9.4.2 Calculation details

The Wannier orbitals representing the rare-earth $4f$ states are constructed from the Kohn-Sham bands within the window $[-\omega_{\text{win}}, \omega_{\text{win}}]$ relative to the Fermi level. The choice of the half-window size ω_{win} is the only significant parameter in our calculations. Indeed, the choice of Hubbard U and Hund's coupling J has limited impact on the results, as we discuss in section 9.7.1. In the results described in the following section, we use $U = 6$ eV and $J_H = 0.85$ eV (see also section 9.5.2).

In order to construct a complete orthonormal basis of Wannier orbitals one needs to choose ω_{win} large enough to include at least all $4f$-like Kohn-Sham bands. It is well known that Wannier orbitals constructed with a small window leak[349] to neighboring sites due to hybridization between $4f$ states and conduction band states. A larger window, on the other hand, results in more localized Wannier orbitals consisting almost exclusively of the corresponding $4f$ partial waves inside the rare-earth atomic sphere [80, 349], as discussed in sections 9.5.2 and 9.7.2 below.

In the present case of rare-earth intermetallics we find a rather weak dependence of CFP to variations of ω_{win} within the reasonable range from 2 to 8 eV, see section 9.7.2. DFT+Hub-I studies of rare-earth

[1] We consider the case of T being much lower than the inter-multiplet splitting, hence, the contribution of excited multiplets into the partition function Z can be neglected

[2] An equivalent approach would be to make the one-electron Hamiltonian that serves as an input to the Hubbard I solver spherically symmetric: both approaches should be equivalent and nearly equally simple to implement.

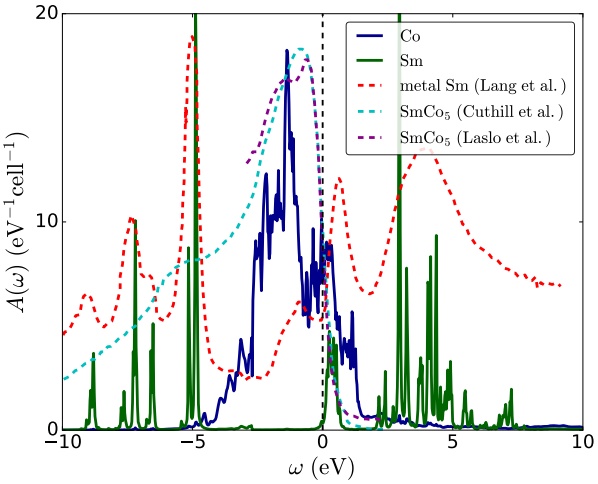

Figure 9.5 – Atom-resolved spectral function of $SmCo_5$ obtained within self-consistent spin-polarized DFT+Hubbard I (full lines). The two inequivalent Co types are summed to give the total Co $3d$ spectral function. The occupied part of the experimental spectrum of $SmCo_5$ (light blue from Ref. [351] and purple from Ref. [352]) and the full experimental spectrum of metal Sm (red, from Ref. [353]) are shown for comparison in dotted lines.

wide-gap insulators show a rather strong sensitivity of calculated CFP to the window size; less-localized small window Wannier $4f$ orbitals result in a better agreement with experimental CFP[350]. Hence, we employ ω_{win} =2 eV in our calculations throughout.

9.5 Results and discussion

In the present section, we apply the calculation scheme derived above to the well known hard magnet $SmCo_5$ for the purpose of testing. Then, we use it on several materials of the $R\text{Fe}_{12}X$ family and discuss their magnetic anisotropy.

9.5.1 Crystal-field parameters in $SmCo_5$

$SmCo_5$ has been studied more extensively than other hard magnetic rare-earth intermetallics, so ample experimental data is available in this case. In particular, several groups measured the CF parameters using inelastic neutron diffraction[327–331]. Therefore, this compound is a good benchmark to test our approach.

$SmCo_5$ has tetragonal space group 91 ($P4_122$). The unit cell contains one formula unit, with one Sm atom and two inequivalent types of Co atoms. The lattice parameters are $a = b = 4.76$ Å and $c = 3.70$ Å, with angles $\alpha = \beta = 90°$ and $\gamma = 120°$. The crystal-field on Sm $4f$ in $SmCo_5$ can be fully described with only four CF parameters: A_2^0, A_4^0, A_6^0, and A_6^6.

The **k**-summed spectral function of $SmCo_5$ is displayed in Fig. 9.5, together with experimental data for $SmCo_5$ and metallic Sm. The calculated CFP and exchange fields for $SmCo_5$ are listed in Table 9.1, together with experimental data. The calculations on $SmCo_5$ are done at the experimental lattice constants.

One may notice that the CF parameter $A_2^0\langle r^2\rangle$ exhibits a strong dependence on the spin polarization; it is about twice larger in the FM phase. For other CF parameters this dependence is small.

	PM	FM		Tils *et al.*	Zhao *et al.*	Givord *et al.*	Sankar *et al.*	Bushow *et al.*
		↑	↓	Ref. [331]	Ref. [330]	Ref. [329]	Ref. [328]	Ref. [327]
$A_2^0\langle r^2\rangle$	-140	-313	-262	-326	-330	-200	-420	-180
$A_4^0\langle r^4\rangle$	-40	-40	-55	-	-45	0	25	0
$A_6^0\langle r^6\rangle$	33	35	25	-	0	50	0	0
$A_6^6\langle r^6\rangle$	-684	-731	-593	-	0	0	6	0
B_{ex} (T)	-	227		260	327.5	260.5	357	298

Table 9.1 – Calculated CF parameters in ferromagnetic (FM) and paramagnetic (PM) $SmCo_5$ in kelvin. For the FM case we list the CF parameters for each spin direction. The exchange field in the FM phase (in tesla) is also listed. For comparison, measured values from several groups are also shown.

	Lattice constant (Å)	
Compound	a	c
$NdFe_{12}$	8.533	4.681
$NdFe_{12}N$	8.521	4.883
$NdFe_{12}Li$	8.668	4.873
$SmFe_{12}$	8.497	4.687
$SmFe_{12}N$	8.517	4.844
$SmFe_{12}Li$	8.640	4.863

Table 9.2 – Conventional unit cell lattice constants used in our calculations. $b = a$, and the angles are $\alpha = \beta = \gamma = 90°$

Our results for $A_2^0\langle r^2\rangle$ are in good agreement with the experimental (rather wide) values, ranging from about -180 to -420 K. The calculated B_{ex} also agrees rather well with the experimental range from 260 to 360 T. One may notice that the experimental measurements were performed at room temperature, hence, in ferromagnetic $SmCo_5$. Also, the most recent experimental values[331] of $A_2^0\langle r^2\rangle$ are in very good agreement with our results for the FM phase.

The main discrepancy between our theoretical and experimental CFP lies in the large value that we find for $A_6^6\langle r^6\rangle$. The high-order CF parameters are usually assumed to be rather small in $SmCo_5$. However, as noted in Ref. [354], experimental inelastic neutron and susceptibility data are not particularly sensitive to those high-order parameters. Hence, they are often assumed to be small from the onset and neglected in the fitting procedure.

9.5.2 Crystal-field parameters in $R\mathbf{Fe}_{12}X$

The $RFe_{12}X$ family (where R is a rare-earth atom and X is a small interstitial atom, e.g. N) has space group $I4/mmm$, with a tetragonal primitive unit cell. The conventional unit cell, with twice the volume and atoms, is orthorhombic. It has equivalent R sites in the corner and the center at Wyckoff position $2a$, X interstitial sites between two nearest R sites on Wyckoff position $2b$, and contains 24 Fe atoms distributed on three inequivalent sites, denoted below Fe_1, Fe_2 and Fe_3 on Wyckoff positions $8j$, $8i$ and $8f$ respectively, as displayed in Fig. 9.6. Calculations are done using the theoretical lattice constants for $RFe_{12}X$, summarized in table 9.2 in the conventional unit cell (from Table II of Ref. [355], or computed with the method therein for the X =Li compounds). The calculated lattice constants agree within 2 % with the measured ones in the more stable $NdFe_{11}Ti(N)$ and $SmFe_{11}Ti(N)$ compounds[355].

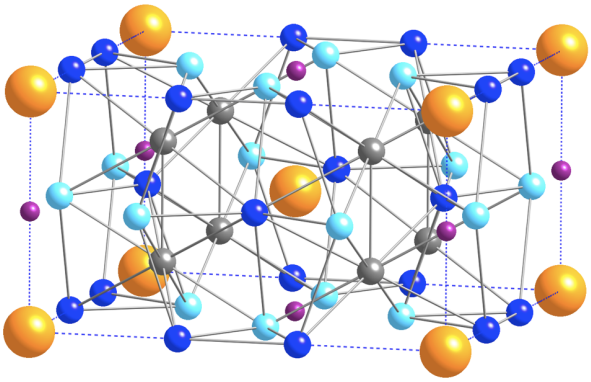

Figure 9.6 – Conventional unit cell of $R\mathrm{Fe}_{12}X$. The rare-earth R sites are yellow, the three types of Fe sites are grey, light and dark blue, and dopant X sites purple.

The DFT calculations are performed with spin-orbit coupling included within the second variational approach. We employ throughout the rotationally-invariant Coulomb vertex specified by Slater integrals $F^0 = U$ =6.0 eV as well as F^2 =10.1 eV, F^4 =6.8 eV, and F^6 =5.0 eV corresponding to Hund's rule coupling J_H =0.85 eV. These values of U and J_H are in agreement with those in the literature[107, 108, 356]. One may notice, that while the values of U and J_H are important to determine the one-electron spectrum of a material, they are expected to have a rather small effect on the crystal-field parameters that we consider in this work[3]. We discuss this dependence in section 9.7.1. DFT+Hub-I calculations are carried out for the temperature of 290 K.

DFT and DFT + Hubbard I electronic structure of $R\mathrm{Fe}_{12}X$

We first compare the electronic structure of $R\mathrm{Fe}_{12}X$ obtained within DFT (LSDA) and DFT+Hub-I. A typical DFT density of states (DOS) and a DFT+Hub-I spectral function for ferromagnetic $R\mathrm{Fe}_{12}X$, namely, for $\mathrm{NdFe}_{12}\mathrm{N}$, are shown in Fig. 9.7. The DFT DOS of Fig. 9.7(a) features a strong polarization of the Fe $3d$ band. N $2p$ states are dispersive, with the bottom of the bands contributing to a peak in the DOS around -6 eV. The Nd $4f$ band is fully spin-polarized and anti-ferromagnetically aligned to Fe $3d$, with the total spin moment within the Nd atomic sphere equal to -2.77 μ_B, i.e. close to the Hund's rule value of 3 μ_B for the Nd^{3+} ion. The Nd majority-spin $4f$ band is pinned at the Fermi level, its double-peak structure is due to spin-orbit splitting. This picture of $4f$ bands pinned at the Fermi level is qualitatively incorrect and illustrates the difficulties of DFT with local or semi-local exchange-correlation functionals to correctly treat strongly-interacting localized valence states.

The spin-polarized DFT+Hub-I spectral function shown in Fig. 9.7(b) was calculated using the averaging approach described in Sec. 9.4.1. It features an almost fully polarized Fe $3d$ band as well as occupied and empty $4f$ states separated, to first approximation, by U, thus forming lower and upper Hubbard bands, respectively. The Hubbard bands are split due to the Hund's rule and spin-orbit couplings into several manifolds with characteristically sharp peaks corresponding to transitions from the ground state to different quasi-atomic multiplets upon electron addition or removal. The $4f$ multiplet structure in lanthanides is known to be only weakly sensitive to the crystalline environment. Indeed, the positions of the Hubbard bands in Fig. 9.7(b) as well as the overall shape of the upper Hubbard band split into two manifolds of multiplet peaks centered at about 2 and 4 eV are in agreement with photoemission and inverse-photoemission spectra of the Nd metal[357]. One also sees that the Nd $4f$ states in DFT+Hub-I are not fully spin-polarized, in contrast to the DFT case. Indeed the Nd spin moment of -1.61 μ_B obtained

[3]In rare-earth ions one typically has $U \gg J_H \gg \lambda$, hence, the atomic multiplet structure is set within the LS-couping scheme. With the crystal-field splitting in lanthanides being typically much smaller than all those energy scales one may neglect the mixture between different multiplets, in that case CFP exhibits only very weak dependence to U and J_H.

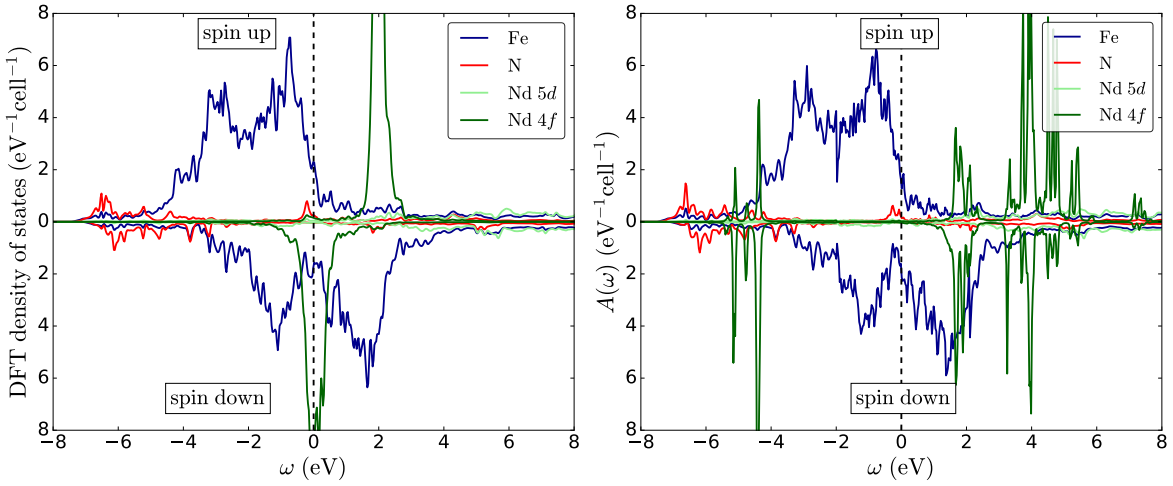

(a) $NdFe_{12}N$ DFT density of states

(b) $NdFe_{12}N$ DFT + Hubbard I spectral function

Figure 9.7 – a. Atom- and orbital-resolved density of states of $NdFe_{12}N$ calculated with the spin-polarized DFT method. b. Atom- and orbital-resolved spectral function of the same compound obtained within self-consistent spin-polarized DFT+Hubbard I. For better readability we take the average over the three types of Fe atoms: the actual total Fe density of states per unit cell is three times larger.

within DFT+Hub-I is only about half of the Hund's rule value and is also aligned antiferromagnetically with respect to the spin moment on iron. The calculated Nd orbital moment is 3.40 μ_B. It is precisely the crystal-field splitting of the Nd $4f$ shell that prevents the full saturation of the Nd magnetization.

Crystal-field parameters and exchange fields in $R\mathbf{Fe}_{12}X$

In the $R\mathrm{Fe}_{12}X$ family, the crystal-field Hamiltonian is entirely parameterized by A_2^0, A_4^0, A_4^4, A_6^0, and A_6^4.

The calculated CF and exchange fields for Nd and Sm $R\mathrm{Fe}_{12}$(N,Li) compounds are listed in Table 9.3 and 9.4, together with the magnetic moments on R and in the full cell. Comparing the different materials, one sees that $R\mathrm{Fe}_{12}$ has the smallest values of $A_2^0\langle r^2\rangle$ (in absolute value), while N insertion enhances $A_2^0\langle r^2\rangle$ up to positive values of about 400 to 600 K. Li insertion has the opposite effect, leading to large negative $A_2^0\langle r^2\rangle$, in particular for R =Nd. We notice some dependence of the CF parameters $A_k^q\langle r^k\rangle$ on the spin direction in the ferromagnetic phase. It is mostly weak, of the order of a few tenths of kelvin for the most important CFP $A_2^0\langle r^2\rangle$, except in $NdFe_{12}N$. It can be significant, though, for higher-order CFP. The magnetic state (paramagnetic or ferromagnetic) has a significant impact on $A_2^0\langle r^2\rangle$ in some compounds: one may notice larger values of $A_2^0\langle r^2\rangle$ for paramagnetic $SmFe_{12}$(N,Li) than for either spin direction in the ferromagnetic phase.

Finally, the total magnetization appears to be slightly reduced in Sm compounds, compared to Nd compounds: in the former, the spin magnetic moment on the rare-earth compensates the orbital magnetic moment, leading to negligible total moment, while the Nd total moment is dominated by the orbital component, and in the same direction as the Fe sub-lattice magnetization.

The sign and overall magnitude of our calculated $A_2^0\langle r^2\rangle$ are in agreement with previous calculations for $R\mathrm{Fe}_{12}$(N) in Ref. [316] using the $4f$-in-core approach, though there are some differences in the precise values. We obtain a similar value for $NdFe_{12}$, a somewhat larger one for $NdFe_{12}N$, a more negative value for $SmFe_{12}$ and a smaller (positive) value for $SmFe_{12}N$. One may notice that the results in Ref. [316] are quite sensitive to different treatments of the "tails" of $4f$ core orbitals: there is no such uncertainty in our approach.

Performing the averaging over the ground state multiplet as described in Eq. 9.10 is crucial to obtain reasonable CFP: the lowest-order CFP $A_2^0\langle r^2\rangle$ is most sensitive to this. The corresponding data without

Table 9.3 – Calculated CF parameters in ferromagnetic (FM) and paramagnetic (PM) $NdFe_{12}$(N,Li) in kelvin. For the FM case we list the CF parameters for each spin direction. The exchange field in the FM phase (in tesla), the spin and orbital magnetic moments of the rare-earth as well as the total magnetic moment per crystal unit cell (in Bohr magneton μ_B) are also listed.

	$NdFe_{12}$			$NdFe_{12}N$			$NdFe_{12}Li$		
	PM	FM		PM	FM		PM	FM	
		↑	↓		↑	↓		↑	↓
$A_2^0\langle r^2\rangle$	-57	-71	-116	486	477	653	-656	-687	-742
$A_4^0\langle r^4\rangle$	-29	-5	-1	107	75	112	-182	-158	-186
$A_4^4\langle r^4\rangle$	-129	-76	-270	7	-105	-141	-118	-60	-228
$A_6^0\langle r^6\rangle$	52	62	54	51	32	63	-24	-17	-31
$A_6^4\langle r^6\rangle$	70	-224	-107	-160	-65	-91	37	-6	96
B_{ex} (T)	-	265		-	217		-	410	
Nd M_{spin}	-	-1.48 μ_B		-	-1.61 μ_B		-	-1.69 μ_B	
Nd M_{orb}	-	2.96 μ_B		-	3.40 μ_B		-	3.28 μ_B	
M_{cell}	-	26.39 μ_B		-	29.15 μ_B		-	27.59 μ_B	

averaging for $NdFe_{12}N$ is $SmCo_5$ are given and discussed in section 9.6.

The lowest-order CF parameters $A_2^0\langle r^2\rangle$ and the corresponding single-ion anisotropy energies K_1 evaluated using (9.7) are displayed in Fig. 9.8. One can see that, while $NdFe_{12}N$ and $NdFe_{12}Li$ exhibit larger $|A_2^0\langle r^2\rangle|$ (upper panel) than their Sm counterparts, this difference is offset by a larger Stevens prefactor of Sm in (9.7), so that the Sm and Nd-based compounds have a magnetic anisotropy coefficient K_1 of similar magnitude. A physically significant difference between Nd and Sm is the opposite sign of their Stevens factors α_J ($\alpha_J = -7/1089$ for Nd, $\alpha_J = 13/315$ for Sm). Consequently, N insertion leads to a large out-of-plane anisotropy for Nd, but in-plane anisotropy for Sm. Li has the opposite effect: doping Li into $SmFe_{12}$ leads to a rather large out-of-plane anisotropy of $SmFe_{12}Li$, of comparable magnitude to that of $NdFe_{12}N$.

Furthermore, an interesting point is that the exchange fields B_{ex} on the rare-earth are enhanced by Li and reduced by N. This is interesting because the exchange field, or exchange coupling between Fe and R, is essential for finite temperature magnetocrystalline anisotropy. The rare-earth-originated anisotropy becomes ineffective at high temperature, and the temperature is characterized by the exchange coupling B_{ex}. In Fig. 9.9, we show the difference between the $4f$ shell atomic energies $E_\perp$ and $E_\parallel$, computed as $E = \text{Tr}[He^{-\beta H}]/\text{Tr}[e^{-\beta H}]$ with H defined in Eq. (9.1) and the exchange field B_{ex} along the z and x axis, respectively. This energy difference is more general than the expression of Eq. (9.7), because it also contains higher order CFP, excited atomic multiplets and non-zero temperature. To compute it, we diagonalize the full Hamiltonian H, without restricting ourselves to the ground state multiplet.

We scale the exchange field B_{ex} by the measured[317] magnetization fraction of the iron sub-lattice $M_{Fe}(T)/M_{Fe}(0)$ at non-zero temperatures, using the measured magnetization ratio of $NdFe_{12}N$ from Hirayama *et al*[317]. This gives quite a different picture than Fig. 9.8: the strongly enhanced exchange coupling due to Li doping causes the magnetocrystalline anisotropy to persist at much higher temperatures than with N doping.

Discussion: Wannier-functions analysis of the effect of interstitials

Let us now analyze the mechanisms determining the CFP on the rare-earth site and, in particular, the impact of the N and Li interstitials on them. We consider the $NdFe_{12}X$ (X =N, Li) compounds as an example. The N atom nominally contains three $2p$ electrons, but in the $R Fe_{12}N$ compounds the N

Table 9.4 – The same quantities as in Table 9.3 for $SmFe_{12}$(N,Li).

	$SmFe_{12}$			$SmFe_{12}N$			$SmFe_{12}Li$		
	PM	FM		PM	FM		PM	FM	
		↑	↓		↑	↓		↑	↓
$A_2^0\langle r^2\rangle$	-32	-184	-211	249	195	225	-458	-297	-272
$A_4^0\langle r^4\rangle$	-11	-21	-18	99	78	70	-116	-68	-71
$A_4^4\langle r^4\rangle$	-215	-41	-136	-122	22	-91	-124	61	-198
$A_6^0\langle r^6\rangle$	47	45	40	71	47	25	-13	-2	-12
$A_6^4\langle r^6\rangle$	-85	-95	-58	-184	-97	-82	44	30	38
B_{ex} (T)	-	232		-	205		-	331	
Sm M_{spin}	-	-3.31 μ_B		-	-2.41 μ_B		-	-3.96 μ_B	
NSmM_{orb}	-	3.29 μ_B		-	2.35 μ_B		-	3.60 μ_B	
M_{cell}	-	24.54 μ_B		-	26.83 μ_B		-	25.77 μ_B	

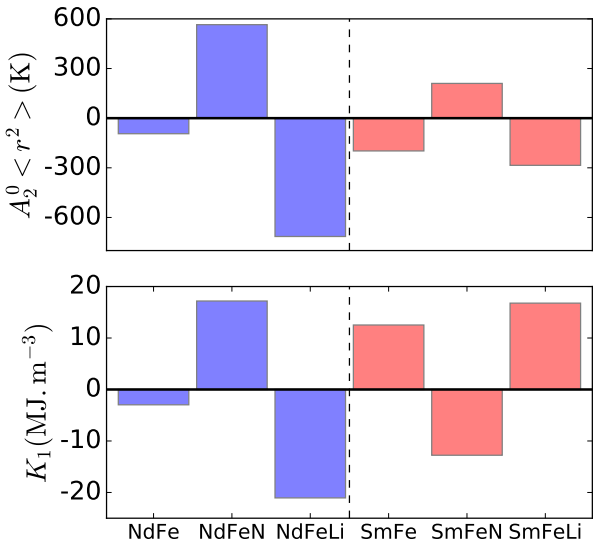

Figure 9.8 – Crystal-field parameters $A_2^0\langle r^2\rangle$ (average for up and down spins in the FM phase) and anisotropy energy K_1 for $R\text{Fe}_{12}X$, with R=Nd,Sm and X is either empty, N or Li (K_1 is obtained from equation 9.7).

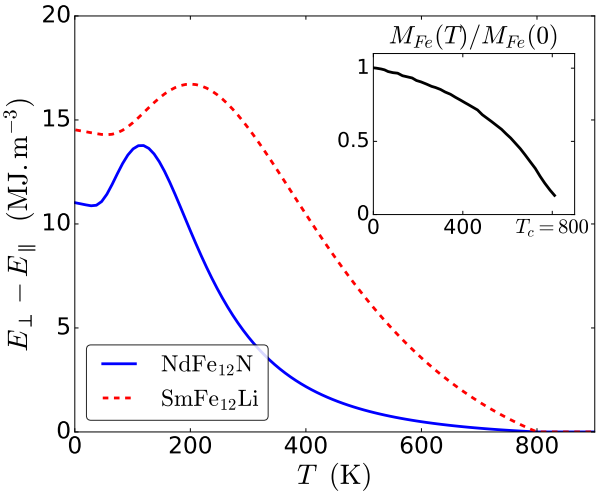

Figure 9.9 – Evolution with temperature of the difference in the $4f$ shell energy $E_\perp - E_\parallel$ between the moments on R and Fe aligned perpendicularly and parallel to the z axis, respectively, for $NdFe_{12}N$ (blue, full line) and $SmFe_{12}Li$ (red, dashed line). Inset: magnetization fraction of the Fe sublattice in $NdFe_{12}N$, as a function of temperature from Hirayama *et al*[317].

$2p$ bands are more than half-filled (Fig. 9.7). To verify this we have also performed a Bader charge-analysis[358] (a technique that allows to attribute the charge density to a given atom in molecules or crystals in a more physically meaningful way than the LAPW atomic spheres) for $NdFe_{12}X$ and found 8.3 electrons on N resulting in an ion charge of -1.3. In contrast, the Li atom is nominally $2s^1$, but it looses its single $2s$ electron inside the $NdFe_{12}$ matrix, the corresponding Bader ion charge is +0.7.

In Fig. 9.10 we display the complex Wannier orbitals constructed for Nd $4f$ states (see Eq. 4.9) with window size $\omega_{\text{win}} = 2$ eV with magnetic quantum numbers $m = 0$ and $m = -3$, in the presence of interstitial N or Li. The orbitals with $m = \pm 3$ do not point towards the N or Li atom, and leak only to neighboring Fe atoms. On the other hand, the orbital with $m = 0$ (corresponding to f_{z^3} cubic orbital) points towards the interstitial site, and shows strong leakage to the interstitial atom, particularly in the Li case. The same applies, to a lesser extent, to the orbitals $m = \pm 1$ that are also pointing towards the interstitials.

The N (Li) insertion has thus two effects on the CFP. The first one is due to the electrostatic interaction between the $4f$ electrons and the interstitial ions. This interaction with the negative N (positive Li) ion pushes the on-site energies of the $m = -1, 0, 1$ orbitals, which point towards the interstitial, to higher (lower) energies.

The second contribution is due to hybridization between the $4f$ states and the N $2p$ (Li $2s$ and $2p$) bands, which is expected to mainly affect the $m = -1, 0, 1$ orbitals pointing towards the interstitial. Mixing with the empty Li $2s$ and $2p$ bands pushes them to lower energies, while the opposite shift is induced due to hybridization with mostly filled N $2p$ located well below rare-earth $4f$ states, see Fig. 9.7. Hence, one sees that both the electrostatic and hybridization effects act in the same direction, raising the on-site energies of the $m = -1, 0, 1$ orbitals in the case of N and lowering them in the case of Li.

This analysis explains the effect of interstitials on the CFP $A_2^0\langle r^2\rangle$. Indeed, the contribution due to $A_2^0\langle r^2\rangle$ into the CF Hamiltonian 9.6 is $A_2^0\langle r^2\rangle \hat{T}_2^0/\lambda_2^0$, where the matrix of the one-electron operator $\hat{T}_2^0/\lambda_2^0$

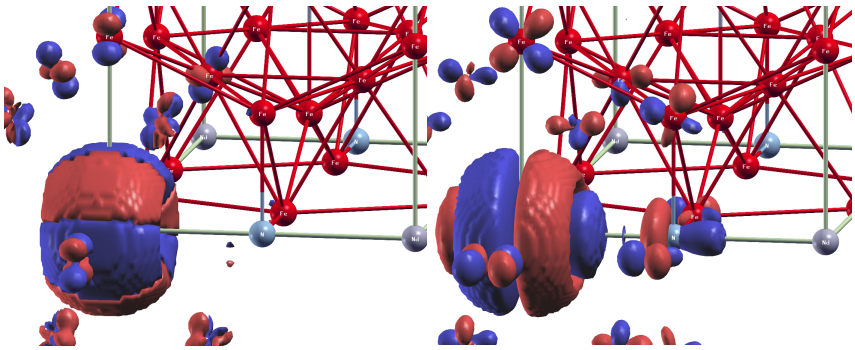

(a) $NdFe_{12}N$, $m = -3$ (b) $NdFe_{12}N$, $m = 0$

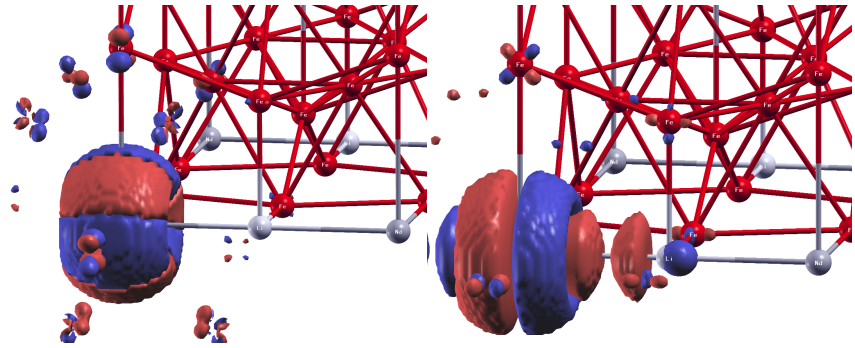

(c) $NdFe_{12}Li$, $m = -3$ (d) $NdFe_{12}Li$, $m = 0$

Figure 9.10 – $4f$ Wannier orbitals of $NdFe_{12}N$ and $NdFe_{12}Li$, for magnetic quantum number $m = -3$ and $m = 0$ and window size $[-2, 2]$ eV. The orbital with $m = 0$ points towards and leak to the N or Li sites, while orbitals with $m = \pm 3$ do not. All of them leak somewhat to the nearest-neighbor Fe atoms. The Wannier functions are constructed using the dmftproj program[359], their real-space representations are generated with the help of the wplot program from the wien2wannier[360] package. Plots are produced using XCrysDen[222].

reads

$$\hat{T}_2^0/\lambda_2^0 = 2 \begin{pmatrix} -\frac{1}{3} & & & & & & \\ & 0 & & & & (0) & \\ & & \frac{1}{5} & & & & \\ & & & \frac{4}{15} & & & \\ & & & & \frac{1}{5} & & \\ & (0) & & & & 0 & \\ & & & & & & -\frac{1}{3} \end{pmatrix}$$

in the basis of complex $4f$ orbitals. Hence, the energy level of $4f$ orbitals $m = \pm 3$ is negatively correlated with $A_2^0\langle r^2\rangle$, while the energy levels of the orbitals with $m = -1, 0, 1$ are positively correlated with $A_2^0\langle r^2\rangle$ (orbitals with $m = \pm 2$ are unaffected by $\hat{O}_l^m$). Thus, the effect of N (Li) insertion is to enhance (reduce) the value of $A_2^0\langle r^2\rangle$.

One may argue that the Hubbard-I approximation neglects the hybridization function in solving the quantum impurity problem, hence, dynamical hybridization to the bath is not included explicitly when solving for the self-energy Σ in the DMFT (Hubbard-I) step of our DFT+Hub-I calculations. However, our Wannier orbitals constructed within the "small" energy window do contain the effect of static hybridization implicitly, which is evidenced by their "leakage" to neighboring sites due to mixing

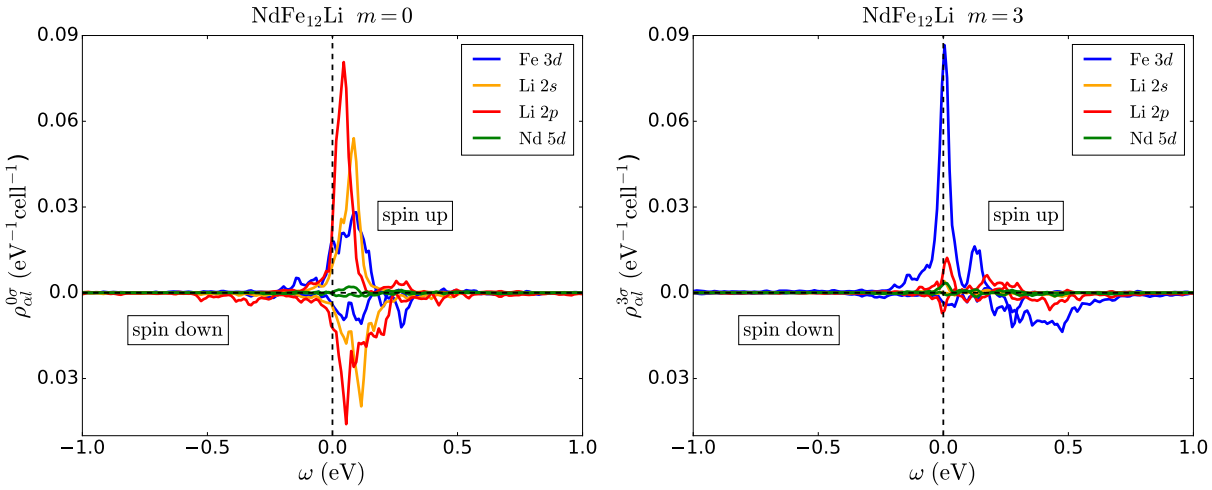

Figure 9.11 – a) Projected spectral functions $\rho^{0\sigma}_{\alpha l}(\omega)$ for the $4f$ orbital with m =0 in $NdFe_{12}Li$, where the atom α and shell l are given in the legend. The magnitude $\rho^{m\sigma}_{\alpha l}(\omega)$ indicates the amount of admixture of the character αl into a given $4f$ orbital, for its precise formulation see Appendix C. b) The same for the $4f$ orbital m =3.

of rare-earth $4f$ states with Fe $3d$, N $2p$ and Li $2s$ bands. The real-space Wannier functions of Fig. 9.10 thus represent a convenient visualization of hybridization between rare-earth and other orbitals. In order to quantify the amount of this admixture of the conduction band states we also expand those extended small-window Wannier orbitals $|w^{\sigma}_{m}(\mathbf{k})\rangle$ in the basis of localized Wannier functions $|\tilde{w}^{\alpha\sigma'}_{lm'}(\mathbf{k})\rangle$ (labeled by spin σ', orbital l and magnetic m' quantum numbers, as well as atomic site α) constructed within a large energy window for all relevant bands. We derive the corresponding projection operators relating $|w^{\sigma}_{m}(\mathbf{k})\rangle$ and $|\tilde{w}^{\alpha\sigma'}_{lm'}(\mathbf{k})\rangle$ in Appendix C. We employ it to extract the corresponding contribution $\tilde{\rho}^{m'\sigma}_{\alpha l}(\omega)$ of the shell l (with $l \neq 4f$) on the site α into the spectral function of the "small-window" $4f$ orbital with indices σm.

The comparison of $\rho^{m\sigma}_{\alpha l}$ for the orbital $m = 0$ and $m = 3$ are shown in Figs. 9.12 and 9.11 for $NdFe_{12}Li$ and $NdFe_{12}N$, respectively. One may notice in Fig.9.11(a) that Nd f_{z^3} ($m = 0$) in $NdFe_{12}Li$ exhibits a strong hybridization with Li $2s$ and $2p$; their contribution is significantly larger than the admixture of Fe $3d$ states. We further observe that spin up states are hybridizing more strongly than spin down states.

In contrast, in the same compound for $m = 3$ (Fig.9.11(b)), there is a peak of hybridization with Fe states but barely any with the Li $2s$ and $2p$ ones. The same difference, but much less pronounced, is noticeable in the case of $NdFe_{12}N$, see Fig.9.12. Hence, one may conclude that the effect of the hybridization with the interstitial on the CF is much larger for Li than for N. In the latter case the electrostatic shift due to the negative charge on N seems to play the leading role.

9.6 Importance of the charge averaging

In this section, we explicitly demonstrate the effect of averaging of $4f$ charge density (eq. 9.10) by comparing the CFP calculated with and without this averaging (but in both cases the $4f$ magnetic density is suppressed following Eq. 9.12) in two materials, $NdFe_{12}N$ and $SmCo_5$, that are known to have an out-of-plane magnetic anisotropy.

The corresponding values are displayed in Table 9.5. One sees that the difference is largest for the lowest-order CFP $A^0_2\langle r^2\rangle$, where calculations without averaging lead to the wrong sign with respect to experiment (suggesting in-plane anisotropy in both cases). Hence, the proper averaging of $4f$ charge

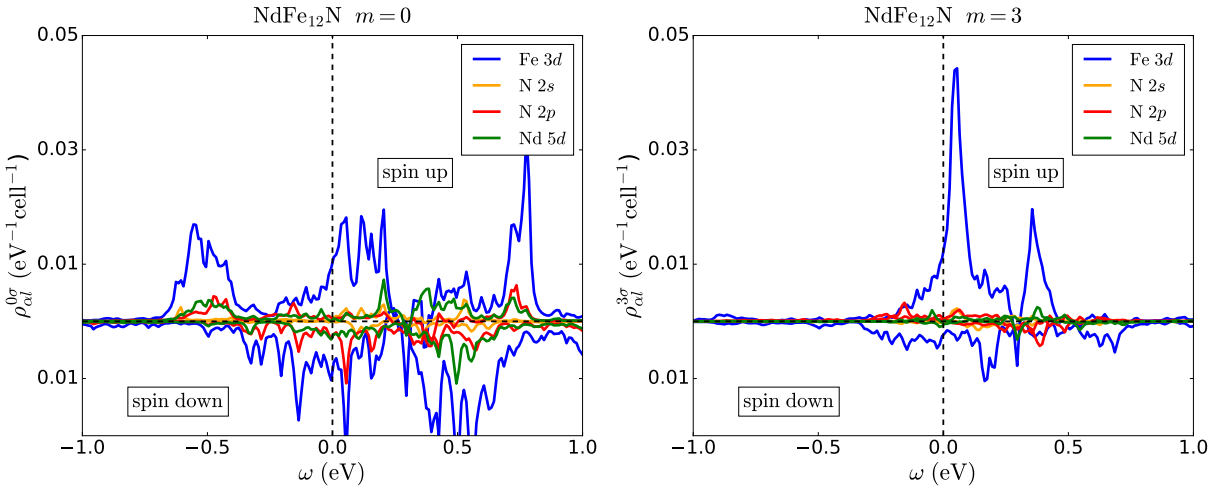

Figure 9.12 – a) Projected spectral functions $\rho^{0\sigma}_{\alpha l}(\omega)$ for the $4f$ orbital with m =0 in $NdFe_{12}N$. For the notation see caption of Fig. 9.11. b) The same for the $4f$ orbital m =3, $\rho^{3\sigma}_{\alpha l}(\omega)$

Table 9.5 – crystal-field parameters and exchange field in $NdFe_{12}N$ and $SmCo_5$ in the ferromagnetic phase, calculated with and without averaging over the ground state multiplet.

	$NdFe_{12}N$				$SmCo_5$			
	with		without		with		without	
	↑	↓	↑	↓	↑	↓	↑	↓
$A^0_2\langle r^2\rangle$	477	653	-190	26	-313	-262	278	331
$A^0_4\langle r^4\rangle$	75	112	30	82	-40	-55	-30	-37
$A^4_4\langle r^4\rangle$	-105	-141	-65	-124	0	-0	0	0
$A^0_6\langle r^6\rangle$	32	63	27	64	35	25	38	25
$A^4_6\langle r^6\rangle$	-65	-91	-61	-112	0	0	0	0
$A^6_6\langle r^6\rangle$	0	-0	0	0	-731	-593	-945	-806
$B_{\rm ex}$ (T)	217		206		227		235	

density is crucial for a correct description of the single-ion anisotropy. For the higher order terms the difference between two approaches is smaller. This suggests that the self-interaction contribution in the CFP has predominantly $l = 2$ symmetry.

9.7 Crystal-field parameters from Density Functional Theory + Hubbard I approximation: sensitivity to the parameters

In this last section, we discuss the importance of the calculation parameters, namely the Coulomb parameters U and J_H and the window size $\omega_{\rm win}$.

9.7.1 Dependence of the results on Coulomb U and Hund's J_H

To perform DFT+DMFT calculations, we have to choose a value for the on-site screened Coulomb interaction parameter U and for the Hund's coupling parameter J_H. Several methods have been developed

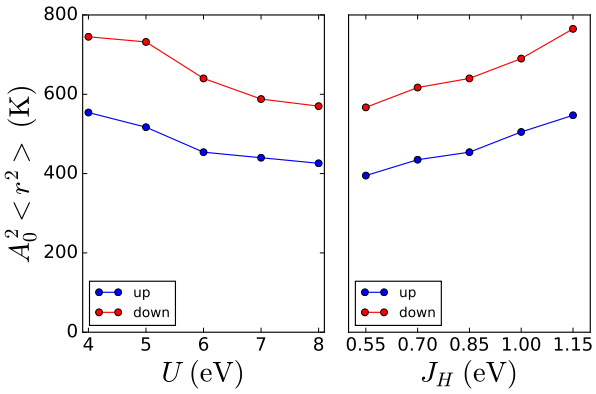

Figure 9.13 – CFP $A_2^0\langle r^2\rangle$ in $NdFe_{12}N$ as a function of U for $J_H = 0.85$ eV (left-hand panel), and as a function of J_H for $U = 6$ eV (right-hand panel). Our reference values are ($U = 6$ eV, $J_H = 0.85$ eV).

in order to compute those parameters from first principles, most notably the constrained local density approximation[112] and, more recently, the constrained random phase approximation[116].

In the present work, however, we do not attempt a first principles determination. We use $U = 6$ eV and $J_H = 0.85$ eV because these values have given satisfactory results in other calculations on rare-earth materials[107, 108]. They are also in line with reported values calculated from first principles[356]. Nevertheless, it is preferable that results obtained by our calculation scheme do not depend too strongly on the value of U and J_H. In Fig. 9.13, we show that the dependence of the CFP $A_2^0\langle r^2\rangle$ in $NdFe_{12}N$ is very moderate, as long as values reasonably close to our reference values are used.

Furthermore, we observe that smaller values of U lead to slightly larger values of $A_2^0\langle r^2\rangle$: this is not surprising if we keep in mind that a large U is favorable to a strong localization of the $4f$ electrons, hence to a weaker coupling to the crystal-field. Conversely, a small J_H favors a stronger orbital polarization and more localized character, and leads to smaller CFP.

9.7.2 Dependence of the results on the window size

Another important parameter of our calculations is the size of the window around the Fermi level that we use to construct the $4f$ Wannier functions. In Fig. 9.14 we compare the Wannier orbitals constructed for the same orbital $m = 0$ in $NdFe_{12}Li$ for two different window sizes: a small window with $\omega_{\text{win}} = 2$ eV, and a large one with $\omega_{\text{win}} = 20$ eV. For the large window, the Wannier orbital (WO) takes essentially pure Nd $4f$ orbital character, while the small-window WO leaks significantly to neighboring sites, in particular, to Li.

The effect of the window size on the CF parameters is shown more quantitatively in Fig. 9.15, which displays those parameters computed for several window choices $[-\omega_{\text{win}}, \omega_{\text{win}}]$ for different materials. The smallest window size of ω_{win} =2 eV is required to enclose all the $4f$-like bands, increasing it to 4 eV includes most of the Fe states and part of the N or Li states inside the window. The largest size of 20 eV gives Wannier functions with essentially pure orbital character. One may notice a relatively mild dependence of the CFP on the choice of the window up to ω_{win} =8 eV.

9.8 Conclusion

In conclusion, we propose a novel first-principles approach for calculating crystal and exchange fields in rare-earth systems. This approach is formulated within the DFT+DMFT framework with local correla-

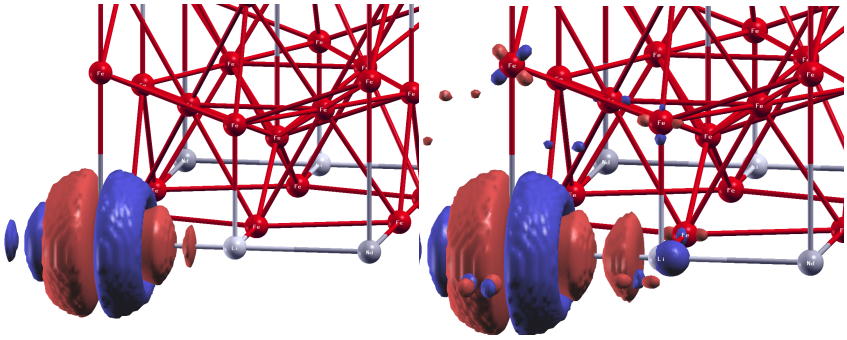

(a) $[-20, 20]$ eV window (b) $[-2, 2]$ eV window

Figure 9.14 – $NdFe_{12}Li$ $4f$ Wannier orbital $m = 0$ constructed with a large window $[-20, 20]$ eV (left) and a small window $[-2, 2]$ eV (right). The use of a large window essentially removes all hybridization between the rare-earth and neighboring atoms.

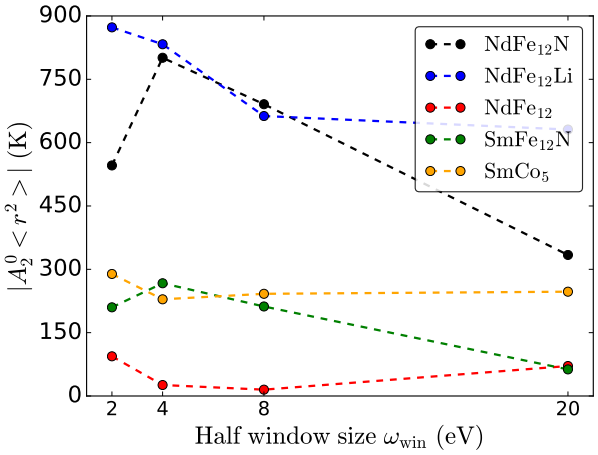

Figure 9.15 – CFP $A_2^0\langle r^2\rangle$ as a function of window size ω_{win} for $NdFe_{12}$, $NdFe_{12}N$ and $NdFe_{12}Li$

tions on the rare-earth $4f$ shell treated within the quasi-atomic Hubbard-I approximation. The $4f$ states are represented by Wannier functions constructed from a narrow energy range of Kohn-Sham states of mainly $4f$ character. We employ a charge-density averaging that suppresses the contribution due to the self-interaction of the $4f$ orbitals to the one-electron Kohn-Sham potential. We thus reduce the effect of this unphysical self-interaction from the crystal-field splitting, while keeping non-spherical contributions to CFP from other bands. Similarly, by removing the contribution due to the $4f$ magnetic density from the exchange-correlation potential we suppress its unphysical contribution to the exchange field at the rare-earth site.

Our *ab initio* scheme reproduces the measured crystal-field parameters in the well-known hard magnet $SmCo_5$. We subsequently applied it to prospective rare-earth hard magnetic intermetallics of the $RFe_{12}X$ family (where R =Nd, Sm and X can be N, Li or vacancy). Our calculations reproduce the strong out-of-plane anisotropy of $NdFe_{12}N$ due to a large positive value of the key CFP $A_2^0\langle r^2\rangle$ induced by insertion of N. Interestingly, we find that interstitial Li has a strong opposite effect, leading to a large negative value of $A_2^0\langle r^2\rangle$. We thus predict a strong out-of-plane anisotropy in the hypothetical compound $SmFe_{12}Li$. We also find the anisotropy in $SmFe_{12}Li$ to persist to higher temperatures as compared to $NdFe_{12}N$. Hence, Sm-based compounds may represent interesting candidates for hard-magnetic applications. Of course, the thermodynamic stability of $SmFe_{12}Li$ and technological feasibility of Li doping still need to be demonstrated by future studies.

We analyzed the effect of N and Li interstitials on $A_2^0\langle r^2\rangle$ by evaluating the Bader charges as well as by studying the leakage of $4f$ Wannier orbitals to interstitial sites and quantifying the $4f$ hybridization with N $2p$ and Li $2s$ states. This analysis demonstrates the importance of hybridization effects when computing CFP.

Extensions of the present approach beyond the Hubbard-I approximation are promising for applications to other rare-earth intermetallics. In particular, a similar DFT+DMFT technique suppressing subtle self-interaction and double-counting contributions to the Kohn-Sham potential might be necessary to study, for example, the impact of a spin-polarized transition-metal sub-lattice on heavy-fermion behavior in Yb-based intermetallics[361, 362]. In Ce-based compounds, too, extensions beyond Hubbard I may be required, since Ce $4f$ electrons tend to have more itinerant character than in rare-earths closer to half-filling.

Chapter 10

Conclusions and Outlook

This thesis has dealt with the problem of calculating the electronic structure of correlated materials. The emphasis has been on "realistic material" calculations from first principles, rather than simple model Hamiltonians like variations of the Hubbard model. This is not to underestimate the usefulness and power of model calculations: model Hamiltonians are and will certainly remain an indispensable tool of solid state physics.

Over the last few years, the number of publicly available software libraries or codes for combining "all electron" electronic structure calculations (such as Density Functional Theory (DFT) or many-body perturbation theory) with more powerful many-body theories going beyond the band picture or perturbation theory (in particular Dynamical Mean-Field Theory, or DMFT) has been steadily increasing. We believe this has significantly lowered the threshold for using such methods, making them more mainstream to study from first principles materials that are known to push DFT to its limits. This development is all the better, for if the second half of the previous century has been dubbed the "age of silicon", we are probably entering the age of oxides (for all its promises, the age of graphene is not quite here yet). Oxides, in turn, are precisely an important class of materials where strong electronic correlations are possible (at least, those that are not natural band insulators).

Though they are becoming more routine, calculations coupling electronic structure codes and many-body techniques (like DFT+DMFT) remain challenging, both from a conceptual and practical point of view. Conceptually, the art of defining low-energy models that consistently integrate out the high-energy dynamics and the motion of valence and core electrons, crudely introduced with the first DFT+U calculations, is still in the process of being refined, and indeed probably still has much way to go. To cite but a few examples, the problems of band alignments (or relative positions of orbitals treated within DMFT), the related problem of the double-counting of interactions, the screened Coulomb interactions (and dynamics thereof), non-local interactions and correlations are still difficult ones. The conceptually more exact methods, like GW + extended DMFT (GW+EDMFT), are still a long way from being used routinely on many-orbital systems, at least without simplifying approximations. From a more practical point of view, DFT+DMFT (or similar) calculations are still not always performed "from first principles". Methods have been devised to estimate the parameters, such as the Coulomb interaction parameter U or Hund's coupling J_H, from *ab initio* electronic structure calculations. Nevertheless, such calculations still require more physical insight from the physicist and fine-tuning of parameters than simple DFT calculations.

In the present manuscript, we have first given an introduction to electronic structure theories, to many-body techniques for strongly interacting electrons, and more importantly to methods that combine both approaches.

In the second part, we have studied from a methodological point of view a simplification to the GW+EDMFT method, dubbed Screened Exchange+DMFT, that contains non-local screened Fock exchange and dynamical local Coulomb interactions in the impurity model. We discuss this as an extension

of a screened exchange generalized Kohn-Sham scheme, and analyse what happens in the limit of a full d shell, where the correlation effects usually obtained in DMFT are expected to be small. We find that the inclusion of non-local exchange partly corrects the position of the filled d states, probably by reducing the self-interaction error. Band renormalization effects due to dynamical screening, present in the GW approximation, are also found to be important. It would be interesting to continue benchmarking the Screened Exchange+DMFT techniques on different materials: oxides, metals, strongly correlated or not. It would also be useful to go beyond using a Yukawa potential to calculate the Screened Exchange part, and to investigate more general static screened Coulomb potentials, computed in the random phase approximation.

In the third and last part of this thesis, we have studied from first principles three types of materials of technological interest.

First, we used charge self-consistent DFT+DMFT calculations within supercells to evaluate the formation energy of monovacancies in paramagnetic α-Fe. We directly calculated the vacancy formation energy in this phase that is poorly described by standard DFT but is well captured within DFT+DMFT and in which the measurements are possible. Being the high-temperature phase, it is also the phase where vacancies are more likely to be present, and where the experimental estimates for their concentrations are the most reliable. Monovacancies are the simplest of point defects, so a next step would be to use a similar method to study more complex properties of point defects: for instance the formation energy of bivacancies, or the migration energy of monovacancies. Doing so may require additional simplifications in the scheme. In the case of monovacancies, it was found that the self-energy on atoms further from the vacancy than the second nearest neighbors was almost equal to the one in the perfect lattice. Hence it is probably not necessary to treat independently all the atoms that are nominally inequivalent in the supercell, potentially reducing the computational cost.

Next, we have studied the metal to insulator transition in the metastable B phase of VO_2. We found that during this transition, where half the V atoms present in the cell form dimers in the low-temperature phase, two effects contribute to the metal to insulator transition. The dimerized V atoms form a bonding state lowered in energy by the on-site Coulomb interaction, leading to a band insulator-like behavior. The remaining V atoms, that are expected to have metallic behavior within DFT, but have reduced hopping possibilities at the Fermi level due to the dimerization of their neighbors, undergo a standard Mott transition. The phase transition of VO_2 (B) is, in that sense, similar to the rutile to M_2 transition that is observed under uniaxial pressure or Cr doping. Motivated by recent experimental findings about oxygen vacancies in VO_2 and about the contribution of oxygen vacancies to the spectral properties of $SrVO_3$, we study within DFT some properties of oxygen vacancies in VO_2. We find that, out of the possible inequivalent positions where an oxygen vacancy can form in VO_2 (B), the preferred ones are located along the c axis. When such a vacancy is created, the e_g state that most hybridizes with the oxygen states on that site is pulled down in energy, forming a localized state with about 1 eV binding energy. With experimental data available so far on VO_2 (B), it is difficult to confirm or rule out the presence of such vacancies.

Finally, we have devised a scheme allowing to calculate the crystal field parameters in rare earth compounds with a precision of a few meV. Our method combines DFT with an atomic (or Hubbard I) approximation to DMFT,which describes the electronic density of the $4f$ shell better than standard DFT with local or semi-local functionals. Enforcing equal occupancy of the states within the ground state $4f$ multiplet, which is equivalent to using a modified double-counting correction, allows us to enforce a spherically symmetric $4f$ partial charge density, thus avoiding a well-known self-interaction error in the crystal field Hamiltonian. Our method is able, to a certain extent, to capture hybridization effects in contrast with most methods designed so far, where the $4f$ electrons are treated like core states in DFT. We benchmark this scheme on the well-known hard magnet compound $SmCo_5$ and then study some properties of the $R\mathrm{Fe}_{12}X$ intermetallics, where R is a rare earth atom (here, Nd or Sm) and X an empty site or a dopant. We study the cases X = N and the more hypothetical X = Li, in order to better understand how the electron-count of the light atom influences the crystal field on the rare earth. This work is aimed to contribute to an ongoing research effort for finding better (or leaner) hard magnetic materials. From a methodological point of view, it would be interesting to confirm the heuristic

observation that Wannier functions constructed in a small energy window, hence not too localized, lead to the best predictions of crystal field parameters.

Appendices

Appendix A

Conventions

A.1 Notations

A.1.1 Time and space variables

- t denotes the real time variable and τ denotes the imaginary time variable
- β denotes the inverse temperature, $\beta = \dfrac{1}{k_{\mathrm{B}}T}$
- $\mathbf{r}$ denotes a (vector) space variable
- $\mathbf{k}$ denotes a (vector) momentum or crystal momentum variable
- ω denotes the real-axis frequency variable
- $i\omega_n = i\dfrac{(2n+1)\pi}{\beta}$ denotes a fermionic imaginary-axis (or Matsubara) frequency
- $i\Omega_n = i\dfrac{2n\pi}{\beta}$ denotes a bosonic imaginary-axis (or Matsubara) frequency

A.1.2 Operators and others

- H denotes a Hamiltonian
- $\mathcal{S}$ or S denotes an action
- Ψ denotes a many-body wave function
- ψ denotes a one-particle wave function
- In a Hamiltonian, $c^\dagger$ and c denote respectively a second-quantization creation and annihilation operator
- In an action, $c^\dagger$ and c denote conjugate Grassmann variables
- $A[B]$ means a quantity A is a functional of B
- σ denotes an electron spin ($\uparrow$ or $\downarrow$), and $\bar{\sigma}$ the opposite spin of σ

A.1.3 Units

- Except in the introductory chapter 1, we use a unit system where $\hbar = m_e = e^2 = 4\pi\varepsilon_0 = 1$
- All units are in electron-volts (eV)

A.2 Fourier transformations

A.2.1 Time-frequency domain

The direct and inverse Fourier transforms in real time and frequency are defined by

$$\begin{aligned} f(\omega) &= \int_{-\infty}^{+\infty} dt e^{i\omega t} f(t) \\ f(t) &= \int_{-\infty}^{+\infty} d\omega e^{-i\omega t} f(\omega) \end{aligned} \tag{A.1}$$

For an imaginary time β-periodic or β-antiperiodic function $f(\tau)$ and its corresponding Matsubara representation $f(i\omega_n)$, where $i\omega_n$ is a fermionic *or* a bosonic Matsubara frequency:

$$\begin{aligned} f(i\omega_n) &= \int_0^{\beta} d\tau e^{i\omega_n \tau} f(\tau) \\ f(\tau) &= \frac{1}{\beta} \sum_{-\infty}^{\infty} e^{-i\omega_n \tau} f(i\omega_n) \end{aligned} \tag{A.2}$$

A.2.2 Space-momentum domain

In the continuum, in a crystal of volume Ω with a periodic potential, the Fourier transform is defined as

$$\begin{aligned} f(\mathbf{k} + \boldsymbol{G}) &= \int_{\Omega} f(\mathbf{r}) e^{-i(\mathbf{k}+\boldsymbol{G}).\mathbf{r}} \\ f(\mathbf{r}) &= \frac{1}{\Omega} \sum_{\mathbf{k},\boldsymbol{G}} f(\mathbf{k} + \boldsymbol{G}) e^{i(\mathbf{k}+\boldsymbol{G}).\mathbf{r}} \end{aligned} \tag{A.3}$$

where $\boldsymbol{G}$ is a vector of the reciprocal lattice and $\mathbf{k}$ belongs to the first Brillouin zone.

Appendix B

Green's functions

B.1 Definitions

Here, we remind the reader of a few useful formulas regarding Green's functions. For a more complete description, see for instance the textbook on many-body physics by Bruus and Flensberg[363]. The Green's function of a many-body system is a propagator, encoding the probability of finding at time t_2 and point $\mathbf{r}_2$ a particle created at time t_1 and point $\mathbf{r}_1$.

B.1.1 Real-time Green's functions

The real-time retarded Green's function is defined as

$$G^R(\mathbf{r}\sigma t, \mathbf{r}'\sigma' t') = -\theta(t'-t)\langle[\Psi(\mathbf{r}\sigma t), \Psi^\dagger(\mathbf{r}'\sigma' t')]_\pm\rangle \tag{B.1}$$

where $\Psi^\dagger(\mathbf{r}\sigma t)r$ and $\Psi(\mathbf{r}\sigma t)$ are the particle creation and annihilation operators in the continuum, and $[A,B]_\pm$ denotes the commutator or anti-commutator for bosonic or fermionic quantities A and B, respectively. $\theta(t)$ is the Heavyside step function, equal to 0 when $t<0$ and 1 when $t\geq 0$. $\langle A\rangle$ denotes the average value of a quantity A, computed using the full Hamiltonian of the system.

The Fourier transform of $G^R(\mathbf{r}\sigma t, \mathbf{r}'\sigma' t')$ is $G^R(\mathbf{k}\sigma\omega, \mathbf{k}'\sigma'\omega')$. For a system invariant by translation in space and time variables, and without spin-flip terms in the many-body Hamiltonian, this can simply be written $G^R(\mathbf{k},\sigma,\omega)$.

By introducing a complete set of states $\sum_n |n\rangle\langle n| = \mathrm{Id}$ into Eq. B.1, we obtain the Lehmann representation:

$$G^R(\mathbf{k},\omega) = \frac{1}{Z}\sum_{nn'} \frac{\langle n|c_\mathbf{k}|n'\rangle\langle n'|c_\mathbf{k}^\dagger|n\rangle}{\omega + E_n - E_{n'} + i\eta}(e^{-\beta E_n} + e^{-\beta E_{n'}}) \tag{B.2}$$

where $i\eta$ is an infinitesimal imaginary shift and Z the partition function of the system with N particles. In particular at zero temperature, either n or n' must be the ground state of the system, so that

$$\begin{aligned} G^R(\mathbf{k},\omega) = &\sum_{A^{(N+1)}} \frac{\langle\Psi_0|c_\mathbf{k}|\Psi_A^{N+1}\rangle\langle\Psi_A^{N+1}|c_\mathbf{k}^\dagger|\Psi_0\rangle}{\omega + (E_A^{N+1} - E_0) + i\eta} \\ &+ \sum_{B^{(N-1)}} \frac{\langle\Psi_B^{N-1}|c_\mathbf{k}|\Psi_0\rangle\langle\Psi_0|c_\mathbf{k}^\dagger|\Psi_B^{N-1}\rangle}{\omega + (E_0 - E_B^{N-1}) + i\eta} \end{aligned} \tag{B.3}$$

where Ψ_A^{N+1} is a many-body eigenstate with $N-1$ particles, Ψ_B^{N-1} is a many-body eigenstate with $N-1$ particles and Ψ_0 is the ground state wave function (with N particles).

The spectral function is defined by

$$A(\mathbf{k},\omega) = -\frac{1}{\pi}\mathrm{Im}G(\mathbf{k},\omega) \tag{B.4}$$

Since the imaginary part of $1/(\omega+i\eta)$ is $-\pi\delta(\omega)$, taking the spectral function derived from Eq. B.3 gives a sum of delta peaks corresponding to one-particle addition (positive ω) or removal (negative ω), with amplitudes given by the matrix elements.

B.1.2 Matsubara Green's functions

The Matsubara (or imaginary time / frequency) Green's function is convenient for calculations at finite temperature. The expression of the Matsubara Green's function is similar to that of Eq. B.1:

$$G^R(\mathbf{r}\sigma\tau,\mathbf{r}'\sigma'\tau') = -\langle\mathcal{T}\Psi(\mathbf{r}\sigma\tau),\Psi^\dagger(\mathbf{r}'\sigma'\tau')\rangle \tag{B.5}$$

where $\mathcal{T}$ is the imaginary time-ordering operator, that orders later times to the left. The corresponding Lehmann representation is

$$G^R(\mathbf{k},i\omega_n) = \frac{1}{Z}\sum_{nn'}\frac{\langle n|c_\mathbf{k}|n'\rangle\langle n'|c_\mathbf{k}^\dagger|n\rangle}{i\omega_n+E_n-E_{n'}}(e^{-\beta E_n}+e^{-\beta E_{n'}}) \tag{B.6}$$

B.2 The self-energy

For a one-particle Hamiltonian $H_0(\mathbf{k})$, the expression of the Green's function is simply obtained as

$$G_0(\mathbf{k},i\omega_n) = [i\omega_n - H_0(\mathbf{k})]^{-1} \tag{B.7}$$

(and analogously for the real-frequency Green's function)

If an additional many-body term is present in the Hamiltonian, a self-energy $\Sigma(\mathbf{k},i\omega_n)$, that behaves like a dynamical potential, can be introduced that encodes the effect of correlations in the system:

$$\begin{aligned} G(\mathbf{k},i\omega_n) &= [i\omega_n - H_0(\mathbf{k}) - \Sigma(\mathbf{k},i\omega_n)]^{-1} \\ &= [G_0(\mathbf{k},i\omega_n)^{-1} - \Sigma(\mathbf{k},i\omega_n)]^{-1} \end{aligned} \tag{B.8}$$

This is one of several ways to write the famous Dyson equation. Another usual form is

$$\begin{aligned} G &= G_0 + G_0\Sigma G_0 + G_0\Sigma G_0\Sigma G_0 + ... \\ &= G_0 + G_0\Sigma(G_0 + G_0\Sigma G_0 + ...) \\ G &= G_0 + G_0\Sigma G \end{aligned} \tag{B.9}$$

Appendix C

Projection of extended Wannier orbitals to localized Wannier basis

In this appendix, we derive the projection operator between localized and extended Wannier spaces used in chapter 9, section 9.5. Consistently with that chapter, we consider here the case of correlated $4f$ orbitals treated within DFT+DMFT. This is simply in order to simplify the notations: the same relations hold for Wannier functions with different orbital character. This derivation can be seen as an extension of the ideas developed in section 4.1.1 and Ref. [80] about the DFT+DMFT projection scheme.

A set of Wannier-like functions $|\tilde{w}^{\alpha\sigma}_{lm}(\mathbf{k})\rangle$ is constructed for an atom α of the unit cell and quantum numbers $(lm\sigma)$ as a combinations of Kohn-Sham Bloch waves for a range of bands within the chosen energy window $\tilde{\mathcal{W}}$:

$$|\tilde{w}^{\alpha\sigma}_{lm}(\mathbf{k})\rangle = \sum_{\nu\in\tilde{\mathcal{W}}} \tilde{P}^{\alpha\sigma}_{lm\nu}(\mathbf{k})|\phi^{k}_{\nu}\rangle \tag{C.1}$$

where ϕ^{k}_{ν} are the Bloch functions and $\tilde{P}^{\alpha\sigma}_{lm\nu}(\mathbf{k})$ is the corresponding matrix element of the projector constructed as described in Refs. [79, 80]. The corresponding real-space Wannier functions are then obtained by a Fourier transformation

$$\tilde{w}^{\alpha\sigma}_{lm}(\mathbf{r}) = \sum_{\mathbf{k}} e^{-i\mathbf{k}.\mathbf{r}}|\tilde{w}^{\alpha\sigma}_{lm}(\mathbf{k})\rangle \tag{C.2}$$

We assume that the window $\tilde{\mathcal{W}}$ in (C.1) is *large*, i.e. that it includes both rare earth $4f$ states and all relevant valence bands that are expected to hybridize with them. In result, with such a large-window construction one obtains a set of mutually-orthogonal and rather well localized Wannier orbtials (WO). In particular, the large-window $4f$ WOs $\tilde{w}^{\alpha\sigma}_{lm}(\mathbf{r})$ almost do not leak onto neighboring sites, as discussed in the previous section, see Fig. 9.14(a). If one constructs as many WOs as the number of Kohn-Sham bands within $\tilde{\mathcal{W}}$ then the projection operator $\tilde{P}(\mathbf{k})$ is just a unitary transformation, hence, (C.1) can be inverted

$$|\phi^{k}_{\nu}\rangle \approx \sum_{\alpha\sigma lm} \left[\tilde{P}^{\alpha\sigma}_{lm\nu}(\mathbf{k})\right]^{*} |\tilde{w}^{\alpha\sigma}_{lm}(\mathbf{k})\rangle \tag{C.3}$$

where the equality is approximate because high-energy empty bands usually cross and, hence, one cannot generally chose such a window as to have the same number of bands for all $\mathbf{k}$-points. However, those high-energy states are far from the relevant region close to the Fermi level, and if one applies (C.3) to the bands within a *small* window $\mathcal{W}$ around the the Fermi energy the resulting small non-unitarity of $P(\mathbf{k})$ can be neglected.

Alternatively, one may construct $4f$ Wannier orbitals from the bands within that small window $\mathcal{W}$

enclosing mainly $4f$-like Kohn-Sham bands:

$$|w_m^\sigma(\mathbf{k})\rangle = \sum_{\nu\in\mathcal{W}} P_{m\nu}^\sigma(\mathbf{k})|\phi_\nu^k\rangle \tag{C.4}$$

where $4f$ WOs are constructed for the single rare earth site in the unit cell for the compounds under consideration. Hence, the site and l labels are suppressed in $|w_m^\sigma(\mathbf{k})\rangle$. The resulting small-window WOs are rather extended in real space, as one sees in Figs. 9.10 and 9.14(b).

Inserting the expansion (C.3) of the KS states $|\phi_\nu^k\rangle$ into (C.4) one obtains

$$\begin{aligned} |w_m^\sigma(\mathbf{k})\rangle &= \sum_{\nu\in \mathrm{W}} \sum_{lm'\sigma'} P_{m\nu}^\sigma(\mathbf{k}) \left[\tilde{P}_{lm'\nu}^{\alpha\sigma'}(\mathbf{k})\right]^* \tilde{w}_{lm'}^{\alpha\sigma'}(\mathbf{k})\rangle \\ &= \sum_{\alpha\sigma' lm'} U_{m,lm'}^{\sigma,\alpha\sigma'}(\mathbf{k})\tilde{w}_{lm'}^{\alpha\sigma'}(\mathbf{k})\rangle \end{aligned} \tag{C.5}$$

where

$$U_{m,l'm'}^{\sigma,\alpha\sigma'}(\mathbf{k}) = \sum_{\nu\in\mathcal{W}} P_{m\nu}^\sigma(\mathbf{k}) \left[\tilde{P}_{lm'\nu}^{\alpha\sigma'}(\mathbf{k})\right]^* \tag{C.6}$$

We use these projectors $U_{m,l'm'}^{\sigma,\alpha\sigma'}(\mathbf{k})$ to project the $4f$ spectral function computed in the small-window WO basis on large-window localized WOs representing the other valence and conduction states.Namely, having obtained the real-axis lattice Green's function in the small-window Wannier basis for the orbital (σm) of the $4f$ shell, $G_{m\sigma}(\mathbf{k},\omega+i\delta)$, as well as the corresponding partial spectral function $\rho_{m\sigma}(\omega) = -\frac{1}{\pi}\mathrm{Im}G_{m\sigma}(\mathbf{k},\omega+i\delta)$, we compute the different orbital contributions into it as follows:

$$\tilde{\rho}_{\alpha l}^{m\sigma}(\omega) = -\frac{1}{\pi}\mathrm{Im}\sum_k \sum_{m'\sigma'} \left[U_{m,lm'}^{\sigma,\alpha\sigma'}(\mathbf{k})\right]^* \times G_{m\sigma}(\mathbf{k},\omega+i\delta)U_{m,lm'}^{\sigma,\alpha\sigma'}(\mathbf{k}) \tag{C.7}$$

where $\tilde{\rho}_{\alpha l}^{m\sigma}(\omega)$ is the fraction of the $4f$ spectral function of orbital index (σm) with the character (αl). Using (C.3) and the orthonormality of small-window WOs

$$\langle w_m^\sigma(\mathbf{k})|w_{m'}^{\sigma'}(\mathbf{k})\rangle = \delta_{mm'}\delta_{\sigma\sigma'} = \sum_\nu \left[P_{m\nu}^\sigma(\mathbf{k})\right]^* P_{m'\nu}^{\sigma'}(\mathbf{k})$$

one may easily show the completeness of the expansion (C.7)

$$\sum_{\alpha l} \tilde{\rho}_{\alpha l}^{m\sigma}(\omega) = \rho_{m\sigma}(\omega)$$

Bibliography

[1] J. Bardeen, L. N. Cooper, and J. R. Schrieffer. "Theory of superconductivity". In: *Physical Review* 108 (5 1957), pp. 1175–1204.

[2] I Leonov, A. Poteryaev, Y. N. Gornostyrev, A. Lichtenstein, M. Katsnelson, V. Anisimov, and D Vollhardt. "Electronic correlations determine the phase stability of iron up to the melting temperature". In: *Scientific reports* 4 (2014).

[3] E. C. Stoner. "Collective electron ferromagnetism". In: *Proceedings of the Royal Society of London A: Mathematical, Physical and Engineering Sciences* 165.922 (1938), pp. 372–414.

[4] C. Kittel. *Introduction to solid state*. Vol. 162. John Wiley & Sons, 1966.

[5] N. W. Ashcroft and N. D. Mermin. "Solid state physics". In: (1976).

[6] P. Nozières and D. Pines. *The theory of quantum liquids*. Perseus, 1999.

[7] P. Coleman. "Many body physics: unfinished revolution". In: *Annales henri poincaré*. Vol. 4. Springer. 2003, pp. 559–580.

[8] L. Landau. "The theory of a Fermi liquid". In: *Soviet Physics JETP-USSR* 3.6 (1957), pp. 920–925.

[9] M. Imada, A. Fujimori, and Y. Tokura. "Metal-insulator transitions". In: *Reviews of Modern Physics* 70.4 (1998), p. 1039.

[10] D. R. Hartree. "The wave mechanics of an atom with a non-Coulomb central field. Part I. theory and methods". In: *Mathematical Proceedings of the Cambridge Philosophical Society* 24.1 (1928), pp. 89–110.

[11] D. R. Hartree. "The wave mechanics of an atom with a non-coulomb central field. Part II. some results and discussion". In: *Mathematical Proceedings of the Cambridge Philosophical Society* 24.1 (1928), pp. 111–132.

[12] V. Fock. "Näherungsmethode zur Lösung des quantenmechanischen Mehrkörperproblems". In: *Zeitschrift für Physik* 61.1 (1930), pp. 126–148.

[13] J. C. Slater. "Note on Hartree's method". In: *Physical Review* 35 (2 1930), pp. 210–211.

[14] P. Hohenberg and W. Kohn. "Inhomogeneous electron gas". In: *Physical Review* 136.3B (1964), B864.

[15] R. O. Jones and O. Gunnarsson. "The density functional formalism, its applications and prospects". In: *Reviews of Modern Physics* 61.3 (1989), p. 689.

[16] E. K. Gross and R. M. Dreizler. *Density functional theory*. Vol. 337. Springer Science & Business Media, 2013.

[17] R. O. Jones. "Density functional theory: its origins, rise to prominence, and future". In: *Reviews of modern physics* 87.3 (2015), p. 897.

[18] W. Kohn and L. J. Sham. "Self-consistent equations including exchange and correlation effects". In: *Physical Review* 140.4A (1965), A1133.

[19] D. M. Ceperley and B. J. Alder. "Ground state of the electron gas by a stochastic method". In: *Physical Review Letters* 45 (7 1980), pp. 566–569.

[20] J. P. Perdew. "Density-functional approximation for the correlation energy of the inhomogeneous electron gas". In: *Physical Review B* 33.12 (1986), p. 8822.

[21] A. D. Becke. "Density-functional exchange-energy approximation with correct asymptotic behavior". In: *Physical Review A* 38 (6 1988), pp. 3098–3100.

[22] J. P. Perdew, J. A. Chevary, S. H. Vosko, K. A. Jackson, M. R. Pederson, D. J. Singh, and C. Fiolhais. "Atoms, molecules, solids, and surfaces: applications of the generalized gradient approximation for exchange and correlation". In: *Physical Review B* 46 (11 1992), pp. 6671–6687.

[23] J. P. Perdew, K. Burke, and M. Ernzerhof. "Generalized gradient approximation made simple". In: *Physical Review Letters* 77 (18 1996), pp. 3865–3868.

[24] A. D. Becke. "A new mixing of Hartree–Fock and local density-functional theories". In: *The Journal of chemical physics* 98.2 (1993), pp. 1372–1377.

[25] D. Singh and L Nordstrom. *Planewaves, pseudopotentials and the LAPW method*. 1994.

[26] O. K. Andersen. "Linear methods in band theory". In: *Physical Review B* 12.8 (1975), p. 3060.

[27] P. Blaha, K. Schwarz, G. Madsen, D. Kvasnicka, and J. Luitz. "Wien2k". In: *An augmented plane wave + local orbitals program for calculating crystal properties* (2001).

[28] L. Hedin. "New method for calculating the one-particle Green's function with application to the electron-gas problem". In: *Physical Review* 139.3A (1965), A796.

[29] F. Aryasetiawan and O. Gunnarsson. "The GW method". In: *Reports on Progress in Physics* 61.3 (1998), p. 237.

[30] L. Hedin. "On correlation effects in electron spectroscopies and the GW approximation". In: *Journal of Physics: Condensed Matter* 11.42 (1999), R489.

[31] R. M. Martin, L. Reining, and D. M. Ceperley. *Interacting electrons*. Cambridge University Press, 2016.

[32] U. von Barth and B. Holm. "Self-consistent GW_0 results for the electron gas: fixed screened potential W_0 within the random-phase approximation". In: *Physical Review B* 54.12 (1996), p. 8411.

[33] E. L. Shirley. "Self-consistent GW and higher-order calculations of electron states in metals". In: *Physical Review B* 54.11 (1996), p. 7758.

[34] G. Mahan. "Comments condens". In: *Matter Phys* 16 (1994), p. 333.

[35] G. Baym and L. P. Kadanoff. "Conservation laws and correlation functions". In: *Physical Review* 124.2 (1961), p. 287.

[36] U. von Barth and B. Holm. "Erratum: self-consistent GW_0 results for the electron gas: fixed screened potential W_0 within the random-phase approximation [Physical Review B 54, 8411 (1996)]". In: *Physical Review B* 55 (1997), pp. 10120–10122.

[37] M. van Schilfgaarde, T. Kotani, and S. Faleev. "Quasiparticle self-consistent GW theory". In: *Physical Review Letters* 96 (22 2006), p. 226402.

[38] B.-C. Shih, Y. Xue, P. Zhang, M. L. Cohen, and S. G. Louie. "Quasiparticle band gap of ZnO: High accuracy from the conventional G_0W_0 approach". In: *Physical Review Letters* 105.14 (2010), p. 146401.

[39] C. Friedrich, M. C. Müller, and S. Blügel. "Band convergence and linearization error correction of all-electron GW calculations: the extreme case of zinc oxide". In: *Physical Review B* 83.8 (2011), p. 081101.

[40] J. Klimeš, M. Kaltak, and G. Kresse. "Predictive GW calculations using plane waves and pseudopotentials". In: *Physical Review B* 90.7 (2014), p. 075125.

[41] J. Hubbard. "Electron correlations in narrow energy bands". In: *Proceedings of the royal society of london a: mathematical, physical and engineering sciences*. Vol. 276. 1365. The Royal Society. 1963, pp. 238–257.

[42] M. C. Gutzwiller. "Effect of correlation on the ferromagnetism of transition metals". In: *Physical Review Letters* 10.5 (1963), p. 159.

[43] J. Kanamori. "Electron correlation and ferromagnetism of transition metals". In: *Progress of Theoretical Physics* 30.3 (1963), pp. 275–289.

[44] P. Anderson. "The resonating valence bond state in La_2CuO_4 and superconductivity". In: (1987).

[45] F. Zhang and T. Rice. "Effective Hamiltonian for the superconducting Cu oxides". In: *Physical Review B* 37.7 (1988), p. 3759.

[46] H. Kino and H. Kontani. "Phase diagram of superconductivity on the anisotropic triangular lattice Hubbard model: an effective model of κ-(BEDT-TTF) salts". In: *Journal of the Physical Society of Japan* 67.11 (1998), pp. 3691–3694.

[47] G. Kotliar and D. Vollhardt. "Strongly correlated materials: insights from dynamical mean-field theory". In: *Physics Today* 57.3 (2004), pp. 53–59.

[48] P. Curie. *Propriétés magnétiques des corps a diverses températures*. 4. Gauthier-Villars et fils, 1895.

[49] P. Weiss. "L'hypothèse du champ moléculaire et la propriété ferromagnétique". In: *Journal de Physique Théorique et Appliquée* 6.1 (1907), pp. 661–690.

[50] G. Parisi and R. Shankar. *Statistical field theory*. 1988.

[51] G. Beni, P. Pincus, and J. Kanamori. "Low-temperature properties of the one-dimensional polaron band. I. Extreme band-narrowing regime". In: *Physical Review B* 10 (5 1974), pp. 1896–1901.

[52] W. Metzner and D. Vollhardt. "Correlated lattice fermions in d=∞ dimensions". In: *Physical Review Letters* 62.3 (1989), p. 324.

[53] E Müller-Hartmann. "Correlated fermions on a lattice in high dimensions". In: *Zeitschrift für Physik B Condensed Matter* 74.4 (1989), pp. 507–512.

[54] A. Georges and G. Kotliar. "Hubbard model in infinite dimensions". In: *Physical Review B* 45.12 (1992), p. 6479.

[55] A. Georges, G. Kotliar, W. Krauth, and M. J. Rozenberg. "Dynamical mean-field theory of strongly correlated fermion systems and the limit of infinite dimensions". In: *Reviews of Modern Physics* 68.1 (1996), p. 13.

[56] P. W. Anderson. "Localized magnetic states in metals". In: *Physical Review* 124.1 (1961), p. 41.

[57] E. Gull, A. J. Millis, A. I. Lichtenstein, A. N. Rubtsov, M. Troyer, and P. Werner. "Continuous-time Monte Carlo methods for quantum impurity models". In: *Rev. Mod. Phys.* 83 (2 2011), pp. 349–404.

[58] J. W. Negele and H. Orland. *Quantum many-particle systems*. Westview, 1988.

[59] A. Georges, F. Mancini, and A. Avella. "Strongly correlated electron materials: dynamical mean-field theory and electronic structure". In: *Aip conference proceedings*. Vol. 715. 1. AIP. 2004, pp. 3–74.

[60] A. N. Rubtsov, M. Katsnelson, and A. Lichtenstein. "Dual boson approach to collective excitations in correlated fermionic systems". In: *Annals of Physics* 327.5 (2012), pp. 1320–1335.

[61] A. Toschi, A. A. Katanin, and K. Held. "Dynamical vertex approximation: a step beyond dynamical mean-field theory". In: *Physical Review B* 75 (4 2007), p. 045118.

[62] T. Ayral and O. Parcollet. "Mott physics and spin fluctuations: a unified framework". In: *Physical Review B* 92.11 (2015), p. 115109.

[63] T. Ayral and O. Parcollet. "Mott physics and collective modes: an atomic approximation of the four-particle irreducible functional". In: *Physical Review B* 94.7 (2016), p. 075159.

[64] A. Rubtsov, M. Katsnelson, and A. Lichtenstein. "Dual fermion approach to nonlocal correlations in the Hubbard model". In: *Physical Review B* 77.3 (2008), p. 033101.

[65] G Rohringer, H Hafermann, A Toschi, A. Katanin, A. Antipov, M. Katsnelson, A. Lichtenstein, A. N. Rubtsov, and K Held. "Diagrammatic routes to non-local correlations beyond dynamical mean field theory". In: *arXiv preprint arXiv:1705.00024* (2017).

[66] A. Galler, P. Thunström, P. Gunacker, J. M. Tomczak, and K. Held. "Ab initio dynamical vertex approximation". In: *Physical Review B* 95 (11 2017), p. 115107.

[67] F Lechermann, A. Lichtenstein, and M Potthoff. "Realistic many-body approaches to materials with strong nonlocal correlations". In: *arXiv preprint arXiv:1704.04176* (2017).

[68] H. A. Bethe. "Statistical theory of superlattices". In: *Proceedings of the Royal Society of London A: Mathematical, Physical and Engineering Sciences* 150.871 (1935), pp. 552–575.

[69] J. Skilling and R. Bryan. "Maximum entropy image reconstruction: general algorithm". In: *Monthly notices of the Royal Astronomical Society* 211.1 (1984), pp. 111–124.

[70] A. Damascelli, Z. Hussain, and Z.-X. Shen. "Angle-resolved photoemission studies of the cuprate superconductors". In: *Rev. Mod. Phys.* 75 (2 2003), pp. 473–541.

[71] W. Brinkman and T. Rice. "Application of Gutzwiller's variational method to the metal-insulator transition". In: *Physical Review B* 2.10 (1970), p. 4302.

[72] G. Sawatzky and J. Allen. "Magnitude and origin of the band gap in NiO". In: *Physical Review Letters* 53.24 (1984), p. 2339.

[73] V. Anisimov, A. Poteryaev, M. Korotin, A. Anokhin, and G Kotliar. "First-principles calculations of the electronic structure and spectra of strongly correlated systems: dynamical mean-field theory". In: *Journal of Physics: Condensed Matter* 9.35 (1997), p. 7359.

[74] A. Lichtenstein and M. Katsnelson. "Ab initio calculations of quasiparticle band structure in correlated systems: LDA++ approach". In: *Physical Review B* 57.12 (1998), p. 6884.

[75] V. I. Anisimov, J. Zaanen, and O. K. Andersen. "Band theory and Mott insulators: Hubbard U instead of Stoner I". In: *Physical Review B* 44.3 (1991), p. 943.

[76] A. Liechtenstein, V. Anisimov, and J Zaanen. "Density-functional theory and strong interactions: orbital ordering in Mott-Hubbard insulators". In: *Physical Review B* 52.8 (1995), R5467.

[77] V. I. Anisimov, F Aryasetiawan, and A. Lichtenstein. "First-principles calculations of the electronic structure and spectra of strongly correlated systems: the LDA+U method". In: *Journal of Physics: Condensed Matter* 9.4 (1997), p. 767.

[78] F. Lechermann, A Georges, A Poteryaev, S Biermann, M Posternak, A Yamasaki, and O. Andersen. "Dynamical mean-field theory using Wannier functions: a flexible route to electronic structure calculations of strongly correlated materials". In: *Physical Review B* 74.12 (2006), p. 125120.

[79] B Amadon, F Lechermann, A Georges, F Jollet, T. Wehling, and A. Lichtenstein. "Plane-wave based electronic structure calculations for correlated materials using dynamical mean-field theory and projected local orbitals". In: *Physical Review B* 77.20 (2008), p. 205112.

[80] M. Aichhorn, L. V. Pourovskii, V. Vildosola, M. Ferrero, O. Parcollet, T. Miyake, A. Georges, and S. Biermann. "Dynamical mean-field theory within an augmented plane-wave framework: assessing electronic correlations in the iron pnictide LaFeAsO". In: *Physical Review B* 80.8 (2009), p. 085101.

[81] G. Kotliar, S. Y. Savrasov, K. Haule, V. S. Oudovenko, O Parcollet, and C. Marianetti. "Electronic structure calculations with dynamical mean-field theory". In: *Reviews of Modern Physics* 78.3 (2006), p. 865.

[82] S. Biermann. "Dynamical mean field theory-based electronic structure calculations for correlated materials". In: *First principles approaches to spectroscopic properties of complex materials*. Springer, 2014, pp. 303–345.

[83] V. I. Anisimov, I. Solovyev, M. Korotin, M. Czyżyk, and G. Sawatzky. "Density-functional theory and NiO photoemission spectra". In: *Physical Review B* 48.23 (1993), p. 16929.

[84] A. Lichtenstein, M. Katsnelson, and G Kotliar. "Finite-temperature magnetism of transition metals: an ab initio dynamical mean-field theory". In: *Physical Review Letters* 87.6 (2001), p. 067205.

[85] A. van Roekeghem. "Electronic coulomb correlations in transition metal pnictides". PhD thesis. Ecole Polytechnique X, 2014.

[86] M. Aichhorn, L. V. Pourovskii, and A. Georges. "Importance of electronic correlations for structural and magnetic properties of the iron pnictide superconductor LaFeAsO". In: *Physical Review B* 84.5 (2011), p. 054529.

[87] G Kotliar and S. Savrasov. "Dynamical mean field theory, model hamiltonians and first principles electronic structure calculations". In: *arXiv preprint cond-mat/0208241* (2002).

[88] S. Y. Savrasov and G. Kotliar. "Spectral density functionals for electronic structure calculations". In: *Physical Review B* 69.24 (2004), p. 245101.

[89] J. M. Luttinger and J. C. Ward. "Ground-state energy of a many-fermion system. II". In: *Physical Review* 118 (5 1960), pp. 1417–1427.

[90] B. Amadon. "A self-consistent DFT+DMFT scheme in the projector augmented wave method: applications to cerium, Ce_2O_3 and Pu_2O_3 with the Hubbard I solver and comparison to DFT+U". In: *Journal of Physics: Condensed Matter* 24.7 (2012), p. 075604.

[91] H. Park, A. J. Millis, and C. A. Marianetti. "Total energy calculations using DFT+DMFT: computing the pressure phase diagram of the rare earth nickelates". In: *Physical Review B* 89.24 (2014), p. 245133.

[92] S.-K. Mo, J. Denlinger, H.-D. Kim, J.-H. Park, J. Allen, A Sekiyama, A Yamasaki, K Kadono, S Suga, Y Saitoh, et al. "Prominent quasiparticle peak in the photoemission spectrum of the metallic phase of V_2O_3". In: *Physical Review Letters* 90.18 (2003), p. 186403.

[93] E Pavarini, S Biermann, A Poteryaev, A. Lichtenstein, A Georges, and O. Andersen. "Mott transition and suppression of orbital fluctuations in orthorhombic $3d^1$ perovskites". In: *Physical Review Letters* 92.17 (2004), p. 176403.

[94] A Sekiyama, H Fujiwara, S Imada, S Suga, H Eisaki, S. Uchida, K Takegahara, H Harima, Y Saitoh, I. Nekrasov, et al. "Mutual experimental and theoretical validation of bulk photoemission spectra of $Sr_{1-x}Ca_xVO_3$". In: *Physical Review Letters* 93.15 (2004), p. 156402.

[95] V. I. Anisimov, D. E. Kondakov, A. V. Kozhevnikov, I. A. Nekrasov, Z. V. Pchelkina, J. W. Allen, S.-K. Mo, H.-D. Kim, P. Metcalf, S. Suga, A. Sekiyama, G. Keller, I. Leonov, X. Ren, and D. Vollhardt. "Full orbital calculation scheme for materials with strongly correlated electrons". In: *Physical Review B* 71.12 (2005), p. 125119.

[96] S Biermann, A Poteryaev, A. Lichtenstein, and A Georges. "Dynamical singlets and correlation-assisted Peierls transition in VO_2". In: *Physical Review Letters* 94.2 (2005), p. 026404.

[97] A. I. Poteryaev, J. M. Tomczak, S. Biermann, A. Georges, A. I. Lichtenstein, A. N. Rubtsov, T. Saha-Dasgupta, and O. K. Andersen. "Enhanced crystal-field splitting and orbital-selective coherence induced by strong correlations in V_2O_3". In: *Physical Review B* 76.8 (2007), p. 085127.

[98] J. M. Tomczak, A. I. Poteryaev, and S. Biermann. "Momentum-resolved spectroscopy of correlated metals: a view from dynamical mean field theory". In: *Comptes Rendus Physique* 10.6 (2009), pp. 537–547.

[99] P. Thunström, I. Di Marco, and O. Eriksson. "Electronic entanglement in late transition metal oxides". In: *Physical Review Letters* 109.18 (2012), p. 186401.

[100] I. Nekrasov, N. Pavlov, and M. Sadovskii. "Consistent LDA+DMFT approach to the electronic structure of transition metal oxides: charge transfer insulators and correlated metals". In: *Journal of Experimental and Theoretical Physics* 116.4 (2013), pp. 620–634.

[101] I Leonov, L. V. Pourovskii, A Georges, and I. Abrikosov. "Magnetic collapse and the behavior of transition metal oxides at high pressure". In: *Physical Review B* 94.15 (2016), p. 155135.

[102] J Sánchez-Barriga, J Minár, J Braun, A Varykhalov, V Boni, I. Di Marco, O Rader, V Bellini, F Manghi, H Ebert, et al. "Quantitative determination of spin-dependent quasiparticle lifetimes and electronic correlations in hcp cobalt". In: *Physical Review B* 82.10 (2010), p. 104414.

[103] I Leonov, A. Poteryaev, V. Anisimov, and D Vollhardt. "Electronic correlations at the $\alpha-\gamma$ structural phase transition in paramagnetic iron". In: *Physical Review Letters* 106.10 (2011), p. 106405.

[104] I Leonov, A. Poteryaev, V. Anisimov, and D Vollhardt. "Calculated phonon spectra of paramagnetic iron at the $\alpha-\gamma$ phase transition". In: *Physical Review B* 85.2 (2012), p. 020401.

[105] L. Pourovskii, J Mravlje, M Ferrero, O. Parcollet, and I. Abrikosov. "Impact of electronic correlations on the equation of state and transport in ε-Fe". In: *Physical Review B* 90.15 (2014), p. 155120.

[106] P. Delange, T. Ayral, S. I. Simak, M. Ferrero, O. Parcollet, S. Biermann, and L. V. Pourovskii. "Large effects of subtle electronic correlations on the energetics of vacancies in α-Fe". In: *Physical Review B* 94.10 (2016), p. 100102.

[107] L. Pourovskii, B. Amadon, S. Biermann, and A. Georges. "Self-consistency over the charge density in dynamical mean-field theory: A linear muffin-tin implementation and some physical implications". In: *Physical Review B* 76.23 (Dec. 2007), p. 235101.

[108] I. L. M. Locht, Y. O. Kvashnin, D. C. M. Rodrigues, M. Pereiro, A. Bergman, L. Bergqvist, A. I. Lichtenstein, M. I. Katsnelson, A. Delin, A. B. Klautau, B. Johansson, I. Di Marco, and O. Eriksson. "Standard model of the rare earths analyzed from the Hubbard I approximation". In: *Physical Review B* 94 (8 2016), p. 085137.

[109] S. Y. Savrasov, G Kotliar, and E. Abrahams. "Correlated electrons in δ-plutonium within a dynamical mean-field picture". In: *Nature* 410.6830 (2001), pp. 793–795.

[110] L. V. Pourovskii, M. Katsnelson, and A. Lichtenstein. "Correlation effects in electronic structure of actinide monochalcogenides". In: *Physical Review B* 72.11 (2005), p. 115106.

[111] J. Kolorenč, A. B. Shick, and A. I. Lichtenstein. "Electronic structure and core-level spectra of light actinide dioxides in the dynamical mean-field theory". In: *Physical Review B* 92.8 (2015), p. 085125.

[112] P. Dederichs, S Blügel, R Zeller, and H Akai. "Ground states of constrained systems: application to cerium impurities". In: *Physical Review Letters* 53.26 (1984), p. 2512.

[113] V. Anisimov and O Gunnarsson. "Density-functional calculation of effective Coulomb interactions in metals". In: *Physical Review B* 43.10 (1991), p. 7570.

[114] F Aryasetiawan, K. Karlsson, O Jepsen, and U Schönberger. "Calculations of Hubbard U from first-principles". In: *Physical Review B* 74.12 (2006), p. 125106.

[115] M Casula, P. Werner, L Vaugier, F. Aryasetiawan, T Miyake, A. Millis, and S Biermann. "Low-energy models for correlated materials: bandwidth renormalization from coulombic screening". In: *Physical Review Letters* 109.12 (2012), p. 126408.

[116] F Aryasetiawan, M Imada, A Georges, G Kotliar, S Biermann, and A. Lichtenstein. "Frequency-dependent local interactions and low-energy effective models from electronic structure calculations". In: *Physical Review B* 70.19 (2004), p. 195104.

[117] P. Hansmann, L. Vaugier, H. Jiang, and S. Biermann. "What about U on surfaces? Extended Hubbard models for adatom systems from first principles". In: *Journal of Physics: Condensed Matter* 25.9 (2013), p. 094005.

[118] C. Martins, M. Aichhorn, L. Vaugier, and S. Biermann. "Reduced effective spin-orbital degeneracy and spin-orbital ordering in paramagnetic transition-metal oxides: sr 2 iro 4 versus sr 2 rho 4". In: *Physical review letters* 107.26 (2011), p. 266404.

[119] L. Vaugier, H. Jiang, and S. Biermann. "Hubbard U and Hund exchange J in transition metal oxides: screening versus localization trends from constrained random phase approximation". In: *Physical Review B* 86.16 (2012), p. 165105.

[120] A. van Roekeghem, T. Ayral, J. M. Tomczak, M. Casula, N. Xu, H. Ding, M. Ferrero, O. Parcollet, H. Jiang, and S. Biermann. "Dynamical correlations and screened exchange on the experimental bench: spectral properties of the cobalt pnictide $BaCo_2As_2$". In: *Physical Review Letters* 113.26 (2014), p. 266403.

[121] T. Miyake, F. Aryasetiawan, and M. Imada. "Ab initio procedure for constructing effective models of correlated materials with entangled band structure". In: *Physical Review B* 80 (15 2009), p. 155134.

[122] A. Lichtenstein and M. Katsnelson. "Antiferromagnetism and d-wave superconductivity in cuprates: a cluster dynamical mean-field theory". In: *Physical Review B* 62.14 (2000), R9283.

[123] G. Kotliar, S. Y. Savrasov, G. Pálsson, and G. Biroli. "Cellular dynamical mean field approach to strongly correlated systems". In: *Physical Review Letters* 87.18 (2001), p. 186401.

[124] M. Hettler, A. Tahvildar-Zadeh, M Jarrell, T. Pruschke, and H. Krishnamurthy. "Nonlocal dynamical correlations of strongly interacting electron systems". In: *Physical Review B* 58.12 (1998), R7475.

[125] T. Maier, M. Jarrell, T. Pruschke, and M. H. Hettler. "Quantum cluster theories". In: *Reviews of Modern Physics* 77.3 (2005), p. 1027.

[126] P. Hansmann, T. Ayral, L. Vaugier, P. Werner, and S. Biermann. "Long-range coulomb interactions in surface systems: a first-principles description within self-consistently combined GW and dynamical mean-field theory". In: *Physical Review Letters* 110 (16 2013), p. 166401.

[127] T. Ayral, P. Werner, and S. Biermann. "Spectral properties of correlated materials: local vertex and nonlocal two-particle correlations from combined GW and dynamical mean field theory". In: *Physical Review Letters* 109 (22 2012), p. 226401.

[128] C. Hotta and N. Furukawa. "Strong coupling theory of the spinless charges on triangular lattices: possible formation of a gapless charge-ordered liquid". In: *Phys. Rev. B* 74 (19 2006), p. 193107.

[129] A. M. Sengupta and A. Georges. "Non-Fermi-liquid behavior near a $T= 0$ spin-glass transition". In: *Physical Review B* 52.14 (1995), p. 10295.

[130] Q. Si and J. L. Smith. "Kosterlitz-Thouless transition and short range spatial correlations in an extended Hubbard model". In: *Physical Review Letters* 77 (16 1996), pp. 3391–3394.

[131] H. Kajueter. "Interpolating perturbation scheme for correlated electron systems". PhD thesis. Rutgers, The State University of New Jersey, 1996.

[132] P. Sun and G. Kotliar. "Extended dynamical mean-field theory and GW method". In: *Physical Review B* 66.8 (2002), p. 085120.

[133] S Biermann, F Aryasetiawan, and A Georges. "First-principles approach to the electronic structure of strongly correlated systems: combining the GW approximation and dynamical mean-field theory". In: *Physical Review Letters* 90.8 (2003), p. 086402.

[134] P. Sun and G. Kotliar. "Many-body approximation scheme beyond GW". In: *Physical Review Letters* 92.19 (2004), p. 196402.

[135] T. Ayral, S. Biermann, and P. Werner. "Screening and nonlocal correlations in the extended hubbard model from self-consistent combined GW and dynamical mean field theory". In: *Physical Review B* 87 (12 2013), p. 125149.

[136] J. M. Tomczak, M. Casula, T. Miyake, F. Aryasetiawan, and S. Biermann. "Combined GW and dynamical mean-field theory: dynamical screening effects in transition metal oxides". In: *EPL (Europhysics Letters)* 100.6 (2012), p. 67001.

[137] J. M. Tomczak, M. Casula, T Miyake, and S. Biermann. "Asymmetry in band widening and quasiparticle lifetimes in $SrVO_3$: competition between screened exchange and local correlations from combined GW and dynamical mean-field theory GW+DMFT". In: *Physical Review B* 90.16 (2014), p. 165138.

[138] T. Ayral, J. Vucicevic, and O. Parcollet. "The fierz convergence criterion: a controlled approach to strongly-interacting systems with small embedded clusters". In: *arXiv preprint arXiv:1706.01388* (2017).

[139] L. Vaugier. "Electronic structure of correlated materials from first principles: Hubbard interaction and Hund's exchange". PhD thesis. Ecole Polytechnique X, 2011.

[140] M. W. Haverkort. "Spin and orbital degrees of freedom in transition metal oxides and oxide thin films studied by soft X-ray absorption spectroscopy". In: *arXiv preprint cond-mat/0505214* (2005).

[141] L. V. Pourovskii, K. T. Delaney, C. G. Van de Walle, N. A. Spaldin, and A. Georges. "Role of atomic multiplets in the electronic structure of rare-earth semiconductors and semimetals". In: *Physical Review Letters* 102 (9 2009), p. 096401.

[142] M. S. Litsarev, I. Di Marco, P. Thunström, and O. Eriksson. "Correlated electronic structure and chemical bonding of cerium pnictides and γ-Ce". In: *Phys. Rev. B* 86 (11 2012), p. 115116.

[143] L. V. Pourovskii, P. Hansmann, M. Ferrero, and A. Georges. "Theoretical prediction and spectroscopic fingerprints of an orbital transition in $CeCu_2Si_2$". In: *Physical review letters* 112.10 (2014), p. 106407.

[144] L. V. Pourovskii. "Two-site fluctuations and multipolar intersite exchange interactions in strongly correlated systems". In: *Physical Review B* 94.11 (2016), p. 115117.

[145] P. Werner, A. Comanac, L. de'Medici, M. Troyer, and A. J. Millis. "Continuous-time solver for quantum impurity models". In: *Phys. Rev. Lett.* 97 (7 2006), p. 076405.

[146] J. E. Hirsch and R. M. Fye. "Monte-Carlo method for magnetic impurities in metals". In: *Physical review letters* 56.23 (1986), p. 2521.

[147] S. Rombouts, K. Heyde, and N. Jachowicz. "Quantum Monte Carlo method for fermions, free of discretization errors". In: *Physical review letters* 82.21 (1999), p. 4155.

[148] A. N. Rubtsov, V. V. Savkin, and A. I. Lichtenstein. "Continuous-time quantum Monte Carlo method for fermions". In: *Physical Review B* 72.3 (2005), p. 035122.

[149] N. Metropolis, A. W. Rosenbluth, M. N. Rosenbluth, A. H. Teller, and E. Teller. "Equation of state calculations by fast computing machines". In: *The journal of chemical physics* 21.6 (1953), pp. 1087–1092.

[150] W. K. Hastings. "Monte Carlo sampling methods using Markov chains and their applications". In: *Biometrika* 57.1 (1970), pp. 97–109.

[151] M. Troyer and U.-J. Wiese. "Computational complexity and fundamental limitations to fermionic quantum monte carlo simulations". In: *Phys. Rev. Lett.* 94 (17 2005), p. 170201.

[152] T. Ayral, S. Biermann, P. Werner, and L. Boehnke. "Influence of fock exchange in combined many-body perturbation and dynamical mean field theory". In: *arXiv preprint arXiv:1701.07718* (2017).

[153] A. van Roekeghem and S. Biermann. "Screened exchange dynamical mean-field theory and its relation to density functional theory: $SrVO_3$ and $SrTiO_3$". In: *EPL (Europhysics Letters)* 108.5 (2014), p. 57003.

[154] S. Biermann. "Dynamical screening effects in correlated electron materials: a progress report on combined many-body perturbation and dynamical mean field theory:GW+ DMFT". In: *Journal of Physics: Condensed Matter* 26.17 (2014), p. 173202.

[155] A. van Roekeghem, P. Richard, X. Shi, S. Wu, L. Zeng, B. Saparov, Y. Ohtsubo, T. Qian, A. S. Sefat, S. Biermann, and H. Ding. "Tetragonal and collapsed-tetragonal phases of $CaFe_2As_2$: a view from angle-resolved photoemission and dynamical mean-field theory". In: *Phys. Rev. B* 93 (24 2016), p. 245139.

[156] M. Hirayama, T. Miyake, M. Imada, and S. Biermann. "Low-energy effective Hamiltonians for correlated electron systems beyond density functional theory". In: *arXiv preprint arXiv:1511.03757* (2015).

[157] J. M. Tomczak, M. van Schilfgaarde, and G. Kotliar. "Many-body effects in iron pnictides and chalcogenides: nonlocal versus dynamic origin of effective masses". In: *Physical Review Letters* 109.23 (2012), p. 237010.

[158] E. Maksimov, I. Maxin, S. Y. Savrasov, and Y. A. Uspenski. "Excitation spectra of semiconductors and insulators: a density-functional approach to many-body theory". In: *Journal of Physics: Condensed Matter* 1.14 (1989), p. 2493.

[159] Y. Takada and A. Chatterjee. "Possibility of a metallic phase in the charge-density-wave–spin-density-wave crossover region in the one-dimensional Hubbard-Holstein model at half filling". In: *Physical Review B* 67.8 (2003), p. 081102.

[160] A. Macridin, G. Sawatzky, and M. Jarrell. "Two-dimensional Hubbard-Holstein bipolaron". In: *Physical Review B* 69.24 (2004), p. 245111.

[161] P. Werner and M. Casula. "Dynamical screening in correlated electron systems – from lattice models to realistic materials". In: *Journal of Physics: Condensed Matter* 28.38 (2016), p. 383001.

[162] I. Lang and Y. A. Firsov. "Kinetic theory of semiconductors with low mobility". In: *Sov. Phys. JETP* 16.5 (1963), p. 1301.

[163] K. Steiner, Y. Nomura, and P. Werner. "Double-expansion impurity solver for multiorbital models with dynamically screened U and J". In: *Physical Review B* 92 (11 2015), p. 115123.

[164] P. Seth, I. Krivenko, M. Ferrero, and O. Parcollet. "TRIQS/CTHYB: a continuous-time quantum Monte Carlo hybridization expansion solver for quantum impurity problems". In: *Computer Physics Communications* 200 (2016), pp. 274 –284.

[165] A Seidl, A Görling, P Vogl, J. Majewski, and M Levy. "Generalized Kohn-Sham schemes and the band-gap problem". In: *Physical Review B* 53.7 (1996), p. 3764.

[166] P. Delange, S. Backes, A. van Roekeghem, L. Pourovskii, H. Jiang, and S. Biermann. "Novel approaches to spectral properties of correlated electron materials: from generalized Kohn-Sham theory to screened exchange dynamical mean field theory". In: *Journal of the Physical Society of Japan* (2017). In press.

[167] J. P. Perdew, R. G. Parr, M. Levy, and J. L. Balduz Jr. "Density-functional theory for fractional particle number: derivative discontinuities of the energy". In: *Physical Review Letters* 49.23 (1982), p. 1691.

[168] B Amadon, S Biermann, A Georges, and F Aryasetiawan. "The $\alpha - \gamma$ transition of cerium is entropy driven". In: *Physical Review Letters* 96.6 (2006), p. 066402.

[169] R. Poole, R. Leckey, J. Jenkin, and J Liesegang. "Photoelectron emission and the d bands of zinc and cadmium". In: *Physical Review B* 8.4 (1973), p. 1401.

[170] F. Himpsel, D. Eastman, E. Koch, and A. Williams. "Experimental $E(k)$ dispersions for the Zn $3d$ states: evidence for itinerant character". In: *Physical Review B* 22.10 (1980), p. 4604.

[171] M. R. Norman. "Application of a screened self-interaction correction to transition metals: copper and zinc". In: *Physical Review B* 29.6 (1984), p. 2956.

[172] F. Aryasetiawan and O. Gunnarsson. "$3d$ semicore states in ZnSe, GaAs, and Ge". In: *Physical Review B* 54 (24 1996), pp. 17564–17567.

[173] M. Oshikiri and F. Aryasetiawan. "Band gaps and quasiparticle energy calculations on ZnO, ZnS, and ZnSe in the zinc-blende structure by the GW approximation". In: *Physical Review B* 60 (15 1999), pp. 10754–10757.

[174] J. P. Perdew and A. Zunger. "Self-interaction correction to density-functional approximations for many-electron systems". In: *Physical Review B* 23 (10 1981), pp. 5048–5079.

[175] H. Jiang, R. I. Gómez-Abal, X.-Z. Li, C. Meisenbichler, C. Ambrosch-Draxl, and M. Scheffler. "FHI-gap: A GW code based on the all-electron augmented plane wave method". In: *Computer Physics Communications* 184.2 (2013), pp. 348–366.

[176] B. Holm and U. von Barth. "Fully self-consistent GW self-energy of the electron gas". In: *Physical Review B* 57 (4 1998), pp. 2108–2117.

[177] H Hasegawa and D. Pettifor. "Microscopic theory of the temperature-pressure phase diagram of iron". In: *Physical Review Letters* 50.2 (1983), p. 130.

[178] V. P. Antropov, M. Katsnelson, M Van Schilfgaarde, and B. Harmon. "Ab initio spin dynamics in magnets". In: *Physical Review Letters* 75.4 (1995), p. 729.

[179] H. Herper, E Hoffmann, and P Entel. "Ab initio full-potential study of the structural and magnetic phase stability of iron". In: *Physical Review B* 60.6 (1999), p. 3839.

[180] K. Carling, G. Wahnström, T. R. Mattsson, A. E. Mattsson, N. Sandberg, and G. Grimvall. "Vacancies in metals: from first-principles calculations to experimental data". In: *Physical Review Letters* 85.18 (2000), p. 3862.

[181] D. A. Andersson and S. I. Simak. "Monovacancy and divacancy formation and migration in copper: a first-principles theory". In: *Physical Review B* 70 (11 2004), p. 115108.

[182] A. Glensk, B. Grabowski, T. Hickel, and J. Neugebauer. "Breakdown of the Arrhenius law in describing vacancy formation energies: the importance of local anharmonicity revealed by *Ab initio* thermodynamics". In: *Physical Review X* 4 (1 2014), p. 011018.

[183] C.-S. Lian, J.-T. Wang, and C. Chen. "Ab initio study of the anharmonic lattice dynamics of iron at the $\gamma - \delta$ phase transition". In: *Physical Review B* 92.18 (2015), p. 184110.

[184] T. Takahashi and W. A. Bassett. "High-pressure polymorph of iron". In: *Science* 145.3631 (1964), pp. 483–486.

[185] B. Dupé, B. Amadon, Y.-P. Pellegrini, and C. Denoual. "Mechanism for the $\alpha \rightarrow \varepsilon$ phase transition in iron". In: *Physical Review B* 87 (2 2013), p. 024103.

[186] P. Pedrazzini, D. Jaccard, G Lapertot, J Flouquet, Y Inada, H Kohara, and Y Onuki. "Probing the extended non-Fermi liquid regimes of MnSi and Fe". In: *Physica B: Condensed Matter* 378 (2006), pp. 165–166.

[187] L. Pourovskii, T Miyake, S Simak, A. V. Ruban, L Dubrovinsky, and I. Abrikosov. "Electronic properties and magnetism of iron at the Earth's inner core conditions". In: *Physical Review B* 87.11 (2013), p. 115130.

[188] L. Pourovskii, J Mravlje, A Georges, S. Simak, and I. Abrikosov. "Fermi-liquid behavior and thermal conductivity of ε-iron at Earth's core conditions". In: *arXiv preprint arXiv:1603.02287* (2016).

[189] A. A. Katanin, A. I. Poteryaev, A. V. Efremov, A. O. Shorikov, S. L. Skornyakov, M. A. Korotin, and V. I. Anisimov. "Orbital-selective formation of local moments in α-iron: first-principles route to an effective model". In: *Physical Review B* 81 (4 2010), p. 045117.

[190] M. Katsnelson and A. Lichtenstein. "LDA++ approach to the electronic structure of magnets: correlation effects in iron". In: *Journal of Physics: Condensed Matter* 11.4 (1999), p. 1037.

[191] M. S. Daw and M. I. Baskes. "Embedded-atom method: derivation and application to impurities, surfaces, and other defects in metals". In: *Physical Review B* 29.12 (1984), p. 6443.

[192] I. Abrikosov, A. Ponomareva, P. Steneteg, S. Barannikova, and B. Alling. "Recent progress in simulations of the paramagnetic state of magnetic materials". In: *Current Opinion in Solid State and Materials Science* 20.2 (2016), pp. 85–106.

[193] L Hadjadj, R Amira, D Hamana, and A Mosbah. "Characterization of precipitation and phase transformations in Al–Zn–Mg alloy by the differential dilatometry". In: *Journal of Alloys and Compounds* 462.1 (2008), pp. 279–283.

[194] R. Siegel. "Positron annihilation spectroscopy". In: *Annual Review of Materials Science* 10.1 (1980), pp. 393–425.

[195] L De Schepper, D Segers, L Dorikens-Vanpraet, M Dorikens, G Knuyt, L. Stals, and P Moser. "Positron annihilation on pure and carbon-doped α-iron in thermal equilibrium". In: *Physical Review B* 27.9 (1983), p. 5257.

[196] S. Kim and W. Buyers. "Vacancy formation energy in iron by positron annihilation". In: *Journal of Physics F: Metal Physics* 8.5 (1978), p. L103.

[197] H Matter, J Winter, and W Triftshäuser. "Phase transformations and vacancy formation energies of transition metals by positron annihilation". In: *Applied physics* 20.2 (1979), pp. 135–140.

[198] H.-E. Schaefer, K Maier, M Weller, D Herlach, A Seeger, and J Diehl. "Vacancy formation in iron investigated by positron annihilation in thermal equilibrium". In: *Scripta Metallurgica* 11.9 (1977), pp. 803–809.

[199] H.-E. Schaefer. "Investigation of thermal equilibrium vacancies in metals by positron annihilation". In: *Physica Status Solidi (A)* 102.1 (1987), pp. 47–65.

[200] C. Freysoldt, B. Grabowski, T. Hickel, J. Neugebauer, G. Kresse, A. Janotti, and C. G. Van de Walle. "First-principles calculations for point defects in solids". In: *Reviews of modern physics* 86.1 (2014), p. 253.

[201] M. Manninen, P Hautojärvi, and R Nieminen. "Screening of light impurities in simple metals". In: *Solid State Communications* 23.11 (1977), pp. 795–798.

[202] B Chakraborty, R. Siegel, and W. Pickett. "Self-consistent electronic structure of a vacancy in aluminum". In: *Physical Review B* 24.10 (1981), p. 5445.

[203] A. V. Ruban. "Thermal vacancies in random alloys in the single-site mean-field approximation". In: *Physical Review B* 93 (13 2016), p. 134115.

[204] R. Armiento and A. E. Mattsson. "Functional designed to include surface effects in self-consistent density functional theory". In: *Physical Review B* 72.8 (2005), p. 085108.

[205] A. E. Mattsson, R. R. Wixom, and R. Armiento. "Electronic surface error in the Si interstitial formation energy". In: *Physical Review B* 77 (15 2008), p. 155211.

[206] R. Nazarov, T. Hickel, and J. Neugebauer. "Vacancy formation energies in fcc metals: influence of exchange-correlation functionals and correction schemes". In: *Physical Review B* 85.14 (2012), p. 144118.

[207] T Korhonen, M. Puska, and R. M. Nieminen. "Vacancy-formation energies for fcc and bcc transition metals". In: *Physical Review B* 51.15 (1995), p. 9526.

[208] B Dorado, M Freyss, B Amadon, M Bertolus, G Jomard, and P Garcia. "Advances in first-principles modeling of point defects in UO_2: f electron correlations and the issue of local energy minima". In: *Journal of Physics: Condensed Matter* 25.33 (2013), p. 333201.

[209] P. A. Korzhavyi, I. A. Abrikosov, B. Johansson, A. Ruban, and H. L. Skriver. "First-principles calculations of the vacancy formation energy in transition and noble metals". In: *Physical Review B* 59.18 (1999), p. 11693.

[210] P. Söderlind, L. Yang, J. A. Moriarty, and J. Wills. "First-principles formation energies of monovacancies in bcc transition metals". In: *Physical Review B* 61.4 (2000), p. 2579.

[211] C Domain and C. Becquart. "Ab initio calculations of defects in Fe and dilute Fe-Cu alloys". In: *Physical Review B* 65.2 (2001), p. 024103.

[212] T. Hoshino, T. Mizuno, M. Asato, and H. Fukushima. "Full-potential KKR calculations for point defect energies in metals, based on the generalized-gradient approximation. I. Vacancy formation energies in fcc and bcc metals." In: *Materials Transactions* 42.11 (2001), pp. 2206–2215.

[213] T Mizuno, M Asato, T Hoshino, and K Kawakami. "First-principles calculations for vacancy formation energies in Ni and Fe: non-local effect beyond the LSDA and magnetism". In: *Journal of magnetism and magnetic materials* 226 (2001), pp. 386–387.

[214] Y. Tateyama and T. Ohno. "Stability and clusterization of hydrogen-vacancy complexes in α-Fe: an ab initio study". In: *Physical Review B* 67.17 (2003), p. 174105.

[215] C.-C. Fu, F. Willaime, and P. Ordejón. "Stability and mobility of mono-and di-interstitials in α-Fe". In: *Physical Review Letters* 92.17 (2004), p. 175503.

[216] P. M. Derlet, D Nguyen-Manh, and S. Dudarev. "Multiscale modeling of crowdion and vacancy defects in body-centered-cubic transition metals". In: *Physical Review B* 76.5 (2007), p. 054107.

[217] P. Olsson, C. Domain, and J. Wallenius. "Ab initio study of Cr interactions with point defects in bcc Fe". In: *Physical Review B* 75.1 (2007), p. 014110.

[218] T. Ohnuma, N. Soneda, and M. Iwasawa. "First-principles calculations of vacancy–solute element interactions in body-centered cubic iron". In: *Acta Materialia* 57.20 (2009), pp. 5947–5955.

[219] D. Kandaskalov, C. Mijoule, and D. Connétable. "Study of multivacancies in alpha Fe". In: *Journal of Nuclear Materials* 441.1 (2013), pp. 168–177.

[220] S. Dudarev. "Density functional theory models for radiation damage". In: *Materials Research* 43.1 (2013), p. 35.

[221] "Full orbital calculation scheme for materials with strongly correlated electrons". In: *Physical Review B* 71 (12 2005), p. 125119.

[222] A. Kokalj. "Computer graphics and graphical user interfaces as tools in simulations of matter at the atomic scale". In: *Computational Materials Science* 28.2 (2003), pp. 155–168.

[223] F. Lechermann, L. Boehnke, D. Grieger, and C. Piefke. "Electron correlation and magnetism at the $LaAlO_3/SrTiO_3$ interface: a DFT+DMFT investigation". In: *Physical Review B* 90 (8 2014), p. 085125.

[224] M. Behrmann and F. Lechermann. "Interface exchange processes in $LaAlO_3/SrTiO_3$ induced by oxygen vacancies". In: *Physical Review B* 92.12 (2015), p. 125148.

[225] S. Backes, T. C. Rödel, F. Fortuna, E. Frantzeskakis, P. Le Fèvre, F. Bertran, M. Kobayashi, R. Yukawa, T. Mitsuhashi, M. Kitamura, K. Horiba, H. Kumigashira, R. Saint-Martin, A. Fouchet, B. Berini, Y. Dumont, A. J. Kim, F. Lechermann, H. O. Jeschke, M. J. Rozenberg, R. Valentí, and A. F. Santander-Syro. "Hubbard band versus oxygen vacancy states in the correlated electron metal $SrVO_3$". In: *Physical Review B* 94 (24 2016), p. 241110.

[226] M. Czyżyk and G. Sawatzky. "Local-density functional and on-site correlations: the electronic structure of La_2CuO_4 and $LaCuO_3$". In: *Physical Review B* 49.20 (1994), p. 14211.

[227] C. Wang, Y. Yang, Y. Zhang, and Y Jia. "A single vacancy diffusion near a Fe (110) surface: a molecular dynamics study". In: *Computational Materials Science* 50.2 (2010), pp. 291–294.

[228] J. Mravlje, M. Aichhorn, T. Miyake, K. Haule, G. Kotliar, and A. Georges. "Coherence-incoherence crossover and the mass-renormalization puzzles in Sr_2RuO_4". In: *Physical Review Letters* 106 (9 2011), p. 096401.

[229] I Leonov, V. Anisimov, and D Vollhardt. "First-principles calculation of atomic forces and structural distortions in strongly correlated materials". In: *Physical Review Letters* 112.14 (2014), p. 146401.

[230] A. Srivastava, H. Rotella, S. Saha, B. Pal, G. Kalon, S. Mathew, M. Motapothula, M. Dykas, P. Yang, E. Okunishi, D. D. Sarma, and T. Venkatesan. "Selective growth of single phase VO_2 (A, B, and M) polymorph thin films". In: *APL materials* 3.2 (2015), p. 026101.

[231] B. Pal, P. Delange, S. Biermann, D. Sarma, et al. In: *in preparation* ().

[232] F. Morin. "Oxides which show a metal-to-insulator transition at the Néel temperature". In: *Physical Review Letters* 3.1 (1959), p. 34.

[233] Z. Yang, C. Ko, and S. Ramanathan. "Oxide electronics utilizing ultrafast metal-insulator transitions". In: *Annual Review of Materials Research* 41 (2011), pp. 337–367.

[234] S. Lee, K. Hippalgaonkar, F. Yang, J. Hong, C. Ko, J. Suh, K. Liu, K. Wang, J. J. Urban, X. Zhang, et al. "Anomalously low electronic thermal conductivity in metallic vanadium dioxide". In: *Science* 355.6323 (2017), pp. 371–374.

[235] M. M. Qazilbash, M. Brehm, B.-G. Chae, P.-C. Ho, G. O. Andreev, B.-J. Kim, S. J. Yun, A. Balatsky, M. Maple, F. Keilmann, et al. "Mott transition in VO_2 revealed by infrared spectroscopy and nano-imaging". In: *Science* 318.5857 (2007), pp. 1750–1753.

[236] R. M. Wentzcovitch, W. W. Schulz, and P. B. Allen. "VO_2: Peierls or Mott-Hubbard? a view from band theory". In: *Physical Review Letters* 72.21 (1994), p. 3389.

[237] T. Rice, H Launois, and J. Pouget. "Comment on "VO_2: Peierls or Mott-Hubbard? A view from band theory"". In: *Physical Review Letters* 73.22 (1994), p. 3042.

[238] W. Brito, M. Aguiar, K Haule, and G Kotliar. "Metal-insulator transition in VO_2: a DFT+ DMFT perspective". In: *Physical Review Letters* 117.5 (2016), p. 056402.

[239] O Nájera, M Civelli, V Dobrosavljević, and M. Rozenberg. "Resolving the VO_2 controversy: Mott mechanism dominates the insulator-to-metal transition". In: *Physical Review B* 95.3 (2017), p. 035113.

[240] V. Eyert. "The metal-insulator transitions of VO_2: a band theoretical approach". In: *arXiv preprint cond-mat/0210558* (2002).

[241] J. B. Goodenough. "Direct cation–cation interactions in several oxides". In: *Physical Review* 117.6 (1960), p. 1442.

[242] J. B. Goodenough. "The two components of the crystallographic transition in VO_2". In: *Journal of Solid State Chemistry* 3.4 (1971), pp. 490–500.

[243] A. Zylbersztejn and N. F. Mott. "Metal-insulator transition in vanadium dioxide". In: *Physical Review B* 11 (11 1975), pp. 4383–4395.

[244] J. Pouget, H Launois, T. Rice, P Dernier, A Gossard, G Villeneuve, and P Hagenmuller. "Dimerization of a linear Heisenberg chain in the insulating phases of $V_{1-x}Cr_xO_2$". In: *Physical Review B* 10.5 (1974), p. 1801.

[245] J. Pouget, H Launois, J. d'Haenens, P Merenda, and T. Rice. "Electron localization induced by uniaxial stress in pure VO_2". In: *Physical Review Letters* 35.13 (1975), p. 873.

[246] T. Huffman, C Hendriks, E. Walter, J. Yoon, H. Ju, R Smith, G. Carr, H Krakauer, and M. Qazilbash. "Insulating phases of vanadium dioxide are Mott-Hubbard insulators". In: *Physical Review B* 95.7 (2017), p. 075125.

[247] Y Oka, N Yamamoto, T Ohtani, and T Takada. "Formation and phase transitions of hydrated vanadium oxides with layered structures". In: *Nippon seramikkusu kyokai gakujutsu ronbunshi* 97.12 (1989), pp. 1441–1445.

[248] Y. Oka, T. Yao, N. Yamamoto, Y. Ueda, and A. Hayashi. "Phase transition and V^{4+}–V^{4+} pairing in VO_2 (B)". In: *Journal of Solid State Chemistry* 105.1 (1993), pp. 271–278.

[249] H. Liu, Y. Wang, K. Wang, E. Hosono, and H. Zhou. "Design and synthesis of a novel nanothorn VO_2 (B) hollow microsphere and their application in lithium-ion batteries". In: *Journal of Materials Chemistry* 19.18 (2009), pp. 2835–2840.

[250] C Marini, E Arcangeletti, D Di Castro, L Baldassare, A Perucchi, S Lupi, L Malavasi, L Boeri, E Pomjakushina, K Conder, et al. "Optical properties of $V_{1-x}Cr_xO_2$ compounds under high pressure". In: *Physical Review B* 77.23 (2008), p. 235111.

[251] C Blaauw, F Leenhouts, F. van der Woude, and G. Sawatzky. "The metal-non-metal transition in VO_2: X-ray photoemission and resistivity measurements". In: *Journal of Physics C: Solid State Physics* 8.4 (1975), p. 459.

[252] S. Shin, S Suga, M Taniguchi, M Seki, H Kanzaki, Y Ueda, K Kosuge, and S Kachi. "Electron correlation energies and metal-insulator transition of VO_2". In: *Proceedings of the 17th international conference on the physics of semiconductors*. Springer. 1985, pp. 1091–1094.

[253] K Okazaki, H Wadati, A Fujimori, M Onoda, Y Muraoka, and Z Hiroi. "Photoemission study of the metal-insulator transition in VO_2/TiO_2 (001): evidence for strong electron-electron and electron-phonon interaction". In: *Physical Review B* 69.16 (2004), p. 165104.

[254] T. Koethe, Z Hu, M. Haverkort, C Schüßler-Langeheine, F Venturini, N. Brookes, O. Tjernberg, W Reichelt, H. Hsieh, H.-J. Lin, et al. "Transfer of spectral weight and symmetry across the metal-insulator transition in VO_2". In: *Physical Review Letters* 97.11 (2006), p. 116402.

[255] S Suga, A Sekiyama, S Imada, T Miyamachi, H Fujiwara, A Yamasaki, K Yoshimura, K Okada, M Yabashi, K Tamasaku, A Higashiya, and T Ishikawa. "8 keV photoemission of the metal–insulator transition system VO_2". In: *New Journal of Physics* 11.10 (2009), p. 103015.

[256] K Saeki, T Wakita, Y Muraoka, M Hirai, T Yokoya, R Eguchi, and S Shin. "Band dispersion near the fermi level for VO_2 thin films grown on TiO_2 (001) substrates". In: *Physical Review B* 80.12 (2009), p. 125406.

[257] M. Haverkort, Z Hu, A. Tanaka, W Reichelt, S. Streltsov, M. Korotin, V. Anisimov, H. Hsieh, H.-J. Lin, C. Chen, et al. "Orbital-assisted metal-insulator transition in VO_2". In: *Physical Review Letters* 95.19 (2005), p. 196404.

[258] R. Eguchi, S. Tsuda, T. Kiss, A. Chainani, Y. Muraoka, Z. Hiroi, and S. Shin. "Electronic structure of VO_2/TiO_2:Nb upon photocarrier injection". In: *Physical Review B* 75 (7 2007), p. 073102.

[259] R. Eguchi, M. Taguchi, M. Matsunami, K. Horiba, K. Yamamoto, Y. Ishida, A. Chainani, Y. Takata, M. Yabashi, D. Miwa, Y. Nishino, K. Tamasaku, T. Ishikawa, Y. Senba, H. Ohashi, Y. Muraoka, Z. Hiroi, and S. Shin. "Photoemission evidence for a Mott-Hubbard metal-insulator transition in VO_2". In: *Physical Review B* 78 (7 2008), p. 075115.

[260] D. Wegkamp, M. Herzog, L. Xian, M. Gatti, P. Cudazzo, C. L. McGahan, R. E. Marvel, R. F. Haglund Jr, A. Rubio, M. Wolf, et al. "Instantaneous band gap collapse in photoexcited monoclinic VO_2 due to photocarrier doping". In: *Physical Review Letters* 113.21 (2014), p. 216401.

[261] J Laverock, S Kittiwatanakul, A. Zakharov, Y. Niu, B Chen, S. Wolf, J. Lu, and K. Smith. "Direct observation of decoupled structural and electronic transitions and an ambient pressure monoclinic-like metallic phase of VO_2". In: *Physical Review Letters* 113.21 (2014), p. 216402.

[262] N. B. Aetukuri, A. X. Gray, M. Drouard, M. Cossale, L. Gao, A. H. Reid, R. Kukreja, H. Ohldag, C. A. Jenkins, E. Arenholz, et al. "Control of the metal-insulator transition in vanadium dioxide by modifying orbital occupancy". In: *Nature Physics* 9.10 (2013), pp. 661–666.

[263] V. R. Morrison, R. P. Chatelain, K. L. Tiwari, A. Hendaoui, A. Bruhács, M. Chaker, and B. J. Siwick. "A photoinduced metal-like phase of monoclinic VO_2 revealed by ultrafast electron diffraction". In: *Science* 346.6208 (2014), pp. 445–448.

[264] E Arcangeletti, L Baldassarre, D Di Castro, S Lupi, L Malavasi, C Marini, A Perucchi, and P Postorino. "Evidence of a pressure-induced metallization process in monoclinic VO_2". In: *Physical Review Letters* 98.19 (2007), p. 196406.

[265] J. Jeong, N. Aetukuri, T. Graf, T. D. Schladt, M. G. Samant, and S. S. Parkin. "Suppression of metal-insulator transition in VO_2 by electric field–induced oxygen vacancy formation". In: *Science* 339.6126 (2013), pp. 1402–1405.

[266] Z. Zhang, F. Zuo, C. Wan, A. Dutta, J. Kim, J. Rensberg, R. Nawrodt, H. H. Park, T. J. Larrabee, X. Guan, Y. Zhou, S. M. Prokes, C. Ronning, V. M. Shalaev, A. Boltasseva, M. A. Kats, and S. Ramanathan. "Evolution of metallicity in vanadium dioxide by creation of oxygen vacancies". In: *Physical Review Applied* 7.3 (2017), p. 034008.

[267] A. Chen, Z. Bi, W. Zhang, J. Jian, Q. Jia, and H. Wang. "Textured metastable VO_2 (B) thin films on $SrTiO_3$ substrates with significantly enhanced conductivity". In: *Applied Physics Letters* 104.7 (2014), p. 071909.

[268] A. Rúa, R. D. Díaz, S. Lysenko, and F. E. Fernández. "Semiconductor-insulator transition in VO_2 (B) thin films grown by pulsed laser deposition". In: *Journal of Applied Physics* 118.12 (2015), p. 125308.

[269] J. Lourembam, A. Srivastava, L.-o.-v. Chan, H Rotella, T Venkatesan, and E. E. Chia. "New insights into the diverse electronic phases of a novel vanadium dioxide polymorph: a terahertz spectroscopy study". In: *Scientific Reports* 5 (2015), p. 9182.

[270] J. Lourembam, A. Srivastava, L. C. Chan La-o vorakiat, T Venkatesan, and E. E. Chia. "Evidence for photoinduced insulator-to-metal transition in B-phase vanadium dioxide". In: *Scientific Reports* 6 (2016).

[271] V Eyert. "VO_2: a novel view from band theory". In: *Physical Review Letters* 107.1 (2011), p. 016401.

[272] R. Grau-Crespo, H. Wang, and U. Schwingenschlögl. "Why the Heyd-Scuseria-Ernzerhof hybrid functional description of VO_2 phases is not correct". In: *Physical Review B* 86 (8 2012), p. 081101.

[273] X. Yuan, Y. Zhang, T. A. Abtew, P. Zhang, and W. Zhang. "VO_2: orbital competition, magnetism, and phase stability". In: *Physical Review B* 86.23 (2012), p. 235103.

[274] A. Liebsch, H. Ishida, and G. Bihlmayer. "Coulomb correlations and orbital polarization in the metal-insulator transition of VO_2". In: *Physical Review B* 71 (8 2005), p. 085109.

[275] A Continenza, S Massidda, and M Posternak. "Self-energy corrections in VO_2 within a model GW scheme". In: *Physical Review B* 60.23 (1999), p. 15699.

[276] M. Gatti, F. Bruneval, V. Olevano, and L. Reining. "Understanding correlations in vanadium dioxide from first principles". In: *Physical Review Letters* 99.26 (2007), p. 266402.

[277] R. Sakuma, T. Miyake, and F. Aryasetiawan. "First-principles study of correlation effects in VO_2". In: *Physical Review B* 78 (7 2008), p. 075106.

[278] J. M. Tomczak and S. Biermann. "Effective band structure of correlated materials: the case of VO_2". In: *Journal of Physics: Condensed Matter* 19.36 (2007), p. 365206.

[279] J. M. Tomczak, F. Aryasetiawan, and S. Biermann. "Effective bandstructure in the insulating phase versus strong dynamical correlations in metallic VO_2". In: *Physical Review B* 78.11 (2008), p. 115103.

[280] J. M. Tomczak and S. Biermann. "Optical properties of correlated materials: generalized Peierls approach and its application to VO_2". In: *Physical Review B* 80.8 (2009), p. 085117.

[281] J. M. Tomczak and S. Biermann. "Materials design using correlated oxides: optical properties of vanadium dioxide". In: *EPL (Europhysics Letters)* 86.3 (2009), p. 37004.

[282] B. Lazarovits, K. Kim, K. Haule, and G. Kotliar. "Effects of strain on the electronic structure of VO_2". In: *Physical Review B* 81.11 (2010), p. 115117.

[283] A. Belozerov, M. Korotin, V. Anisimov, and A. Poteryaev. "Monoclinic M_1 phase of VO_2: Mott-Hubbard versus band insulator". In: *Physical Review B* 85.4 (2012), p. 045109.

[284] Z. He and A. J. Millis. "Photoinduced phase transitions in narrow-gap Mott insulators: the case of VO_2". In: *Physical Review B* 93.11 (2016), p. 115126.

[285] M. Korotin, N. Skorikov, and V. Anisimov. "Variation of orbital symmetry of the localized $3d^1$ electron of the V^{4+} ion upon the metal-insulator transition in VO_2". In: *arXiv preprint cond-mat/0301347* (2003).

[286] B.-C. Shih, T. A. Abtew, X. Yuan, W. Zhang, and P. Zhang. "Screened coulomb interactions of localized electrons in transition metals and transition-metal oxides". In: *Physical Review B* 86 (16 2012), p. 165124.

[287] P. Seth, P. Hansmann, A. van Roekeghem, L. Vaugier, and S. Biermann. "Towards a first-principles determination of effective Coulomb interactions in correlated electron materials: role of intershell interactions". In: *arXiv preprint arXiv:1508.07466* (2015).

[288] A. F. Santander-Syro, O. Copie, T. Kondo, F. Fortuna, S. Pailhes, R. Weht, X. G. Qiu, F. Bertran, A. Nicolaou, A. Taleb-Ibrahimi, P. Le Fevre, G. Herranz, M. Bibes, N. Reyren, Y. Apertet, P. Lecoeur, A. Barthelemy, and M. J. Rozenberg. "Two-dimensional electron gas with universal subbands at the surface of $SrTiO_3$". In: *Nature* 469.7329 (Jan. 2011), pp. 189–193.

[289] W Meevasana, P. King, R. He, S.-K. Mo, M Hashimoto, A. Tamai, P Songsiriritthigul, F. Baumberger, and Z.-X. Shen. "Creation and control of a two-dimensional electron liquid at the bare $SrTiO_3$ surface". In: *arXiv preprint arXiv:1010.0763* (2010).

[290] T. C. Rödel, F. Fortuna, F. Bertran, M. Gabay, M. J. Rozenberg, A. F. Santander-Syro, and P. Le Fèvre. "Engineering two-dimensional electron gases at the (001) and (101) surfaces of TiO_2 anatase using light". In: *Physical Review B* 92 (4 2015), p. 041106.

[291] C. Lin, C. Mitra, and A. A. Demkov. "Orbital ordering under reduced symmetry in transition metal perovskites: oxygen vacancy in $SrTiO_3$". In: *Physical Review B* 86 (16 2012), p. 161102.

[292] H. O. Jeschke, J. Shen, and R. Valentí. "Localized versus itinerant states created by multiple oxygen vacancies in $SrTiO_3$". In: *New Journal of Physics* 17.2 (2015), p. 023034.

[293] M. Altmeyer, H. O. Jeschke, O. Hijano-Cubelos, C. Martins, F. Lechermann, K. Koepernik, A. F. Santander-Syro, M. J. Rozenberg, R. Valentí, and M. Gabay. "Magnetism, spin texture, and in-gap states: atomic specialization at the surface of oxygen-deficient $SrTiO_3$". In: *Physical Review Letters* 116 (15 2016), p. 157203.

[294] P. Delange, S. Biermann, T. Miyake, and L. Pourovskii. "Crystal-field splittings in rare-earth-based hard magnets: an ab initio approach". In: *Phys. Rev. B* 96 (15 2017), p. 155132.

[295] E. Pavarini. *Crystal-field theory, tight-binding method and Jahn-Teller effect*. 2012.

[296] H. Bethe. "Termaufspaltung in Kristallen". In: *Annalen der Physik* 395.2 (1929), pp. 133–208.

[297] J. H. Van Vleck. "Theory of the variations in paramagnetic anisotropy among different salts of the iron group". In: *Physical Review* 41 (2 1932), pp. 208–215.

[298] C. J. Ballhausen. *Ligand field theory*. Vol. 241. McGraw-Hill, New York, 1962.

[299] T. Demiray, D. Nath, and F. Hummel. "Zircon-vanadium blue pigment". In: *Journal of the American Ceramic Society* 53.1 (1970), pp. 1–4.

[300] M Dondi, G Cruciani, G Guarini, F Matteucci, and M Raimondo. "The role of counterions (Mo, Nb, Sb, W) in Cr-, Mn-, Ni-and V-doped rutile ceramic pigments: part 2. colour and technological properties". In: *Ceramics international* 32.4 (2006), pp. 393–405.

[301] B. Henderson and R. H. Bartram. *Crystal-field engineering of solid-state laser materials*. Vol. 25. Cambridge University Press, 2005.

[302] F. Hund. "Zur Deutung der Molekelspektren. I". In: *Zeitschrift für Physik* 40.10 (1927), pp. 742–764.

[303] F. Hund. "Zur Deutung der Molekelspektren. II". In: *Zeitschrift für Physik* 42.2 (1927), pp. 93–120.

[304] M. Korotin, S. Y. Ezhov, I. Solovyev, V. Anisimov, D. Khomskii, and G. Sawatzky. "Intermediate-spin state and properties of $LaCoO_3$". In: *Physical Review B* 54.8 (1996), p. 5309.

[305] D. J. Newman and B. Ng. "The superposition model of crystal fields". In: *Reports on Progress in Physics* 52.6 (1989), p. 699.

[306] J. Mulak and Z. Gajek. *The effective crystal field potential*. Elsevier, 2000.

[307] D. J. Newman and B. Ng. *Crystal field handbook*. Cambridge University Press, 2007.

[308] K. Stevens. "Matrix elements and operator equivalents connected with the magnetic properties of rare earth ions". In: *Proceedings of the Physical Society. Section A* 65.3 (1952), p. 209.

[309] M. T. Hutchings. "Point-charge calculations of energy levels of magnetic ions in crystalline electric fields". In: *Solid state physics* 16 (1964), pp. 227–273.

[310] B. G. Wybourne and W. F. Meggers. *Spectroscopic properties of rare earths*. 1965.

[311] K Strnat. "The recent development of permanent magnet materials containing rare earth metals". In: *IEEE Transactions on Magnetics* 6.2 (1970), pp. 182–190.

[312] J. Herbst. "$R_2Fe_{14}B$ materials: Intrinsic properties and technological aspects". In: *Reviews of Modern Physics* 63.4 (1991), p. 819.

[313] J. Coey. "Hard magnetic materials: a perspective". In: *IEEE Transactions on Magnetics* 47.12 (2011), pp. 4671–4681.

[314] W. Körner, G. Krugel, and C. Elsässer. "Theoretical screening of intermetallic $ThMn_{12}$-type phases for new hard-magnetic compounds with low rare earth content". In: *Scientific reports* 6 (2016).

[315] S Suzuki, T Kuno, K Urushibata, K Kobayashi, N Sakuma, K Washio, M Yano, A Kato, and A Manabe. "A new magnet material with $ThMn_{12}$ structure: $(Nd_{1-x}Zr_x)(Fe_{1-y}Co_y)_{11+z}Ti_{1-z}N_\alpha$ (α= 0.6–1.3)". In: *Journal of Magnetism and Magnetic Materials* 401 (2016), pp. 259–268.

[316] Y. Harashima, K. Terakura, H. Kino, S. Ishibashi, and T. Miyake. "Nitrogen as the best interstitial dopant among X= B, C, N, O, and F for strong permanent magnet $NdFe_{11}TiX$: first-principles study". In: *Physical Review B* 92.18 (2015), p. 184426.

[317] Y Hirayama, Y. Takahashi, S Hirosawa, and K Hono. "$NdFe_{12}N_x$ hard-magnetic compound with high magnetization and anisotropy field". In: *Scripta Materialia* 95 (2015), pp. 70–72.

[318] T. Miyake, K. Terakura, Y. Harashima, H. Kino, and S. Ishibashi. "First-principles study of magnetocrystalline anisotropy and magnetization in $NdFe_{12}$, $NdFe_{11}Ti$, and $NdFe_{11}TiN$". In: *Journal of the Physical Society of Japan* 83.4 (2014), p. 043702.

[319] J. M. D. Coey. *Rare-earth iron permanent magnets*. 54. Oxford University Press, 1996.

[320] O. Gutfleisch, M. A. Willard, E. Brück, C. H. Chen, S. Sankar, and J. P. Liu. "Magnetic materials and devices for the 21st century: stronger, lighter, and more energy efficient". In: *Advanced materials* 23.7 (2011), pp. 821–842.

[321] E. K. Delczeg-Czirjak, A. Edström, M Werwiński, J. Rusz, N. V. Skorodumova, L. Vitos, and O. Eriksson. "Stabilization of the tetragonal distortion of Fe_xCo_{1-x} alloys by C impurities: a potential new permanent magnet". In: *Physical Review B* 89.14 (2014), p. 144403.

[322] Y. Harashima, K. Terakura, H. Kino, S. Ishibashi, and T. Miyake. "First-principles study on stability and magnetism of $NdFe_{11}M$ and $NdFe_{11}MN$ for M= Ti, V, Cr, Mn, Fe, Co, Ni, Cu, Zn". In: *Journal of Applied Physics* 120.20 (2016), p. 203904.

[323] M. Matsumoto, H. Akai, Y. Harashima, S. Doi, and T. Miyake. "Relevance of $4f$-$3d$ exchange to finite-temperature magnetism of rare-earth permanent magnets: an ab-initio-based spin model approach for $NdFe_{12}N$". In: *Journal of Applied Physics* 119.21 (2016), p. 213901.

[324] R Skomski and D. Sellmyer. "Anisotropy of rare-earth magnets". In: *Journal of Rare Earths* 27.4 (2009), pp. 675–679.

[325] P. Porcher, M. C. Dos Santos, and O. Malta. "Relationship between phenomenological crystal field parameters and the crystal structure: the simple overlap model". In: *Physical Chemistry Chemical Physics* 1.3 (1999), pp. 397–405.

[326] C Brecher, H Samelson, A Lempicki, R Riley, and T Peters. "Polarized spectra and crystal-field parameters of Eu^{3+} in YVO_4". In: *Physical Review* 155.2 (1967), p. 178.

[327] K. Buschow, A. Van Diepen, and H. De Wijn. "Crystal-field anisotropy of Sm^{3+} in $SmCo_5$". In: *Solid State Communications* 15.5 (1974), pp. 903–906.

[328] S. Sankar, V. Rao, E Segal, W. Wallace, W. Frederick, and H. Garrett. "Magnetocrystalline anisotropy of $SmCo_5$ and its interpretation on a crystal-field model". In: *Physical Review B* 11.1 (1975), p. 435.

[329] D Givord, J Laforest, J Schweizer, and F Tasset. "Temperature dependence of the samarium magnetic form factor in $SmCo_5$". In: *Journal of Applied Physics* 50.B3 (1979), pp. 2008–2010.

[330] Z. Tie-Song, J. Han-Min, G. Guang-Hua, H. Xiu-Feng, and C. Hong. "Magnetic properties of R ions in RCo_5 compounds (R= Pr, Nd, Sm, Gd, Tb, Dy, Ho, and Er)". In: *Physical Review B* 43.10 (1991), p. 8593.

[331] P Tils, M Loewenhaupt, K. Buschow, and R. Eccleston. "Crystal and exchange fields in $SmCo_5$ studied by inelastic neutron scattering". In: *Journal of alloys and compounds* 289.1 (1999), pp. 28–31.

[332] R Coehoorn. "First principles band structure calculations for rare earth-transition metal compounds: magnetization, hyperfine parameters and magnetocrystalline anisotropy". In: *Journal of Magnetism and Magnetic Materials* 99.1 (1991), pp. 55–70.

[333] G. Daalderop, P. Kelly, and M. Schuurmans. "Magnetocrystalline anisotropy of $RECo_5$ compounds". In: *Journal of Magnetism and Magnetic Materials* 104 (1992), pp. 737–738.

[334] L. Steinbeck, M. Richter, H. Eschrig, and U. Nitzsche. "Calculated crystal-field parameters for rare-earth impurities in noble metals". In: *Physical Review B* 49.23 (1994), p. 16289.

[335] P Novák and J Kuriplach. "Calculation of crystal-field parameters in the RNi_5 (R = rare earth) system". In: *Physical Review B* 50.4 (1994), p. 2085.

[336] L. Steinbeck, M. Richter, U. Nitzsche, and H. Eschrig. "Ab initio calculation of electronic structure, crystal field, and intrinsic magnetic properties of Sm_2Fe_{17}, $Sm_2Fe_{17}N_3$, $Sm_2Fe_{17}C_3$, and Sm_2Co_{17}". In: *Physical Review B* 53.11 (1996), p. 7111.

[337] P Novák. "Calculated crystal field parameters in RCo_5 and RNi_5 systems". In: *Physica Status Solidi (B)* 198.2 (1996), pp. 729–740.

[338] L. Ning and G. P. Brivio. "Density functional theory calculation of crystal-field energy levels for Yb^{3+} in the $Cs_2Na_2YbF_6$ crystal". In: *Physical Review B* 75 (23 2007), p. 235126.

[339] P Novák and M Diviš. "Crystal field parameters of praseodymium in oxides". In: *Physica Status Solidi (B)* 244.9 (2007), pp. 3168–3177.

[340] L. Hu, M. F. Reid, C.-K. Duan, S. Xia, and M. Yin. "Extraction of crystal-field parameters for lanthanide ions from quantum-chemical calculations". In: *Journal of Physics: Condensed Matter* 23.4 (2011), p. 045501.

[341] P Novák, K Knížek, and J Kuneš. "Crystal field parameters with Wannier functions: application to rare-earth aluminates". In: *Physical Review B* 87.20 (2013), p. 205139.

[342] M. W. Haverkort, M. Zwierzycki, and O. K. Andersen. "Multiplet ligand-field theory using Wannier orbitals". In: *Physical Review B* 85 (16 2012), p. 165113.

[343] F. Aquilante, L. De Vico, N. Ferré, G. Ghigo, P.-å. Malmqvist, P. Neogrády, T. B. Pedersen, M. Pitoňák, M. Reiher, B. O. Roos, et al. "MOLCAS 7: the next generation". In: *Journal of computational chemistry* 31.1 (2010), pp. 224–247.

[344] L. Ungur and L. F. Chibotaru. "Ab initio crystal field for lanthanides". In: *Chemistry-A European Journal* 23.15 (2017), pp. 3708–3718.

[345] M. Brooks, O Eriksson, J. Wills, and B Johansson. "Density functional theory of crystal field quasiparticle excitations and the *a*b initio calculation of spin Hamiltonian parameters". In: *Physical Review Letters* 79.13 (1997), p. 2546.

[346] S. Lebègue, G. Santi, A. Svane, O. Bengone, M. Katsnelson, A. Lichtenstein, and O. Eriksson. "Electronic structure and spectroscopic properties of thulium monochalcogenides". In: *Physical Review B* 72.24 (2005), p. 245102.

[347] S. Lebègue, A. Svane, M. Katsnelson, A. Lichtenstein, and O. Eriksson. "Multiplet effects in the electronic structure of heavy rare-earth metals". In: *Journal of Physics: Condensed Matter* 18.27 (2006), p. 6329.

[348] K. Haule. "Exact double counting in combining the dynamical mean field theory and the density functional theory". In: *Phys. Rev. Lett.* 115 (19 2015), p. 196403.

[349] M. Aichhorn, L. V. Pourovskii, P. Seth, V. Vildosola, M. Zingl, O. E. Peil, X. Deng, J. Mravlje, G. J. Kraberger, C. Martins, et al. "TRIQS/DFTTools: a TRIQS application for *a*b initio calculations of correlated materials". In: *Computer Physics Communications* 204 (2016), pp. 200–208.

[350] L. Pourovskii. "Crystal field splitting in rare-earth oxyfluorides and oxychlorides". to be published.

[351] J. Cuthill, A. McAlister, N. Erickson, and R. Watson. "X-ray photoemission studies of rare earth hard magnets". In: *AIP Conference Proceedings* 18.1 (1974), pp. 1039–1043.

[352] A Laslo, R Dudric, M Neumann, O Isnard, M Coldea, and V Pop. "Effects of m= si, ga and al for co substitution on the electronic properties of rco 4 m as probed by xps". In: *Solid State Communications* 199 (2014), pp. 43–46.

[353] J. Lang, Y Baer, and P. Cox. "Study of the 4f and valence band density of states in rare-earth metals. ii. experiment and results". In: *Journal of Physics F: Metal Physics* 11.1 (1981), p. 121.

[354] K. Hummler and M. Fähnle. "Full-potential linear-muffin-tin-orbital calculations of the magnetic properties of rare-earth transition-metal intermetallics. I. description of the formalism and application to the series RCo_5 (R = rare-earth atom)". In: *Physical Review B* 53 (6 1996), pp. 3272–3289.

[355] Y. Harashima, K. Terakura, H. Kino, S. Ishibashi, and T. Miyake. "First-principles study of structural and magnetic properties of $R(Fe, Ti)_{11}$ and $R(Fe, Ti)_{12}N$ (R= Nd, Sm, Y)". In: *Proceedings of computational science workshop 2014 (csw2014)*. 2015, p. 011021.

[356] F. Nilsson, R. Sakuma, and F. Aryasetiawan. "*A*B INITIO calculations of the Hubbard U for the early lanthanides using the constrained random-phase approximation". In: *Physical Review B* 88 (12 2013), p. 125123.

[357] J. K. Lang, Y Baer, and P. A. Cox. "Study of the $4f$ and valence band density of states in rare-earth metals. II. experiment and results". In: *Journal of Physics F: Metal Physics* 11.1 (1981), p. 121.

[358] R. F. Bader. "Atoms in molecules: a quantum theory, international series of monographs on chemistry, 22". In: *Oxford University Press* 36.3 (1990), pp. 354–360.

[359] M. Aichhorn, L. V. Pourovskii, P. Seth, V. Vildosola, M. Zingl, O. E. Peil, X. Deng, J. Mravlje, G. J. Kraberger, C. Martins, et al. "TRIQS/DFTTools: A TRIQS application for ab initio calculations of correlated materials". In: *arXiv preprint arXiv:1511.01302* (2015).

[360] J. Kuneš, R. Arita, P. Wissgott, A. Toschi, H. Ikeda, and K. Held. "Wien2wannier: from linearized augmented plane waves to maximally localized Wannier functions". In: *Computer Physics Communications* 181.11 (2010), pp. 1888–1895.

[361] T. Mazet, D. Malterre, M. Fran çois, C. Dallera, M. Grioni, and G. Monaco. "Nonpareil Yb behavior in $YbMn_6Ge_{6-x}Sn_x$". In: *Physical Review Letters* 111 (9 2013), p. 096402.

[362] T. Mazet, D. Malterre, M. Fran çois, L. Eichenberger, M. Grioni, C. Dallera, and G. Monaco. "Composition and temperature dependence of the Yb valence in $YbMn_6Ge_{6-x}Sn_x$ studied by RIXS". In: *Physical Review B* 92 (7 2015), p. 075105.

[363] H. Bruus and K. Flensberg. *Many-body quantum theory in condensed matter physics: an introduction*. Oxford University Press, 2004.

Appendix D

Publications

PHYSICAL REVIEW B **94**, 100102(R) (2016)

Large effects of subtle electronic correlations on the energetics of vacancies in α-Fe

Pascal Delange,[1] Thomas Ayral,[2] Sergei I. Simak,[3] Michel Ferrero,[1,4] Olivier Parcollet,[2]
Silke Biermann,[1,4] and Leonid Pourovskii[1,4,5]

[1]*Centre de Physique Théorique, École Polytechnique, CNRS, Université Paris-Saclay, 91128 Palaiseau Cedex, France*
[2]*Institut de Physique Théorique (IPhT), CEA, CNRS, UMR 3681, 91191 Gif-sur-Yvette, France*
[3]*Department of Physics, Chemistry and Biology (IFM), Linköping University, SE-58183 Linköping, Sweden*
[4]*Collège de France, 11 place Marcelin Berthelot, 75005 Paris, France*
[5]*Materials Modeling and Development Laboratory, National University of Science and Technology "MISIS," Moscow, Russia*

(Received 14 June 2016; revised manuscript received 3 August 2016; published 21 September 2016)

We study the effect of electronic Coulomb correlations on the vacancy formation energy in paramagnetic α-Fe within *ab initio* dynamical mean-field theory. The calculated value for the formation energy is substantially lower than in standard density-functional calculations and in excellent agreement with experiment. The reduction is caused by an enhancement of electronic correlations at the nearest neighbors of the vacancy. This effect is explained by subtle changes in the corresponding spectral function of the d electrons. The local lattice relaxations around the vacancy are substantially increased by many-body effects.

DOI: 10.1103/PhysRevB.94.100102

Point defects, such as vacancies, play an important role for the mechanical and thermodynamic properties of materials [1]. However, the experimental determination of vacancy formation or migration energies is difficult. Even the best available techniques, the differential dilatometry and the positron annihilation spectroscopy, suffer from large error bars, and the discrepancies between different measurements on one and the same material may be significant. Therefore, *ab initio* theoretical calculations are an indispensable tool for developing a better understanding of the defect properties of materials [2].

Early density-functional theory (DFT) calculations in the local density approximation (LDA) have predicted formation energies of vacancies in simple metals in good agreement with experiment [3,4]. Despite a large body of successful calculations, it has later been recognized that the nice agreement with experiment could often be the effect of the cancellation of errors in the exchange and correlation parts of the density functional [5]. As has been discussed by Ruban [6], despite the structural simplicity of vacancies, their energetics is still one of the least reliable physical properties determined in first-principles calculations.

In transition metals, where the open d shells are often poorly described in LDA or the generalized gradient approximation (GGA), the quality of results of DFT calculations for point defect properties is rather unpredictable and strongly material dependent. There have been several attempts to improve the available functionals (see, e.g., Refs. [7–10]). We notice that the predicted vacancy formation energies seem to be especially poor for $3d$ transition metals, for which many-body effects are fairly important, in particular in the paramagnetic state and body-centered cubic (bcc) crystal structure [11]. Likewise, DFT has limitations for point defect calculations in correlated lanthanide or actinide oxides with $4f$ or $5f$ electrons, for example in the case of uranium oxides used in the nuclear industry [12].

Among the $3d$ transition metals, iron is a particularly complex system, where the strength of electronic correlations is very sensitive to the lattice structure and magnetic state. However, from a practical point of view, vacancies in iron and steels are of particular interest because they affect a number of important characteristics of the metal, e.g., toughness and ductility. Iron's low-temperature ferromagnetic bcc α phase is a weakly renormalized Fermi liquid [13] well described within DFT [14–16]. However, the same α-Fe in the high-temperature paramagnetic phase exhibits a strongly correlated non-Fermi-liquid behavior [17–19] with DFT calculations failing to describe its structural parameters (lattice constants, bulk modulus, or even the shape of the crystal) [18]. The low-temperature paramagnetic hexagonal ϵ phase stabilized by pressure is also rather strongly correlated [13] (though less so as compared to paramagnetic α-Fe), exhibiting a large electron-electron scattering contribution to the resistivity [20] as well as unconventional superconductivity [21,22]. All this hints at a strong sensitivity of many-body effects in Fe to local disturbances of the crystalline order (e.g., to point defects) that cannot be captured easily within standard DFT. Indeed, extensive DFT calculations of α-Fe [23–34] predict a monovacancy formation energy about 30%–40% higher than the measured values, with significant scatter depending on the DFT implementation used (see also Table II in Ref. [35]). In contrast to other $3d$ metals, this formation energy has been somewhat reliably determined thanks to extensive experiments [36–40].

The deficiencies of standard DFT to describe ϵ-Fe and paramagnetic α-Fe have been successfully corrected by combining it with a dynamical mean-field theory (DMFT) [41,42] treatment of the local repulsion between $3d$ electrons. *Ab initio* calculations using this DFT+DMFT approach [43,44] were able to reproduce the ground-state properties and phonon spectra of the α and δ phase [18,45,46] as well as the equation of state of ϵ-Fe [13]. It is thus likely that an explicit treatment of many-body effects within DMFT will also correct the severe problems of DFT in describing point defects in iron.

Hence, in the present work we have developed the state-of-the-art DFT+DMFT method [47–50] into a scheme for studying vacancy properties. We have applied our technique to a single vacancy in paramagnetic α-Fe, where positron annihilation measurements have been performed on pure iron without further approximations (contrary to the formation energy in

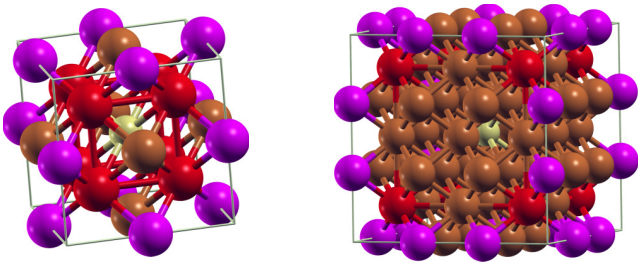

(a) $2 \times 2 \times 2$ supercell (b) $3 \times 3 \times 3$ supercell

FIG. 1. The $2 \times 2 \times 2$ and $3 \times 3 \times 3$ supercells with the vacancy in the corner. Different colors indicate the atom nearest to the vacancy (red), the second nearest (purple), and the furthest (the central atom, yellow). Generated with XCRYSDEN [52].

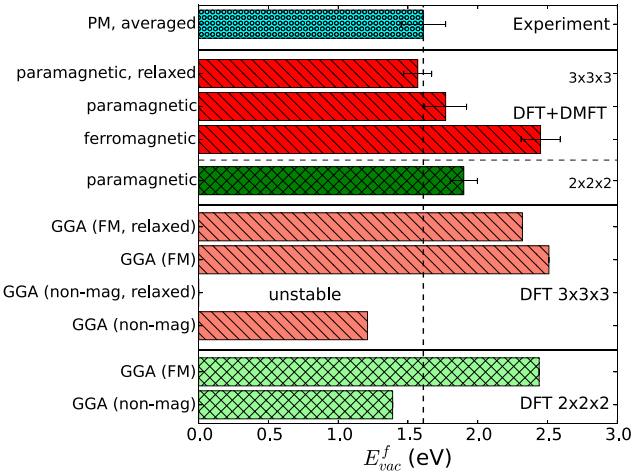

FIG. 2. Vacancy formation energies calculated by different methods (GGA and DFT+DMFT) in the different setups: small and large supercell, relaxed or not, nonmagnetic, paramagnetic (PM) or ferromagnetic (FM). Calculations are performed at the equilibrium volume for the relevant setup. The average of experimental values is shown for comparison [36–40].

the ferromagnetic phase). We have computed the electronic structure around the vacancy as well as the vacancy's formation energy, taking into account local lattice distortions around the defect. We do not treat here the high-temperature face-centered cubic phase, or temperatures close to the melting point, where the influence of the (anharmonic) lattice vibrations may play a crucial role [5,10,51] and the bcc phase is stabilized again. Compared to ferromagnetic DFT calculations, a significant reduction of the theoretical formation energy is obtained, with calculated values in remarkable agreement with experimental estimates [36–40]. We trace back this reduction to rather subtle effects of the vacancy on the local density of states and hybridization with its nearest neighbors.

We model a single vacancy in bcc Fe using the $2 \times 2 \times 2$ and $3 \times 3 \times 3$ cubic supercells represented in Fig. 1, with the vacancy placed at the origin of the supercells. We compute the vacancy formation energy from the supercell total energy using the standard formula

$$E^f_{\text{vac}} = E^{\text{vac}}(N-1) - \frac{N-1}{N} E^{\text{no vac}}(N), \qquad (1)$$

where N is the number of atoms in the ideal supercell, $E^{\text{no vac}}(N)$ is the total energy of the ideal supercell containing N atoms and no vacancy, and $E^{\text{vac}}(N-1)$ is the total energy of the same supercell with a vacancy (hence $N-1$ atoms). N is 16 in the $2 \times 2 \times 2$ supercell and 54 in the $3 \times 3 \times 3$ supercell, corresponding to vacancy concentrations of 6.25% and 1.85%, respectively.

Our calculations have been carried out using a fully charge self-consistent implementation of DFT+DMFT [53,54] based on the TRIQS package [55,56], with LDA as DFT exchange-correlation potential. This implementation is based on the full potential linearized augmented plane-wave WIEN2K code [57]. The on-site density-density interaction between those orbitals is parametrized by the Slater parameter $F_0 = U = 4.3$ eV and the Hund's rule coupling $J = 1.0$ eV that were previously used in the DFT+DMFT calculations of α and ϵ-Fe of Ref. [13]. The same work reproduced almost exactly the experimental lattice parameter of 2.86 Å, hence we perform our DFT+DMFT calculations at the experimental volume. Other DFT calculations were performed at the corresponding theoretical volume. Technical details about the DFT and DFT+DMFT calculations are included in the Supplemental Material [35]. The calculation of a vacancy formation energy using supercells with seven inequivalent atomic sites has become possible thanks to the use of a continuous-time quantum Monte Carlo hybridization expansion algorithm [58] in the segment representation for the solution of the local impurity problems (Backes *et al.* (Ref. [59]) and Behrmann *et al.* (Ref. [60]) have reported about the effect of vacancies on magnetism within DFT+DMFT). All DFT+DMFT calculations were performed at a temperature of 1162 K.

The vacancy formation energies obtained within DFT+DMFT together with different DFT results and experimental values are shown in Fig. 2 (see also Table I of the Supplemental Material [35]). The resulting value for E^f_{vac} in DFT+DMFT is 1.77 eV for the unrelaxed 54-atom supercell with lattice relaxations reducing it further to $E^f_{\text{vac}} = 1.56 \pm 0.13$ eV, in excellent agreement with the mean experimental value of about 1.6 eV. We also calculated E^f_{vac} within DFT+DMFT for the unrelaxed ferromagnetic phase obtaining a higher value of 2.45 ± 0.15 eV. Experiments indeed seem to confirm that E^f_{vac} in the ferromagnetic phase should be larger than in the nonmagnetic one [39,40], although direct low-temperature measurements of E^f_{vac} in the ferromagnetic phase with positron annihilation spectroscopy are notoriously difficult.

DFT (GGA) calculations assuming ferromagnetic bcc Fe predict a significantly larger value E^f_{vac} of 2.51 and 2.32 eV for an unrelaxed and a fully relaxed cell, respectively. Hence, one sees that many-body effects included within DMFT reduce E^f_{vac} for the paramagnetic phase by about 0.7 eV. The impact of correlation effects for ferromagnetic α-Fe is much less significant, in agreement with the predicted suppression of dynamic correlations in this phase [13]. Indeed, the large static spin splitting in the ferromagnetic phase leads to a suppression of dynamical correlations, which explains

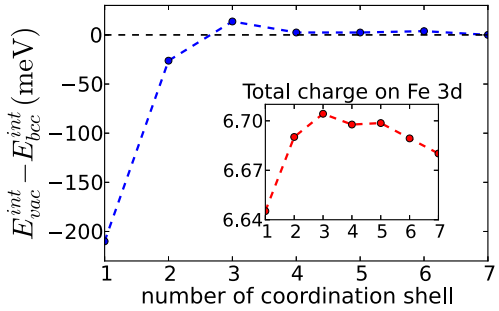

FIG. 3. Difference in the interaction energy per atom, before and after adding a vacancy. Inset: Fe 3d charge in the cell with vacancy.

why DFT works well in the ferromagnetic, but not in the paramagnetic phase of α-Fe. The vacancy formation energies obtained with nonmagnetic DFT calculations are even lower than the measured values, with $E^f_{\rm vac} \approx 1.5$ eV in unrelaxed GGA. They have, however, very little physical meaning: DFT in general fails dramatically for the paramagnetic phase, which is reflected by the fact that α-Fe is not dynamically stable and the predicted lattice parameter would be significantly smaller in nonmagnetic DFT. Hence, using our relaxed positions in a nonmagnetic DFT calculation gives an (unphysical) negative vacancy formation energy. Thus, the strongly reduced value of $E^f_{\rm vac}$ in nonmagnetic DFT calculations compared to ferromagnetic ones may be due to a spurious cancellation of errors.

The total energy in DFT+DMFT is

$$E^{\rm tot}_{\rm DMFT} = {\rm Tr}\big(\hat{\epsilon}_k \hat{\rho}^{\rm DMFT}_k\big) + E[\rho^{\rm DMFT}] + (E_{\rm Hub} - E_{\rm DC}), \quad (2)$$

where $\hat{\rho}^{\rm DMFT}_k$ is the density matrix for crystal momentum k, $\hat{\epsilon}_k$ the corresponding LDA Hamiltonian and $E[\rho^{\rm DMFT}]$ only depends explicitly on the charge density. $E_{\rm Hub} = \frac{1}{2}\sum_{ij} U_{ij}\langle n_i n_j\rangle$ is the Coulomb interaction between Fe 3d electrons (i and j are orbital indices and U_{ij} is the density-density Coulomb matrix), and $E_{\rm DC}$ is the double-counting term that estimates the energy already present in LDA (see Supplemental Material for the details [35]). When one removes an atom from the cell to create a vacancy, all three terms in Eq. (2) change. Figure 3 shows the difference in the third term, $E^{\rm int} = E_{\rm Hub} - E_{\rm DC}$, on each respective atom of the supercell before and after removing an atom. Summing this up and taking into account the multiplicity of the atoms in the cell yields a change $\Delta E^{\rm int} \approx -1.6$ eV, that is compensated by a larger change in $E[\rho^{\rm DMFT}]$ due to a redistribution of the charge density, as wave functions from DFT+DMFT are more localized. The contributions from the second and third coordination shells compensate one another, so that the net change in the interaction energy only comes from the first nearest neighbor. This is due to good metallic screening, and is in good agreement with embedded atom method calculations of iron vacancies near a surface [61] that show the vacancy formation energy becomes equal to the bulk value for the vacancy located in the third layer or deeper.

The self-energy of the vacancy's first coordination shell shows a significant difference from the bulk bcc-Fe self-energy, as shown in Figs. 4(a) and 4(b). t_{2g} states, but also e_g states to a lesser extent, become more strongly correlated

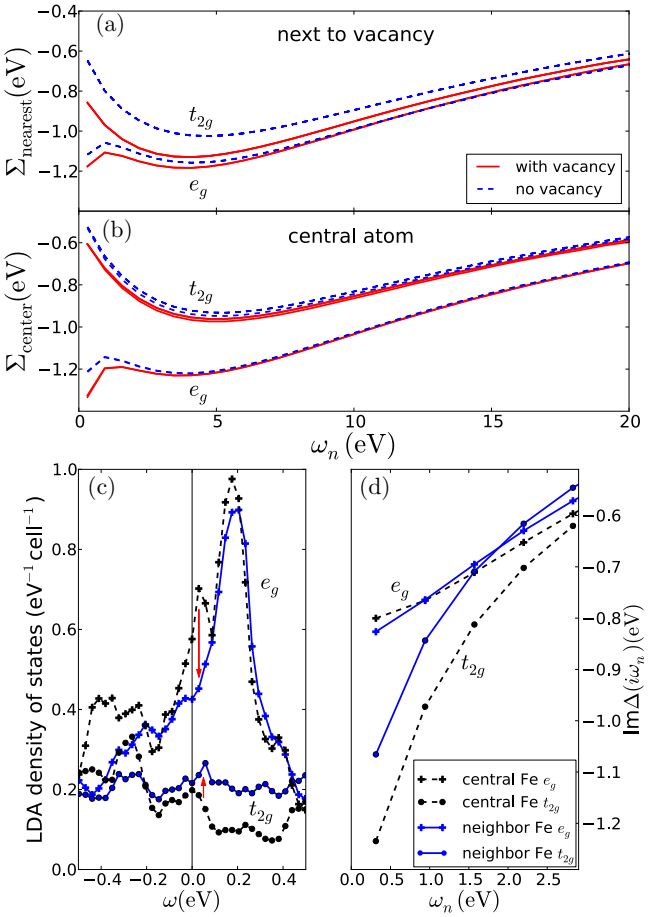

FIG. 4. Imaginary part of the Matsubara self-energies for (a) the vacancy nearest neighbor and (b) central atom in the $3 \times 3 \times 3$ supercell with a vacancy present (red, full) or without it (blue, dashed). Correlations become stronger on the atom nearest to the vacancy, while the difference between e_g and t_{2g} is strongly reduced. (c) LDA density of states around the Fermi level and (d) hybridization function on the Matsubara axis for the nearest neighbors (blue, full) to the vacancy, and for the central atom (black, dashed). The full Fe 3d DOS is shown in the Supplemental Material [35].

(less coherent) with a larger Im$\Sigma(i\omega)$. A larger absolute value of the imaginary part of the self-energy at low frequencies means a shorter quasiparticle lifetime, synonymous to stronger dynamic correlations. This difference almost vanishes for the self-energy of the atoms further than the nearest neighbor, in agreement with the variation of the interaction energy shown in Fig. 3. Stronger correlations on the atoms near the vacancy imply that a more correct description of the 3d electrons of the Fe atoms in DFT+DMFT, already important to predict the crystal structure and lattice parameter, is especially crucial when estimating the energetics of the vacancy and indeed leads to a smaller formation energy. Note that the self-energies are slightly atom dependent even in the absence of a vacancy in our calculations, due to an artificial symmetry breaking in the supercell in DFT calculations and the nonrotational invariance of the density-density Hubbard Hamiltonian. However, we compare self-energies and interaction energies in a consistent, atom-to-atom way.

The enhancement of the nearest-neighbor self-energy can be traced back to a change in the hybridization function. As can be seen in Fig. 4(d), the imaginary-frequency hybridization function, in particular for the t_{2g} states, is reduced at low frequencies for the atom near the vacancy. This reduction is due to an increase in the corresponding t_{2g} partial density of states (DOS) in the vicinity of the Fermi level, E_F, as one can see in Fig. 4(c). A larger DOS at E_F induces a suppression of low-energy hopping leading to stronger correlation [19,62]: at the first iteration of DMFT, $\mathrm{Im}\Delta(i0^+) = -\pi\rho_F/[\mathrm{Re}G_{\mathrm{loc}}(i0^+)^2 + (\pi\rho_F)^2] \approx -1/(\pi\rho_F)$, with ρ_F the LDA DOS. The enhancement of the nearest-neighbor e_g self-energy is smaller and the corresponding DOS at E_F even decreases compared to the bulk case. This decrease in the value of the DOS exactly at E_F is compensated by an overall narrowing of the e_g peak in the vicinity of E_F [see Fig. 4(c)]. Hence, the resulting hybridization function for e_g is still suppressed starting from the second Matsubara point.

Next, we calculated the relaxed atomic positions in DFT+DMFT around the vacancy. Computing atomic forces in DFT+DMFT is rather complicated [63], so we obtained the relaxed atomic positions by moving atoms and minimizing the total energies. We performed a relaxation of the atoms around the vacancy in two steps, in order to reduce the computational effort. We first performed the full relaxation in spin-polarized GGA (at its corresponding theoretical volume, computing atomic forces), to obtain an initial guess of the atomic positions. We observe a shift of the first coordination shell towards the vacancy by about 4%, and a shift of the second coordination shell away from the vacancy by about 1.5%, while all the other atoms do not move significantly, in agreement with previous calculations [25]. In the second step, the positions of the two first nearest neighbors were relaxed within DFT+DMFT. In Fig. 5 we show the total energy (minus an offset depending on the method used, GGA or DFT+DMFT) of the supercell as a function of the relaxed position of the nearest and second nearest neighbor of the vacancy. Each site was moved independently, preserving the symmetry of the cell, while the positions of others were fixed at their fractional GGA values. We obtain the following results: in DFT+DMFT, for paramagnetic α-Fe, the first nearest neighbor relaxes by 5.7% towards the vacancy, while the second nearest neighbor relaxes away from it by 0.7%. One sees that many-body effects have a significant impact on the nearest-neighbor relaxation, enhancing it by almost 50%. Overall, relaxing the two first coordination shells in full DFT+DMFT reduces the vacancy formation energy by 0.21 eV.

In conclusion, we have shown that local many-body effects are crucial for explaining a relatively low vacancy formation energy in α-Fe. The presence of a vacancy induces rather subtle changes in the local electronic structure of its surroundings, leading to a moderate increase in the strength of correlations at neighboring sites. This moderate increase has, however, a very significant impact on the vacancy energetics. When the effect of local relaxations is included, the calculated vacancy formation energy is reduced by about 0.7 eV compared with the corresponding DFT value and is in excellent agreement with experiment. The predicted magnitude of nearest-neighbor relaxations is about 50% larger compared to the one obtained within DFT. This remarkable sensitivity to correlation effects is most probably pertinent to other types of defects in iron that are of the crucial importance for mechanical properties and thermodynamics of steels, e.g., interstitial sites, stacking faults, and dislocations.

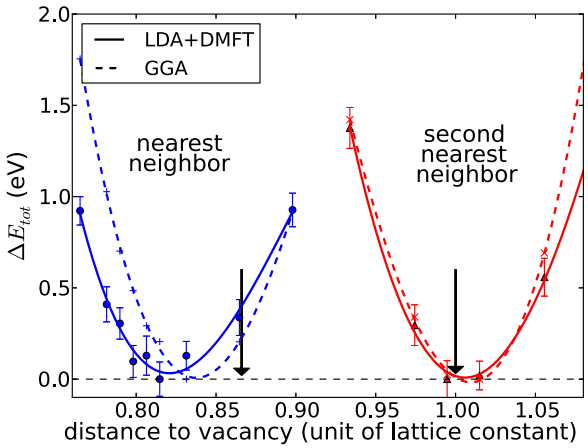

FIG. 5. Total energy vs distance to the vacancy (as a fraction of the lattice parameter) for the first nearest neighbor (blue) and the second nearest neighbor (red), in DFT+DMFT (full line) and GGA (dashed line). The black arrows show the position of the atoms in the unrelaxed bcc supercell.

L.P. acknowledges financial support of the Ministry of Education and Science of the Russian Federation in the framework of Increase Competitiveness Program of NUST MISiS (No. K2-2016-013). L.P. and S.I.S. acknowledge computational resources provided by the Swedish National Infrastructure for Computing (SNIC) at the National Supercomputer Centre (NSC) and PDC Center for High Performance Computing. S.I.S. acknowledges the Swedish Research Council (VR) Project No. 2014-4750, LiLi-NFM, and the Swedish Government Strategic Research Area in Materials Science on Functional Materials at Linköping University (Faculty Grant SFO-Mat-LiU No. 2009 00971). O.P. acknowledges support by the FP7/ERC, under Grant Agreement No. 278472-MottMetals. This work was further supported by IDRIS/GENCI Orsay under project t2016091393, and the European Research Council under the European Unions Seventh Framework Programme (FP7/2007-2013)/ERC Grant Agreements No. 617196 (CORRELMAT) and No. 319286 (Q-MAC).

[1] W. D. Callister and D. G. Rethwisch, *Materials Science and Engineering: An Introduction* (Wiley, New York, 2007), Vol. 7.

[2] C. Freysoldt, B. Grabowski, T. Hickel, J. Neugebauer, G. Kresse, A. Janotti, and C. G. Van de Walle, Rev. Mod. Phys. **86**, 253 (2014).

[3] M. Manninen, P. Hautojärvi, and R. Nieminen, Solid State Commun. **23**, 795 (1977).
[4] B. Chakraborty, R. W. Siegel, and W. E. Pickett, Phys. Rev. B **24**, 5445 (1981).
[5] K. Carling, G. Wahnström, T. R. Mattsson, A. E. Mattsson, N. Sandberg, and G. Grimvall, Phys. Rev. Lett. **85**, 3862 (2000).
[6] A.V. Ruban, Phys. Rev. B **93**, 134115 (2016).
[7] R. Armiento and A. E. Mattsson, Phys. Rev. B **72**, 085108 (2005).
[8] A. E. Mattsson, R. R. Wixom, and R. Armiento, Phys. Rev. B **77**, 155211 (2008).
[9] R. Nazarov, T. Hickel, and J. Neugebauer, Phys. Rev. B **85**, 144118 (2012).
[10] A. Glensk, B. Grabowski, T. Hickel, and J. Neugebauer, Phys. Rev. X **4**, 011018 (2014).
[11] T. Korhonen, M. J. Puska, and R. M. Nieminen, Phys. Rev. B **51**, 9526 (1995).
[12] B. Dorado, M. Freyss, B. Amadon, M. Bertolus, G. Jomard, and P. Garcia, J. Phys.: Condens. Matter **25**, 333201 (2013).
[13] L. V. Pourovskii, J. Mravlje, M. Ferrero, O. Parcollet, and I. A. Abrikosov, Phys. Rev. B **90**, 155120 (2014).
[14] V. L. Moruzzi, P. M. Marcus, K. Schwarz, and P. Mohn, Phys. Rev. B **34**, 1784 (1986).
[15] L. Stixrude, R. E. Cohen, and D. J. Singh, Phys. Rev. B **50**, 6442 (1994).
[16] P. Söderlind, J. A. Moriarty, and J. M. Wills, Phys. Rev. B **53**, 14063 (1996).
[17] A. A. Katanin, A. I. Poteryaev, A. V. Efremov, A. O. Shorikov, S. L. Skornyakov, M. A. Korotin, and V. I. Anisimov, Phys. Rev. B **81**, 045117 (2010).
[18] I. Leonov, A. I. Poteryaev, V. I. Anisimov, and D. Vollhardt, Phys. Rev. Lett. **106**, 106405 (2011).
[19] L. V. Pourovskii, T. Miyake, S. I. Simak, A. V. Ruban, L. Dubrovinsky, and I. A. Abrikosov, Phys. Rev. B **87**, 115130 (2013).
[20] D. Jaccard and A. T. Holmes, Phys. B (Amsterdam, Neth.) **359-361**, 333 (2005).
[21] K. Shimizu, T. Kimura, S. Furomoto, K. Takeda, K. Kontani, Y. Onuki, and K. Amaya, Nature (London) **412**, 316 (2000).
[22] I. I. Mazin, D. A. Papaconstantopoulos, and M. J. Mehl, Phys. Rev. B **65**, 100511 (2002).
[23] P. A. Korzhavyi, I. A. Abrikosov, B. Johansson, A. V. Ruban, and H. L. Skriver, Phys. Rev. B **59**, 11693 (1999).
[24] P. Söderlind, L. H. Yang, J. A. Moriarty, and J. M. Wills, Phys. Rev. B **61**, 2579 (2000).
[25] C. Domain and C. S. Becquart, Phys. Rev. B **65**, 024103 (2001).
[26] T. Hoshino, T. Mizuno, M. Asato, and H. Fukushima, Mater. Trans. **42**, 2206 (2001).
[27] T. Mizuno, M. Asato, T. Hoshino, and K. Kawakami, J. Magn. Magn. Mater. **226**, 386 (2001).
[28] Y. Tateyama and T. Ohno, Phys. Rev. B **67**, 174105 (2003).
[29] C.-C. Fu, F. Willaime, and P. Ordejón, Phys. Rev. Lett. **92**, 175503 (2004).
[30] P. M. Derlet, D. Nguyen-Manh, and S. L. Dudarev, Phys. Rev. B **76**, 054107 (2007).
[31] P. Olsson, C. Domain, and J. Wallenius, Phys. Rev. B **75**, 014110 (2007).
[32] T. Ohnuma, N. Soneda, and M. Iwasawa, Acta Mater. **57**, 5947 (2009).
[33] D. Kandaskalov, C. Mijoule, and D. Connétable, J. Nucl. Mater. **441**, 168 (2013).
[34] S. Dudarev, Mater. Res. **43**, 35 (2013).
[35] See Supplemental Material at http://link.aps.org/supplemental/10.1103/PhysRevB.94.100102 for details on the DFT and DMFT methodology, as well as an extensive overview of our and other groups' theoretical and experimental results.
[36] H.-E. Schaefer, K. Maier, M. Weller, D. Herlach, A. Seeger, and J. Diehl, Scr. Metall. **11**, 803 (1977).
[37] S. Kim and W. Buyers, J. Phys. F **8**, L103 (1978).
[38] H. Matter, J. Winter, and W. Triftshäuser, Appl. Phys. **20**, 135 (1979).
[39] L. De Schepper, D. Segers, L. Dorikens-Vanpraet, M. Dorikens, G. Knuyt, L. M. Stals, and P. Moser, Phys. Rev. B **27**, 5257 (1983).
[40] H.-E. Schaefer, Phys. Status Solidi A **102**, 47 (1987).
[41] A. Georges, G. Kotliar, W. Krauth, and M. J. Rozenberg, Rev. Mod. Phys. **68**, 13 (1996).
[42] G. Kotliar and D. Vollhardt, Phys. Today **57** (3), 53 (2004).
[43] V. Anisimov, A. Poteryaev, M. Korotin, A. Anokhin, and G. Kotliar, J. Phys.: Condens. Matter **9**, 7359 (1997).
[44] A. I. Lichtenstein and M. I. Katsnelson, Phys. Rev. B **57**, 6884 (1998).
[45] I. Leonov, A. I. Poteryaev, V. I. Anisimov, and D. Vollhardt, Phys. Rev. B **85**, 020401 (2012).
[46] I. Leonov, A. Poteryaev, Y. N. Gornostyrev, A. Lichtenstein, M. Katsnelson, V. I. Anisimov, and D. Vollhardt, Sci. Rep. **4**, 5585 (2014).
[47] G. Kotliar, S. Y. Savrasov, K. Haule, V. S. Oudovenko, O. Parcollet, and C. Marianetti, Rev. Mod. Phys. **78**, 865 (2006).
[48] S. Biermann, in *Electronic Structure of Transition Metal Compounds: DFT-DMFT Approach*, edited by K. H. Jürgen Buschow, R. W. Cahn, M. C. Flemings, B. Ilschner (print), and E. J. Kramer, S. Mahajan, P. Veyssire (updates), Encyclopedia of Materials: Science and Technology (Elsevier, Oxford, 2006), pp. 1–9.
[49] F. Lechermann, A. Georges, A. Poteryaev, S. Biermann, M. Posternak, A. Yamasaki, and O. K. Andersen, Phys. Rev. B **74**, 125120 (2006).
[50] V. I. Anisimov, D. E. Kondakov, A. V. Kozhevnikov, I. A. Nekrasov, Z. V. Pchelkina, J. W. Allen, S.-K. Mo, H.-D. Kim, P. Metcalf, S. Suga *et al.*, Phys. Rev. B **71**, 125119 (2005).
[51] D. A. Andersson and S. I. Simak, Phys. Rev. B **70**, 115108 (2004).
[52] A. Kokalj, Comput. Mater. Sci. **28**, 155 (2003).
[53] M. Aichhorn, L. Pourovskii, V. Vildosola, M. Ferrero, O. Parcollet, T. Miyake, A. Georges, and S. Biermann, Phys. Rev. B **80**, 085101 (2009).
[54] M. Aichhorn, L. Pourovskii, and A. Georges, Phys. Rev. B **84**, 054529 (2011).
[55] O. Parcollet, M. Ferrero, T. Ayral, H. Hafermann, I. Krivenko, L. Messio, and P. Seth, Comput. Phys. Commun. **196**, 398 (2015).
[56] M. Aichhorn, L. Pourovskii, P. Seth, V. Vildosola, M. Zingl, O. E. Peil, X. Deng, J. Mravlje, G. J. Kraberger, C. Martins *et al.*, Comput. Phys. Commun. **204**, 200 (2016).
[57] P. Blaha, K. Schwarz, G. Madsen, D. Kvasnicka, and J. Luitz, *WIEN2k, An Augmented Plane Wave + Local Orbitals Program*

for Calculating Crystal Properties (Karlheinz Schwarz, Techn. Universität Wien, Austria, 2001).

[58] E. Gull, A. J. Millis, A. I. Lichtenstein, A. N. Rubtsov, M. Troyer, and P. Werner, Rev. Mod. Phys. **83**, 349 (2011).

[59] S. Backes, T. C. Rödel, F. Fortuna, E. Frantzeskakis, P. Le Fèvre, F. Bertran, M. Kobayashi, R. Yukawa, T. Mitsuhashi, M. Kitamura *et al.*, arXiv:1602.06909.

[60] M. Behrmann and F. Lechermann, Phys. Rev. B **92**, 125148 (2015).

[61] C. Wang, Y. Yang, Y. Zhang, and Y. Jia, Comput. Mater. Sci. **50**, 291 (2010).

[62] J. Mravlje, M. Aichhorn, T. Miyake, K. Haule, G. Kotliar, and A. Georges, Phys. Rev. Lett. **106**, 096401 (2011).

[63] I. Leonov, V. I. Anisimov, and D. Vollhardt, Phys. Rev. Lett. **112**, 146401 (2014).

Novel Approaches to Spectral Properties of Correlated Electron Materials: From Generalized Kohn-Sham Theory to Screened Exchange Dynamical Mean Field Theory

Pascal Delange[1 *], Steffen Backes[1 †], Ambroise van Roekeghem[2 ‡], Leonid Pourovskii[1,3 §], Hong Jiang[4 ¶], and Silke Biermann[1,3,5 ‖]

[1]*Centre de Physique Théorique, École Polytechnique, 91128 Palaiseau, France*
[2]*CEA, LITEN, 17 Rue des Martyrs, 38054 Grenoble, France*
[3]*Collège de France, 11 place Marcelin Berthelot, 75005 Paris, France*
[4]*College of Chemistry and Molecular Engineering, Peking University, 100871 Beijing, China*
[5]*European Theoretical Spectroscopy Facility (ETSF), Europe*

The most intriguing properties of emergent materials are typically consequences of highly correlated quantum states of their electronic degrees of freedom. Describing those materials from first principles remains a challenge for modern condensed matter theory. Here, we review, apply and discuss novel approaches to spectral properties of correlated electron materials, assessing current day predictive capabilities of electronic structure calculations. In particular, we focus on the recent Screened Exchange Dynamical Mean-Field Theory scheme and its relation to generalized Kohn-Sham Theory. These concepts are illustrated on the transition metal pnictide $BaCo_2As_2$ and elemental zinc and cadmium.

1. Introduction

Technological progress has been intimately related with progress in materials science since its very early days. The last century has seen the development of refined capabilities for materials elaboration, characterisation and control of properties, culminating among others in the unprecedented possibilities of the digital age: materials properties have become an object of theoretical *simulations*, stimulating systematic searches for systems with desired characteristics. This branch of condensed matter physics is continuously evolving into a true new pillar of materials science, where the theoretical assessment of solid state systems becomes a fundamental tool for materials screening.

Obviously, the success of this program hinges on the degree of *predictive* power of modern simulation techniques, which have to allow for performing calculations without introducing adjustable parameters. This requirement is even more severe since the most popular branch of *ab initio* calculations, the Density Functional Theory (DFT) approach, is restricted to ground state properties of the solid, while most properties of potential technological interest stem from excited states: the calculation of any type of transport phenomenon, for example electric, thermal, thermoelectric or magnetoelectric transport, of optical or spectroscopic properties, or of magnetic, charge- or orbital susceptibilites requires the accurate assessment of highly non-trivial response functions within a finite-temperature description.

It is not a coincidence that the materials with the most exotic features are also most challenging to get to grips with from a theoretical point of view: both the complexity of their properties and the difficulty of their description are in fact a consequence of the very nature of the underlying electronic structure: typically, one is dealing with transition metal, lanthanide or actinide compounds, where the electrons in partially filled d- or f-shells strongly interact with each other through electron-electron Coulomb interactions, leading to highly entangled many-body quantum states.

Even when using a simplified description of the solid in terms of an effective lattice model, assessing these quantum correlated states is a tremendous challenge. If *local* quantum fluctuations on a given atomic site are dominant, dynamical mean-field theory (DMFT)[1,2] yields an accurate description of the system. In particular, DMFT captures both the strong coupling Mott-insulating limit and the weakly interacting band limit of the Hubbard model, and is able to describe the salient spectral features of a correlated metal with coexisting quasi-particle and Hubbard peaks even in the intermediate correlation regime. In the multi-orbital case, additional degrees of freedom can lead to even richer physics with unconventional (e.g. orbital-selective) behavior,[3] or complex ordering phenomena.[4–9]

In order to recover the material-specific character of the calculations, DMFT has been combined with DFT[10,11] into the so-called "DFT+DMFT" scheme, which is nowadays one of the most popular workhorses of electronic structure theory for correlated electron materials. Successful applications include transition metals,[12–14] transition metal oxides,[4,15–26] lanthanide[27,28] or actinide[29–32] systems. Comparisons be-

*pascal.delange@polytechnique.edu
†steffen.backes@polytechnique.edu
‡ambroise.vanroekeghem@gmail.com
§leonid@cpht.polytechnique.fr
¶jianghchem@pku.edu.cn
‖biermann@cpht.polytechnique.fr

tween calculated and measured spectral functions have sometimes led to impressive agreement.[33,34] However, despite these successes the construction of the Hamiltonian used in these calculations is rather *ad hoc* and remains a limitation to the predictive power of the approach. Therefore, the elaboration of more systematic interfaces between electronic structure and many-body theory has become an active area of research.[35]

In this work, we review a recent scheme combining screened exchange and DMFT.[36–38] We discuss its relation to many-body perturbation theory and generalized Kohn-Sham (KS) Theory and analyse the effects included at the different levels of the theory. As an illustration we describe its application to the low-energy spectral properties of the cobalt pnictide $BaCo_2As_2$.

How does a theory thas has been designed for strongly correlated materials reduce to an *a priori* simpler version in the case of a weakly correlated system ? For methods based on DFT that include only the static on-site Coulomb interaction between localized states, like DFT+U[39] or DFT+DMFT, the spectrum in the limit of vanishing Hubbard interactions reduces trivially to the Kohn-Sham spectrum of DFT. For more complex interfaces of electronic structure and many-body theory which we will discuss here, however, it is a non-trivial question and allows for interesting possibilities to check their consistency. Here, we will discuss this issue on the example of the transition metals zinc and cadmium. This also allows us to comment on the challenge of including states in a wider energy range, identifying a challenging problem on these seemingly "simple" systems.

The paper is organised as follows: in section 2 we review how Screened Exchange Dynamical Mean Field Theory derives from the combined many-body perturbation theory + dynamical mean field scheme "GW+DMFT". In section 3 we analyse the relation of screened exchange schemes to generalized KS theory. Section 4 provides an example of the application of such methods to $BaCo_2As_2$, while section 5 discusses the electronic structure of elemental zinc and cadmium within a simplified approach. Finally, we conclude in section 6.

2. From GW+DMFT to Screened Exchange Dynamical Mean Field Theory

Improving the predictive power of methods that combine electronic structure and many-body theory poses the challenge of properly connecting the two worlds, without double counting of interactions or screening. At the heart of this challenge lies the mismatch between the density-based description of DFT and the Green's function formalism used at the many-body level, as well as the difficulty of incorporating the feedback of high-energy screening processes governed by the unscreened Coulomb interaction onto the low-energy electronic structure. Conceptually speaking, these difficulties can be avoided by working on a large energy scale in the continuum with the full long-range Coulomb interactions, and a Green's function-based formalism even at the level of the weakly correlated states. These features are realised within the combined many-body perturbation theory and dynamical mean field theory scheme "GW+DMFT":[40–49] screening is assessed by the random phase approximation in the continuum, augmented by a local vertex correction, while the starting electronic structure for the DMFT calculation can be roughly interpreted as a "non-local GW" calculation.[50]

Screened Exchange Dynamical Mean Field Theory[36–38] can be understood as an approximation to this full GW+DMFT scheme. It is based on the recent observation[36,50] that within the *GW* approximation the correction to LDA can be split into two contributions: a local dynamical self-energy $\Sigma_{loc}(\omega)$ and a k-dependent but static self-energy $\Sigma_{nloc}(k)$, which does not contain any local component. If such a separation was strictly valid in the full energy range, the non-local static part of the full self-energy would be given by the non-local Hartree-Fock contribution, since the dynamical part vanishes at high frequency. In many realistic systems such a decomposition holds to a good approximation in the low-energy regime that we are interested in, where the static part $\Sigma_{nloc}(k)$ is quite different from the Fock exchange term. It is approximately given by a screened exchange self-energy, leading to a decomposition of the *GW* self-energy into $\Sigma_{GW} = [GW(\nu = 0)]_{nonloc} + [GW]_{loc}$. Here, the first term is a screened exchange contribution arising from the screened interaction $W(\nu)$ evaluated at zero frequency $W(\nu = 0)$. The second term is the local projection of the *GW* self-energy. It is simply given by the *GW* self-energy evaluated using a local propagator G_{loc} and the local screened Coulomb interaction W_{loc}. Exactly as in GW+DMFT, Screened Exchange Dynamical Mean Field Theory replaces this term by a non-perturbative one: it is calculated from an effective local impurity problem with dynamical interactions. In current practical applications of Screened Exchange + DMFT the RPA-screened Coulomb potential W has been replaced by its long-wavelength limit, which reduces to a simple Yukawa-form.[36]

Quite generally the dynamical character of the interactions results in an additional renormalization Z_B of the hopping amplitudes, which can be understood as an *electronic polaron* effect: the coupling of the electrons to plasmonic screening degrees of freedom leads to an effective mass enhancement corresponding to the hopping reduction, manifesting itself as a narrowing of the band. This effect can be estimated from the plasmon density of modes as given by the imaginary part of the frequency dependent interaction W. An explicit expression for Z_B has been derived in Ref. 51.

3. Relation to Generalized Kohn-Sham Theory

Screened Exchange Dynamical Mean Field Theory can also be viewed as a specific approximation to a spectral density functional theory based on the Generalized Kohn-Sham (GKS) scheme of Seidl *et al.*[52] In GKS theory, alternative choices for the reference system that are different than the familiar Kohn-Sham system of DFT are explored. In particular, a generalized Kohn-Sham scheme where the reference system is a screened exchange Hamiltonian can be constructed. The main motivation for the inclusion of screened

exchange in the literature has been to improve upon the band gap problem in semiconductors. Indeed, it can be shown that the screened exchange contribution, which corresponds to a non-local potential, effectively reintroduces to some degree the derivative discontinuity that is missing in the pure DFT description based on local exchange-correlation potentials.[53] Since the derivative discontinuity corresponds to the discrepancy between the true gap and the Kohn-Sham gap in exact DFT, a substantial improvement of the theoretical estimate for band gaps can be expected on physical grounds and has indeed been found. Here, our goal is somewhat different: motivated by the analysis of the role of screened exchange in GW+DMFT described above, we would like to connect the Screened Exchange DMFT scheme introduced above to generalized KS schemes making direct use of the non-local screened exchange potential.

With this aim in mind, we briefly review the generalized Kohn-Sham construction in the case an effective Kohn-Sham system including screened exchange. Hereby, we follow closely Seidl *et al.*,[52] both in notation and presentation. First, one defines a functional

$$S\left[\Phi\right] = \left\langle \Phi \left| \hat{T} \right| \Phi \right\rangle + U_H\left[\{\phi_i\}\right] + E_x^{sx}\left[\{\phi_i\}\right] \tag{1}$$

that includes, in addition to the familiar kinetic energy term $\langle\Phi|\hat{T}|\Phi\rangle$ and the Hartree energy $U_H\left[\{\phi_i\}\right]$ also the screened Fock term

$$E_x^{sx}\left[\{\phi_i\}\right] = -\sum_{i<j}^{N}\int d\boldsymbol{r}d\boldsymbol{r}' \times \frac{\phi_i^*(\boldsymbol{r})\phi_j^*(\boldsymbol{r}')e^{-k_{\mathrm{TF}}|\boldsymbol{r}-\boldsymbol{r}'|}\phi_j(\boldsymbol{r})\phi_i(\boldsymbol{r}')}{|\boldsymbol{r}-\boldsymbol{r}'|} \tag{2}$$

Here, Φ are Slater determinants of single-particle states ϕ_i. k_{TF} is the Thomas Fermi wave vector. In order to derive a functional of the density Seidl *et al.* define a functional F^s via the minimisation

$$F^S\left[\rho\right] = \min_{\Phi\to\rho(\boldsymbol{r})} S\left[\Phi\right] = \min_{\{\phi_i\}\to\rho(\boldsymbol{r})} S\left[\{\phi_i\}\right] \tag{3}$$

Next we define the energy functional

$$E^S\left[\{\phi_i\}; v_{eff}\right] = S\left[\{\phi_i\}\right] + \int d\boldsymbol{r} v_{eff}(\boldsymbol{r})\rho(\boldsymbol{r}) \tag{4}$$

where now the potential v_{eff} does not only include the external potential v as in usual DFT, but also a contribution by the exchange-correlation part

$$v_{eff} = v + v_{xc}^{sx}\left[\rho\right]. \tag{5}$$

The additional contribution, the generalized (local) exchange-correlation potential

$$v_{xc}^{sx} = \frac{\partial E_{xc}^{sx}\left[\rho\right]}{\partial\rho}. \tag{6}$$

is the functional derivative of the generalized (local) exchange-correlation functional

$$E_{xc}^{sx}\left[\rho\right] = E_{xc}\left[\rho\right] - E_x^{sx}\left[\rho\right] + T\left[\rho\right] - T^{sx}\left[\rho\right] \tag{7}$$

which comprises the difference between the exchange-correlation potential of standard Kohn-Sham DFT and the non-local exchange energy defined above, as well as the difference between the kinetic energies of the standard and generalized Kohn-Sham systems. The functional derivative will eventually have to be evaluated self-consistently at the converged density.

This construction leads to the generalized Kohn-Sham equations

$$-\nabla^2\phi_i(\boldsymbol{r}) + v(\boldsymbol{r})\phi_i(\boldsymbol{r}) + u\left([\rho];\boldsymbol{r}\right)\phi_i(\boldsymbol{r}) - \int d\boldsymbol{r}' v_x^{sx,\mathrm{NL}}(\boldsymbol{r},\boldsymbol{r}')\phi_i(\boldsymbol{r}') + v_{xc}^{sx}\left([\rho];\boldsymbol{r}\right)\phi_i(\boldsymbol{r}) = \varepsilon_i\phi_i \tag{8}$$

with the Hartree potential u and the non-local screened Fock potential

$$v_x^{sx,\mathrm{NL}}(\boldsymbol{r},\boldsymbol{r}') = -\sum_{j=1}^{N}\frac{\phi_i(\boldsymbol{r})e^{-k_{\mathrm{TF}}|\boldsymbol{r}-\boldsymbol{r}'|}\phi_j^*(\boldsymbol{r}')}{|\boldsymbol{r}-\boldsymbol{r}'|}. \tag{9}$$

and the effective (local) generalized Kohn Sham potential v_{xc}^{sx} defined above. The generalized Kohn-Sham equations have the form

$$\hat{O}\left[\{\phi_i\}\right]\phi_j + \hat{v}_{eff}\phi_j = \epsilon_j\phi_j \tag{10}$$

where $\hat{O}$ is a non-local operator, generalizing the standard Kohn-Sham operator consisting solely of kinetic energy and Hartree potential.

The ground state energy for a system in the external potential v is then given by the expression

$$E_{\mathrm{SEx-DFT}}\left[v\right] = F^S\left[\rho_0^S\left[v_{eff}\right]\right] + E_{xc}^{sx}\left[\rho_0^S\left[v_{eff}\right]\right] + \int dr v(r)\rho_0^S\left[v_{eff}\right] \tag{11}$$

Now, the relation to Screened Exchange DMFT is becoming clear: one may construct a spectral density functional in the same spirit as in DFT+DMFT,[54] but starting from the generalized KS functional. In 55, the expression for the total energy within the standard DFT+DMFT case was derived to be

$$E = E_{\mathrm{DFT}} - \sum_l \epsilon_l^{\mathrm{KS}} + \langle H_{\mathrm{KS}}\rangle + \langle(H_{int} - H_{dc})\rangle \tag{12}$$

where $\sum_l \epsilon_l^{\mathrm{KS}}$ is the sum of the occupied Kohn-Sham eigenvalues, $\langle H_{\mathrm{KS}}\rangle = \mathrm{tr}\left[H_{KS}\hat{G}\right]$, and H_{int} and H_{dc} denote the local interaction part of the Hamiltonian and the corresponding double counting term, respectively.

Instead of using the usual Kohn-Sham Hamiltonian for the construction of the one-body part, Screened Exchange DMFT relies on the generalized Kohn-Sham reference system that includes the screened exchange potential. The generalization of (12) to the present case thus replaces the Kohn-Sham Hamiltonian H_{KS} in the expression for the energy by its non-local form, keeping track of the effective potential part:

$$E = E_{\mathrm{SEx-DFT}} - \sum_l \epsilon_l^{\mathrm{SEx-KS}} + \langle\hat{O} + \hat{v}_{eff}\rangle$$

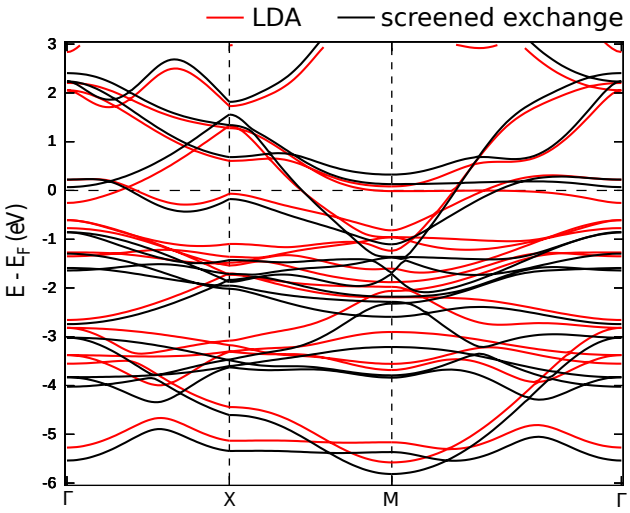

Fig. 1. (Color online) Kohn-Sham band structure of $BaCo_2As_2$ within DFT-LDA (red lines) and the screened exchange approximation (black lines).

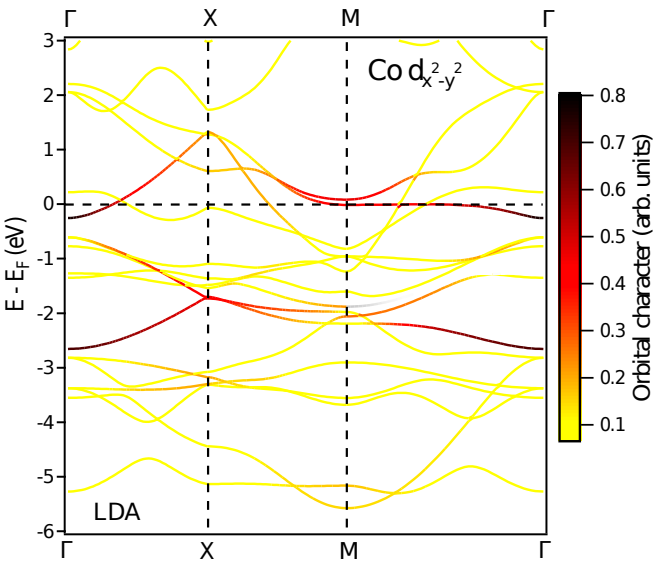

Fig. 2. (Color online) Kohn-Sham band structure of $BaCo_2As_2$ within DFT-LDA, projected on the $d_{x^2-y^2}$ orbital.

$$+\langle (H_{int}(V_{ee}, \lambda_s, \omega_s) - H_{dc}) \rangle \qquad (13)$$

Furthermore, the local interaction term is taken in the more general form of a dynamical interaction, thus corresponding to a local Hubbard term with *unscreened* interactions and local Einstein plasmons of energy ω_s coupling to the electrons via coupling strength λ_s.

This concludes our description of the generalized Kohn-Sham interpretation of Screened Exchange DMFT, resulting in particular in an energy functional expression. However, in the practical calculations presented in the following we do not minimise the full energy expression as given above, but rather work at the converged DFT density and then investigate spectral properties using the Screened Exchange DMFT formalism. This amounts to a one-shot Screened Exchange-DFT+DMFT calculation that uses the DFT density as a starting point. The advantage of such an approach is obvious: Numerically, this procedure allows us to avoid the expensive evaluation of non-local exchange terms within the self-consistency cycle of GKS theory. Moreover, as is well-known, while severe deviations of the true spectrum from the Kohn-Sham spectrum are quite common, the ground state density obtained even from approximate DFT functionals is often a good representation of the true one. In the case of the *exact* DFT functional, our approach would also lead to the exact ground state density and energy, with additional improvements of the spectrum over standard Kohn-Sham DFT.

4. Results on $BaCo_2As_2$

As a first illustration of Screened Exchange DMFT, we review calculations on $BaCo_2As_2$, which is the fully Co-substituted representative of the so-called "122" family of the iron-based superconductors, isostructural to the prototypical parent compound $BaFe_2As_2$. The Fe → Co substitution has however important consequences: the nominal filling of the $3d$ states changes from d^6 to d^7, which strongly reduces the degree of Coulomb correlations, making $BaCo_2As_2$ a moderately correlated compound.[36,56] Indeed, the power-law deviations from Fermi liquid behavior above an extremely low coherence temperature discussed in the Fe-based compounds[57] are a consequence of the d^6 configuration and strong intra-atomic exchange interactions. This is no longer the case in the cobalt pnictides, where angle-resolved photoemission spectroscopy (ARPES) identifies well-defined and long-lived quasiparticle excitations with relatively weak mass renormalization. Nevertheless, the DFT-LDA derived Fermi surface differs from experiment.[36,56,58,59] Therefore, $BaCo_2As_2$ provides an ideal testing ground for new approaches to spectroscopic properties. We do not discuss here the details of yet another interesting question, which is the absence of ferromagnetism despite a high value of the DFT density of states at the Fermi level, suggestive of Stoner ferromagnetism, but refer the reader to Ref. 36, where the solution to this puzzle was discussed in detail.

Fig. 1 shows the DFT band structure of $BaCo_2As_2$, in comparison to a screened exchange calculation. As in the iron-based pnictides, the dominantly $3d$-derived states are located around the Fermi level; in this case in a window of about -3 eV to 2 eV. As compared to the parent iron pnictides with $3d^6$ configuration of the Fe shell, the Fermi surface topology is modified due to the larger $3d^7$ filling. The hole pocket at the Γ point that is present in most Fe-based pnictide compounds is pushed below the Fermi level, as well as the band forming the electron pocket at M, which is now fully filled. In standard DFT-LDA (see Fig. 2), a characteristic flat band of dominant $x^2 - y^2$ character lies directly on the Fermi level around the M point, giving rise to a huge peak in the density of states.

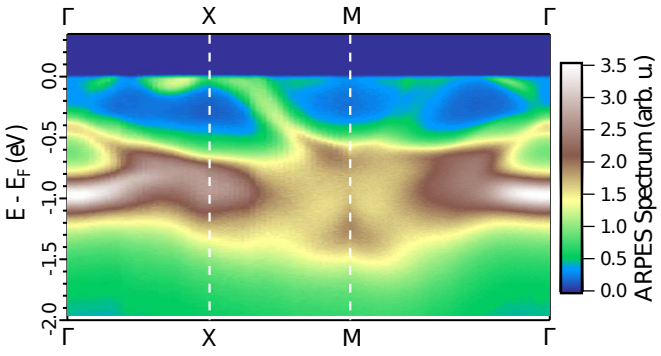

Fig. 3. (Color online) Angle-resolved photoemission spectrum of $BaCo_2As_2$. Adapted from Ref. 36.

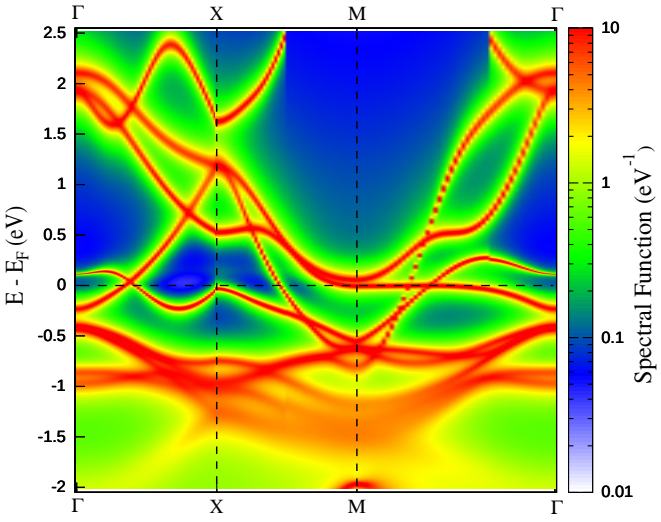

Fig. 4. (Color online) k-resolved spectral function of $BaCo_2As_2$ within LDA+DMFT. Adapted from Ref. 36.

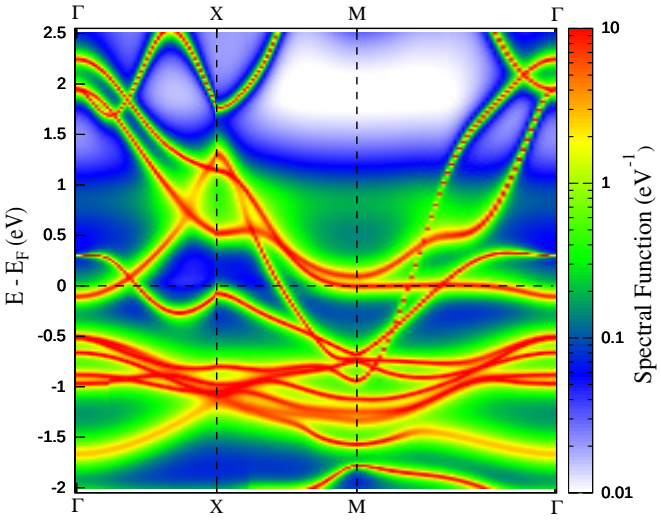

Fig. 5. (Color online) k-resolved spectral function of $BaCo_2As_2$ within Screened Exchange DMFT (with dynamical interactions). Adapted from Ref. 36.

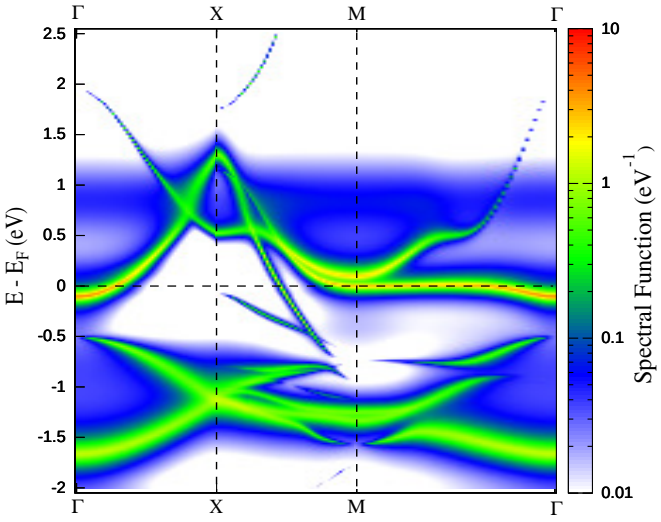

Fig. 6. (Color online) k-resolved spectral function of $BaCo_2As_2$ within Screened Exchange DMFT (with dynamical interactions), projected on the $d_{x^2-y^2}$ orbital. Adapted from Ref. 36.

The close proximity of this band to the Fermi level will render its energy highly sensitive to the details of the calculation and thus provides a perfect benchmark for improved computational techniques.

Comparison to angle-resolved photoemission experiments,[36] as reproduced in Fig. 3, reveals that the overall bandwidth of the LDA band structure is too wide by roughly a factor of 1.5. In a DFT+DMFT calculation, as shown in Fig. 4, this band renormalisation is reproduced, giving an overall occupied bandwidth of about 1.5 eV. The fine details of the Fermi surface, and in particular the position of the flat $x^2 - y^2$ band are however not well described. For a detailed comparison we refer the reader to Ref. 36.

Including screened exchange in the form of a Yukawa potential on top of DFT, as shown in Fig. 1 widens the band by a considerable amount as compared to DFT-LDA. Even more striking are the modifications at the Fermi level: the $x^2 - y^2$ band has been shifted above the Fermi level, with an energy at the M point of about 0.15 eV above E_F. While the lowering of the filling of this band improves the agreement between theory and experiment, the shift is too large to reproduce the experimental Fermi surface. However, when applying DMFT with dynamical interactions on top of the screened exchange Hamiltonian, equivalent to the one-shot Screened Exchange DMFT procedure described above, this band is renormalized by the electronic interactions and ends up again close (but above!) the Fermi level. Its energy is slightly higher than in DFT-LDA and is now in excellent agreement with the experimental Fermi surface. A more detailed analysis presented in Ref.[36] reveals that also the higher energy features such as the bands within the range of up to 2 eV are well reproduced in this one-shot Screened Exchange DMFT approach.

The comparison of the band structures and spectral func-

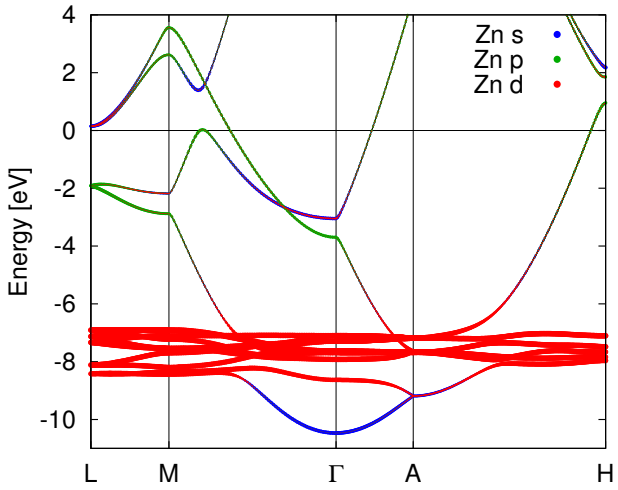

Fig. 7. (Color online) The band structure of elemental Zn calculated within DFT. The orbital character is indicated by the intensity of the different colors.

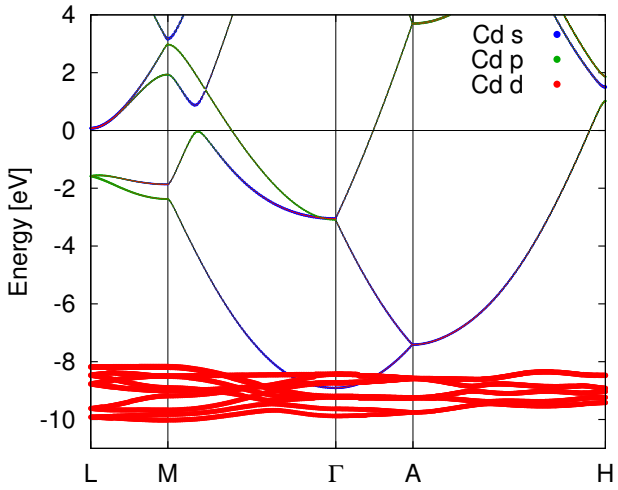

Fig. 8. (Color online) The band structure of elemental Cd calculated within DFT. The orbital character is indicated by the intensity of the different colors.

tions within the different computational schemes illustrates the effects of the different terms in an instructive way: Improving on the description of exchange by replacing the local exchange as contained in DFT-LDA by a non-local screened Fock exchange widens the bandwidth and strongly "overcorrects" the Fermi surface. Improving at the same time on the correlation part by applying DMFT with frequency-dependent interactions then leads to a partial cancellation of the band widening, giving an overall bandwidth surprisingly close to the LDA+DMFT one. This suggests that the good description of the overall bandwidth in DFT+DMFT is the result of an error cancellation between the local approximation to exchange and partial neglect of correlations. However, the Fermi surface is strongly modified by the non-local corrections, leading to a significant improvement over LDA+DMFT and resulting in good agreement with experiment.

These findings might suggest that possible inconsistencies between theoretical and experimental Fermi surfaces that are observed in many pnictide materials could be corrected by adding simple non-local self-energy corrections stemming from screened exchange effects. Whether this treatment can fully account for the "red-blue shift" of Fermi surface pockets found in the experimental-theoretical comparisons[60] is a most interesting topic for future research. The current example may give rise to optimism.

5. How does Screened Exchange Dynamical Mean Field Theory behave for weakly correlated materials?

Hamiltonians built as combinations of a DFT part and local Hubbard-type interaction terms trivially reduce to the DFT Kohn-Sham electronic structure when assuming that in weakly correlated materials the effective local interactions become negligible. The question of the recovery of the weakly interacting limit is, however, more interesting in the case of Screened Exchange DMFT. While the static part of the effective local interaction may be assumed to lose its importance, band widening by the replacement of the DFT exchange correlation potential by the non-local exchange-correlation GW self-energy persists. On the other hand, plasmonic effects are also present in weakly correlated materials and continue to renormalize the low-energy band structure through electron-plasmon coupling. This raises the question of what the resulting spectra for weakly correlated materials look like in screened exchange + DMFT.

In Ref. 38, this question has been studied for early transition metal perovskites, where it was found that the band widening effect induced by non-local exchange and the electronic polaron effect counteract each other and tend to approximately cancel, thus resulting in a low-energy electronic structure close to the DFT Kohn-Sham band structure as long as static Hubbard interactions are disregarded. Here, we address this question in the case of the seemingly "simple" transition metals zinc and cadmium.

Both elements nominally display a d^{10} configuration, with fully occupied $3d$ orbitals in the case of Zn and $4d$ in the case of Cd, the dominantly d-derived bands being located several eV below the Fermi level. In Fig. 7 and Fig. 8 we show the band structure calculated within DFT for both materials. Here and in the following we use the experimental crystal structure. DFT puts the occupied d states at around -8 eV in Zn and -9 eV in Cd. The conducting states of this transition metal are formed by dispersive $4s(5s)$ in Zn(Cd) states around the Fermi level, that hybridize with the p-manifold.

These facts raise the immediate expectation of negligibly small correlation effects on the occupied d shells. An effective Hubbard interaction calculated for the d-manifold within the constrained random phase approximation coincides with the fully screened interaction, since as a consequence of the

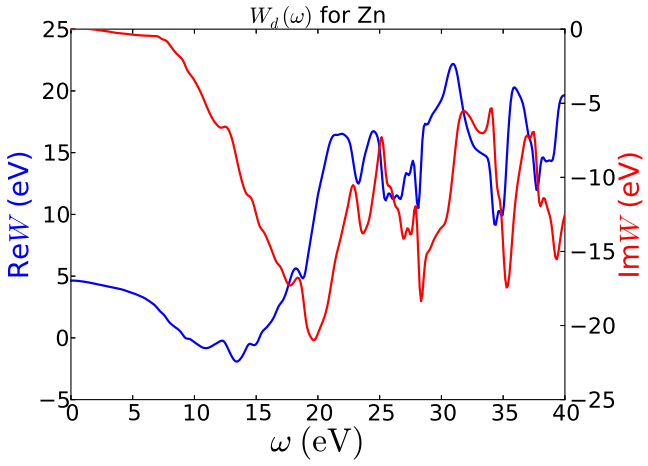

Fig. 9. (Color online) The fully screened effective local Hubbard interaction on the 3*d* manifold for Zn.

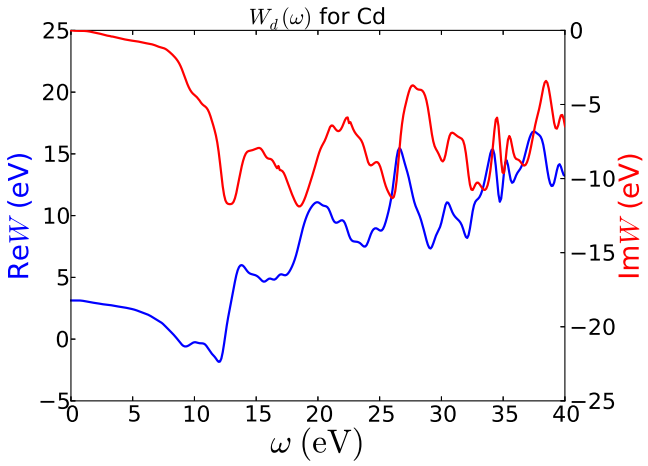

Fig. 10. (Color online) The fully screened effective local Hubbard interaction on the 4*d* manifold for Cd.

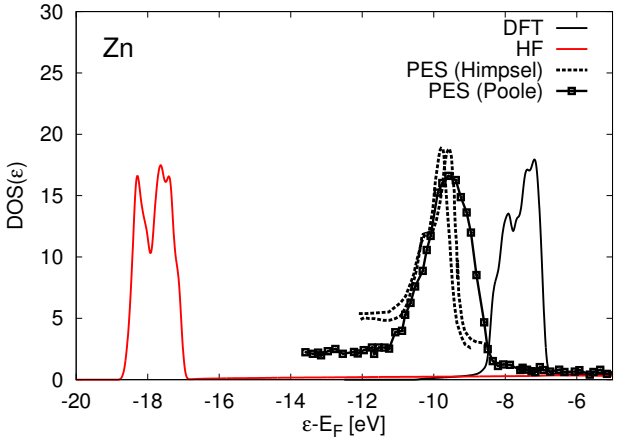

Fig. 11. (Color online) The Density of States of elemental Zn calculated within Density Functional Theory (DFT, black solid line) and Hartree-Fock (HF, red solid line) in comparison with Photoemission experiments[61,62] (dashed line, symbols). Density Functional Theory (DFT) calculations underestimate the binding energy of the Zn 3*d* states, while the HF overestimates the binding energy significantly (see explanation in the text).

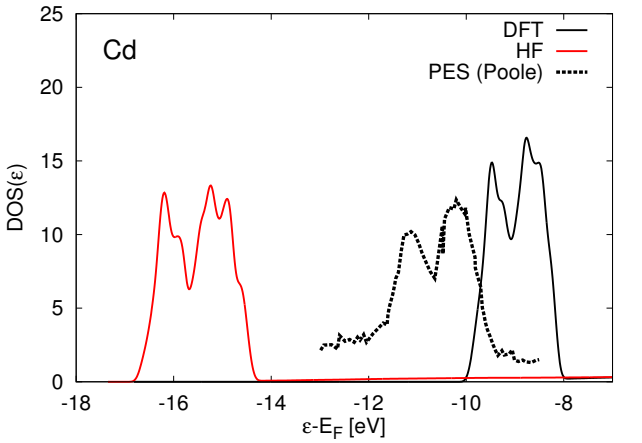

Fig. 12. (Color online) The Density of States of elemental Cd calculated within Density Functional Theory (DFT, black solid line) and Hartree-Fock (HF, red solid line) in comparison with Photoemission experiments[61] (dashed line, symbols). Density Functional Theory (DFT) calculations underestimate the binding energy of the Cd 3*d* states, while the HF overestimates the binding energy significantly (see explanation in the text).

complete filling of the d-shell there are no intra-d transitions to be cut out as opposed to an open shell system, where transitions inside the shell contribute to screening effects.

Figs. 9 and 10 display the local component of this fully screened interaction projected on the *d*-manifold. The low-frequency limit approaches a value of 4.8 eV and 3.1 eV for Zn and Cd respectively. Even though this value is similar to their oxides, which are open shell systems, where correlations on the *d* states are significant, the high binding energy of these states far away from the Fermi level effectively prevents dynamical fluctuations. This suggests that screened exchange + DMFT should in fact reduce to screened exchange renormalized by the bosonic factor Z_B discussed above. Nevertheless, this does not mean that static effects of the interaction are properly treated in DFT. Even if this were the case, there is no reason that the DFT Kohn-Sham spectrum, being derived from an effective non-interacting system, provides an accurate description of the experimental situation.

Figs. 11 and 12 compare the experimental photoemission spectra[61,62] from the literature to the density of states (DOS) derived from DFT and Hartree-Fock (HF) theory. The resulting discrepancy in terms of an underestimation of the binding energy of the *d* states in DFT of several eV had been noted in the literature before:[63–65] Norman *et a.l*[63] discussed it in terms of a self-interaction error, proposing a correction in

terms of an approximate substraction of self-interaction contributions contained in DFT.[66] Hartree-Fock calculations are, on the one hand, self-interaction free, but on the other hand – due to the absence of screening – widen all bands and place the *d*-bands far too low in energy, as can be seen in Figs. 11 and 12.

Since local dynamical correlations can assumed to be small as discussed before, an improved treatment of the screened interaction *and* the self-interaction correction at the same time is likely to improve the shortcomings of Hartree-Fock, resp. DFT. Here we will discuss the two possible extensions of Screened Exchange plus a bosonic renormalization factor Z_B and the GW approximation. The computationally cheaper option of screened exchange is including only static exchange contributions with a Yukawa-type interaction potential, and an effective renormalization Z_B which originates from the spectral weight transfer to plasmonic excitations. GW is computationally more demanding, but has the advantage of treating the dynamical part of the screening and correlation. Even though both methods include a self-interaction correction, the self-interaction contained in the Hartree term is not completely cancelled since the exchange contributions are derived from a screened interaction and not the bare one, as opposed to the Hartree term.

In Figs. 13 and 14 we show comparisons of the DOS of zinc and cadmium, calculated within DFT, screened Exchange($+Z_B$) and GW[67] to photoemission spectra. In the GW calculation we used $7 \times 7 \times 3$ k-points and 5 additional high-energy local orbitals. Interestingly, while in both systems the GW approximation provides a significant correction of the DFT Kohn-Sham spectrum in the right direction, but still underestimates the binding energy, the screened exchange scheme places the d-states too low in energy for Zn while providing a slightly better estimate than GW in Cd. The addition of the bosonic renormalization factor Z_B merely renormalizes the d bandwidth but keeps the average level position constant.

This raises the interesting question of which effects are missing in screened exchange and GW? The incomplete cancellation of the self-interaction in both approaches is expected to lead to an overall underestimation of the binding energy, since the additional unphysical interaction increases the energy of the d states. A more accurate estimate of this term would lead to an improvement of GW in both systems, but an even larger error of screened exchange in Zn. Another effect neglected in screened exchange is the Coulomb hole contribution: this term, discussed by Hedin as part of the "Coulomb hole screened exchange (COHSEX)" approximation translates the fact that the presence of an electron at a position r pushes away charge at r (in the language of a lattice model, the charge-charge correlation function exhibits a reduction of the double occupancy), and the interaction of this effective positive charge with the electron presents an energy gain expressed in the form of an interaction of the electron with a "Coulomb hole". This term, contained in GW but not in screened exchange, also increases the binding energy.

This leads to the overall picture that screened exchange

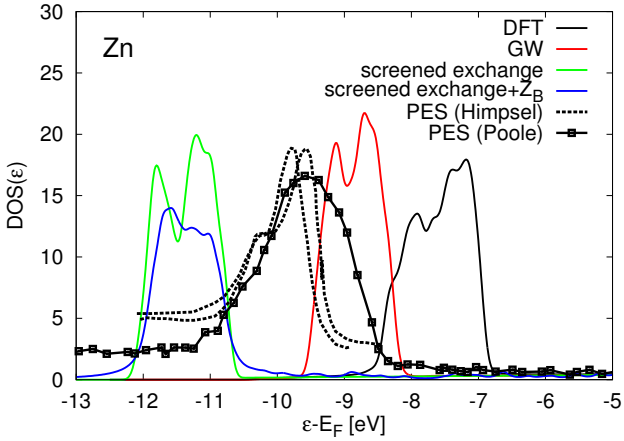

Fig. 13. (Color online) The Density of States of elemental Zn calculated within different theoretical methods (solid lines), in comparison with Photoemission experiments[61,62] (dashed line, symbols). Density Functional Theory (DFT) calculations significantly underestimate the binding energy of the Zn 3*d* states, while the GW approximation obtains a much better agreement. Screened exchange overestimates the binding energy significantly.

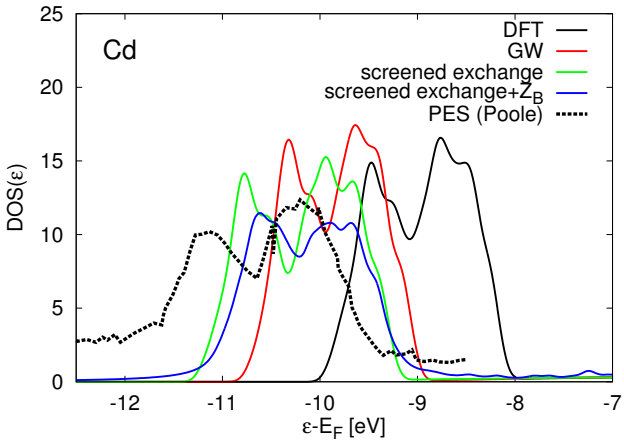

Fig. 14. (Color online) The Density of States of elemental Cd calculated within different theoretical methods (solid lines), in comparison with Photoemission experiments[61] (dashed line). DFT calculations significantly underestimate the binding energy of the Cd 4*d* states, while the GW approximation and also screened exchange obtain a much better agreement.

with the inclusion of the static corrections just discussed has a tendency to overestimate the binding energy in general, while GW underestimates it. The obvious difference between the two methods is the dynamical treatment of the screened interaction, which is treated more appropriately in GW, but it is not clear *a priori* whether the *static* approximation of the screened interaction or the approximated *form* of the screened interaction in terms of a Yukawa potential gives rise to the difference between screened exchange and GW.

The GW description of zinc and cadmium is close to the experiment. The remaining discrepancy to experiment is likely

explained by remaining self-interaction contributions and/or missing self-consistency. Self-consistency (or quasiparticle self-consistency) has been investigated in the homogeneous electron gas[68] and various solid state systems.[69] These questions are left for future work.

6. Conclusions

In this work we have reviewed and applied existing as well as novel approaches to obtain spectral properties of correlated electron materials. Guided by the need of a proper treatment of the long-range Coulomb interaction and non-local exchange effects we presented a lightweight version of the general GW+DMFT approach, the so-called Screened Exchange DMFT. It can be derived as a simplication to GW+DMFT in terms of a generalized screened exchange DFT scheme where local interactions are treated by dynamical DMFT.

Analysis and the application of a simplifed form of this scheme to $BaCo_2As_2$ indeed showed that non-local exchange and electronic screening lead to significant corrections to the electronic spectrum which are necessary to obtain a proper description of the experimental observations.

Furthermore, we discussed the case of the elemental transition metals Zn and Cd, where strong local correlations are unimportant but the position of the occupied d manifold is very sensitive to a proper treatment of screened exchange effects.

SB and AvR thank their collaborators of Refs.36 and 37 for the fruitful collaborations and discussions. This work was supported by IDRIS/GENCI Orsay under project t2017091393, the European Research Council under its Consolidator Grant scheme (project 617196), and the ECOS-Sud grant A13E04. HJ acknowledges financial support from National Natural Science Foundation (21373017, 21621061) and the National Basic Research Program of China (2013CB933400).

1) A. Georges, G. Kotliar, W. Krauth, and M. J. Rozenberg: Reviews of Modern Physics **68** (1996) 13.
2) G. Kotliar and D. Vollhardt: Physics Today **March 2004** (2004) 53.
3) S. Biermann, L. de' Medici, and A. Georges: Phys. Rev. Lett. **95** (2005) 206401.
4) E. Pavarini, S. Biermann, A. Poteryaev, A. I. Lichtenstein, A. Georges, and O. K. Andersen: Phys. Rev. Lett. **92** (2004) 176403.
5) C. Martins, M. Aichhorn, L. Vaugier, and S. Biermann: Phys. Rev. Lett. **107** (2011) 266404.
6) R. Arita, J. Kuneš, A. V. Kozhevnikov, A. G. Eguiluz, and M. Imada: Phys. Rev. Lett. **108** (2012) 086403.
7) K.-H. Ahn, K.-W. Lee, and J. Kuneš: Journal of Physics: Condensed Matter **27** (2015) 085602.
8) J. Kuneš and V. Křápek: Phys. Rev. Lett. **106** (2011) 256401.
9) J. Kuneš: Phys. Rev. B **90** (2014) 235140.
10) V. Anisimov, A. Poteryaev, M. Korotin, A. Anokhin, and G. Kotliar: Journal of Physics: Condensed Matter **9** (1997) 7359.
11) A. Lichtenstein and M. Katsnelson: Physical Review B **57** (1998) 6884.
12) A. I. Lichtenstein, M. I. Katsnelson, and G. Kotliar: Phys. Rev. Lett. **87** (2001) 067205.
13) P. Delange, T. Ayral, S. I. Simak, M. Ferrero, O. Parcollet, S. Biermann, and L. Pourovskii: Phys. Rev. B **94** (2016) 100102.
14) J. Sánchez-Barriga, J. Minár, J. Braun, A. Varykhalov, V. Boni, I. Di Marco, O. Rader, V. Bellini, F. Manghi, H. Ebert, M. I. Katsnelson, A. I. Lichtenstein, O. Eriksson, W. Eberhardt, H. A. Dürr, and J. Fink: Phys. Rev. B **82** (2010) 104414.
15) S. Biermann, A. Poteryaev, A. I. Lichtenstein, and A. Georges: Phys. Rev. Lett. **94** (2005) 026404.
16) A. I. Poteryaev, J. M. Tomczak, S. Biermann, A. Georges, A. I. Lichtenstein, A. N. Rubtsov, T. Saha-Dasgupta, and O. K. Andersen: Phys. Rev. B **76** (2007) 085127.
17) J. M. Tomczak and S. Biermann: Journal of Physics: Condensed Matter **19** (2007) 365206.
18) J. M. Tomczak and S. Biermann: EPL (Europhysics Letters) **86** (2009) 37004.
19) J. M. Tomczak and S. Biermann: Journal of Physics: Condensed Matter **21** (2009) 064209.
20) J. M. Tomczak, A. I. Poteryaev, and S. Biermann: Comptes Rendus Physique **10** (2009) 537 .
21) I. A. Nekrasov, N. S. Pavlov, and M. V. Sadovskii: Journal of Experimental and Theoretical Physics **116** (2013) 620.
22) P. Thunström, I. Di Marco, and O. Eriksson: Phys. Rev. Lett. **109** (2012) 186401.
23) I. Leonov, L. Pourovskii, A. Georges, and I. A. Abrikosov: Phys. Rev. B **94** (2016) 155135.
24) V. I. Anisimov, D. E. Kondakov, A. V. Kozhevnikov, I. A. Nekrasov, Z. V. Pchelkina, J. W. Allen, S.-K. Mo, H.-D. Kim, P. Metcalf, S. Suga, A. Sekiyama, G. Keller, I. Leonov, X. Ren, and D. Vollhardt: Phys. Rev. B **71** (2005) 125119.
25) A. Sekiyama, H. Fujiwara, S. Imada, S. Suga, H. Eisaki, S. I. Uchida, K. Takegahara, H. Harima, Y. Saitoh, I. A. Nekrasov, G. Keller, D. E. Kondakov, A. V. Kozhevnikov, T. Pruschke, K. Held, D. Vollhardt, and V. I. Anisimov: Phys. Rev. Lett. **93** (2004) 156402.
26) S. K. Mo, J. D. Denlinger, H. D. Kim, J. H. Park, J. W. Allen, A. Sekiyama, A. Yamasaki, K. Kadono, S. Suga, Y. Saitoh, T. Muro, P. Metcalf, G. Keller, K. Held, V. Eyert, V. I. Anisimov, and D. Vollhardt: Phys. Rev. Lett. **90** (2003) 186403.
27) L. V. Pourovskii, B. Amadon, S. Biermann, and A. Georges: Phys. Rev. B **76** (2007) 235101.
28) I. L. M. Locht, Y. O. Kvashnin, D. C. M. Rodrigues, M. Pereiro, A. Bergman, L. Bergqvist, A. I. Lichtenstein, M. I. Katsnelson, A. Delin, A. B. Klautau, B. Johansson, I. Di Marco, and O. Eriksson: Phys. Rev. B **94** (2016) 085137.
29) S. Y. Savrasov, G. Kotliar, and E. Abrahams: Nature **410** (2001) 793.
30) L. V. Pourovskii, M. I. Katsnelson, and A. I. Lichtenstein: Phys. Rev. B **72** (2005) 115106.
31) J. Kolorenc, A. B. Shick, and A. I. Lichtenstein: Phys. Rev. B **92** (2015) 085125.
32) L. V. Pourovskii, G. Kotliar, M. I. Katsnelson, and A. I. Lichtenstein: Phys. Rev. B **75** (2007) 235107.
33) J.-Z. Ma, A. van Roekeghem, P. Richard, Z.-H. Liu, H. Miao, L.-K. Zeng, N. Xu, M. Shi, C. Cao, J.-B. He, G.-F. Chen, Y.-L. Sun, G.-H. Cao, S.-C. Wang, S. Biermann, T. Qian, and H. Ding: Phys. Rev. Lett. **113** (2014) 266407.
34) S. Backes, H. O. Jeschke, and R. Valentí: Phys. Rev. B **92** (2015) 195128.
35) M. Hirayama, T. Miyake, M. Imada, and S. Biermann: arxiv.org **arXiv:1511.03757** (2015).
36) A. van Roekeghem, T. Ayral, J. M. Tomczak, M. Casula, N. Xu, H. Ding, M. Ferrero, O. Parcollet, H. Jiang, and S. Biermann: Phys. Rev. Lett. **113** (2014) 266403.
37) A. van Roekeghem, P. Richard, X. Shi, S. Wu, L. Zeng, B. Saparov, Y. Ohtsubo, T. Qian, A. S. Sefat, S. Biermann, and H. Ding: Phys. Rev. B **93** (2016) 245139.
38) A. van Roekeghem and S. Biermann: EPL (Europhysics Letters) **108** (2014) 57003.
39) V. I. Anisimov, F. Aryasetiawan, and A. I. Lichtenstein: J. Phys. Condensed Matter **9** (1997) 767.
40) S. Biermann, F. Aryasetiawan, and A. Georges: Phys. Rev. Lett. **90** (2003) 086402.

41) P. Sun and G. Kotliar: Phys. Rev. Lett. **92** (2004) 196402.
42) J. M. Tomczak, M. Casula, T. Miyake, and S. Biermann: EPL (Europhysics Letters) **100** (2012) 67001.
43) S. Biermann: Journal of Physics: Condensed Matter **26** (2014) 173202.
44) T. Ayral, P. Werner, and S. Biermann: Physical Review Letters **109** (2012) 226401.
45) T. Ayral, S. Biermann, and P. Werner: Physical Review B **87** (2013) 125149.
46) P. Hansmann, T. Ayral, L. Vaugier, P. Werner, and S. Biermann: Physical Review Letters **110** (2013) 166401.
47) L. Huang, T. Ayral, S. Biermann, and P. Werner: Phys. Rev. B **90** (2014) 195114.
48) L. Boehnke, F. Nilsson, F. Aryasetiawan, and P. Werner: Physical Review B **94** (2016) 201106.
49) T. Ayral, S. Biermann, P. Werner, and L. V. Boehnke: in preparation (2017).
50) J. M. Tomczak, M. Casula, T. Miyake, and S. Biermann: Phys. Rev. B **90** (2014) 165138.
51) M. Casula, P. Werner, L. Vaugier, F. Aryasetiawan, T. Miyake, A. J. Millis, and S. Biermann: Phys. Rev. Lett. **109** (2012) 126408.
52) A. Seidl, A. Görling, P. Vogl, J. Majewski, and M. Levy: Physical Review B **53** (1996) 3764.
53) J. P. Perdew, R. G. Parr, M. Levy, and J. L. Balduz: Phys. Rev. Lett. **49** (1982) 1691.
54) G. Kotliar, S. Y. Savrasov, K. Haule, V. S. Oudovenko, O. Parcollet, and C. A. Marianetti: Rev. Mod. Phys. **78** (2006) 865.
55) B. Amadon, S. Biermann, A. Georges, and F. Aryasetiawan: Phys. Rev. Lett. **96** (2006) 066402.
56) N. Xu, P. Richard, A. van Roekeghem, P. Zhang, H. Miao, W.-L. Zhang, T. Qian, M. Ferrero, A. S. Sefat, S. Biermann, and H. Ding: Phys. Rev. X **3** (2013) 011006.
57) P. Werner, M. Casula, T. Miyake, F. Aryasetiawan, A. J. Millis, and S. Biermann: Nature Physics **8** (2012) 331.
58) R. S. Dhaka, Y. Lee, V. K. Anand, D. C. Johnston, B. N. Harmon, and A. Kaminski: Phys. Rev. B **87** (2013) 214516.
59) J. Mansart, P. Le Fèvre, F. m. c. Bertran, A. Forget, D. Colson, and V. Brouet: Phys. Rev. B **94** (2016) 235147.
60) V. Brouet, F. Rullier-Albenque, M. Marsi, B. Mansart, M. Aichhorn, S. Biermann, J. Faure, L. Perfetti, A. Taleb-Ibrahimi, P. Le Fèvre, F. Bertran, A. Forget, and D. Colson: Phys. Rev. Lett. **105** (2010) 087001.
61) R. Poole, R. Leckey, J. Jenkin, and J. Liesegang: Physical Review B **8** (1973) 1401.
62) F. Himpsel, D. Eastman, E. Koch, and A. Williams: Physical Review B **22** (1980) 4604.
63) M. R. Norman: Physical Review B **29** (1984) 2956.
64) F. Aryasetiawan and O. Gunnarsson: Phys. Rev. B **54** (1996) 17564.
65) M. Oshikiri and F. Aryasetiawan: Phys. Rev. B **60** (1999) 10754.
66) J. P. Perdew and A. Zunger: Phys. Rev. B **23** (1981) 5048.
67) H. Jiang, R. I. Gómez-Abal, X.-Z. Li, C. Meisenbichler, C. Ambrosch-Draxl, and M. Scheffler: Computer Physics Communications **184** (2013) 348.
68) B. Holm and U. von Barth: Phys. Rev. B **57** (1998) 2108.
69) M. van Schilfgaarde, T. Kotani, and S. Faleev: Phys. Rev. Lett. **96** (2006) 226402.

Crystal-field splittings in rare-earth-based hard magnets: An *ab initio* approach

Pascal Delange,[1] Silke Biermann,[1,2] Takashi Miyake,[3] and Leonid Pourovskii[1,2,4]

[1]*Centre de Physique Théorique, École Polytechnique, CNRS, Université Paris-Saclay, 91128 Palaiseau Cedex, France*

[2]*Collège de France, 11 place Marcelin Berthelot, 75005 Paris, France*

[3]*CD-FMat, AIST, Tsukuba 305-8568, Japan*

[4]*Materials Modeling and Development Laboratory, National University of Science and Technology "MISIS," Moscow 119049, Russia*

(Received 22 May 2017; revised manuscript received 12 September 2017; published 23 October 2017)

We apply the first-principles density functional theory + dynamical mean-field theory framework to evaluate the crystal-field splitting on rare-earth sites in hard magnetic intermetallics. An atomic (Hubbard-I) approximation is employed for local correlations on the rare-earth $4f$ shell and self-consistency in the charge density is implemented. We reduce the density functional theory self-interaction contribution to the crystal-field splitting by properly averaging the $4f$ charge density before recalculating the one-electron Kohn-Sham potential. Our approach is shown to reproduce the experimental crystal-field splitting in the prototypical rare-earth hard magnet $SmCo_5$. Applying it to RFe_{12} and $RFe_{12}X$ hard magnets (R = Nd, Sm and X = N, Li), we obtain in particular a large positive value of the crystal-field parameter $A_2^0\langle r^2\rangle$ in $NdFe_{12}N$ resulting in a strong out-of-plane anisotropy observed experimentally. The sign of $A_2^0\langle r^2\rangle$ is predicted to be reversed by substituting N with Li, leading to a strong out-of-plane anisotropy in $SmFe_{12}Li$. We discuss the origin of this strong impact of N and Li interstitials on the crystal-field splitting on rare-earth sites.

DOI: 10.1103/PhysRevB.96.155132

I. INTRODUCTION

Permanent magnets are a key component of modern electronic devices, ranging from electric motors to medical imaging. An important breakthrough in the quest for high-performance permanent magnets was the discovery of rare-earth intermetallic magnets, starting with $SmCo_5$ in 1966 [1]. Since its discovery in 1982, the champion of hard magnets has been $Nd_2Fe_{14}B$ [2]. More recently, rare-earth iron-based hard magnets $RFe_{12}X$ with the $ThMn_{12}$ structure such as $NdFe_{12}N$ have been under renewed scrutiny [3–7]. The underlying reason is the high price and strategical importance of rare earths and cobalt, and the ongoing research effort to find good permanent magnets with reduced rare-earth concentration [8]. The $ThMn_{12}$ structure has a reduced ratio of rare earth vs transition metal compared to $Nd_2Fe_{14}B$, but nevertheless conserves strong hard magnetic properties (large magnetization and Curie temperature, and strong anisotropy) when doped with light elements such as nitrogen [4–6].

The main physical ingredients for a rare-earth hard magnet are the high magnetic anisotropy energy provided by rare-earth ions combined with the high magnetization and Curie temperature from the transition metal sublattice, typically composed of Fe or Co atoms [8–10]. The $3d$ transition metal atoms carry little anisotropy; because of their rather small spin-orbit coupling, their magnetization direction is essentially fixed by that of the rare-earth ion through an exchange coupling. The majority of rare-earth elements, especially heavy rare-earth elements, are very expensive. Moreover, the magnetic moment of heavy rare earth is normally antiparallel to the transition-metal one reducing the net magnetization [8]. Hence, one advantage of new compounds like $RFe_{12}X$ is a reduced rare-earth concentration. In turn, a higher Fe concentration is favorable for achieving a large magnetization, which is another advantage of $RFe_{12}X$ compounds. However, this reduced rare-earth concentration means each rare-earth ion must contribute a strong magnetic anisotropy to keep the overall magnetic hardness. The preferred magnetization direction (in-plane or out-of-plane) of a given rare-earth ion is determined by the interplay between the crystal-field (CF) splitting and spin-orbit (SO) interaction. To the first order, the crystalline magnetic anisotropy energy reads

$$E_A \approx K_1 \sin^2\theta,$$

where θ is the angle between the magnetization and the easy axis, and

$$K_1 = -3J\left(J - \tfrac{1}{2}\right)\alpha_J A_2^0\langle r^2\rangle n_R, \tag{1}$$

where J is the total angular momentum for the rare-earth $4f$ shell, n_R is the concentration of rare-earth atoms, α_J is the corresponding Stevens factor, and $A_2^0\langle r^2\rangle$ is the lowest-order crystal-field parameter (CFP). Additional small doping of light elements is also found to strongly modify the anisotropy by affecting the rare-earth CF splitting [5,11,12]. They also modify the structural stability: doping B makes the $Nd_2Fe_{14}B$ phase more stable, while interstitial nitrogen has only a minor effect in structural stability.

It follows that the CF splitting on the rare-earth $4f$ shell is a crucial quantity defining the magnetic hardness of rare-earth intermetallics. The theoretical search for new rare-earth hard magnets thus requires a reliable approach to calculating CFP. The importance of crystal-field effects for the optical, magnetic, and other properties of solids has been recognized long ago, and semiempirical models of the CF Hamiltonian, such as the point charge model [13] and the superposition model [14], have been developed since the 1960s. While they provide an inexpensive and physically transparent description of CF parameters, their predictive power is limited as they require experimental input to determine the actual values. Experimental information is readily available for large band-gap rare-earth insulators, where the CFP can be extracted from measurements of dipole-forbidden optical transitions between f states [15]. In the case of rare-earth intermetallics,

where the f-f transitions are hidden by the optical response of conduction electrons, inelastic neutron spectroscopy can be used to determine CFP [16–20], but its results are more ambiguous as one needs to sort out the contributions of phonons and the effect of intersite exchange interactions.

Ab initio calculations do not rely on experimental input and can have truly predictive power. First-principles techniques for computing the CF parameters [7,21–29] can be separated into two main approaches. The first one [7,22–27] consists of extracting the nonspherical Kohn-Sham potential V_{lm} and the $4f$ charge density ρ_{4f} around the rare-earth site and then computing the corresponding crystal-field parameter. As the density functional theory (DFT) is not able to fully capture the physics of partially filled localized $4f$ shells, one imposes their localization by treating the $4f$ orbitals as semicore states. The nonspherical $4f$ charge density $\rho_{4f}(\boldsymbol{r})$ of the rare-earth ion includes an unphysical contribution to the CFP stemming from the local-density-approximation (LDA) self-interaction error. This is usually corrected by spherically averaging the $4f$ charge density, but then approximations have to be made for the long-range "tails" of $\rho_{4f}(\boldsymbol{r})$.

The importance of excluding the self-interaction of the nonspherical part of the partial $4f$ charge density to obtain proper crystal-field energies was first recognized by Brooks *et al.* in a publication aimed at calculating the spin Hamiltonian parameters of rare-earth compounds [30].

In the second, more recent, approach the $4f$ states are represented by Wannier functions [28,29,31], while the charge density and, correspondingly, the Kohn-Sham potential are generated by self-consistent DFT calculations with $4f$ states treated as semicore. An additional *ad hoc* parameter is used to correct the charge transfer energy between $4f$ and conduction bands.

One may also mention recent work on determining the CFP of lanthanides and transition metals using quantum-chemical methods, in particular, in order to understand the properties of magnetic molecules. Such approaches employ, for instance, the complete active space self-consistent field method [32] or multireference second order perturbation theory [33]. Here, however, we choose to focus on perfect crystals rather than on molecules.

Overall, *ab initio* calculations of CFP for rare-earth ions are a formidable theoretical problem, due to generally small values of those CFP and their extreme sensitivity to computational details. The main weak point of previously proposed DFT-based approaches is that they are not able to correctly treat the localized valence $4f$ states. Hence, the charge density is derived under the drastic approximation of treating them as fully localized core states, spherically averaged inside the atomic sphere. The DFT+U method provides a more realistic treatment for the $4f$ density in the limit of strong ordered magnetism. However, it is usually not able to capture the true quasiatomic (multiplet) nature of rare-earth shells in the paramagnetic or partially polarized state. The DFT+U calculations can nevertheless be used to estimate the CFP by converging them to the on-site density matrix corresponding to a given atomic wave function. The CF splitting can then be evaluated from the difference in DFT+U total energy between such calculations for relevant CF states. This method in fact makes use of the (usually inconvenient) tendency of DFT+U to remain in a local energy minimum instead of converging to the ground-state density. Zhou *et al.* [34] employed this approach together with an orbital-dependent self-interaction correction [35], to obtain total energies for different orbital occupancies in UO_2 and deduce its CFP.

In this work we propose an approach to *ab initio* CFP calculations based on self-consistent DFT+dynamical mean-field theory (DFT+DMFT) [36,37] treating the local many-body problem for the $4f$ shell in the quasiatomic (Hubbard-I) approximation. While this approach of using DFT+DMFT with the Hubbard-I approximation, which we may call DFT+Hub-I, is rather simple and computationally efficient, it was shown to capture not only the $4f$ multiplet structure in the paramagnetic state [37–41] and in the ferromagnetic state [42], but also the $4f$–conduction band exchange interaction and the resulting exchange splitting of the Fermi surface [40]. This scheme also provides a rather natural way of averaging the $4f$ partial density to reduce the self-interaction error from the CF Hamiltonian. We validate it by applying it to the well-known hard magnet $SmCo_5$, for which the crystal-field splitting has been measured in multiple experiments [16–20]. We then apply our method to much less investigated new hard magnets of the $R\mathrm{Fe}_{12}X$ family, computing their CFP for different rare-earth elements (Sm or Nd) and considering N and Li interstitials. Our calculations predict the hypothetical $\mathrm{SmFe}_{12}\mathrm{Li}$ compound to possess a strong axial anisotropy and, possibly, interesting hard magnetic properties.

The paper is organized as follows: in Sec. II A we introduce basic notions as well as relevant notations of the CF theory. Our first-principles computational approach is presented in more details in Sec. II B. Our results for the DFT+Hub-I electronic structure and CFP for the $R\mathrm{Fe}_{12}(X)$ hard magnets are presented in Secs. III A and III B, respectively. In Sec. IV we analyze the shape $4f$ Wannier functions (WF) in real space and employ a projective approach to evaluate the WF localization and the contribution of hybridization effects to CFP.

II. METHOD

A. Crystal-field parameters: Notation and symmetry

We start by introducing crystal-field parameter notations. The local Hamiltonian for a rare-earth ion with a partially filled $4f$ shell subject to the exchange field created by the transition-metal sublattice and to a crystal-field potential reads

$$\hat{H} = \hat{H}_{\mathrm{1el}} + \hat{H}_U = \hat{E}_0 + \lambda \sum_i s_i l_i + 2\mu_B B_{\mathrm{ex}} \hat{S}_a + \hat{H}_{\mathrm{cf}} + \hat{H}_U, \tag{2}$$

where the one-electron part of the Hamiltonian corresponds to the first four terms on the right-hand side, namely, a uniform shift, spin-orbit, exchange-field, and crystal-field terms. $\hat{S}_a$ is the in-plane or out-of-plane spin operator, corresponding to the case where B_{ex} is along x or z, respectively. $\hat{H}_U$ represents the electron-electron Coulomb repulsion term of the many-body Hamiltonian. The crystal-field term $\hat{H}_{\mathrm{cf}}$ is defined as the nonspherically symmetric part of the one-electron Hamiltonian. The corresponding nonspherical part $V_{\mathrm{ns}}(\boldsymbol{r})$ of the one-electron potential can be expanded into spherical

harmonics as follows:

$$V_{\rm ns}(\boldsymbol{r}) = \sum_{k=1}^{\infty}\sum_{q=-k}^{k} A_k^q(r) Y_{kq}(\hat{\boldsymbol{r}}), \tag{3}$$

where $Y_{kq}(\hat{\boldsymbol{r}})$ is the spherical harmonic function with total angular moment k and projected angular moment q. The matrix elements of $V_{\rm ns}(\boldsymbol{r})$ between $4f$ orbitals define $\hat{H}_{\rm cf}$. Due to the properties of the spherical harmonics, only A_k^q for $k \leqslant 2l$, i.e., $k \leqslant 6$ in the case of an f shell, can contribute to $\hat{H}_{\rm cf}$. In the point-charge CF calculations $A_k^q(r)$ is reduced to $A_k^q r^k$. While we do not assume this form for $A_k^q(r)$ in the present formalism we still employ the now standard notation $\langle A_k^q(r)\rangle \equiv A_k^q\langle r^k\rangle$. For historic reasons, several conventions exist for the parametrization of $\hat{H}_{\rm cf}$, leading to a rather confusing variety of definitions for the crystal-field parameters. Using the so-called Stevens operator equivalents [43], $\hat{H}_{\rm cf}$ is decomposed as follows:

$$\hat{H}_{\rm cf} = \sum_{kq} A_k^q\langle r^k\rangle \Theta_k(J)\hat{O}_k^q, \tag{4}$$

where $\hat{O}_k^q$ is the Stevens operator equivalent, and $A_k^q\langle r^k\rangle$, as explained above, is the standard notation for the crystal-field parameter for given k and q. $\Theta_k(J)$ is the Stevens factor for a given ground-state multiplet defined by the quantum number J. $\Theta_k(J)$ for $k = 2$, 4, and 6 are often designated by α_J, β_J, and γ_J, respectively. The Stevens operator equivalents are more convenient for analytical calculations and somewhat outdated, but they are still extensively used in the literature. For numerical calculations it is more convenient to express $\hat{H}_{\rm cf}$ in terms of Wybourne's [44] spherical tensor operators $\hat{C}_k^q$:

$$\hat{H}_{\rm cf} = \sum_{kq} B_k^q \hat{C}_k^q, \tag{5}$$

where $\hat{C}_k^q$ are defined by

$$C_k^q(\hat{\boldsymbol{r}}) = \sqrt{4\pi/(2k+1)}\,Y_{kq}(\hat{\boldsymbol{r}}).$$

Moreover, the CFP can be made real by employing the Hermitian combination of Wybourne's operators $\hat{T}_k^q$ defined by

$$\hat{T}_k^0 = \hat{C}_k^0 \quad \text{and} \quad \hat{T}_k^{\pm|q|} = \sqrt{\pm 1}\big[\hat{C}_k^{-|q|} \pm (-1)^{|q|}\hat{C}_k^{|q|}\big].$$

$\hat{H}_{\rm cf}$ can then be expressed as

$$\hat{H}_{\rm cf} = \sum_{kq} L_k^q \hat{T}_k^q, \tag{6}$$

with a set of real parameters L_k^q. L_k^q are linked to the Stevens CFP $A_k^q\langle r^l\rangle$ by a set of positive prefactors $\lambda_{kq} = A_k^q\langle r^k\rangle / L_k^q$. For a more extensive discussion of CFP conventions see, e.g., Refs. [14,45,46].

The number of *a priori* nonzero CF parameters $A_k^q\langle r^k\rangle$ is constrained by the point-group symmetry of a given rare-earth site. In particular, in the presence of inversion symmetry, $V_{\rm ns}(\hat{\boldsymbol{r}}) = V_{\rm ns}(-\hat{\boldsymbol{r}})$, only $A_k^q\langle r^k\rangle$ for even k can be nonzero [cf. Eq. (3)]. Other point-group symmetries further reduce the number of relevant $A_k^q\langle r^k\rangle$. As a consequence, the crystal field on Sm $4f$ in $SmCo_5$ can be fully described with only four CF parameters: $A_2^0\langle r^2\rangle$, $A_4^0\langle r^4\rangle$, $A_6^0\langle r^6\rangle$, and $A_6^6\langle r^6\rangle$. In the case of the $R{\rm Fe}_{12}X$ family, the relevant parameters are $A_2^0\langle r^2\rangle$, $A_4^0\langle r^4\rangle$, $A_4^4\langle r^4\rangle$, $A_6^0\langle r^6\rangle$, and $A_6^4\langle r^6\rangle$.

In our calculations, we extract the set of parameters L_k^q (or $A_k^q\langle r^k\rangle$), as well as $B_{\rm ex}$ and λ by a least-square fit of *ab initio* $\hat{H}_{\rm 1el}$ (using the usual Frobenius norm) obtained within DFT+Hub-I [see Eq. (7) in the next section]. Note that one may assign a spin label to the CF parameters in Eqs. (5) and (6), hence allowing for different CF potentials for spin up and down electrons. We found that this improves the fit for spin-polarized $\hat{H}_{\rm 1el}$.

B. Calculational approach

We employ the DFT+Hub-I approach [47] based on the TRIQS library [48] and the full potential linearized augmented plane-wave Wien-2k [49] band structure code in conjunction with the projective Wannier-orbitals construction [50,51]. The charge-density self-consistency [52,53] is implemented as described in Ref. [54]. The Hubbard-I impurity solver is provided by the TRIQS library.

The Wannier orbitals representing the rare-earth $4f$ states are constructed from the Kohn-Sham bands within the window $[-\omega_{\rm win},\omega_{\rm win}] = [-2,2]$ eV relative to the Fermi level. The choice of the half-window size $\omega_{\rm win}$ is the only significant parameter in our calculations (indeed, the choice of Hubbard U and Hund's coupling J has limited impact on the results, as we demonstrate in Appendix D). In order to construct a complete orthonormal basis of Wannier orbitals one needs to choose $\omega_{\rm win}$ large enough to include at least all $4f$-like Kohn-Sham bands. Wannier orbitals constructed with a "small window" leak [47] to neighboring sites due to hybridization between $4f$ states and conduction band states. A larger window results in more localized Wannier orbitals consisting almost exclusively of the corresponding $4f$ partial waves inside the rare-earth atomic sphere [47,51], as discussed in Sec. IV and Appendix E below. DFT+Hub-I studies of rare-earth wide-gap insulators show a rather strong sensitivity of calculated CFP to the window size; less-localized small window Wannier $4f$ orbitals result in a better agreement with experimental CFP [55]. In the present case of rare-earth intermetallics we find a rather weak dependence of CFP to variations of $\omega_{\rm win}$ within the reasonable range from 2 to 8 eV, see Appendix E. Hence, we employ $\omega_{\rm win} = 2$ eV in our calculations throughout.

In the Hubbard-I approximation the hybridization function is neglected and solving of the DMFT impurity problem is reduced to the diagonalization of the atomic Hamiltonian (2). The one-electron part $\hat{H}_{\rm 1el}$ of Eq. (2) is then given by [53]

$$\hat{H}_{\rm 1el} = -\mu + \langle H^{ff}\rangle - \Sigma_{\rm DC}, \tag{7}$$

where μ is the chemical potential, $\langle H^{ff}\rangle$ is the Kohn-Sham Hamiltonian projected to the basis of $4f$ Wannier orbitals and summed over the Brillouin zone, $\Sigma_{\rm DC}$ is the double-counting correction term for which we employ the fully localized-limit (FLL) form [56] that is known to work best for localized states such as $4f$ orbitals. In our calculations, we evaluate the FLL double counting using the occupancy of the DMFT local Green's function, which comes out to be close to the nominal $4f$ occupancy of the corresponding 3+ rare-earth ion. If the nominal occupancy is used in FLL DC instead one obtains almost the same CFP, with differences no larger than 10 to 20 K.

We carry out DFT+Hub-I iterations until convergence in the total energy with precision 10^{-5} Ry is reached and then extract the CFP from Eq. (7) as described in the previous section.

Self-consistent DFT+Hub-I calculations produce a nonspherical one-electron Kohn-Sham potential (3), that includes several nonspherical contributions acting on $4f$ states: the long-range electrostatic (Madelung) interaction, as well as the local-density-approximation (LDA) exchange-correlation potential due to the conduction electrons and $4f$ states themselves. This last "intra-$4f$ shell" contribution to the exchange-correlation potential should be removed within DFT+Hub-I, since the on-site interaction H_U between $4f$ states is already treated explicitly within DMFT. Hence, the intra-$4f$ shell contribution in the one-electron part $\hat{H}_{\rm 1el}$ of Eq. (2) due to LDA is counted twice and should be removed by a double-counting correction. Moreover, this contribution includes the LDA self-interaction error for localized states directly impacting CFP: for low-lying CF levels, the self-interaction error will be larger than for less occupied excited CF states.

In order to reduce the self-interaction error in the CFP we enforce uniform occupancy of all states within the $4f$ ground-state multiplet in our self-consistent DFT+Hub-I calculations. To that end, we define the imaginary-frequency atomic (Hubbard-I) Green's function at the fermionic Matsubara frequency $\omega_n = (2n+1)\pi T$, where T is the temperature, as follows:

$$G^{\rm at}_{ab}(i\omega_n) = \frac{1}{M}\sum_{\substack{\gamma\in{\rm GSM}\\ \delta\notin{\rm GSM}}}\left(\frac{\langle\gamma|f_a|\delta\rangle\langle\delta|f_b^\dagger|\gamma\rangle}{i\omega_n - E_\gamma + E_\delta} + \frac{\langle\delta|f_a|\gamma\rangle\langle\gamma|f_b^\dagger|\delta\rangle}{i\omega_n + E_\gamma - E_\delta}\right), \tag{8}$$

where the eigenstates $|\gamma\rangle$ and $|\delta\rangle$ with eigenenergies E_γ and E_δ are obtained by diagonalization of Eq. (2) and belong to the ground-state multiplet (GSM) and excited multiplets, respectively, a and b label $4f$ orbitals, M is the degeneracy of the GSM. In other words, to obtain Eq. (8) we substitute the standard Boltzmann weight $X_\gamma = e^{-E_\gamma/T}/Z$, where Z is the partition function, with the uniform weight $\tilde{X}_\gamma = 1/M$ for the GSM and $\tilde{X}_\delta = 0$ for excited multiplets in the spectral representation of the Green's function [57,58]. In practice, the degeneracy of the ground-state multiplet M is chosen to be the same as for the corresponding free ion, hence it is given by Hund's rules. Therefore, $M = 10$ for Nd and $M = 6$ for Sm. The self-energy thus obtained is then plugged back into the self-consistency cycle. This leads to a spherically averaged contribution from the $4f$ orbitals, both inside and outside the rare-earth atomic sphere, while nonspherical contributions from other states are taken into account. We verified the validity of this method by calculating the density matrix from the local Green's function and transforming it to the relativistic basis of one-electron $J = \frac{5}{2}$ and $J = \frac{7}{2}$ orbitals. With the averaging, the resulting density matrix is made of two identity blocks with deviations of the order of few percent, to be compared with over 50% without the averaging.

Conceptually speaking, our approach amounts to replacing Eq. (7) by

$$\hat{H}_{\rm 1el} = -\mu + \langle H^{ff}\rangle - \Sigma_{\rm DC} - v_{\rm KS}[\rho_{spd} + \rho_{4f}] + v_{\rm KS}[\rho_{spd} + \bar{\rho}_{4f}], \tag{9}$$

where $v_{\rm KS}[\rho]$ is the Kohn-Sham potential ($v_{\rm KS} = v_{\rm Hartree} + v_{\rm xc}$) evaluated from the total electronic density ρ and then projected to the basis of $4f$ Wannier orbitals. ρ_{4f} designates the projected electronic density belonging to the rare-earth's $4f$ orbitals, $\bar{\rho}_{4f}$ is the same density, spherically averaged, and ρ_{spd} designates all the remaining density, belonging to all atoms' s, p, and d orbitals.

The same approach is used in the spin-polarized DFT+Hub-I calculations: in this case the exchange splitting is also removed within the GSM. We found, however, that this averaging is not sufficient, since the value of the exchange field within our DFT+Hub-I iterations may become larger than the intermultiplet splitting. Hence we also directly remove the $4f$ spin polarization from the resulting DFT+Hub-I density matrix. For a given $\mathbf{k}$-point the "averaged" density matrix $\tilde{N}^{\mathbf{k}}$ in the Bloch basis reads

$$\tilde{N}^{\mathbf{k}} = N^{\mathbf{k}} + \tfrac{1}{2}P^\dagger(\mathbf{k})[Tn^{ff}(\mathbf{k})T^\dagger - n^{ff}(\mathbf{k})]P(\mathbf{k}), \tag{10}$$

where $N^{\mathbf{k}}$ is the density matrix in the Bloch basis calculated as described in Refs. [47,54], $P(\mathbf{k})$ is the projector [47,51] between the Wannier and Bloch spaces, $n^{ff}(\mathbf{k})$ is the density matrix in the Wannier basis, and T is the time-reversal operator. The averaged density matrix $\tilde{N}^{\mathbf{k}}$ is then used to recalculate the electron density at the next DFT iteration as described in Ref. [54]. The contribution of $4f$ states to the spin density and local-spin-density-approximation (LSDA) exchange field is thus suppressed. The resulting exchange field is due to the polarization of the transition-metal sublattice, as expected for hard magnetic rare-earth intermetallics. In contrast, direct spin-polarized DFT+Hub-I calculations without the averaging would lead to a large unphysical exchange field on rare-earth sites due to the magnetization density of $4f$ electrons themselves.

In Appendix A we benchmark the present method on the prototypical rare-earth hard magnet $SmCo_5$, for which several measurements of CFP exist, and show good agreement between calculated and measured CFPs. Moreover, the actual eigenstates of the Sm $4f$ shell in $SmCo_5$ obtained within DFT+HubI are also in very good agreement with previous neutron scattering and magnetic form-factor measurements, see Appendix B.

C. Calculational details

The $R{\rm Fe}_{12}X$ family has the space group $I4/mmm$, with a tetragonal primitive unit cell. The conventional unit cell, with twice the volume and the atoms, is orthorhombic. It has equivalent R sites in the corner and the center at Wyckoff position $2a$, X interstitial sites between two nearest R sites at Wyckoff position $2b$, and contains 24 Fe atoms on three inequivalent sites, denoted below Fe_1, Fe_2, and Fe_3 at Wyckoff positions $8j$, $8i$, and $8f$, respectively, as displayed in Fig. 1. Calculations are done at the theoretical lattice constants for $R{\rm Fe}_{12}X$, summarized in Table I in the conventional unit cell (from Table II of Ref. [59] and from this work). The calculated lattice constants agree within 2% with the measured ones in the more stable $NdFe_{11}Ti(N)$ and $SmFe_{11}Ti(N)$ compounds [59].

The DFT calculations are performed with spin-orbit coupling included within the second variational approach. We

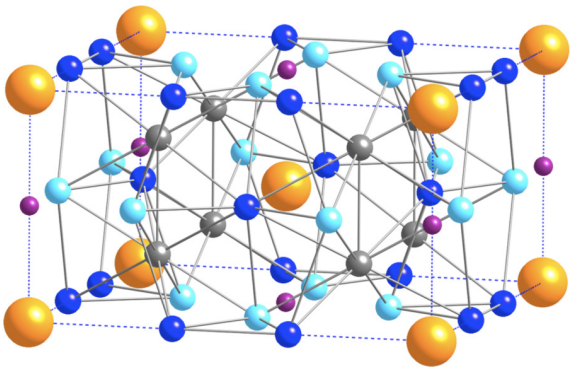

FIG. 1. Conventional unit cell of $R\mathrm{Fe}_{12}X$. The rare-earth R sites are yellow, the three types of Fe sites are gray, light blue, and dark blue, and dopant X sites purple.

employ throughout the rotationally invariant Coulomb vertex specified by Slater integrals $F^0 = U = 6.0$ eV as well as $F^2 = 10.13$, $F^4 = 6.77$, and $F^6 = 5.01$ eV corresponding to Hund's rule coupling $J_H = 0.85$ eV. These values of U and J_H are in agreement with those in the literature [41,53,60]. One may notice, that while the values of U and J_H are important to determine the one-electron spectrum of a material, they are expected to have a rather small effect on the crystal-field parameters that we consider in this work [61]. We discuss this dependence in Appendix D. DFT+Hub-I calculations are carried out for the temperature of 290 K.

III. RESULTS

A. DFT and DFT+Hubbard-I electronic structure of $R\mathrm{Fe}_{12}X$

We first compare the electronic structure of $R\mathrm{Fe}_{12}X$ obtained within DFT (LSDA) and DFT+Hub-I. A typical DFT density of states (DOS) and a DFT+Hub-I spectral function for ferromagnetic $R\mathrm{Fe}_{12}X$, namely, for $\mathrm{NdFe}_{12}\mathrm{N}$, are shown in Fig. 2. The DFT DOS of Fig. 2(a) features a strong polarization of the Fe $3d$ band. N $2p$ states are dispersive, with the bottom of the bands contributing to a peak in the DOS around -6 eV. The Nd $4f$ band is fully spin polarized and antiferromagnetically aligned to Fe $3d$, with the total spin moment within the Nd atomic sphere equal to $-2.77\ \mu_B$, i.e., close to the Hund's rule value of $3\ \mu_B$ for the Nd^{3+} ion. The Nd majority-spin $4f$ band is pinned at the Fermi level, its double-peak structure is due to spin-orbit splitting. This picture of $4f$ bands pinned at the Fermi level is qualitatively incorrect and illustrates the difficulties of DFT with local or semilocal exchange-correlation functionals to correctly treat strongly interacting localized valence states.

TABLE I. Conventional unit cell lattice constants used in our calculations. $b = a$, and the angles are $\alpha = \beta = \gamma = 90^\circ$.

Compound	Lattice constant (Å)	
	a	c
NdFe_{12}	8.533	4.681
$\mathrm{NdFe}_{12}\mathrm{N}$	8.521	4.883
$\mathrm{NdFe}_{12}\mathrm{Li}$	8.668	4.873
SmFe_{12}	8.497	4.687
$\mathrm{SmFe}_{12}\mathrm{N}$	8.517	4.844
$\mathrm{SmFe}_{12}\mathrm{Li}$	8.640	4.863

The spin-polarized DFT+Hub-I spectral function shown in Fig. 2 was calculated using the averaging approach described in Sec. II B. It features an almost fully polarized Fe $3d$ band as well as occupied and empty $4f$ states separated, to first approximation, by U, thus forming lower and upper Hubbard bands, respectively. The Hubbard bands are split due to the Hund's rule and spin-orbit couplings into several manifolds with characteristically sharp peaks corresponding to transitions from the ground state to different quasiatomic multiplets upon electron addition or removal. The $4f$ multiplet structure in lanthanides is known to be only weakly sensitive to the crystalline environment. Indeed, the positions of the Hubbard bands in Fig. 2(b) as well as the overall shape of the upper Hubbard band split into two manifolds of multiplet peaks centered at about 2 and 4 eV are in agreement with photoemission and inverse-photoemission spectra of the Nd metal [62]. One also sees that the Nd $4f$ states in DFT+Hub-I are not fully spin polarized, in contrast to the DFT case. Indeed the Nd spin moment of $-1.61\ \mu_B$ obtained within DFT+Hub-I is only about half of the Hund's rule value and is also aligned antiferromagnetically with respect to the spin moment on iron. The calculated Nd orbital moment is $3.40\ \mu_B$. It is precisely the crystal-field splitting of the Nd $4f$ shell that prevents the full saturation of the Nd magnetization.

B. Crystal-field parameters and exchange fields in $R\mathrm{Fe}_{12}X$

The calculated CF and exchange fields for Nd and Sm $R\mathrm{Fe}_{12}$(N,Li) compounds are listed in Tables II and III, together with the magnetic moments on R and in the full cell. Comparing the different materials, one sees that $R\mathrm{Fe}_{12}$ has the smallest values of $A_2^0\langle r^2\rangle$ (in absolute value), while N insertion enhances $A_2^0\langle r^2\rangle$ up to positive values of about 400 to 600 K. Li insertion has the opposite effect, leading to large negative $A_2^0\langle r^2\rangle$, in particular for $R = \mathrm{Nd}$. We notice some dependence of the CF parameters $A_k^q\langle r^k\rangle$ on the spin direction in the ferromagnetic phase. It is mostly weak, of the order of a few tenths of Kelvin for the most important CFP $A_2^0\langle r^2\rangle$, except in $\mathrm{NdFe}_{12}\mathrm{N}$. It can be significant, though, for higher-order CFP. The magnetic state (paramagnetic of ferromagnetic) has a significant impact on $A_2^0\langle r^2\rangle$ in some compounds: one may notice larger values of $A_2^0\langle r^2\rangle$ for paramagnetic SmFe_{12}(N,Li) than for either spin direction in the ferromagnetic phase.

Finally, the total magnetization appears to be slightly reduced in Sm compounds, compared to Nd compounds: in the former, the spin magnetic moment on the rare earth compensates the orbital magnetic moment, leading to negligible total moment, while Nd presents a total moment dominated by the orbital component, and in the same direction as the Fe sublattice magnetization.

The sign and overall magnitude of our calculated $A_2^0\langle r^2\rangle$ are in agreement with previous calculations for $R\mathrm{Fe}_{12}$(N) in Ref. [5] using the $4f$-in-core approach, though there are some differences in the precise values. We obtain a similar value for NdFe_{12}, a somewhat larger one for $\mathrm{NdFe}_{12}\mathrm{N}$, a more negative value for SmFe_{12}, and a smaller (positive) value for $\mathrm{SmFe}_{12}\mathrm{N}$. One may notice that the results in Ref. [5] are quite sensitive

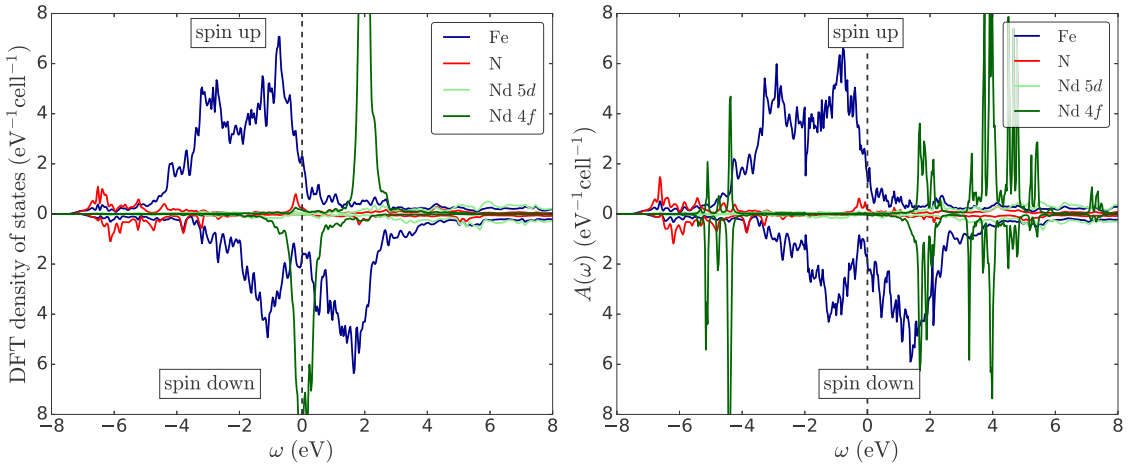

(a) $NdFe_{12}N$ DFT density of states (b) $NdFe_{12}N$ DFT + Hubbard I spectral function

FIG. 2. (a) Atom- and orbital-resolved density of states of $NdFe_{12}N$ calculated with the spin-polarized DFT method. (b) Atom- and orbital-resolved spectral function of the same compound obtained within self-consistent spin-polarized DFT+Hubbard-I. For better readability we take the average over the three types of Fe atoms: the actual total Fe density of states per unit cell is three times larger.

to different treatments of the "tails" of $4f$ core orbitals: there is no such uncertainty in our approach.

The lowest-order CF parameters $A_2^0\langle r^2\rangle$ and the corresponding single-ion anisotropy energies K_1 evaluated using Eq. (1) are displayed in Fig. 3. One may see that, while $NdFe_{12}N$ and $NdFe_{12}Li$ exhibit larger $|A_2^0\langle r^2\rangle|$ (upper panel) than their Sm counterparts, this difference is offset by a larger Stevens prefactor of Sm in Eq. (1), so that the Sm- and Nd-based compounds have a magnetic anisotropy coefficient K_1 of similar magnitude. An important difference between Nd and Sm is the different signs of their Stevens factors α_J ($\alpha_J = -7/1089$ for Nd, $\alpha_J = 13/315$ for Sm). Consequently, N insertion leads to a large out-of-plane anisotropy for Nd, but in-plane anisotropy for Sm. Li has the opposite effect: doping Li into $SmFe_{12}$ leads to a rather large out-of-plane anisotropy of $SmFe_{12}Li$, of comparable magnitude to that of $NdFe_{12}N$.

Performing the averaging over the ground-state multiplet as described in Eq. (8) is crucial to obtain reasonable CFP: the lowest-order CFP $A_2^0\langle r^2\rangle$ is most sensitive to this. The corresponding data without averaging for $NdFe_{12}N$ are given and discussed in Appendix C.

For the sake of comparison with future experiments we list low-energy eigenvalues and eigenstates of all $RFe_{12}X$ compounds in Appendix B. It is interesting to notice that eigenstates of the ground-state $J = 5/2$ multiplet of Sm (Table VI) are often found to exhibit a significant admixture from exited $J = 7/2$ states; the Nd $J = 9/2$ states (Table V) contain a significantly lower admixture from the first exited multiplet.

A last interesting point is that the exchange fields B_{ex} on the rare earth are enhanced by Li and reduced by N. This is useful because the exchange field, or exchange coupling between Fe and R, is essential for finite temperature magnetocrystalline anisotropy. The rare-earth-originated anisotropy becomes ineffective at high temperature, and this threshold temperature is determined by the exchange coupling B_{ex}. In Fig. 4 we show the difference between the $4f$ shell atomic energies $E_\perp$ and $E_\parallel$, computed as $E = \text{Tr}[\hat{H}e^{-\beta\hat{H}}]/\text{Tr}[e^{-\beta\hat{H}}]$ with $\hat{H}$ defined in

TABLE II. Calculated CF parameters in ferromagnetic (FM) and paramagnetic (PM) $NdFe_{12}$(N,Li) in Kelvin. For the FM case we list the CF parameters for each spin direction. The exchange field in the FM phase (in Tesla), the spin and orbital magnetic moments of the rare earth as well as the total magnetic moment per crystal unit cell (in Bohr magneton μ_B) are also listed.

	$NdFe_{12}$			$NdFe_{12}N$			$NdFe_{12}Li$		
	PM	FM		PM	FM		PM	FM	
		↑	↓		↑	↓		↑	↓
$A_2^0\langle r^2\rangle$	−57	−71	−116	486	477	653	−656	−687	−742
$A_4^0\langle r^4\rangle$	−29	−5	−1	107	75	112	−182	−158	−186
$A_4^4\langle r^4\rangle$	−129	−76	−270	7	−105	−141	−118	−60	−228
$A_6^0\langle r^6\rangle$	52	62	54	51	32	63	−24	−17	−31
$A_6^4\langle r^6\rangle$	70	−224	−107	−160	−65	−91	37	−6	96
B_{ex} (T)	–	265		–	217		–	410	
Nd M_{spin}	–	$-1.48\,\mu_B$		–	$-1.61\,\mu_B$		–	$-1.69\,\mu_B$	
Nd M_{orb}	–	$2.96\,\mu_B$		–	$3.40\,\mu_B$		–	$3.28\,\mu_B$	
M_{cell}	–	$26.39\,\mu_B$		–	$29.15\,\mu_B$		–	$27.59\,\mu_B$	

TABLE III. The same quantities as in Table II for $SmFe_{12}$(N,Li).

	$SmFe_{12}$			$SmFe_{12}N$			$SmFe_{12}Li$		
	PM	FM		PM	FM		PM	FM	
		↑	↓		↑	↓		↑	↓
$A_2^0\langle r^2\rangle$	−32	−184	−211	249	195	225	−458	−297	−272
$A_4^0\langle r^4\rangle$	−11	−21	−18	99	78	70	−116	−68	−71
$A_4^4\langle r^4\rangle$	−215	−41	−136	−122	22	−91	−124	61	−198
$A_6^0\langle r^6\rangle$	47	45	40	71	47	25	−13	−2	−12
$A_6^4\langle r^6\rangle$	−85	−95	−58	−184	−97	−82	44	30	38
B_{ex} (T)	–	232		–	205		–	331	
Sm M_{spin}	–	−3.31 μ_B		–	−2.41 μ_B		–	−3.96 μ_B	
Sm M_{orb}	–	3.29 μ_B		–	2.35 μ_B		–	3.60 μ_B	
M_{cell}	–	24.54 μ_B		–	26.83 μ_B		–	25.77 μ_B	

Eq. (2) and the exchange field B_{ex} is along the z axis (along the c lattice parameter) and x axis (along the a lattice parameter), respectively. We scale the exchange field B_{ex} by a coefficient $M_{Fe}(T)/M_{Fe}(0)$ at nonzero temperatures, using the measured magnetization ratio of $NdFe_{12}N$ from Hirayama *et al.* [6]. The energy difference plotted in Fig. 4 is more general than the expression of Eq. (1), because it also contains higher order CFP and nonzero temperature; to compute $E_\perp$ and $E_\parallel$ we diagonalize the full Hamiltonian $\hat{H}$, without restricting ourselves to the ground-state multiplet. This gives quite a different picture than Fig. 3: the strongly enhanced exchange coupling due to Li doping causes the magnetocrystalline anisotropy to persist at much higher temperatures than with N doping.

IV. DISCUSSION: THE EFFECT OF HYBRIDIZATION WITH THE INTERSTITIALS

Let us now analyze the mechanisms determining the CFP on the rare-earth site and, in particular, the impact of the N and Li interstitials on them. We consider the $NdFe_{12}X$ (X = Ni, Li) compounds as an example. The N atom nominally carries three $2p$ electrons, but in the $RFe_{12}N$ compounds the N $2p$ bands are more than half-filled (Fig. 2). To verify this we have also performed a Bader-charge analysis [63] for $NdFe_{12}X$ and found 8.3 electrons on N resulting in an ion charge of −1.3. In contrast, the Li atom is nominally $2s^1$, but it looses its single $2s$ electron inside the $NdFe_{12}$ matrix, the corresponding Bader ion charge is +0.7.

In Fig. 5 we display the complex Wannier orbitals constructed for Nd $4f$ states with window size $\omega_{win} = 2$ eV with magnetic quantum numbers $m = 0$ and $m = -3$, in the presence of interstitial N or Li. The orbitals with $m = \pm 3$ do not point towards the N or Li atom, and leak only to neighboring Fe atoms. On the other hand, the orbital with $m = 0$ (corresponding to f_{z^3} cubic orbital) points towards the interstitial site, and shows strong leakage to the interstitial atom, particularly in the Li case. The same applies, to a lesser extent, to the orbitals $m = \pm 1$ that are also pointing towards the interstitials.

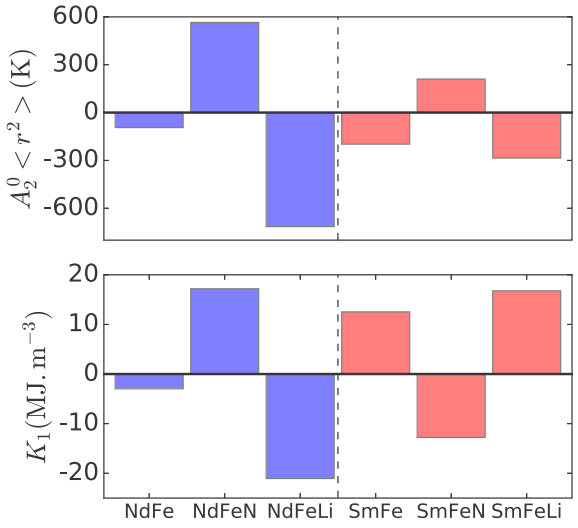

FIG. 3. Crystal-field parameters $A_2^0\langle r^2\rangle$ (average for up and down spins in the FM phase) and anisotropy energy K_1 for $RFe_{12}X$, with R = Nd,Sm and X is either empty, N, or Li [K_1 is obtained from Eq. (1)].

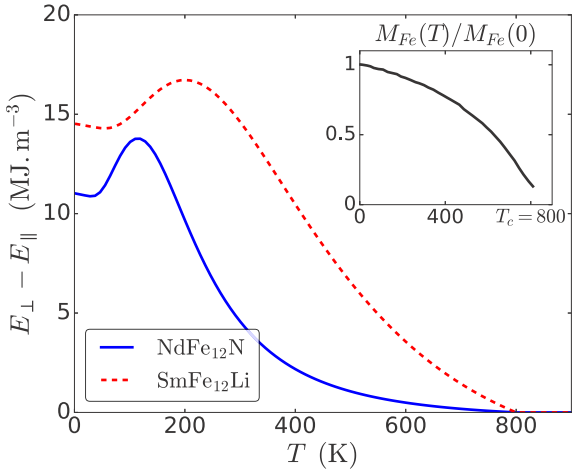

FIG. 4. Evolution with temperature of the difference in the $4f$ shell energy $E_\perp - E_\parallel$ between the moments on R and Fe aligned perpendicularly and parallel to the z axis, respectively, for $NdFe_{12}N$ (blue, full line) and $SmFe_{12}Li$ (red, dashed line). Inset: Magnetization fraction of the Fe sublattice in $NdFe_{12}N$, as a function of temperature from Hirayama *et al.* [6].

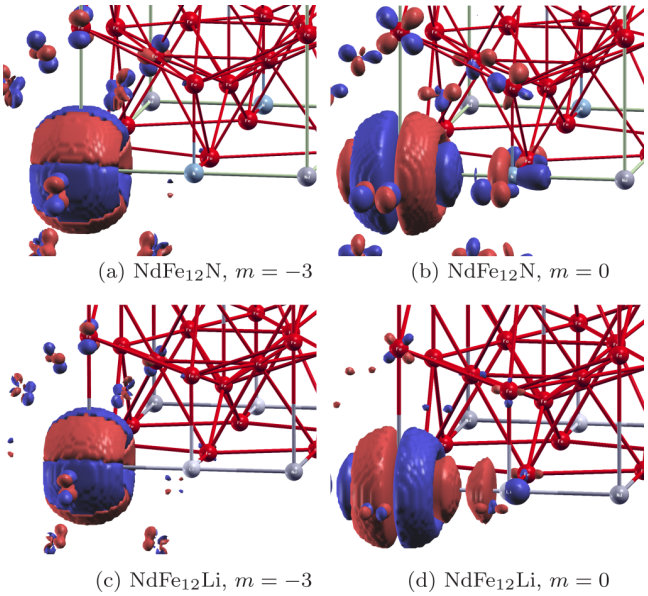

(a) $NdFe_{12}N$, $m=-3$ (b) $NdFe_{12}N$, $m=0$

(c) $NdFe_{12}Li$, $m=-3$ (d) $NdFe_{12}Li$, $m=0$

FIG. 5. $4f$ Wannier orbitals of $NdFe_{12}N$ and $NdFe_{12}Li$, for magnetic quantum number $m=-3$ and $m=0$ and window size $[-2,2]$ eV. The orbital with $m=0$ points towards and leak to the N or Li sites, while orbitals with $m=\pm 3$ do not. All of them leak somewhat to the nearest-neighbor Fe atoms.

The N (Li) insertion has thus two effects on the CFP. The first one is due to the electrostatic interaction between the $4f$ electrons and the interstitial ions. This interaction with the negative N (positive Li) ion pushes the on-site energies of the $m=-1,0,1$ orbitals, which point towards the interstitial, to higher (lower) energies.

The second contribution is due to hybridization between the $4f$ states and the N $2p$ (Li $2s$ and $2p$) bands, which is expected to mainly affect the $m=-1,0,1$ orbitals pointing towards the interstitial. Mixing with the empty Li $2s$ and $2p$ bands pushes them to lower energies, while the opposite shift is induced due to hybridization with mostly filled N $2p$ located well below rare-earth $4f$ states, see Fig. 2. Hence, one sees that both the electrostatic and hybridization effects act in the same direction, raising the on-site energies of the $m=-1,0,1$ orbitals in the case of N and lowering them in the case of Li.

This analysis explains the effect of interstitials on the CFP $A_2^0\langle r^2\rangle$. Indeed, the contribution due to $A_2^0\langle r^2\rangle$ into the CF Hamiltonian (6) is $A_2^0\langle r^2\rangle \hat{T}_2^0/\lambda_2^0$, where the matrix of the one-electron operator $\hat{T}_2^0/\lambda_2^0$ (6) reads

$$\hat{T}_2^0/\lambda_2^0 = 2\begin{pmatrix} -\frac{1}{3} & & & & & & \\ & 0 & & & & (0) & \\ & & \frac{1}{5} & & & & \\ & & & \frac{4}{15} & & & \\ & & & & \frac{1}{5} & & \\ & (0) & & & & 0 & \\ & & & & & & -\frac{1}{3} \end{pmatrix}$$

in the basis of complex $4f$ orbitals. Hence, the energy level of $4f$ orbitals $m=\pm 3$ is negatively correlated with $A_2^0\langle r^2\rangle$, while the energy levels of the orbitals with $m=-1,0,1$ are positively correlated with $A_2^0\langle r^2\rangle$ (orbitals with $m=\pm 2$ are unaffected by $\hat{T}_2^0/\lambda_2^0$). Thus, the effect of N (Li) insertion is to enhance (reduce) the value of $A_2^0\langle r^2\rangle$.

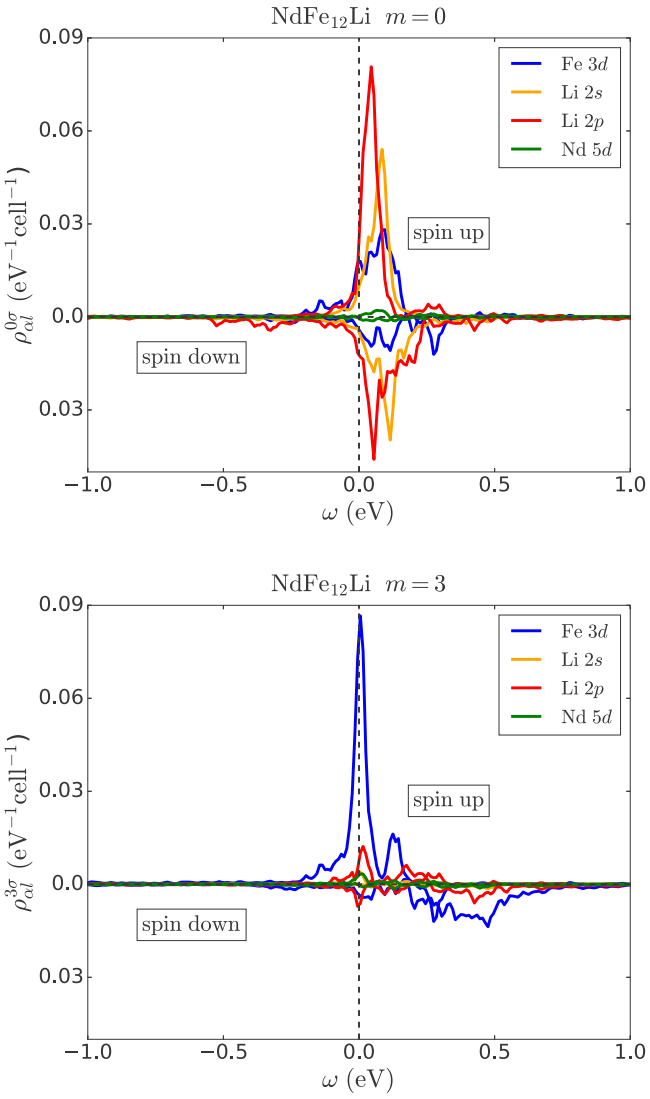

FIG. 6. (a) Projected spectral functions $\rho_{\alpha l}^{0\sigma}(\omega)$ for the $4f$ orbital with $m=0$ in $NdFe_{12}Li$, where the atom α and shell l are given in the legend. The magnitude $\rho_{\alpha l}^{m\sigma}(\omega)$ indicates the amount of admixture of the character αl into a given $4f$ orbital, for its precise formulation see the text. (b) The same for the $4f$ orbital $m=3$.

One may argue that the Hubbard-I approximation neglects the hybridization function in solving the quantum impurity problem, hence, hybridization to the bath is not included explicitly when solving for the self-energy Σ in the DMFT (Hubbard-I) step of our DFT+Hub-I calculations. However, our Wannier orbitals constructed within the "small" energy window do contain the effect of hybridization implicitly, which is evidenced by their "leakage" to neighboring sites due to mixing of rare-earth $4f$ states with Fe $3d$, N $2p$, and Li $2s$ bands. The real-space Wannier functions of Fig. 5 thus represent a convenient visualization of hybridization between rare earth and other orbitals. In order to quantify the amount of this admixture of the conduction band states we

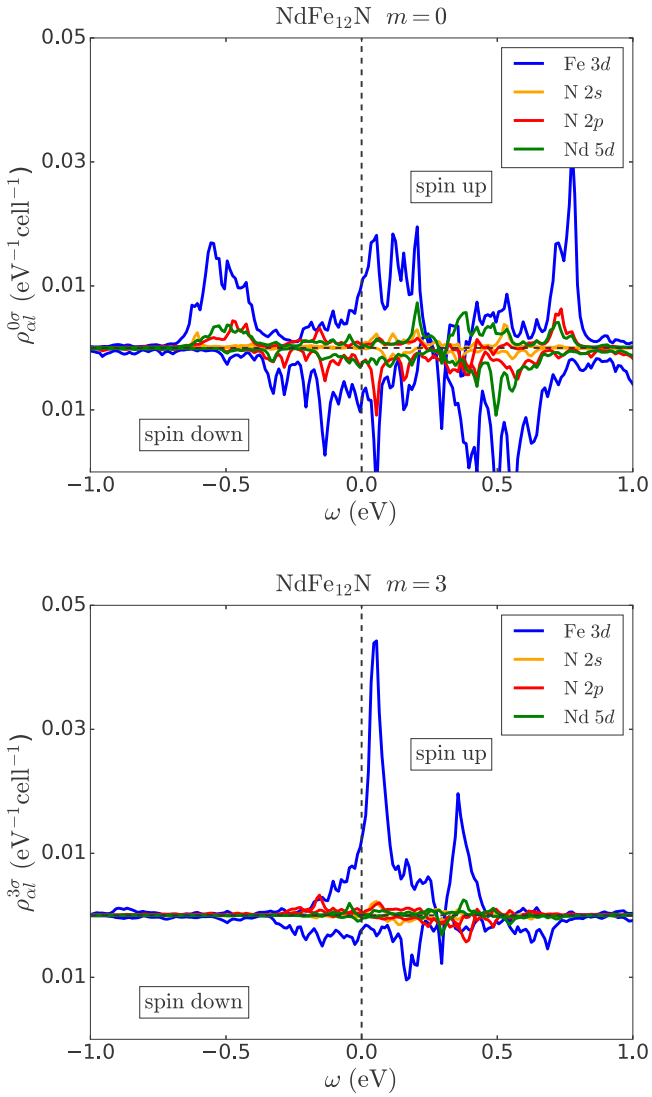

FIG. 7. (a) Projected spectral functions $\rho^{0\sigma}_{\alpha l}(\omega)$ for the $4f$ orbital with $m = 0$ in $NdFe_{12}N$. For the notation see the caption of Fig. 6. (b) The same for the $4f$ orbital $m = 3$, $\rho^{3\sigma}_{\alpha l}(\omega)$.

also expand those extended small-window Wannier orbitals $|w^{\sigma}_{m}(\mathbf{k})\rangle$ in the basis of localized Wannier functions $|\tilde{w}^{\alpha\sigma'}_{lm'}(\mathbf{k})\rangle$ (labeled by spin σ', orbital l, and magnetic m' quantum numbers, as well as atomic site α) constructed within a large energy window for all relevant bands. In Appendix F we derive the corresponding projection operators relating $|w^{\sigma}_{m}(\mathbf{k})\rangle$ and $|\tilde{w}^{\alpha\sigma'}_{lm'}(\mathbf{k})\rangle$. We employ it to extract the corresponding contribution $\tilde{\rho}^{m\sigma}_{\alpha l}(\omega)$ of the shell l on the site α into the spectral function of the "small-window" $4f$ orbital σm.

The comparison of $\rho^{m\sigma}_{\alpha l}$ for the orbital $m = 0$ and $m = 3$ are shown in Figs. 6 and 7 for $NdFe_{12}N$ and $NdFe_{12}Li$, respectively. One may notice in Fig. 6(a) that Nd f_{z^3} ($m = 0$) in $NdFe_{12}Li$ exhibits a strong hybridization with Li $2s$ and $2p$; their contribution is significantly larger than the admixture of Fe $3d$ states. We further observe that spin up states are hybridizing more strongly than spin down states. In contrast, in the same compound for $m = 3$ [Fig. 6(b)], there is a peak of hybridization with Fe states but barely any with the Li $2s$ and $2p$ ones. The same difference, but much less pronounced, is noticeable in the case of $NdFe_{12}N$, see Fig. 7. Hence, one may conclude, that the effect of the hybridization with the interstitial on the CF is much larger for Li than for N. In the latter case the electrostatic shift due to the negative charge on N seems to play the leading role.

V. CONCLUSION

In conclusion, we propose a novel first-principles approach for calculating crystal and exchange fields in rare-earth systems. This approach is formulated within the DFT+DMFT framework with local correlations on the rare-earth $4f$ shell treated within the quasiatomic Hubbard-I approximation. The $4f$ states are represented by Wannier functions constructed from a narrow energy range of Kohn-Sham states of mainly $4f$ character. We employ a charge-density averaging that suppresses the contribution due to the self-interaction of the $4f$ orbitals to the one-electron Kohn-Sham potential. We thus reduce the effect of this unphysical self-interaction from the crystal-field splitting, while keeping nonspherical contributions to CFP from other bands. Similarly, by removing the contribution due to the $4f$ magnetic density from the exchange-correlation potential we suppress its unphysical contribution to the exchange field at the rare-earth site.

The present approach is effectively free from adjustable parameters and can be applied to evaluate CFP in any localized lanthanide compound. While in the present work we chose the value for the on-site interaction parameters U and J, they can in principle be evaluated using constrained local-density or random-phase approximation [64]. Moreover, we show that the crystal-field splitting exhibits a rather weak dependence on the value of U chosen within a reasonable range for lanthanide $4f$ shells (4 to 8 eV). Our choice for the local basis representing $4f$ orbitals, namely, that we construct it from a narrow range of Kohn-Sham bands with heavy $4f$ character, is physically motivated as it allows for the impact of the hybridization on the CFP being included within DFT+Hub-I.

We apply this approach to evaluate the crystal and exchange-field potentials as well as the resulting single-ion magnetic anisotropies in several rare-earth hard magnetic intermetallics. First, we verify that our *ab initio* scheme reproduces the measured crystal-field parameters (CFP) in the well-known hard magnet $SmCo_5$. We subsequently apply it to prospective rare-earth hard magnetic intermetallics of the $RFe_{12}X$ family (where R = Nd, Sm and X can be N, Li, or vacancy). Our calculations reproduce the strong out-of-plane anisotropy of $NdFe_{12}N$ due to a large positive value of the key CFP $A^0_2\langle r^2\rangle$ induced by insertion of N. Interestingly, we find that interstitial Li has a strong opposite effect, leading to a large negative value of $A^0_2\langle r^2\rangle$. We thus predict a strong out-of-plane anisotropy in the hypothetical compound $SmFe_{12}Li$. We also find the anisotropy in $SmFe_{12}Li$ to persist to higher temperatures as compared to $NdFe_{12}N$. Hence, Sm-based compounds may represent interesting candidates for hard magnetic applications. Of course, the thermodynamic stability of $SmFe_{12}Li$ and technological feasibility of Li doping still need to be demonstrated by future studies.

We analyze the effect of N and Li interstitials on $A^0_2\langle r^2\rangle$ by evaluating the Bader charges as well as by studying the leakage

of $4f$ Wannier orbitals to interstitial sites and quantifying the $4f$ hybridization with N $2p$ and Li $2s$ states.

Extensions of the present approach beyond the Hubbard-I approximation are promising for applications to other rare-earth intermetallics. In particular, a similar DFT+DMFT technique suppressing subtle self-interaction and double-counting contributions to the Kohn-Sham potential might be necessary to study, for example, the impact of a spin-polarized transition-metal sublattice on heavy-fermion behavior in Yb-based intermetallics [65,66].

ACKNOWLEDGMENTS

This work was supported by IDRIS/GENCI Orsay under project t2017091393, the ECOS-Sud Grant No. A13E04, the French Agence Nationale de la Recherche in the framework of the international collaborative DFG-ANR project RE-MAP, and the European Research Council under its Consolidator Grant scheme (project 617196). L.P. acknowledges the financial support of the Ministry of Education and Science of the Russian Federation (Grant No. 14.Y26.31.0005). T.M. acknowledges the financial support by the Ministry of Education, Culture, Sports, Science and Technology (MEXT) of Japan as a social and scientific priority issue (creation of new functional devices and high-performance materials to support next-generation industries, CDMSI) to be tackled by using post-K computer, and also by MEXT KAKENHI Grant No. 16H06345. We thank Tilmann Hickel, Halil Soezen, Antoine Georges, and Dominique Givord for useful discussions.

APPENDIX A: CRYSTAL-FIELD PARAMETERS IN $SmCo_5$

$SmCo_5$ has been studied more extensively than other hard magnetic rare-earth intermetallics, so ample experimental data are available in this case. In particular, several groups estimated the CF parameters using inelastic neutron scattering or magnetization measurements. Therefore, this compound is a good benchmark to test our approach. $SmCo_5$ has already been studied within DFT+Hub-I to evaluate its ground-state magnetization and photoemission spectra [42], but the CF parameters were not calculated in this work.

The calculated spectral function of $SmCo_5$ is shown in Fig. 8. We find a total magnetic moment on the $4f$ shell of Sm of 0.42 μ_B, antiparallel with the Co moments. This compares well with the measured value of 0.38 μ_B at 4.2 K [18].

The calculated CFP and exchange fields for $SmCo_5$ are listed in Table IV, together with experimental data. The calculations on $SmCo_5$ are done at the experimental lattice constants.

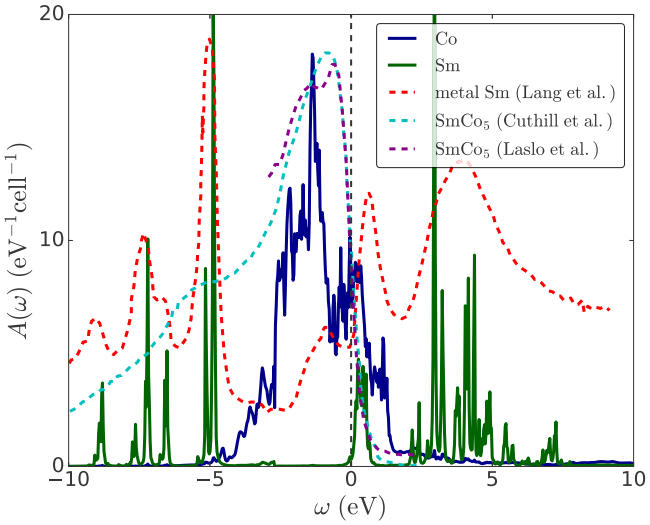

FIG. 8. Atom-resolved spectral function of $SmCo_5$ obtained within self-consistent spin-polarized DFT+Hubbard-I (full lines). The two inequivalent Co types are summed to give the total Co $3d$ spectral function. The occupied part of the experimental spectrum of $SmCo_5$ (light blue from Ref. [67] and purple from Ref. [68]) and the full experimental spectrum of metal Sm (red, from Ref. [62]) are shown for comparison in dotted lines.

One may notice that the CF parameter $A_2^0\langle r^2\rangle$ exhibits a strong dependence on the spin polarization; it is about twice larger in the FM phase. For other CF parameters this dependence is small.

Our results for $A_2^0\langle r^2\rangle$ are in good agreement with the experimental (rather wide) range from about -180 to -420 K. The calculated $B_{\rm ex}$ also agrees rather well with the experimental range from 260 to 360 T. One may notice that the experimental measurements were performed at room temperature, hence, in ferromagnetic $SmCo_5$. Also, the most recent experimental values [20] of $A_2^0\langle r^2\rangle$ are in very good agreement with our results for the FM phase.

The main discrepancy between our theoretical and experimental CFP lies in the large value that we find for $A_6^6\langle r^6\rangle$. The high-order CF parameters are usually assumed to be rather small in $SmCo_5$. However, as noted in Ref. [70], experimental inelastic neutron and susceptibility data are not particularly sensitive to those high-order parameters. Hence, they are often assumed to be small from the onset and neglected in the fitting procedure.

In order to facilitate the reproducibility of our calculations, we provide below the one-electron Hamiltonian of Eq. (7) for a converged, ferromagnetic calculation of $SmCo_5$, used to obtain the CFP of Table IV.

$$\hat{H}_{\rm 1el}^{\uparrow\uparrow} = \begin{pmatrix} -26.5763 & 0 & 0 & 0 & 0 & 0 & 0.0235 \\ 0 & -26.5003 & 0 & 0 & 0 & 0 & 0 \\ 0 & 0 & -26.4465 & 0 & 0 & 0 & 0 \\ 0 & 0 & 0 & -26.3511 & 0 & 0 & 0 \\ 0 & 0 & 0 & 0 & -26.2796 & 0 & 0 \\ 0 & 0 & 0 & 0 & 0 & -26.1675 & 0 \\ 0.0235 & 0 & 0 & 0 & 0 & 0 & -26.0800 \end{pmatrix},$$

TABLE IV. Calculated CF parameters in ferromagnetic (FM) and paramagnetic (PM) $SmCo_5$ in Kelvin. For the FM case we list the CF parameters for each spin direction. The exchange field in the FM phase (in Tesla) is also listed. For comparison, measured and calculated values from several groups are also given. References corresponding to an experimental work are denoted by the symbol †.

	PM	FM		Tils *et al.*	Zhao *et al.*	Givord *et al.*	Sankar *et al.*	Bushow *et al.*	Richter *et al.*	Hummler *et al.*	Novak *et al.*
		↑	↓	Ref. [20]†	Ref. [19]†	Ref. [18]†	Ref. [17]†	Ref. [16]†	Ref. [69]	Ref. [70]	Ref. [71]
$A_2^0\langle r^2\rangle$	−140	−313	−262	−326	−330	−200	−420	−180	−755	−509	−160
$A_4^0\langle r^4\rangle$	−40	−40	−55	–	−45	0	25	0	−37	−20	−33
$A_6^0\langle r^6\rangle$	33	35	25	–	0	50	0	0	11	2	40
$A_6^6\langle r^6\rangle$	−684	−731	−593	–	0	0	6	0	290	−55	168
B_{ex} (T)	–	227		260	327.5	260.5	357	298	–	279	–

$$\hat{H}_{1el}^{\downarrow\downarrow} = \begin{pmatrix} -26.1093 & 0 & 0 & 0 & 0 & 0 & 0.0191 \\ 0 & -26.1926 & 0 & 0 & 0 & 0 & 0 \\ 0 & 0 & -26.3023 & 0 & 0 & 0 & 0 \\ 0 & 0 & 0 & -26.3802 & 0 & 0 & 0 \\ 0 & 0 & 0 & 0 & -26.4688 & 0 & 0 \\ 0 & 0 & 0 & 0 & 0 & -26.5252 & 0 \\ 0.0191 & 0 & 0 & 0 & 0 & 0 & -26.6069 \end{pmatrix},$$

$$\hat{H}_{1el}^{\uparrow\downarrow} = (\hat{H}_{1el}^{\downarrow\uparrow})^{\dagger} = \begin{pmatrix} 0 & 0.2032 & 0 & 0 & 0 & 0 & 0 \\ 0 & 0 & 0.2632 & 0 & 0 & 0 & 0 \\ 0 & 0 & 0 & 0.2893 & 0 & 0 & 0 \\ 0 & 0 & 0 & 0 & 0.2886 & 0 & 0 \\ 0 & 0 & 0 & 0 & 0 & 0.2633 & 0 \\ -0.0002 & 0 & 0 & 0 & 0 & 0 & 0.2036 \\ 0 & -0.0003 & 0 & 0 & 0 & 0 & 0 \end{pmatrix},$$

where

$$\hat{H}_{1el} = \begin{pmatrix} \hat{H}_{1el}^{\uparrow\uparrow} & \hat{H}_{1el}^{\uparrow\downarrow} \\ \hat{H}_{1el}^{\downarrow\uparrow} & \hat{H}_{1el}^{\downarrow\downarrow} \end{pmatrix}.$$

APPENDIX B: EIGENENERGIES AND EIGENSTATES OF THE 4*f* SHELLS IN $SmCo_5$ AND $RFe_{12}X$

In this Appendix we present the actual converged eigenfunctions and eigenstates of the $4f$ shell obtained within our DFT+Hub-I approach. In Tables V and VI we list those eigenenergies and the corresponding wave functions for the ground-state multiplet, as well as for the lowest-energy state of the first exited multiplet, in all the materials considered. The eigenenergies are given with respect to the ground state. The eigenvalues are expanded in the basis of total angular momentum J as $\sum_{J,m_J} a(J,m_J)|J;m_J\rangle$; we include all contributions with $|a(J,m_J)| > 0.03$.

One sees that the eigenstates of Sm belonging to the ground-state multiplet feature a rather significant admixture of the exited $J = 7/2$ multiplet. The intermultiplet mixing is markedly lower in the case of Nd.

To our awareness, only $4f$ eigenstates in $SmCo_5$ have been measured to date. Our calculated intra- and intermultiplet splittings are in good agreement with the results of of Tils *et al.* [20] and Givord *et al.* [18], see the lowest panel of Table VI. Moreover, the actual eigenstates and their order are also in very good agreement with the magnetic form-factor measurements [18,72], especially for the lowest-energy states [73].

APPENDIX C: IMPORTANCE OF THE CHARGE AVERAGING

In this Appendix we explicitly demonstrate the effect of averaging of $4f$ charge density [Eq. (8)] by comparing the CFP calculated with and without this averaging [but in both cases the $4f$ magnetic density is suppressed following Eq. (10)] in two materials, $NdFe_{12}N$ and $SmCo_5$, that are known to have an out-of-plane magnetic anisotropy.

The corresponding values are displayed in Table VII. One sees that the difference is largest for the lowest-order CFP $A_2^0\langle r^2\rangle$, where calculations without averaging lead to the wrong sign with respect to experiment (suggesting in-plane anisotropy in both cases). Hence, the proper averaging of $4f$ charge density is crucial for a correct description of the single-ion anisotropy. For the higher order terms the difference between two approaches is smaller. This suggests that the self-interaction contribution in the CFP has predominantly $l = 2$ symmetry.

APPENDIX D: DEPENDENCE OF RESULTS ON COULOMB *U* AND HUND'S J_H

To perform DFT+DMFT calculations, we have to choose a value for the on-site screened Coulomb interaction parameter

TABLE V. Energies (in meV) and wave functions (expanded in the total angular momentum J basis) of the atomic eigenstates in the ground-state multiplet (GSM) and of the lowest eigenstate of the first excited multiplet (FEM) for $NdFe_{12}X$.

		$NdFe_{12}$
GSM	0	$0.996\|9/2;+9/2\rangle + 0.081\|11/2;+9/2\rangle$
	8	$0.995\|9/2;+5/2\rangle + 0.094\|11/2;+5/2\rangle$
	18	$0.989\|9/2;+3/2\rangle + 0.145\|11/2;+3/2\rangle - 0.037\|9/2;-5/2\rangle$
	18	$0.999\|9/2;+7/2\rangle + 0.042\|11/2;+7/2\rangle$
	39	$0.989\|9/2;+1/2\rangle + 0.145\|11/2;+1/2\rangle - 0.032\|9/2;-7/2\rangle$
	51	$0.996\|9/2;-3/2\rangle + 0.085\|11/2;-3/2\rangle$
	51	$0.994\|9/2;-1/2\rangle + 0.105\|11/2;-1/2\rangle$
	56	$0.992\|9/2;-5/2\rangle + 0.121\|11/2;-5/2\rangle + 0.038\|9/2;+3/2\rangle$
	82	$0.985\|9/2;-7/2\rangle + 0.166\|11/2;-7/2\rangle + 0.033\|9/2;+1/2\rangle$
	88	$0.998\|9/2;-9/2\rangle + 0.057\|11/2;-9/2\rangle$
FEM	309	$0.987\|11/2;+5/2\rangle + 0.126\|13/2;+5/2\rangle - 0.093\|9/2;+5/2\rangle - 0.046\|11/2;-3/2\rangle$
		$NdFe_{12}N$
GSM	0	$0.994\|9/2;+9/2\rangle + 0.092\|11/2;+9/2\rangle - 0.054\|9/2;+1/2\rangle$
	32	$0.998\|9/2;+5/2\rangle + 0.065\|11/2;+5/2\rangle$
	38	$0.994\|9/2;+3/2\rangle + 0.106\|11/2;+3/2\rangle$
	41	$0.997\|9/2;+7/2\rangle - 0.065\|9/2;-1/2\rangle$
	56	$0.993\|9/2;+1/2\rangle + 0.101\|11/2;+1/2\rangle + 0.055\|9/2;+9/2\rangle$
	66	$0.998\|9/2;-3/2\rangle + 0.052\|11/2;-3/2\rangle$
	66	$0.966\|9/2;-1/2\rangle - 0.242\|9/2;-9/2\rangle + 0.064\|9/2;+7/2\rangle + 0.061\|11/2;-1/2\rangle$
	67	$0.996\|9/2;-5/2\rangle + 0.077\|11/2;-5/2\rangle$
	73	$0.970\|9/2;-9/2\rangle + 0.241\|9/2;-1/2\rangle$
	80	$0.996\|9/2;-7/2\rangle + 0.093\|11/2;-7/2\rangle$
FEM	301	$0.994\|11/2;+11/2\rangle + 0.091\|13/2;+11/2\rangle - 0.051\|11/2;+3/2\rangle$
		$NdFe_{12}Li$
GSM	0	$0.993\|9/2;+7/2\rangle + 0.116\|11/2;+7/2\rangle$
	16	$0.990\|9/2;+5/2\rangle + 0.137\|11/2;+5/2\rangle$
	24	$0.994\|9/2;+9/2\rangle + 0.105\|9/2;+1/2\rangle$
	31	$0.989\|9/2;+3/2\rangle + 0.137\|11/2;+3/2\rangle - 0.041\|9/2;-5/2\rangle$
	40	$0.983\|9/2;+1/2\rangle + 0.146\|11/2;+1/2\rangle - 0.107\|9/2;+9/2\rangle$
	51	$0.986\|9/2;-1/2\rangle + 0.163\|11/2;-1/2\rangle$
	65	$0.985\|9/2;-3/2\rangle + 0.166\|11/2;-3/2\rangle$
	80	$0.988\|9/2;-5/2\rangle + 0.148\|11/2;-5/2\rangle + 0.042\|9/2;+3/2\rangle$
	93	$0.990\|9/2;-7/2\rangle + 0.135\|11/2;-7/2\rangle$
	126	$0.984\|9/2;-9/2\rangle + 0.179\|11/2;-9/2\rangle$
FEM	319	$0.983\|11/2;+7/2\rangle + 0.134\|13/2;+7/2\rangle - 0.116\|9/2;+7/2\rangle + 0.042\|11/2;-1/2\rangle$

U and for the Hund's coupling parameter J_H. Several methods have been developed in order to compute those parameters from first principles, most notably the constrained local density approximation [74] and, more recently, the constrained random phase approximation [64].

In the present work, however, we do not attempt a first principles determination. We use $U = 6$ eV and $J_H = 0.85$ eV because these values have given satisfactory results in other calculations on rare-earth materials [41,53]. They are also in line with reported values calculated from first principles [60]. Nevertheless, it is preferable that results obtained by our calculation scheme do not depend too strongly on the value of U and J_H. In Fig. 9 we show that the dependence of the CFP $A_2^0\langle r^2\rangle$ in $NdFe_{12}N$ is very moderate, as long as the values of U and J are chosen within a reasonable ranges for rare-earth ions.

Furthermore, we observe that smaller values of U lead to slightly larger values of $A_2^0\langle r^2\rangle$: this is not surprising if we keep in mind that a large U is favorable to a strong localization of the $4f$ electrons, hence to a weaker coupling to the crystal field.

APPENDIX E: DEPENDENCE OF RESULTS ON WINDOW SIZE

Another important parameter of our calculations is the size of the window around the Fermi level that we use to construct the $4f$ Wannier functions. In Fig. 10 we compare the Wannier orbitals constructed for the same orbital $m = 0$ in $NdFe_{12}Li$ for two different window sizes: a small window with $\omega_{\text{win}} = 2$ eV, and a large one with $\omega_{\text{win}} = 20$ eV. For the large window, the Wannier orbital (WO) takes essentially pure Nd $4f$ orbital character, while the small-window WO leaks significantly to neighboring sites, in particular, to Li.

The effect of the window size on the CF parameters is shown more quantitatively in Fig. 11, which displays those

TABLE VI. Same as Table V, for $SmFe_{12}X$ and $SmCo_5$. For $SmCo_5$, between brackets next to the calculated energies: energies of the atomic eigenstates measured by Tils *et al.* (left, Ref. [20]) and Givord *et al.* (right, Ref. [18]). Note that only Tils *et al.* directly measure the eigenenergies, while Givord *et al.* obtain them from an atomic Hamiltonian fitted to reproduce the measured magnetic form factor.

	$SmFe_{12}$	
GSM	0	$0.986\|5/2;+5/2\rangle + 0.164\|7/2;+5/2\rangle$
	27	$0.983\|5/2;+3/2\rangle + 0.183\|7/2;+3/2\rangle$
	47	$0.968\|5/2;+1/2\rangle + 0.245\|7/2;+1/2\rangle + 0.043\|9/2;+1/2\rangle$
	69	$0.977\|5/2;-1/2\rangle + 0.209\|7/2;-1/2\rangle + 0.041\|9/2;-1/2\rangle$
	85	$0.976\|5/2;-3/2\rangle + 0.218\|7/2;-3/2\rangle$
	99	$0.987\|5/2;-5/2\rangle + 0.159\|7/2;-5/2\rangle + 0.032\|9/2;-5/2\rangle$
FEM	191	$0.987\|7/2;+7/2\rangle + 0.154\|9/2;+7/2\rangle + 0.034\|7/2;-1/2\rangle$
	$SmFe_{12}N$	
GSM	0	$0.997\|5/2;+5/2\rangle + 0.079\|7/2;+5/2\rangle$
	2	$0.990\|5/2;+3/2\rangle + 0.143\|7/2;+3/2\rangle$
	13	$0.976\|5/2;+1/2\rangle + 0.216\|7/2;+1/2\rangle$
	31	$0.982\|5/2;-1/2\rangle + 0.186\|7/2;-1/2\rangle + 0.035\|9/2;-1/2\rangle$
	48	$0.978\|5/2;-3/2\rangle + 0.209\|7/2;-3/2\rangle$
	75	$0.971\|5/2;-5/2\rangle + 0.238\|7/2;-5/2\rangle$
FEM	176	$0.988\|7/2;+5/2\rangle + 0.129\|9/2;+5/2\rangle - 0.078\|5/2;+5/2\rangle$
	$SmFe_{12}Li$	
GSM	0	$0.977\|5/2;+5/2\rangle + 0.212\|7/2;+5/2\rangle + 0.037\|9/2;+5/2\rangle$
	39	$0.965\|5/2;+3/2\rangle + 0.256\|7/2;+3/2\rangle + 0.047\|9/2;+3/2\rangle$
	67	$0.960\|5/2;+1/2\rangle + 0.278\|7/2;+1/2\rangle + 0.042\|9/2;+1/2\rangle$
	90	$0.946\|5/2;-1/2\rangle + 0.318\|7/2;-1/2\rangle + 0.051\|9/2;-1/2\rangle$
	116	$0.941\|5/2;-3/2\rangle + 0.330\|7/2;-3/2\rangle + 0.068\|9/2;-3/2\rangle$
	137	$0.974\|5/2;-5/2\rangle + 0.221\|7/2;-5/2\rangle + 0.053\|9/2;-5/2\rangle$
FEM	202	$0.977\|7/2;+7/2\rangle + 0.211\|9/2;+7/2\rangle + 0.035\|11/2;+7/2\rangle$
	$SmCo_5$	
GSM	0 (0 / 0)	$0.984\|5/2;+5/2\rangle + 0.171\|7/2;+5/2\rangle$
	33 (31 / 28)	$0.983\|5/2;+3/2\rangle + 0.181\|7/2;+3/2\rangle$
	52(– / 47)	$0.973\|5/2;+1/2\rangle + 0.225\|7/2;+1/2\rangle + 0.033\|9/2;+1/2\rangle$
	71(– / 73)	$0.977\|5/2;-1/2\rangle + 0.209\|7/2;-1/2\rangle + 0.035\|9/2;-1/2\rangle$
	86(– / 91)	$0.977\|5/2;-3/2\rangle + 0.211\|7/2;-3/2\rangle - 0.032\|9/2;+9/2\rangle$
	95(– / 109)	$0.989\|5/2;-5/2\rangle + 0.122\|7/2;-5/2\rangle + 0.073\|7/2;+7/2\rangle + 0.033\|9/2;-5/2\rangle$
FEM	188 (166 / –)	$0.963\|7/2;+7/2\rangle + 0.187\|7/2;-5/2\rangle + 0.164\|9/2;+7/2\rangle - 0.093\|5/2;-5/2\rangle$

parameters computed for several window choices $[-\omega_{\text{win}},\omega_{\text{win}}]$ for different materials. The smallest window size of $\omega_{\text{win}} = 2$ eV is required to enclose all the $4f$-like bands, increasing it to 4 eV includes most of the Fe states and part of the N or Li states inside the window. The largest size of 20 eV gives Wannier functions with essentially pure orbital character. One may notice a relatively mild dependence of the CFP on the choice of the window up to $\omega_{\text{win}} = 8$ eV.

TABLE VII. Crystal-field parameters and exchange field in $NdFe_{12}N$ and $SmCo_5$ in the ferromagnetic phase, calculated with and without averaging over the ground-state multiplet.

	$NdFe_{12}N$				$SmCo_5$			
	with		without		with		without	
	↑	↓	↑	↓	↑	↓	↑	↓
$A_2^0\langle r^2\rangle$	477	653	−190	26	−313	−262	278	331
$A_4^0\langle r^4\rangle$	75	112	30	82	−40	−55	−30	−37
$A_4^4\langle r^4\rangle$	−105	−141	−65	−124	0	0	0	0
$A_6^0\langle r^6\rangle$	32	63	27	64	35	25	38	25
$A_6^4\langle r^6\rangle$	−65	−91	−61	−112	0	0	0	0
$A_6^6\langle r^6\rangle$	0	0	0	0	−731	−593	−945	−806
B_{ex} (T)	217		206		227		235	

APPENDIX F: PROJECTION OF EXTENDED WANNIER ORBITALS TO LOCALIZED WANNIER BASIS

In this Appendix we derive the projection operator between localized and extended Wannier spaces. A set of Wannier-like functions $|\tilde{w}_{lm}^{\alpha\sigma}(\mathbf{k})\rangle$ is constructed for an atom α of the unit cell and quantum numbers $(lm\sigma)$ as a combinations of Kohn-Sham Bloch waves for a range of bands within the chosen energy window $\tilde{\mathcal{W}}$:

$$\left|\tilde{w}_{lm}^{\alpha\sigma}(\mathbf{k})\right\rangle = \sum_{\nu\in\tilde{\mathcal{W}}} \tilde{P}_{lm\nu}^{\alpha\sigma}(\mathbf{k})\left|\phi_\nu^k\right\rangle, \tag{F1}$$

where ϕ_ν^k are the Bloch functions and $\tilde{P}_{lm\nu}^{\alpha\sigma}(\mathbf{k})$ is the corresponding matrix element of the projector constructed as

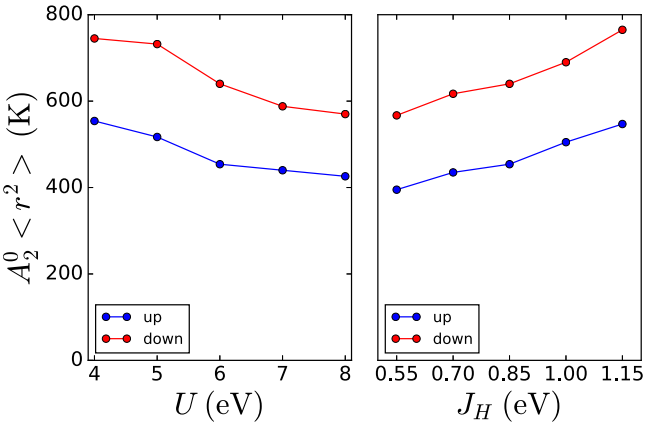

FIG. 9. CFP $A_2^0\langle r^2\rangle$ in $NdFe_{12}N$ as a function of U for $J_H = 0.85$ eV (left-hand panel), and as a function of J_H for $U = 6$ eV (right-hand panel). Our reference values are ($U = 6$ eV, $J_H = 0.85$ eV).

described in Refs. [50,51]. The corresponding real-space Wannier functions are then obtained by a Fourier transformation

$$\tilde{w}_{lm}^{\alpha\sigma}(\mathbf{r}) = \sum_{\mathbf{k}} e^{-i\mathbf{k}.\mathbf{r}} \left|\tilde{w}_{lm}^{\alpha\sigma}(\mathbf{k})\right\rangle. \tag{F2}$$

We assume that the window $\tilde{\mathcal{W}}$ in Eq. (F1) is *large*, i.e., that it includes both rare-earth $4f$ states and all relevant valence bands that are expected to hybridize with them. As a result, with such a large-window construction one obtains a set of mutually orthogonal and rather well localized Wannier orbtials (WO). In particular, the large-window $4f$ WOs $\tilde{w}_{lm}^{\alpha\sigma}(\mathbf{r})$ almost do not leak onto neighboring sites, as discussed in the previous section, see Fig. 10(a). If one constructs as many WOs as the number of Kohn-Sham bands within $\tilde{\mathcal{W}}$ then the projection operator $\tilde{P}(\mathbf{k})$ is just a unitary transformation, hence, Eq. (F1) can be inverted

$$\left|\phi_\nu^k\right\rangle \approx \sum_{\alpha\sigma lm} \left[\tilde{P}_{lm\nu}^{\alpha\sigma}(\mathbf{k})\right]^* \left|\tilde{w}_{lm}^{\alpha\sigma}(\mathbf{k})\right\rangle, \tag{F3}$$

where the equality is approximate because high-energy empty bands usually cross and, hence, one cannot generally chose such a window as to have the same number of bands for all $\mathbf{k}$ points. However, those high-energy states are far from the relevant region close to the Fermi level, and if one applies Eq. (F3) to the bands within a *small* window $\mathcal{W}$ around the the

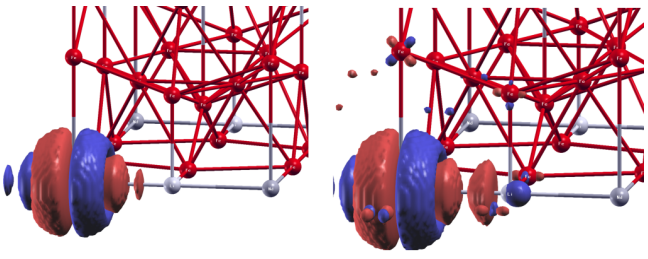

(a) $[-20, 20]$ eV window (b) $[-2, 2]$ eV window

FIG. 10. $NdFe_{12}Li$ $4f$ Wannier orbital $m = 0$ constructed with a large window $[-20,20]$ eV (left) and a small window $[-2,2]$ eV (right). The use of a large window essentially removes all hybridization between the rare-earth and neighboring atoms.

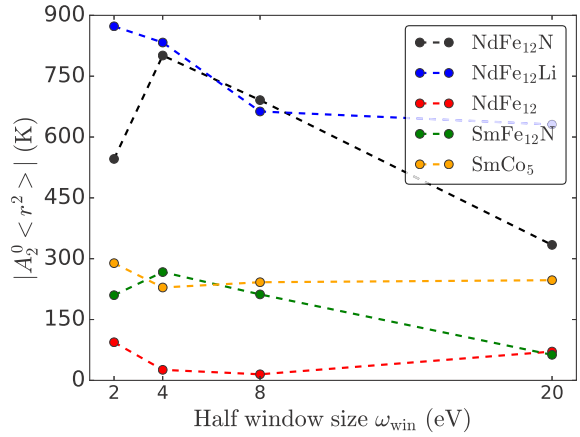

FIG. 11. Absolute value of the CFP $A_2^0\langle r^2\rangle$ as a function of window size $\omega_{\rm win}$ for $NdFe_{12}$, $NdFe_{12}N$, $NdFe_{12}Li$, and $SmCo_5$.

Fermi energy the resulting small nonunitarity of $P(\mathbf{k})$ can be neglected.

Alternatively, one may construct $4f$ Wannier orbitals from the bands within that small window $\mathcal{W}$ enclosing mainly $4f$-like Kohn-Sham bands:

$$\left|w_m^\sigma(\mathbf{k})\right\rangle = \sum_{\nu\in\mathcal{W}} P_{m\nu}^\sigma(\mathbf{k})\left|\phi_\nu^k\right\rangle, \tag{F4}$$

where $4f$ WOs are constructed for the single rare-earth site in the unit cell for the compounds under consideration. Hence, the site and l labels are suppressed in $|w_m^\sigma(\mathbf{k})\rangle$. The resulting small-window WOs are rather extended in real space, as one sees in Figs. 5 and 10(b).

Inserting the expansion Eq. (F3) of the KS states $|\phi_\nu^k\rangle$ into Eq. (F4) one obtains

$$\begin{aligned}\left|w_m^\sigma(\mathbf{k})\right\rangle &= \sum_{\nu\in\mathcal{W}}\sum_{lm'\sigma'} P_{m\nu}^\sigma(\mathbf{k})\left[\tilde{P}_{lm'\nu}^{\alpha\sigma'}(\mathbf{k})\right]^*\left|\tilde{w}_{lm'}^{\alpha\sigma'}(\mathbf{k})\right\rangle \\ &= \sum_{\alpha\sigma' lm'} U_{m,lm'}^{\sigma,\alpha\sigma'}(\mathbf{k})\left|\tilde{w}_{lm'}^{\alpha\sigma'}(\mathbf{k})\right\rangle,\end{aligned} \tag{F5}$$

where

$$U_{m,l'm'}^{\sigma,\alpha\sigma'}(\mathbf{k}) = \sum_{\nu\in\mathcal{W}} P_{m\nu}^\sigma(\mathbf{k})\left[\tilde{P}_{lm'\nu}^{\alpha\sigma'}(\mathbf{k})\right]^*. \tag{F6}$$

We use these projectors $U_{m,l'm'}^{\sigma,\alpha\sigma'}(\mathbf{k})$ to project the $4f$ spectral function computed in the small-window WO basis on large-window localized WOs representing other states (Fe $3d$, N $2p$, Li $2s$, and so on). Namely, having obtained the real-axis lattice Green's function in the small-window Wannier basis for the orbital (σm) of the $4f$ shell $G_{m\sigma}(\mathbf{k},\omega + i\delta)$, as well as the corresponding partial spectral function $\rho_{m\sigma}(\omega) = -\frac{1}{\pi}\mathrm{Im}G_{m\sigma}(\mathbf{k},\omega + i\delta)$, we compute the different orbital contributions into it as follows:

$$\begin{aligned}\tilde{\rho}_{\alpha l}^{m\sigma}(\omega) = -\frac{1}{\pi}\mathrm{Im}\sum_k\sum_{m'\sigma'}&\left[U_{m,lm'}^{\sigma,\alpha\sigma'}(\mathbf{k})\right]^* \\ &\times G_{m\sigma}(\mathbf{k},\omega + i\delta)U_{m,lm'}^{\sigma,\alpha\sigma'}(\mathbf{k}),\end{aligned} \tag{F7}$$

where $\tilde{\rho}_{\alpha l}^{m\sigma}(\omega)$ is the fraction of the $4f$ spectral function of orbital index (σm) with the character (αl). Using Eq. (F3) and

the orthonormality of small-window WOs:

$$\left\langle w_m^{\sigma}(\mathbf{k})\middle| w_{m'}^{\sigma'}(\mathbf{k})\right\rangle = \delta_{mm'}\delta_{\sigma\sigma'} = \sum_{\nu}\left[P_{m\nu}^{\sigma}(\mathbf{k})\right]^{*} P_{m'\nu}^{\sigma'}(\mathbf{k}),$$

one may easily show the completeness of the expansion (F7)

$$\sum_{\alpha l}\tilde{\rho}_{\alpha l}^{m\sigma}(\omega) = \rho_{m\sigma}(\omega).$$

[1] K. Strnat, IEEE Trans. Magn. **6**, 182 (1970).
[2] J. Herbst, Rev. Mod. Phys. **63**, 819 (1991).
[3] W. Körner, G. Krugel, and C. Elsässer, Sci. Rep. **6**, 24686 (2016).
[4] S. Suzuki, T. Kuno, K. Urushibata, K. Kobayashi, N. Sakuma, K. Washio, M. Yano, A. Kato, and A. Manabe, J. Magn. Magn. Mater. **401**, 259 (2016).
[5] Y. Harashima, K. Terakura, H. Kino, S. Ishibashi, and T. Miyake, Phys. Rev. B **92**, 184426 (2015).
[6] Y. Hirayama, Y. Takahashi, S. Hirosawa, and K. Hono, Scr. Mater. **95**, 70 (2015).
[7] T. Miyake, K. Terakura, Y. Harashima, H. Kino, and S. Ishibashi, J. Phys. Soc. Jpn. **83**, 043702 (2014).
[8] J. Coey, IEEE Trans. Magn. **47**, 4671 (2011).
[9] J. M. D. Coey, *Rare-Earth Iron Permanent Magnets* (Oxford University Press, Oxford, 1996), Vol. 54.
[10] O. Gutfleisch, M. A. Willard, E. Brück, C. H. Chen, S. Sankar, and J. P. Liu, Adv. Mater. **23**, 821 (2011).
[11] M. Matsumoto, H. Akai, Y. Harashima, S. Doi, and T. Miyake, J. Appl. Phys. **119**, 213901 (2016).
[12] Y. Harashima, K. Terakura, H. Kino, S. Ishibashi, and T. Miyake, J. Appl. Phys. **120**, 203904 (2016).
[13] M. T. Hutchings, Solid State Phys. **16**, 227 (1964).
[14] D. Newman and B. Ng, Rep. Prog. Phys. **52**, 699 (1989).
[15] C. Brecher, H. Samelson, A. Lempicki, R. Riley, and T. Peters, Phys. Rev. **155**, 178 (1967).
[16] K. H. J. Buschow, A. M. van Diepen, and H. W. de Wijn, Solid State Commun. **15**, 903 (1974).
[17] S. Sankar, V. Rao, E. Segal, W. Wallace, W. Frederick, and H. Garrett, Phys. Rev. B **11**, 435 (1975).
[18] D. Givord, J. Laforest, J. Schweizer, and F. Tasset, J. Appl. Phys. **50**, 2008 (1979).
[19] Z. Tie-Song, J. Han-Min, G. Guang-Hua, H. Xiu-Feng, and C. Hong, Phys. Rev. B **43**, 8593 (1991).
[20] P. Tils, M. Loewenhaupt, K. Buschow, and R. Eccleston, J. Alloys Compd. **289**, 28 (1999).
[21] R. Coehoorn, J. Magn. Magn. Mater. **99**, 55 (1991).
[22] G. Daalderop, P. Kelly, and M. Schuurmans, J. Magn. Magn. Mater. **104**, 737 (1992).
[23] L. Steinbeck, M. Richter, H. Eschrig, and U. Nitzsche, Phys. Rev. B **49**, 16289 (1994).
[24] P. Novák and J. Kuriplach, Phys. Rev. B **50**, 2085 (1994).
[25] L. Steinbeck, M. Richter, U. Nitzsche, and H. Eschrig, Phys. Rev. B **53**, 7111 (1996).
[26] P. Novák, Phys. Status Solidi B **198**, 729 (1996).
[27] L. Ning and G. P. Brivio, Phys. Rev. B **75**, 235126 (2007).
[28] L. Hu, M. F. Reid, C.-K. Duan, S. Xia, and M. Yin, J. Phys.: Condens. Matter **23**, 045501 (2011).
[29] P. Novák, K. Knížek, and J. Kuneš, Phys. Rev. B **87**, 205139 (2013).
[30] M. Brooks, O. Eriksson, J. Wills, and B. Johansson, Phys. Rev. Lett. **79**, 2546 (1997).
[31] M. W. Haverkort, M. Zwierzycki, and O. K. Andersen, Phys. Rev. B **85**, 165113 (2012).
[32] S. T. Liddle and J. van Slageren, Chem. Soc. Rev. **44**, 6655 (2015).
[33] L. Ungur and L. F. Chibotaru, Chem. Eur. J. **23**, 3708 (2017).
[34] F. Zhou, V. Ozoliņš *et al.*, Phys. Rev. B **83**, 085106 (2011).
[35] F. Zhou, V. Ozoliņš *et al.*, Phys. Rev. B **80**, 125127 (2009).
[36] V. I. Anisimov, A. I. Poteryaev, M. A. Korotin, A. O. Anokhin, and G. Kotliar, J. Phys.: Condens. Matter **9**, 7359 (1997).
[37] A. Lichtenstein and M. Katsnelson, Phys. Rev. B **57**, 6884 (1998).
[38] S. Lebègue, G. Santi, A. Svane, O. Bengone, M. Katsnelson, A. Lichtenstein, and O. Eriksson, Phys. Rev. B **72**, 245102 (2005).
[39] S. Lebègue, A. Svane, M. Katsnelson, A. Lichtenstein, and O. Eriksson, J. Phys.: Condens. Matter **18**, 6329 (2006).
[40] L. V. Pourovskii, K. T. Delaney, C. G. Van de Walle, N. A. Spaldin, and A. Georges, Phys. Rev. Lett. **102**, 096401 (2009).
[41] I. L. M. Locht, Y. O. Kvashnin, D. C. M. Rodrigues, M. Pereiro, A. Bergman, L. Bergqvist, A. I. Lichtenstein, M. I. Katsnelson, A. Delin, A. B. Klautau *et al.*, Phys. Rev. B **94**, 085137 (2016).
[42] O. Grånäs, I. D. Marco, P. Thunström, L. Nordström, O. Eriksson, T. Björkman, and J. Wills, Comput. Mater. Sci. **55**, 295 (2012).
[43] K. Stevens, Proc. Phys. Soc. Sect. A **65**, 209 (1952).
[44] B. G. Wybourne and W. F. Meggers, *Spectroscopic Properties of Rare Earths* (Interscience Publishers, New York, 1965).
[45] J. Mulak and Z. Gajek, *The Effective Crystal Field Potential* (Elsevier, Amsterdam, 2000).
[46] D. J. Newman and B. Ng, *Crystal Field Handbook* (Cambridge University Press, Cambridge, 2007).
[47] M. Aichhorn, L. Pourovskii, P. Seth, V. Vildosola, M. Zingl, O. E. Peil, X. Deng, J. Mravlje, G. J. Kraberger, C. Martins *et al.*, Comput. Phys. Commun. **204**, 200 (2016).
[48] O. Parcollet, M. Ferrero, T. Ayral, H. Hafermann, I. Krivenko, L. Messio, and P. Seth, Comput. Phys. Commun. **196**, 398 (2015).
[49] P. Blaha, K. Schwarz, G. Madsen, D. Kvasnicka, and J. Luitz, *WIEN2k, An Augmented Plane Wave + Local Orbitals Program for Calculating Crystal Properties* (Techn. Universitat Wien, Austria, 2001).
[50] B. Amadon, F. Lechermann, A. Georges, F. Jollet, T. O. Wehling, and A. I. Lichtenstein, Phys. Rev. B **77**, 205112 (2008).
[51] M. Aichhorn, L. Pourovskii, V. Vildosola, M. Ferrero, O. Parcollet, T. Miyake, A. Georges, and S. Biermann, Phys. Rev. B **80**, 085101 (2009).
[52] F. Lechermann, A. Georges, A. Poteryaev, S. Biermann, M. Posternak, A. Yamasaki, and O. Andersen, Phys. Rev. B **74**, 125120 (2006).
[53] L. V. Pourovskii, B. Amadon, S. Biermann, and A. Georges, Phys. Rev. B **76**, 235101 (2007).
[54] M. Aichhorn, L. Pourovskii, and A. Georges, Phys. Rev. B **84**, 054529 (2011).
[55] L. Pourovskii (private communication).

[56] M. Czyżyk and G. Sawatzky, Phys. Rev. B **49**, 14211 (1994).
[57] We consider the case of T being much lower than the intermultiplet splitting, hence the contribution of excited multiplets into the partition function Z can be neglected
[58] An equivalent approach would be to make the one-electron Hamiltonian that serves as an input to the Hubbard-I solver spherically symmetric: Both approaches should be equivalent and nearly equally simple to implement.
[59] Y. Harashima, K. Terakura, H. Kino, S. Ishibashi, and T. Miyake, in *Proceedings of Computational Science Workshop 2014 (CSW2014)* (2015), p. 011021.
[60] F. Nilsson, R. Sakuma, and F. Aryasetiawan, Phys. Rev. B **88**, 125123 (2013).
[61] In rare earth ions one typically has $U \gg J_H \gg \lambda$, hence, the atomic multiplet structure is set within the LS-coupling scheme. With the crystal field splitting in lanthanides being typically much smaller than all those energy scales one may neglect the mixture between different multiplets, in that case CFP exhibits only very weak dependence to U and J_H.
[62] J. K. Lang, Y. Baer, and P. A. Cox, J. Phys. F **11**, 121 (1981).
[63] R. F. W. Bader, *Atoms in Molecules: A Quantum Theory* (Clarendon Press, Oxford, 1990).
[64] F. Aryasetiawan, M. Imada, A. Georges, G. Kotliar, S. Biermann, and A. I. Lichtenstein, Phys. Rev. B **70**, 195104 (2004).
[65] T. Mazet, D. Malterre, M. François, C. Dallera, M. Grioni, and G. Monaco, Phys. Rev. Lett. **111**, 096402 (2013).
[66] T. Mazet, D. Malterre, M. François, L. Eichenberger, M. Grioni, C. Dallera, and G. Monaco, Phys. Rev. B **92**, 075105 (2015).
[67] J. Cuthill, A. McAlister, N. Erickson, and R. Watson, AIP Conf. Proc. **18**, 1039 (1974).
[68] A. Laslo, R. Dudric, M. Neumann, O. Isnard, M. Coldea, and V. Pop, Solid State Commun. **199**, 43 (2014).
[69] M. Richter, L. Steinbeck, U. Nitzsche, P. M. Oppeneer, and H. Eschrig, J. Alloys Compd. **225**, 469 (1995).
[70] K. Hummler and M. Fähnle, Phys. Rev. B **53**, 3272 (1996).
[71] P. Novak and J. Kuriplach, IEEE Trans. Magn. **30**, 1036 (1994).
[72] J. Laforest, Ph.D. thesis, USM-INP, Grenoble, 1981.
[73] The opposite sign of the $J = 7/2$ contributions in Refs. [18,72] with respect to ours is due to their choice for the coordination frame, with the z axis aligned to the spin moment of Sm. We align z with the spin of Co sublattice, hence opposite to the Sm spin. Flipping the direction of the z axis leads to the change in the relative sign between the $J = 5/2$ and $J = 7/2$ contributions. There is a mismatch between the signs of m_J in $|J,m_J\rangle$ reported in Refs. [18,72]. The correct signs are reported in Ref. [72] (D. Givord, private communication).
[74] P. Dederichs, S. Blügel, R. Zeller, and H. Akai, Phys. Rev. Lett. **53**, 2512 (1984).

ÉCOLE DOCTORALE
Physique en île-de-France (EDPIF)

Titre : Physique à N corps des électrons dans les composes de métaux de transition et de terre rares : structure électronique, propriétés magnétiques et défauts cristallins ponctuels à partir des premiers principes

Mots clés : structure électronique, électrons corrélés, physique à N corps, calculs *ab initio*, théorie du champ moyen dynamique

Résumé :

Les propriétés structurelles, magnétiques et de conduction des matériaux sont déterminées par le comportement des électrons qui lient leurs atomes.

Parmi les plus importantes avancées technologiques du 20e siècle ont eu lieu dans le domaine des semi-conducteurs, dans lesquels les électrons se comportent comment un gaz peu dense interagissant faiblement. Pour les applications technologiques à venir, en revanche, les oxydes sont parmi les matériaux les plus prometteurs.

Dans les oxydes de métaux de transition ou de terres rares, ainsi que dans certains métaux purs et alliages, la répulsion entre électrons peut donner lieu à des propriétés exotiques et à des transitions de phase.

Dans cette thèse, nous avons développé des méthodes partant des "premiers principes" de la physique pour évaluer le comportement d'électrons en interaction et les propriétés physiques qui en découlent. Nous avons appliqué ces outils à plusieurs matériaux dont le fer, le dioxyde de vanadium et les aimants permanents.

Title: Many-electron effects in transition metal and rare earth compounds: Electronic structure, magnetic properties and point defects from first principles

Keywords: many-body physics, correlated electrons, ab initio calculation, electronic structure, dynamical mean-field theory

Abstract:

The structural, spectral, magnetic, and many other properties of materials are mostly determined by the behavior of the electrons that glue the atoms together.

Some of the most important technological advances of the 20th century were made in the field of semi-conductors, where electrons behave like a dilute gas of weakly interacting particles. In contrast, many of the most promising materials for technological applications today are oxides.

In transition metal or rare earth oxides, but also in some pure metals or alloys, the Coulomb repulsion between the electrons can give rise to exotic properties and phase transitions.

In this thesis, we developed and applied first-principles (i.e. based on fundamental laws of physics) methods to evaluate the behavior of electrons interacting with each other and the physical properties stemming from it.

We use these tools to study several materials of fundamental and technological interest, in particular iron, vanadium dioxide and hard magnets.

Université Paris-Saclay
Espace Technologique / Immeuble Discovery
Route de l'Orme aux Merisiers RD 128 / 91190 Saint-Aubin, France